Sol-gel Planar Lightwave Circuits for Sensing and Telecommunications

by
Robert Copperwhite

A thesis presented to Dublin City University
for the Degree of Doctor of Philosophy

Research supervisor:
Prof. Brian MacCraith
School of Physical Sciences
National Centre for Sensor Research
Dublin City University

July 2008

Declaration

I hereby certify that this material, which I now submit for assessment on the programme of study leading to the award of Doctor of Philosophy is entirely my own work, that I have exercised reasonable care to ensure that the work is original, and does not to the best of my knowledge breach any law of copyright, and has not been taken from the work of others save and to the extent that such work has been cited and acknowledged within the text of my work.

Signed: ..... (Candidate) ID No.: .....

Date: .....

Acknowledgements

Over the past years, so many people have given me so much of their time, professional help and friendship it's hard to know where to start. Firstly, I want to give particular thanks to my supervisor Prof. Brian MacCraith for the fantastic opportunity he gave me carry out my PhD in such a multi-disciplinary research environment. Thank you for your encouragement and advice.

To all the group (in particular the coffee room crowd) thanks for your friendship, and I'm sure I learnt something useful from all those crosswords! Same goes for all who have passed through SG07 (Gemma, Raph, Aimeric, Brian). Thanks to Dorota and Aoibheann for talking me down off a few ledges during the write up period, and to Dorota for being a LaTeX svengali (and also helping with last-minute printing and binding!). Major thanks to Mohamed, for all of the enjoyable conversations and sol-gel explanations. Also thanks to Mohamed, Helen and Conor for finding time to read through drafts of the thesis and making helpful suggestions, as well as helping to prepare me for the viva.

Outside of DCU, I used to have a great crowd of close friends, who I virtually abandoned before I started writing up. Hopefully some of ye have stuck around!! Thanks for putting up with my disappearance over the last few months, now, ye won't be able to get rid of me! Most of all, thanks to all my family, Dad, Shirley, Diana and David (and not forgetting Mum), for supporting and encouraging me through it all.

Table of Contents

Abstract

This work describes the development of a telecommunications switch, sensor platforms for high resolution measurement of refractive index, and a fluorescence-based biosensor. All of these devices are based on optical waveguides fabricated from UV photocurable hybrid sol-gel materials. To address each application, the optical waveguides have been fabricated in a planar geometry referred to as planar lightwave circuits (PLCs). PLCs permit the manipulation of light on the micro-scale permiting development of miniature and compact devices.

A ground-up approach to development has been adopted starting with modelling and design of each platform, material development, and leading on to fabrication and characterisation of the optical devices. Modelling has been carried out using beam propagation method software. In parallel with platform development, sol-gel material optimisation work has included the identification of photoreactive instabilities in the initial sol-gel material and the successful adaptation of the formulation. Fabrication involved use of a UV mask alignment instrument, and development of a direct laser writing system.

In the area of telecommunications, an optical switch aimed at protection and restoration in networks has been successfully developed. It employs a Mach-Zehnder interferometer configuration which exploits the high thermo-optic effect of the sol-gel material in order to switch the input light signal between the output ports. In parallel with the Mach-Zehnder design a novel design based on multimode interference couplers was also successfully implemented.

The refractive index sensing platforms are suitable for the detection of any chemical/biochemical change that results in an accompanying refractive index change. As a proof of principle, the basic platform was adapted as a humidity sensor by the deposition of a humidity-sensitive porous sol-gel layer. For a fluorescence-based biosensor platform, the evanescent field of the waveguide is used to excite fluorescence from a multitude of different surface bound biomolecules, allowing their detection and quantification. As verification, a mouse IgG immunoassay was successfully carried out on the platform. This is a generic multi-analyte platform which can be applied to the detection of any analyte in areas as diverse as biomedical diagnostics, biowarfare detection, food safety, and narcotics detection to name a few.

Chapter 1

Introduction

Over the last three decades, the demand for planar lightwave circuits (PLC) for telecommunication and sensing applications has grown exponentially to become a multi-billion dollar industry. A promising technology for the development of these components is the use of photocurable hybrid materials, synthesised via the sol gel process. This process allows the production of advanced multifunctional materials, from which it is possible to fabricate compact, low-cost and mass-producible devices which can match and exceed performances of many of the established materials routinely used for PLC fabrication.

1.1 Optical Waveguiding

Optical waveguiding was first demonstrated by Daniel Colladon and Jacques Babinet in Paris during the 1840s. The Irish physicist John Tyndall later popularised the effect via public displays, where he showed how light could be guided through a jet of water flowing from a tank (see Figure 1.1). This demonstration

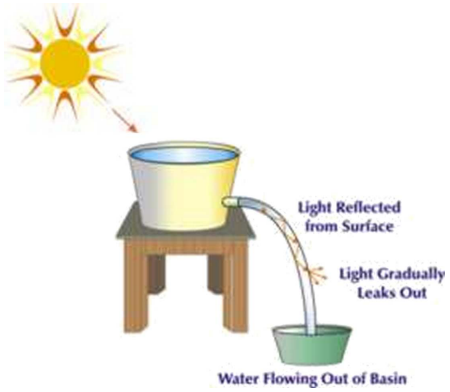

Figure 1.1: *Demonstration of light waveguiding in a water jet by Tyndall*

of waveguiding exploited the internal reflection of light at the boundary between a high and low refractive medium (core and cladding - in this case, water and air respectively) as illustrated by the ray diagram in Figure 1.2. Quartz rod waveguides were proposed as a means of illumination in medicine and dentistry towards the late 1800's, but the first serious exploitation of optical fibers appeared in the mid-1950's when the first fiberscope was developed by Kapany [1]. The fiberscope found use in remote imaging applications, for weld inspection in harsh environments such as aircraft fuel tanks, and the first endoscopic examinations. With the invention of the semiconductor laser in the early 1960's [2], the ability of light to carry information was seriously considered for the first time. Alexander Graham Bell reported the development of the photophone in 1880, for the transmission of speech using a light beam. However, the limitations of this method were the lack of suitable light sources, and the problem that light transmission in the atmosphere is restricted to line of sight, and severely affected by environmental perturbations such as rain, fog, snow, etc.. [3].

The development of the laser in the 1960's solved the first of these difficulties, with improvements in the guiding performance of optical fibers addressing the need for a suitable transmission medium [4]. These two technologies combined to make possible the telecommunications revolution. With the high frequencies of the visible and near-infrared portions of the electromagnetic spectrum, the laser potentially offered an information carrying capacity (bandwidth) 10,000 times greater than that commonly available in radio communication systems of the time [2].

In parallel with the optical communications revolution, another revolution was taking place: the development of electronic integrated circuits (ICs). In recent decades, continuous advances in electronics have revolutionised the speed with which we perform computing and communications of all kinds [5, 6]. Three key technologies were combined to create a platform that enabled the integrated electronics revolution: semiconductor materials, automated microfabrication processes, and integrated electronic circuit design. The combination of these three

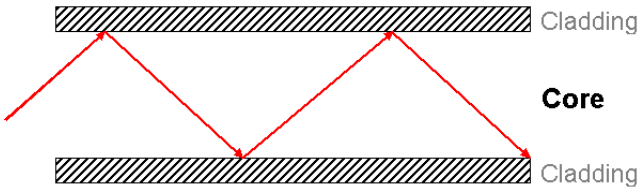

Figure 1.2: *Light guiding by total internal reflection in an optical fiber*

factors has allowed the mass-manufacturing of low-cost integrated circuitry.

1.2 Planar Lightwave Circuits

As optical fiber networks were implemented during the late 1970's, new components began to appear in which waveguides were patterned in thin dielectric layers on a silicon substrate, akin to electronic circuits. The drive towards dense, miniaturised components in the semiconductor electronics industry was now being mirrored in the optical communications industry. This technology has become widespread, with components needed to perform a wide variety of optical networking functions such as, splitting, switching, wavelength filtering, signal attenuation/amplification and dispersion compensation to name a few [2]. The term used to describe this technology is "integrated optics", "planar waveguide circuits" or "planar lightwave circuits" (PLCs), which is the term that will be employed throughout this work. PLC technology has grown over the years into a multi-billion dollar industry, employing many of the same microfabrication techniques and materials developed for semiconductor electronics industry.

Although the initial impetus for PLC research was provided by optical communications, from an early stage other potential applications that could benefit from the control of light in a microscale package were clearly apparent. As the technology matured, PLCs were increasingly employed in the area of sensing, where the ability to control and manipulate light was ideally suited to the development of novel optical probes [7]. In all applications of PLC technology, the prime advantages of this technology are clear; they provide a mass-producible, low-cost and high yield route to the fabrication of miniature components which have the capacity to perform multiple functions on a single chip.

The primary aim of this work has been the development of novel hybrid sol-gel materials and microfabrication techniques which permit the high quality and low-cost mass-production of PLCs for a variety of applications. Here, the intrinsic advantages of PLC platforms have been exploited for the fabrication of novel telecommunications switches based on the thermo-optic effect. A number of novel PLC sensing platforms have also been developed, focused on refractometric- and fluorescence-based detection formats.

1.3 Sol-gel Materials for Planar Lightwave Circuits

Sol-gel materials are a class of optical quality materials synthesised via a chemical process. At a fundamental level, the sol-gel process typically involves the mixture of a chemical precursor (usually a metal alkoxide) with water, which after aging for a period of time, chemically evolves to produce an inorganic network within the liquid phase [9]. Coating of these materials (sols), often by means of dip-, spin- or spray-coating, results in the formation of high optical quality thin films (gels), the properties of which can be tuned very precisely by selecting appropriate precursors and processing conditions. Figure 1.3 illustrates the diversity of coloured hybrid coatings that can be obtained by embedding or grafting organic chromophores in a sol-gel.

Pure inorganic sol-gels have been used for many years, but a relatively new area of sol-gel research has gained increasing attention over the past decade. Hybrid sol-gel materials share the same basic processing principles with the inorganic sols described above. However, they are classified as hybrid because they contain both an inorganic and an organic component in the final material, owing to the use of hybrid precursors during the synthesis [8, 10].

The advent of hybrid materials has opened the door to a wide variety of engineered materials. Multiple functionalities are often incorporated in a single hybrid material, which can serve the needs of diverse applications - ranging from electrochromic coatings for windows [11–13], corrosion protection [14, 15], porous sensor membranes for gas phase sensing [16, 17], entrapment of biomolecular

Figure 1.3: *Crystal and other types of glassware coated with dye-doped hybrid sol-gel materials [8]*

probes for biosensors [18, 19], to name a few.

One of the most promising areas of employment has been in the area of optics, in particular for fabrication of PLCs. With reference to the work reported here, the organic precursor contains a photosensitive organic moiety, which makes it possible to directly photopattern the thin film to form planar channel waveguides as illustrated by Figure 1.4. These are the fundamental building-blocks of all PLCs.

Many authors have drawn attention to the advantages of hybrid sol-gel materials for PLC fabrication in comparison to the more established techniques [5, 20–22]

- in comparison to established deposition technique for the waveguide core layer such as chemical vapor deposition (CVD) which can take several days, hybrid sol-gels materials allow the most rapid PLC fabrication only rivalled by polymer processing techniques
- the technique uses inexpensive materials and equipment (UV mask aligner compared to a CVD system)
- can be synthesised at room temperature without the need for sophisticated equipment
- can be processed at moderate temperature ($\sim$ 100-150 °C) and ambient pressure
- can be functionalised to give active properties to the material such as thermo- or electro-activity for use in switching
- due to direct photopatterning, sol-gel PLC devices do not suffer from waveguide scattering losses of the indirectly patterned PLCs, which are induced by reactive ion etching (RIE) processes that result in rough sidewalls

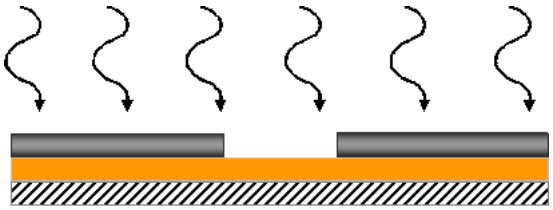

Figure 1.4: *Illustration of the selective irradiation of photosensitive film by a photolithographic process*

- by combining the advantages of the inorganic network (mechanical strength and thermal resistance) with the organic functional groups the best properties of both can be obtained in a single material

In this work, the characterisation of a number of hybrid sol-gel materials for PLC fabrication is presented. The materials and techniques developed have been applied to a number of sensing and telecommunications platforms which are outlined in the following Section.

1.4 Applications of Hybrid Sol-gel Materials

1.4.1 Sensing

As mentioned above, a number of sensing platforms have been designed and developed during the course of this work. The word "sensor" is derived from the Latin "sentire" which means 'to feel'. Sensors are defined as "devices that provide continuous and reversible monitoring of physical parameters, or of the concentration of chemical or biological target analytes" [23]. They are rapidly becoming integrated with many facets of daily life, such as wireless motion sensors for security, force sensing technology used in video games and sensors monitoring indoor air quality and chemical and biological environmental pollutants.

The different types of sensors are classified according to the method of transduction: mechanical, electrochemical or optical. Within the area of optical sensing, further classification can be made according to the sensing principle employed. Direct optical sensors are used when an intrinsic physical property of an analyte such as absorption at a particular wavelength or refractive index, changes when the concentration of the analyte changes [24]. Reagent-mediated sensor platforms employ an reagent such as a fluorescent label in order to signal the presence of an analyte (for example, the detection of molecular biorecognition by means of fluorescently labelled probe molecules) [25]. Both direct and reagent-mediated sensor platforms have been developed in this work, based on hybrid sol-gel PLCs.

The direct sensing platforms developed are refractometric, that is, they measure extremely small changes in refractive index of the medium in the sensing region. The reagent-mediated sensing format explored, has centered on the development of a fluorescence-based sensing platform for multianalyte biosensing.

1.4.1.1 Refractometric sensor platforms

The refractometric sensors developed in this work are generic in principle, allowing the detection of any analyte, the refractive index of which changes in response to changing analyte concentration. As a proof-of-principle the sensor platforms were coated with a humidity sensing layer in this instance. However, many applications exist for refractometric sensing platforms, with particular use for biosensing - specifically reagent/label-free biosensing where the presence of the analyte in a biological test solution causes a detectable refractive index change on the surface of the sensor platform.

1.4.1.2 Fluorescence-based biosensor platform

The development of a PLC-based biosensor platform is presented here, utilising the key advantages of PLCs and the sol-gel process to create a multianalyte biosensor platform. Biosensing is defined as the detection of molecular recognition events which signal the presence of a specific analyte in a biological test solution. The generic platform developed in this work can potentially be applied to a wide variety of applications in biosensing.

One of the most promising applications of biosensors is in the area of point-of-care (POC) biodiagnostic testing [26–28]. This field would benefit greatly from the widespread availability of biodiagnostic tests which could be conducted outside of hospital laboratories. Such a technology has many potential social and economic consequences, where people can be kept out of hospitals by earlier interventions made in a doctors clinic setting. This has positive impacts on healthcare for all concerned, producing better outcomes from treatment due to the ability to diagnose disease at an earlier stage, possibly even before the onset of clinical symptoms.

In critical care settings, POC tests permit the generation of results more rapidly, allowing appropriate interventions to take place at an earlier stage. The development of multianalyte biosensors is a current deficiency in the market [29]. There are a number of clinical diagnosis situations that would benefit greatly from the availability of a rapid multianalyte panel of biosensor spots on a POC chip.

1.4.2 Telecommunications

As mentioned previously, PLC research has been driven by the telecommunications sector throughout its history, only later branching into other applications such as sensing. With the increased demands for bandwidth from todays consumers, optical fiber links are moving increasingly close to the end-user, with fiber-to-the-home (FTTH) being implemented in some countries such as Japan, South Korea and the U.S.A. [30, 31]

The bandwidth bottleneck presented by the 'last-mile' electrical links to consumers are mainly responsible for current limitations in telecommunications. Therefore, a shift to all-optical networks will eventually become a reality as demand continues to grow exponentially, driven by the internet, gaming, voice over IP (VoIP) and many other applications [31, 32]. Up until recently, signals in the optical network have typically been routed and regenerated by converting from the optical to the electrical domain (using a photodetector), and then retransmitting the same signal into the appropriate output fiber for routing, or simply amplifying it for regeneration. These components are known as optical-electrical-optical (OEO) components. However, as the bandwidth increases beyond 10 Gbit/s the OEO components begin to get more expensive, overly complex and suffer from huge power dissipation and thermal problems.

The solution to this problem is to process information entirely in the optical domain, using "all-optical" components to perform the same functions as the currently employed OEO components. This is the main motivation behind the development of an optical switch in this project. The objective was to exploit the low-cost sol-gel materials and process to fabricate a thermo-optical switch which is activated by means of the high thermo-optic response of the sol-gel materials.

1.5 Thesis Structure

This Chapter prefaces the thesis with an introduction to planar lightwave circuits, hybrid sol-gel materials, and introduces the main applications addressed by the developed technologies, sensing and telecommunications.

In Chapter 2, the principles of optical waveguiding are presented in their most general form, focussing primarily on an asymmetric slab waveguide. In addition the operating principles of multi-mode interference couplers (MMICs), directional couplers and the beam propagation method (BPM) are outlined.

Chapter 3 outlines the theoretical aspects of microfabrication using UV photolithography. A direct laser writing system has been constructed, and the means by which it produces a focused laser spot are presented.

Chapter 4 deals with the development, optimisation and characterisation of a number of sol-gel materials. Particular emphasis has been given to the experimental steps involved in the identification of the source of instability in the so-called 'baseline' sol-gel formulation. This led to subsequent optimisation of the material removing the source of photoinstability.

The final Chapters deal with the application of the theory, fabrication systems and materials presented in Chapters 2-4. Chapter 5 presents work that has been carried out on a family of novel refractometric sensing platforms. Chapter 6 outlines the application of the microfabrication techniques and sol-gel materials for the development of a multianalyte biosensor platform. Finally, in a break from sensors development, Chapter 7 reports on the development of a novel thermo-optic switch for application in the all-optical telecommunication networks, which are currently coming on stream.

1.6 Research Objectives

The primary objectives of work presented in this thesis are:

1. To develop photolithographic microfabrication processes necessary for the formation of PLCs
2. To design and simulate a range of novel PLC platforms for application in:
   (a) Refractometric sensing
   (b) Fluorescence-based multianalyte biosensing
   (c) Optical telecommunications switching
3. To characterise a range of photocurable hybrid sol-gel materials for the fabrication of planar waveguides
4. To apply the developed materials and processes to fabricate and characterise the performance of the PLC platforms listed in point 2.

References

[1] D. R. Goff and K. S. Hansen, *Fiber Optic Reference Guide: A Practical Guide to Communications Technology.* Focal Press, 1999.

[2] D. L. Lee, *Electromagnetic principles of integrated optics.* New York: Wiley, 1986.

[3] J. M. Senior, *Optical fiber communications : principles and practice 2nd ed.*, 1992.

[4] D. Marcuse, *Theory of dielectric optical waveguides.* New York: Academic Press, 1974.

[5] L. Eldada, "Optical communication components," *Review of Scientific Instruments*, vol. 75, pp. 575–593, 2004.

[6] H. Ma, A. K. Y. Jen, and L. R. Dalton, "Polymer-based optical waveguides: Materials, processing, and devices," *Advanced Materials*, vol. 14, pp. 1339–1365, 2002.

[7] P. V. Lambeck, "Integrated optical sensors for the chemical domain," *Measurement Science & Technology*, vol. 17, pp. R93–R116, 2006.

[8] C. Sanchez, B. Lebeau, F. Chaput, and J. P. Boilot, "Optical properties of functional hybrid organic-inorganic nanocomposites," *Advanced Materials*, vol. 15, pp. 1969–1994, 2003.

[9] C. J. Brinker and G. W. Scherer, *Sol-gel science : The physics and chemistry of sol-gel processing.* Academic Press, New York, 1990.

[10] C. Sanchez and F. Ribot, "Design of hybrid organic-inorganic materials synthesized via sol-gel chemistry," *New Journal of Chemistry*, vol. 18, pp. 1007–1047, 1994.

[11] C. O. Avellaneda, K. Dahmouche, and L. O. S. Bulhoes, "All sol-gel electrochromic smart windows: CeO_2-TiO_2/ormolyte," *Molecular Crystals and Liquid Crystals*, vol. 374, pp. 113–118, 2002.

[12] E. Avendano, L. Berggren, G. A. Niklasson, C. G. Granqvist, and A. Azens, "Electrochromic materials and devices: Brief survey and new data on optical absorption in tungsten oxide and nickel oxide films," *Thin Solid Films*, vol. 496, pp. 30–36, 2006.

[13] A. Karuppasamy and A. Subrahmanyam, "Studies on electrochromic smart windows based on titanium doped WO_3 thin films," *Thin Solid Films*, vol. 516, pp. 175–178, 2007.

[14] A. S. Hamdy, "Advanced nano-particles anti-corrosion ceria based sol gel coatings for aluminum alloys," *Materials Letters*, vol. 60, no. 21-22, pp. 2633–2637, 2006.

[15] V. Moutarlier, B. Neveu, and M. P. Gigandet, "Evolution of corrosion protection for sol-gel coatings doped with inorganic inhibitors," *Surface and Coatings Technology*, vol. 202, no. 10, pp. 2052–2058, 2008.

[16] C. Higgins, D. Wencel, C. S. Burke, B. D. MacCraith, and C. McDonagh, "Novel hybrid optical sensor materials for in-breath O-2 analysis," *Analyst*, vol. 133, no. 2, pp. 241–247, 2008.

[17] B. F. Lei, B. Li, H. R. Zhang, S. Z. Lu, Z. H. Zheng, W. L. Li, and Y. Wang, "Mesostructured silica chemically doped with Ru-II as a superior optical oxygen sensor," *Advanced Functional Materials*, vol. 16, pp. 1883–1891, 2006.

[18] T. R. Besanger and J. D. Brennan, "Entrapment of membrane proteins in sol-gel derived silica," *Journal of Sol-Gel Science and Technology*, vol. 40, pp. 209–225, 2006.

[19] R. Gupta and N. K. Chaudhury, "Entrapment of biomolecules in sol-gel matrix for applications in biosensors: Problems and future prospects," *Biosensors & Bioelectronics*, vol. 22, pp. 2387–2399, 2007.

[20] L. Eldada, "Advances in telecom and datacom optical components," *Optical Engineering*, vol. 40, pp. 1165–1178, 2001.

[21] P. Coudray, P. Etienne, J. Porque, Y. Moreau, and S. I. Najafi, "Integrated optical devices achieved by sol-gel process," in *Integrated Optics Devices II*, vol. 3278, pp. 252–258, 1998, Proceedings of SPIE

[22] S. I. Najafi, T. Touam, R. Sara, M. P. Andrews, and M. A. Fardad, "Sol-gel glass waveguide and grating on silicon," *Journal of Lightwave Technology*, vol. 16, no. 9, pp. 1640–1646, 1998.

[23] H. K. Tnshoff and I. Inasaki, *Sensors in Manufacturing*. Wiley-VCH Verlag, 2002.

[24] C. McDonagh, C. S. Burke, and B. D. MacCraith, "Optical chemical sensors," *Chemical reviews*, vol. 108, pp. 400–422, 2008.

[25] S. M. Borisov and O. S. Wolfbeis, "Optical biosensors," *Chemical Reviews*, vol. 108, no. 2, pp. 423–461, 2008.

[26] S. A. Soper, K. Brown, A. Ellington, B. Frazier, G. Garcia-Manero, V. Gau, S. I. Gutman, D. F. Hayes, B. Korte, J. L. Landers, D. Larson, F. Ligler, A. Majumdar, M. Mascini, D. Nolte, Z. Rosenzweig, J. Wang, and D. Wilson, "Point-of-care biosensor systems for cancer diagnostics/prognostics," *Biosensors & Bioelectronics*, vol. 21, no. 10, pp. 1932–1942, 2006.

[27] J. Wang, "Electrochemical biosensors: Towards point-of-care cancer diagnostics," *Biosensors & Bioelectronics*, vol. 21, no. 10, pp. 1887–1892, 2006.

[28] A. Rasooly, "Moving biosensors to point-of-care cancer diagnostics," *Biosensors & Bioelectronics*, vol. 21, no. 10, pp. 1847–1850, 2006.

[29] "Frost & Sullivan, world biosensors market report," Tech. Rep., 2005.

[30] M. Abrams, "FTTP deployments in the United States and Japan-equipment choices and service provider imperatives," *Journal of Lightwave Technology*, vol. 23, pp. 236–246, 2005.

[31] M. J. O'Mahony, C. Politi, D. Klonidis, R. Nejabati, and D. Simeonidou, "Future optical networks," *Journal of Lightwave Technology*, vol. 24, pp. 4684–4696, 2006.

[32] S. A. Karim and P. Hovell, "Everything over IP - an overview of the strategic change in voice and data networks," *BT Technology Journal*, vol. 25, pp. 198–204, 2007.

Chapter 2

Waveguiding

2.1 Introduction

Planar waveguides are used throughout this work for the formation of novel sensing and telecommunication switch platforms. Generally, they comprised a high refractive index core surrounded by lower refractive index layers. In order to explain the principle by which waveguiding occurs, the most general and simple structure - the asymmetric slab waveguide - is examined in detail, deriving the conditions for wave propagation, leading to the introduction of the evanescent wave. The basic properties of the multi-mode interference coupler, and directional coupler structures are described, as they pertain to work in subsequent chapters. Finally, a brief summary of the numerical methods employed in this work for PLC simulation is presented.

2.2 Asymmetric Slab Waveguide

The asymmetric slab waveguide is the most general waveguide format, and is used in this Section to explain the physical principles that underlie waveguiding. To understand the physics of waveguiding, two approaches are commonly adopted: ray optics and wave optics. The ray optic approach is outlined briefly, serving to introduce the core concepts of waveguiding before adopting wave optics for a more rigorous examination of the subject.

2.2.1 Ray Optic Approach

As a first step, the standard slab waveguide structure is described in Figure 2.1, where the waveguide core (refractive index n_g) is surrounded on top and below by two layers (the substrate and the superstrate/cover layer) both having a lower refractive index than the core (n_s and n_l respectively). The higher refractive index of the core is a critical requirement of optical waveguides, so that light can propagate along the waveguide with minimal loss by total internal reflection (TIR) off the upper and lower waveguide boundaries. Total internal reflection refers to the total reflection of a light ray travelling from a high to a lower refractive index medium. The conditions for total internal reflection are dictated by Snell's law of refraction, where the angle of incidence of the light ray (θ_i) must exceed the critical angle (θ_c).

In the case of an asymmetric slab waveguide the critical angles for each interface are defined as follows,

$$\theta_c^l = \sin^{-1}\left(\frac{n_l}{n_g}\right) \qquad \text{Waveguide - cover interface} \tag{2.1}$$

$$\theta_c^s = \sin^{-1}\left(\frac{n_s}{n_g}\right) \qquad \text{Waveguide - substrate interface} \tag{2.2}$$

where $n_g > n_s > n_l$ for the purposes of this explanation.

Brief examination of the Fresnel reflection coefficient, which is equal to the ratio of the reflected to incident electric field amplitudes, is revealing in this case. The Fresnel reflection coefficient for transverse electric (TE) waves [1], r_{TE} is,

$$r_{TE} = \frac{E_{0r}}{E_{0i}} = \frac{\cos(\theta_i) - \sqrt{\sin^2(\theta_c) - \sin^2(\theta_i)}}{\cos(\theta_i) + \sqrt{\sin^2(\theta_c) - \sin^2(\theta_i)}}. \tag{2.3}$$

In the case of TIR, it is evident that r_{TE} is a complex quantity since $\sin^2(\theta_c) -$

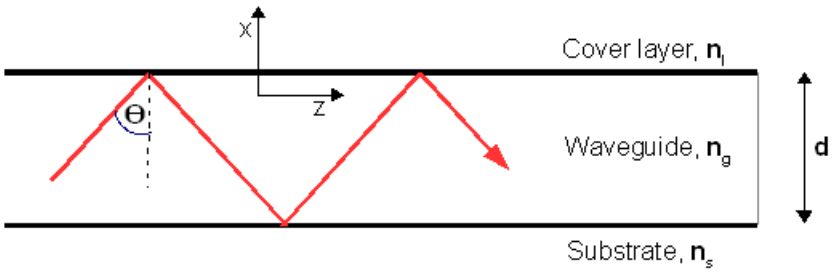

Figure 2.1: *An asymmetric slab waveguide with guided mode:* $\theta_c^s < \theta < 90°$

$\sin^2(\theta_i) < 1$. The physical consequence of this is that the modulus of the complex reflection coefficient is alway equal to 1 for all $\pi/2 > \theta_i > \theta_c$ (i.e. $|r_{TE}| = \sqrt{rr*} = 1$, meaning that in this range of angles all incident light is reflected).

As outlined above, the angle of incidence of the ray determines whether or not TIR can occur. Depending upon this angle, three different waveguide propagation behaviors can result. These are:

- $\theta_c^l < \theta_i < 90°$: This range corresponds to total internal reflection of light from both the lower and the upper waveguide boundary, which results in propagation of a guided wave with low loss, as depicted in Figure 2.1.
- $\theta_c^s < \theta_i < \theta_c^l$: In this range the light is confined by TIR at the waveguide-cover interface. However, at the waveguide-substrate interface it is free to escape and so this is called a cover radiation mode.

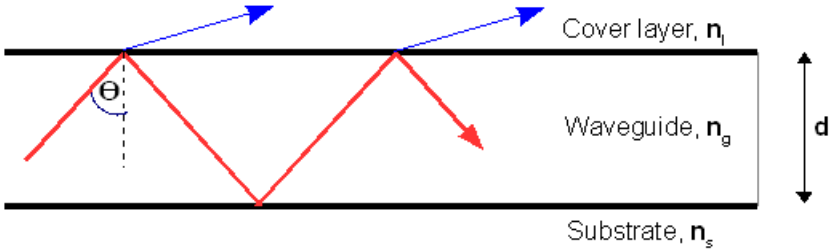

Figure 2.2: *Cover radiation mode.* $\theta_c^l < \theta < \theta_c^l$

- $\theta_i < \theta_c^s$: This situation results in light escaping at both the substrate and the cover interfaces, resulting in a substrate-cover radiation mode.

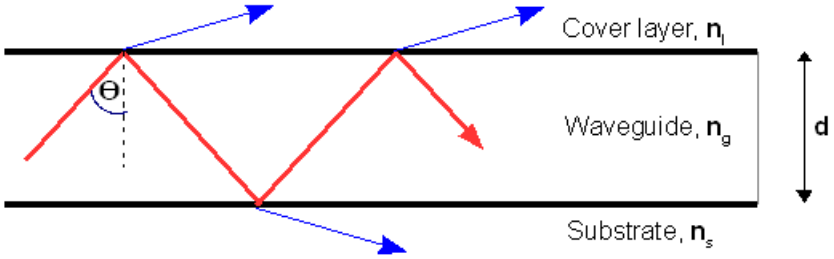

Figure 2.3: *Substrate-cover radiation mode.* $\theta < \theta_c^s$

2.2.2 Wave Optic Approach

The ray optic approach allows a simple introduction to light propagation within a waveguide. However, the wave optic treatment of the subject permits a more

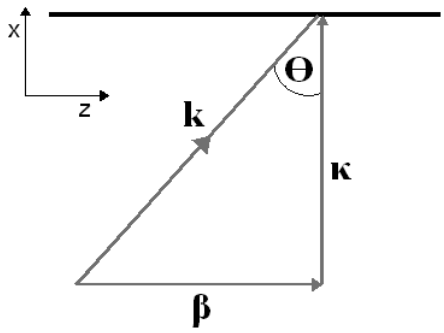

Figure 2.4: *Wavevector diagram showing the propagation constant (k), and the longitudinal and transverse propagation constants ((β) and κ respectively)*

rigorous determination of the propagation conditions of a particular waveguide structure, and the purpose of this Section is to derive the waveguide propagation condition. The first step toward this goal is to introduce the effective refractive index. This is a characteristic of a waveguide derived from the propagation constant, k (k=$k_0 n_g$), where $k_0 = 2\pi/\lambda_0$, with λ_0 being the free space light wavelength. Drawing from the ray optic approach, the propagation constant can be considered as a vector pointing in the direction of the ray, as illustrated in Figure 2.4. The longitudinal and transverse wavevectors shown in Figure 2.4 (β and κ respectively) are fundamental waveguiding parameters, and are defined as,

$$\beta = k_0 n_g \sin\theta \tag{2.4}$$

and

$$\kappa = k_0 n_g \cos\theta = \sqrt{k^2 - \beta^2}. \tag{2.5}$$

Having introduced the propagation wavevectors, another fundamental waveguiding parameter is the effective refractive index, which is defined as,

$$n_{\text{eff}} = n_g \sin\theta \tag{2.6}$$

Using this definition of n_{eff}, it is clear that this quantity provides a link between the ray optic approach to waveguide mode analysis (defined by the incident angle θ) and the wave optics approach characterised by n_{eff}.

Derivation of the propagation conditions for a lossless dielectric medium begins with the Maxwell Equations, which are

$$\nabla \times \tilde{E} = -\mu_0 \frac{\partial \tilde{H}}{\partial t} \tag{2.7}$$

and

$$\nabla \times \tilde{H} = \epsilon_0 n^2 \frac{\partial \tilde{E}}{\partial t} \tag{2.8}$$

where ϵ_0 and μ_0 are the dielectric permitivity and magnetic permeability of free space respectively and n is the refractive index of the dielectric medium.

Analysis of a slab waveguide of infinite extent in the y-direction greatly simplifies the steps necessary to derive the mode propagation condition. The analysis for a transverse electric (TE) mode is given here, where the electric field is perpendicular to both the propagation direction z, and the plane of incidence (x-z plane). Therefore only three electric/magnetic vectorial field components exist: E_y, H_x and H_z.

In order to simplify the Maxwell equations to arrive at a wave equation for the slab structure, the approach taken by Marcuse is shown here [2]. Assuming that the z dependence of the mode fields is given by the function exp(-jβz), and that the fields are strictly time harmonic, the electric and magnetic fields in the slab can be expressed as,

$$\tilde{E} = E_y(x)\exp(j(\omega t - \beta z)) \tag{2.9}$$

$$\tilde{H} = H(x)\exp(j(\omega t - \beta z)) \tag{2.10}$$

Substituting these equations into equations 2.7 and 2.8, and exploiting the fact that $\partial/\partial y = 0$, for a slab waveguide, results in the following identities,

$$-j\beta H_x - (\partial H_z/\partial x) = j\epsilon_0 n^2 E_y \tag{2.11}$$

$$j\beta E_y = -j\omega\mu_0 H_x \tag{2.12}$$

$$\partial E_y/\partial x = -j\omega\mu_0 H_z \tag{2.13}$$

Using equations 2.12 and 2.13, it is possible to obtain the H components in terms of the E_y component,

$$H_x = -(\beta/\omega\mu_0)E_y \tag{2.14}$$

and

$$H_z = -(j/\omega\mu_0)\partial E_y/\partial x \tag{2.15}$$

Substitution of equations 2.14 and 2.15 into equation 2.11 yields the simplified one-dimensional wave equation for the E_y component (for TE mode),

$$\left(\frac{\partial^2 E_y}{\partial x^2}\right) + (k^2 - \beta^2)E_y = 0 \tag{2.16}$$

The general solution of equation 2.16 is,

$$E_y(x) = E_0 \exp\left(\pm jx\sqrt{k^2 - \beta^2}\right) = E_0 \exp\left(\pm j\kappa x\right) \tag{2.17}$$

where κ is defined in equation 2.5. In the waveguide core $k_0 n_g > \beta$, and so equation 2.17 is unaltered and remains complex and oscillatory in this region.

In the substrate and cover, $k_0 n_s < k_0 n_c < \beta$, and so the complex factor in equation 2.17 is eliminated as follows,

$$E_y(x) = E_0 \exp\left(-x\sqrt{\beta^2 - k_{s,l}^2}\right) = E_{0y} \exp\left(-\alpha_{s,c} x\right) \tag{2.18}$$

where $\alpha_{s,l}$ is an attenuation constant of the structure in the substrate or cover layers respectively $\left(\alpha_{s,l} = \sqrt{\beta^2 - k_{s,l}^2}\right)$.

The TE mode distributions ($E_y(x,z)$) can be summarised as follows;

$$E_y(x,z) = \left\{ \begin{array}{c} E_l \exp[-\alpha_l x] \\ E_g \cos(\kappa x + \psi) \\ E_s \exp[+\alpha_s x] \end{array} \right\} \exp(-j\beta z) \qquad \begin{array}{l} \text{Cover} \\ \text{Waveguide} \\ \text{Substrate} \end{array} \tag{2.19}$$

where ψ is a phase term, representing the asymmetry of the structure. Examination of the mode distributions in the cover and substrate reveals that the transmitted wave propagates parallel to the waveguide surface at the same rate as the guided wave. However, the mode distribution contains another component that is attenuated exponentially in the x direction, the evanescent wave. The penetration depth of the evanescent wave ($d_p = 1/\alpha$) is an important factor, quantifying the distance along the x direction that the transmitted wave travels into the sub/superstrate medium.

By exploiting the requirement of continuity of tangential E and H at both interfaces, i.e. at $x = \pm d/2$, and applying the boundary conditions at these interfaces [3], it is possible to write

$$\frac{\kappa d}{2} + \psi = \frac{1}{2}\phi_l^{TE} \pm n\pi \tag{2.20}$$

$$\frac{\kappa d}{2} - \psi = \frac{1}{2}\phi_s^{TE} \pm m\pi \tag{2.21}$$

where ϕ_l^{TE} and ϕ_s^{TE} are the Fresnel phase shifts that light under goes upon TIR

at an interface, and may be derived from the phase of equation 2.3, resulting in

$$\phi_l^{TE} = 2\tan^{-1}\left(\frac{\mu_g \alpha_l}{\mu_l \kappa}\right) \tag{2.22}$$

$$\phi_s^{TE} = 2\tan^{-1}\left(\frac{\mu_g \alpha_s}{\mu_s \kappa}\right). \tag{2.23}$$

Adding equations 2.20 and 2.21 has the effect of eliminating ψ to produce the following relation,

$$2\kappa d - \phi_l^{TE} - \phi_s^{TE} = 2p\pi \qquad p = 0, 1, ... \tag{2.24}$$

Equation 2.24 is a generalised guiding condition for TE modes within an asymmetric slab waveguide.

2.2.2.1 Dispersion relation for the asymmetric slab waveguide

In order to obtain a plot of ω vs β for each waveguide mode, the guidance condition derived in equation 2.24 must be solved numerically for β at a number of frequencies. First, β, ϕ_l^{TE}, ϕ_s^{TE}, ω_l and ω_s are substituted into the guidance condition to obtain,

$$d\sqrt{\omega^2\mu_g\epsilon_g - \beta^2} = p\pi + \tan^{-1}\left(\frac{\mu_g\sqrt{\beta^2 - \omega^2\mu_l\epsilon_l}}{\mu_l\sqrt{\omega^2\mu_g\epsilon_g - \beta^2}}\right) + \tan^{-1}\left(\frac{\mu_g\sqrt{\beta^2 - \omega^2\mu_s\epsilon_s}}{\mu_s\sqrt{\omega^2\mu_g\epsilon_g - \beta^2}}\right) \tag{2.25}$$

Knowing that $\beta = \omega\sqrt{\mu_0\epsilon_{\text{eff}}}$ and making the reasonable assumption that all regions are magnetically equivalent ($\mu_g = \mu_s = \mu_l = \mu_0$) results in a further simplification, which yields

$$d\omega\sqrt{\mu_0}\sqrt{\epsilon_g - \epsilon_{\text{eff}}} = p\pi + \tan^{-1}\left(\sqrt{\frac{\epsilon_{\text{eff}} - \epsilon_l}{\epsilon_g - \epsilon_{\text{eff}}}}\right) + \tan^{-1}\left(\sqrt{\frac{\epsilon_{\text{eff}} - \epsilon_s}{\epsilon_g - \epsilon_{\text{eff}}}}\right) \tag{2.26}$$

This equation can now be rewritten in terms of the normalised parameters as,

$$V\sqrt{1-b} = p\pi + \tan^{-1}\left(\sqrt{\frac{b + a^{TE}}{1-b}}\right) + \tan^{-1}\left(\sqrt{\frac{b}{1-b}}\right) \tag{2.27}$$

where b is the normalised waveguide index, a^{TE} is a measure of the asymmetry of the waveguide and V is a normalised frequency parameter that is a measure of the number of modes a waveguide can support (also called the V number) [3].

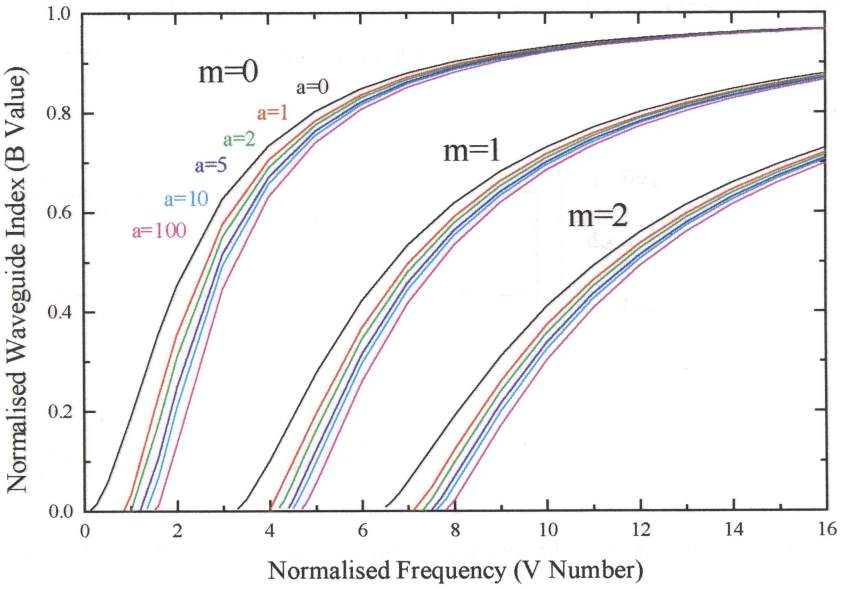

Figure 2.5: *Dispersion curve for TE modes in a slab waveguide*

These parameters are defined as follows:

$$b = \frac{\epsilon_{\text{eff}} - \epsilon_s}{\epsilon_g - \epsilon_s} \tag{2.28}$$

$$a^{TE} = \frac{\epsilon_s - \epsilon_l}{\epsilon_g - \epsilon_s} \tag{2.29}$$

$$V = k_0 d\sqrt{(\epsilon_g - \epsilon_s)/\epsilon_0} \tag{2.30}$$

Equation 2.27 fully describes the guidance condition for TE modes within a planar asymmetric slab waveguide and yields the dispersion plot shown in Figure 2.5. Such a plot enables the rapid determination of the properties of any guided mode. Examination of Figure 2.5 shows that for all of the modes displayed, there is a critical value of the normalised frequency (V), below which the guided mode is not supported by the waveguide structure in question (characterised by its normalised effective index). This value of V is normally referred to as the cutoff frequency (V_m) of the guided mode and can be calculated as follows,

$$\mathrm{V_m} = \mathrm{V_0} + \mathrm{m}\pi \tag{2.31}$$

where $\mathrm{V_0} = \tan^{-1}\sqrt{a}$ is the cut-off value of the fundamental mode and m is the mode number. Cut-off occurs when the effective refractive index of the mode is less than or equal to the refractive index of the cover or substrate.

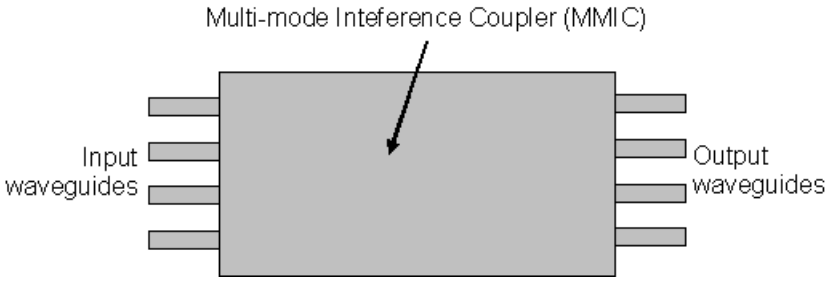

Figure 2.6: *General structure of an MMIC*

2.3 Multi-mode Interference Coupler Theory

A multi-mode interference coupler (MMIC) is composed of a multi-mode waveguide, to which at least one single-mode input and output waveguide is attached for delivering and collecting light, as shown in Figure 2.6. MMICs have developed rapidly in recent years since their introduction by Ulrich and Ankele [5–7]. They are widely used in many PLCs, such as power splitters [8], ring lasers [9], optical switches [10, 11], and wavelength division multiplexers/demultiplexers [12, 13]. In this work they are employed for switching (Chapter 7), power division (Chapter 6), and in a novel application for MMICs, refractometric sensing (Chapter 5).

When the input light enters the MMIC section, high-order modes of the multi-mode waveguide section are excited. Through the interference between the excited modes, images of the input light can be formed, which are known as self-images. The MMIC operates by producing single and multiple self-images of its input light distribution at various points along its length, as shown by the simulation image in Figure 2.7. The theoretical treatment of self-image formation in an

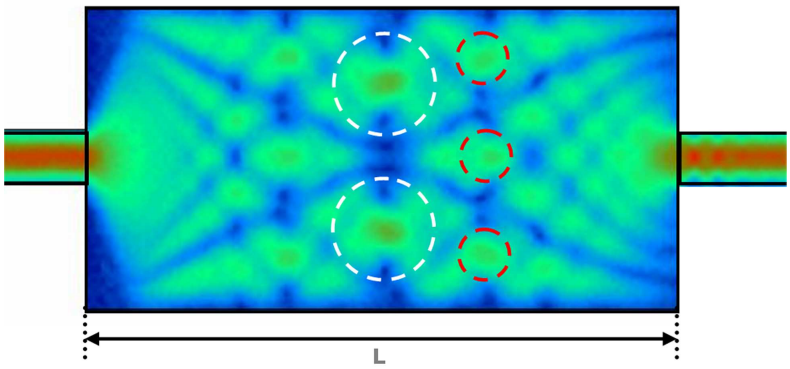

Figure 2.7: *Simulation image (using BPM software) of the electric field distribution with multiple self-images in an MMIC*

MMIC is taken from Ref. [14]. The relation between the transverse wavenumber κ_ν and the longitudinal propagation constant β of the νth order mode can be described, as before, by the dispersion equation:

$$k_0^2 n_g^2 = \kappa_\nu^2 + \beta_\nu^2 \tag{2.32}$$

For strong guiding waveguides, we have

$$\kappa_\nu = (\nu + 1)\pi / W_e \tag{2.33}$$

where W_e is the effective width of the multi-mode section. From a physical perspective, this condition requires that an integer number of half wavelengths must fit across the width of the multi-mode waveguide in order for a particular mode to be supported. By substituting equation 2.33 into 2.32 and using the paraxial approximation ($\kappa \ll k_0 n_g$), the propagation constant β_ν can be expressed as:

$$\beta_\nu \approx n_{co} k_0 - \frac{(\nu+1)^2 \pi \lambda}{4 W_e^2 n_{co}} \tag{2.34}$$

where n_{co} and n_{cl} is the refractive index of the MMIC core and cladding respectively. The beat length between the fundamental and the first mode can be defined as:

$$L_\pi = \frac{\pi}{\beta_0 - \beta_1} = \frac{4 n_{co} W_e^2}{3\lambda} \tag{2.35}$$

and equation 2.34 can be rewritten as:

$$\beta_\nu \approx \beta_0 - \frac{\nu(\nu+2)\pi}{3 L_\pi} \tag{2.36}$$

By assuming that the MMIC has at least a few guided modes and that the radiative modes of the MMIC section are not excited, the input field $\Psi(x,0)$ can be expanded in terms of all the guided modes in the multi-mode region:

$$\Psi(x,0) = \sum_\nu c_\nu \psi_\nu(x) \tag{2.37}$$

where $\psi_\nu(x)$ is the νth order mode distribution and c_ν is the νth order, orthogonal mode excitation coefficient, given by:

$$c_\nu = \frac{\int \Psi(x,0)\psi_\nu(x)dx}{\sqrt{\int \psi_\nu^2(x)dx}} \tag{2.38}$$

The field $\psi(x,z)$ propagating along the z direction can be expressed as a super-

position of all the guided modes, that is

$$\psi(x,z) = \sum_{\nu} c_\nu \psi_\nu(x) \exp\left[j(\omega t - \beta_\nu z)\right] \tag{2.39}$$

Finally, by substituting equation 2.36 into 2.39 the equation specifying the field within the MMIC section is arrived at:

$$\psi(x,z) = \sum_{\nu} c_\nu \psi_\nu(x) \exp\left[j\frac{\nu(\nu+2)\pi}{3L_\pi}z\right] .\exp\left[j(\omega t - \beta_\nu z)\right] \tag{2.40}$$

From equation 2.40, one can easily find that the field at z = L is determined by the mode excitation coefficient c_ν and the phase term: $\exp\left[j\frac{\nu(\nu+2)\pi}{3L_\pi}z\right]$. Under certain conditions, the field at z = L will be a reproduction of the input field. By using the symmetry and anti-symmetry of the even and odd modes with respect to the plane at x = W/2, equation 2.40 shows that $\psi(x, z = L)$ will be a self-image of $\psi(x, z = 0)$ if the phase term satisfies the following condition,

$$\exp\left[j\frac{\nu(\nu+2)\pi}{3L_\pi}z\right] = 1 \quad \text{or} \quad (-1)^\nu \tag{2.41}$$

in which case it can be seen that equations 2.40 and 2.37 are equivalent, i.e., the field at z = L is a reproduction of the field at z = 0. However, depending upon the excitation position, some of the modes will not be excited. This results in some special cases which can be analysed as follows:

General Interference

General interference means that there is no specific restriction on the excitation position. It is found that there are N-folded images of the input field at a distance L from z = 0:

$$L = \frac{3ML_\pi}{N} \tag{2.42}$$

where M indicates the imaging periodicity along z (known as the self-image rank). At this length, N-fold images are positioned at x_i with phase ϕ_i given by the following:

$$x_i = p(2i - N)\frac{W_e}{N} \tag{2.43}$$

$$\phi_i = p(N - i)\frac{\pi}{N} \tag{2.44}$$

Paired Interference

The modes ν=2, 5, 8,..., present a odd symmetry at x=$\pm W_e/6$. By launching an even symmetric field at these positions, the excitation coefficients c_ν will be zero for ν=2, 5, 8,..., since the overlap integrals of equation 2.38 between even symmetric input field and the odd symmetric modes will vanish. For the other excited modes with $c_\nu \neq 0$ we have:

$$\mathrm{mod}_3\left[\nu(\nu+2)\right] = 0 \qquad \text{for } \nu \neq 2, 5, 8, ... \tag{2.45}$$

Therefore, the length periodicity of the mode phase of equation 2.41 will be reduced three times. N folded self-images of the input field will be obtained at:

$$L = \frac{ML_\pi}{N} \tag{2.46}$$

The modes contributing to the imaging are mode pairs 0-1, 3-4, 6-7..., thus this mechanism is called paired interference. For this case, the number of the input waveguides is limited to two (at x = $\pm W_e/6$).

Symmetric Interference

If the excitation field is launched at the centre of the multi-mode region, only the even symmetric modes will be excited ($c_\nu = 0$ for ν odd). For this case, we have:

$$\mathrm{mod}_4\left[\nu(\nu+2)\right] = 0 \qquad \text{for } \nu \text{ even} \tag{2.47}$$

With this condition, the length periodicity of the mode phase of equation 2.41 will be reduced four times. Therefore, N-fold self-images of the input field will be obtained at:

$$L = \frac{3ML_\pi}{4N} \tag{2.48}$$

Since only the even modes are excited, the imaging is obtained by combinations of the even symmetric modes, and the mechanism is called symmetric interference. One should note that in this case the number of the input waveguides is limited to one (at x = 0), and this condition has been exploited in the development of a refractometric sensing platform presented in Chapter 5.

2.4 Directional Coupler Theory

A directional coupler in its most basic configuration, consists of two waveguides formed in close proximity as shown in Figure 2.8, so that light from waveguide A can couple into waveguide B via its evanescent wave, and vice versa. As light propagates in the waveguides, light is continuously transferred from one waveguide to the other and then back again in a spatially periodic fashion. This continuous transfer of light from one waveguide to another is primarily used for power splitting, though it has been exploited in Chapter 5 for refractometric sensing. The following treatment of directional coupler theory is taken from [15]. The coupled mode equations express the change in field amplitude in one of the waveguides in terms of the field amplitude in the other waveguide such that,

$$\frac{dA(z)}{dz} = \kappa_{ab} B(z) \exp(-2j\delta z) \tag{2.49}$$

$$\frac{dB(z)}{dz} = \kappa_{ba} A(z) \exp(-2j\delta z) \tag{2.50}$$

where κ_{ab} and κ_{ba} are the coupling coefficients (from waveguide a to b, and b to a respectively), and δ is the normalised phase deviation and is related to the difference in the propagation constants of the two modes and the spatial variation of the perturbation. Considering that light is initially injected only into one of the waveguides such that;

$$A(z=0) = 0 \qquad\qquad B(z=0) = B_0 \tag{2.51}$$

the solution to the coupled mode equations in equation 2.50 are therefore,

$$A(z) = \frac{\kappa_{ab} B_0}{\sqrt{\kappa^2 + \delta^2}} \exp(-j\delta z) \sin\left(z\sqrt{\kappa^2 + \delta^2}\right) \tag{2.52}$$

$$B(z) = B_0 \exp(j\delta z) \left[\cos\left(z\sqrt{\kappa^2 + \delta^2}\right) - \frac{j\delta}{\sqrt{\kappa^2 + \delta^2}} \sin\left(z\sqrt{\kappa^2 + \delta^2}\right)\right] \tag{2.53}$$

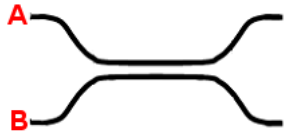

Figure 2.8: *General structure of a directional coupler*

where $\kappa = |\kappa_{ab}| = |\kappa_{ba}|$. Pertaining to the thermo-optic switch developed in Chapter 7, complete coupling of light from one waveguide to the other is desired, and this condition is expressed only for phase matching ($\delta = 0$), such that

$$A(z) = B_0(\kappa_{ab}/\kappa)\sin(\kappa z) \tag{2.54}$$

$$B(z) = B_0\cos(\kappa z) \tag{2.55}$$

The complete transfer of light from waveguide A to B in this case, occurs at the coupling length,

$$L_c = \frac{\pi}{2\kappa} \tag{2.56}$$

where, κ, the coupling coefficient is calculated according to the following equation:

$$\kappa = \frac{\beta_s - \beta_a}{2} = \frac{\pi(n_{\text{eff}_0} - n_{\text{eff}_1})}{\lambda}. \tag{2.57}$$

where β_s and β_a refer to the symmetric and anti-symmetric system modes of the directional coupler, and n_{eff_0} and n_{eff_1} are the effective refractive indices of these modes. Equations 2.56 and 2.57 provide a convenient means of specifying the length of a directional coupler for complete power transfer. For equal power splitting, a length of $\text{L}_c/2$ is required, as described in Chapter 7.

2.5 Numerical Methods

Throughout this work, simulation of PLC devices has been carried out using cross-sectional mode solvers, and Beam Propagation Methods (BPM), which are accurate numerical methods which allow simulation of the behaviour of light in a PLC. This section serves to give a brief background to these numerical techniques.

2.5.1 Mode Solvers

The basic function of cross-sectional mode solvers is to provide an accurate means by which the electric/magnetic field distribution in a waveguide cross-sectional structure can be calculated. There are a number of different algorithms available to achieve this aim, some basic (e.g. Effective index method, Marcatili method) and some more advanced algorithms (including, Multi-grid finite difference algorithms, and the "Bend 2D" algorithm which is the most accurate of all [16], and is therefore used in this work).

The mode solver was used for two main purposes. Firstly, they are an indispensable tool for specification of the waveguide parameter necessary for single-mode operation: waveguide cross-sectional dimensions, and refractive index contrast between the waveguide core and the surrounding cladding. Secondly, the mode solver is especially useful as a means to calculate the effective refractive index of a waveguide structure, which was used in the design of both directional coupler and MMIC-based devices in this work.

2.5.2 The Beam Propagation Method (BPM)

Throughout this work, the Beam Propagation Method (BPM) has been employed for simulation of the propagation of light in the various PLC platforms that have been designed and developed (using OlympiOs Integrated Optics Software, C2V, Netherlands). The purpose of these simulations has been two-fold: firstly, to verify the operating principles of the platforms prior to fabrication, and secondly, BPM data were used as a means of specifying the device dimensions necessary for the platforms to effectively carry out their functions.

The BPM algorithm is a numerical method of solving the Helmholtz wave equation [16],

$$\nabla^2 \tilde{E} + k^2 \tilde{E} = 0 \tag{2.58}$$

the 1D version of which was derived here for the asymmetric slab waveguide (equation 2.16). It does this by means of the slowly varying envelope approximation (SVEA), in which the electric field is divided into a slowly varying envelope function ($\phi(x, y, z)$) and a fast oscillatory phase term ($\exp(-j\beta z)$), such that [16, 17],

$$\tilde{E}(x, y, z) = \phi(x, y, z)\exp(-j\beta z). \tag{2.59}$$

Substitution of equation 2.59 into equation 2.58 yields the following expression [17],

$$\left(\frac{\partial^2 \phi}{\partial z^2}\right) - 2j\beta\left(\frac{\partial \phi}{\partial z}\right) + \nabla_\perp^2 \phi + (k^2 - \beta^2)\phi = 0 \tag{2.60}$$

where $\nabla_\perp^2 = \partial^2/\partial x^2 + \partial^2/\partial y^2$, which is the Laplacian operator in the lateral direction. The first term ($\partial^2\phi/\partial z^2$) is disregarded in BPM simulations so as to arrive at an expression that is first-order in z, greatly reducing computation time.

A mode solver is used to establish the starting field distribution and propagation constants, which are typically used as initial conditions for a BPM simulation [18]. This starting condition is then propagated along the z direction

in discrete steps (defined by the z discretisation of the simulation) as shown in Figure 2.9, using equation 2.60 in a finite difference calculation (see Appendix B).

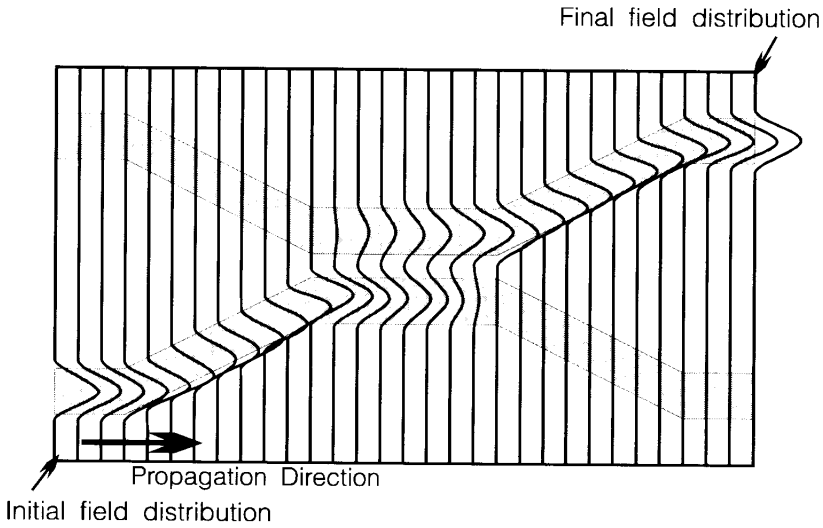

Figure 2.9: *Example of a wave propagating in discrete steps through a structure (directional coupler) [16]*

2.6 Summary

Waveguide theory as it pertains to planar waveguide structures has been detailed in this Chapter. In particular, the guidance conditions within an asymmetric slab waveguide were derived using a wave optics approach. The evanescent wave was also introduced, being of particular relevance in Chapter 6 where it is exploited for fluorescence excitation in a biosensor platform. The theory of the MMIC was outlined, which is relevant to applications in Chapters 5, 6 and 7. Directional coupler theory was presented, which pertains to the development of an optical switch in Chapter 7. Finally, the numerical methods used in this work for PLC simulation were presented, including some of their basic operating principles.

References

[1] T. Tamir, *Guided-wave optoelectronics: 2nd ed.* Berlin; New York: Springer-Verlag, 1990.

[2] D. Marcuse, *Theory of dielectric optical waveguides.* New York: Academic Press, 1974.

[3] D. L. Lee, *Electromagnetic principles of integrated optics.* New York: Wiley, 1986.

[4] E. Hecht, *Optics.* Reading, Mass.: Addison-Wesley, 2002.

[5] R. Ulrich, "Light-propagation and imaging in planar optical waveguides," *Nouvelle Revue d'Optique*, vol. 6, no. 5, pp. 253–262, 1975.

[6] R. Ulrich and G. Ankele, "Self-imaging in homogeneous planar optical-waveguides," *Applied Physics Letters*, vol. 27, no. 6, pp. 337–339, 1975.

[7] R. Ulrich and T. Kamiya, "Resolution of self-images in planar optical waveguides," *Journal of the Optical Society of America*, vol. 68, no. 5, pp. 583–592, 1978.

[8] L. B. Soldano, F. B. Veerman, M. K. Smit, B. H. Verbeek, A. H. Dubost, and E. C. M. Pennings, "Planar monomode optical couplers based on multimode interference effects," *Journal of Lightwave Technology*, vol. 10, pp. 1843–1850, 1992.

[9] R. van Roijen, E. C. M. Pennings, M. J. N. van Stalen, T. van Dongen, B. H. Verbeek, and J. van der Heijden, "Compact InP-based ring lasers employing multimode interference couplers and combiners," *Applied Physics Letters*, vol. 64, no. 14, pp. 1753–1755, 1994.

[10] K. R. Kribich, H. Barry, R. Copperwhite, B. Kolodziejczyk, K. O'Dwyer, J. M. Sabattie, and B. D. MacCraith, "Thermo-optic switches using sol-gel processed hybrid materials," *Proceedings of SPIE*, vol. 5451, p. 518, 2004.

[11] N. S. Lagali, M. R. Paiam, R. I. MacDonald, K. Worhoff, and A. Driessen, "Analysis of generalized Mach-Zehnder interferometers for variable-ratio power splitting and optimized switching," *Journal of Lightwave Technology*, vol. 17, pp. 2542–2550, 1999.

[12] M. R. Paiam and R. I. MacDonald, "12-channel phased-array wavelength multiplexer with multimode interference couplers," *IEEE Photonics Technology Letters*, vol. 10, no. 2, pp. 241–243, 1998.

[13] Y. Hibino, "Recent advances in high-density and large-scale AWG multi/demultiplexers with higher index-contrast silica-based PLCs," *IEEE Journal on Selected Topics in Quantum Electronics*, vol. 8, no. 6, pp. 1090–1101, 2002.

[14] L. B. Soldano and E. C. M. Pennings, "Optical multi-mode interference devices based on self-imaging: principles and applications," *Journal of Lightwave Technology*, vol. 13, no. 4, pp. 615–627, 1995.

[15] K. J. Ebeling, *Integrated optoelectronics : waveguide optics, photonics, semiconductors*. New York: Springer-Verlag, 1993.

[16] *OlympIOs Integrated Optics Software Manual, Volume 2, Alcatel Optronics Version 5.0*. 2002.

[17] K. Kawano and T. Kitoh, *Introduction to Optical Waveguide Analysis - Solving Maxwell's Equations and the Schrodinger Equation*. Canada: John Wiley Sons, 2001.

[18] J. Dakin and R. G. W. Brown, *Handbook of Optoelectronics*. Inst. of Physics Pub. Inc., 2006.

Chapter 3

Microfabrication Techniques and Systems

3.1 Introduction

In this Section, the microfabrication techniques employed for planar lightwave circuits fabrication are explained, along with some pertinent physical principles underlying the techniques. Firstly, sol-gel thin film deposition techniques are outlined. Then the UV photolithographic techniques used for sol-gel thin film photopatterning are presented. Two techniques have been developed: a UV mask alignment technique and a direct laser writing technique. UV mask alignment is a well developed technique widely used in the semiconductor industry. The construction of the direct writing system is explained, showing how the UV laser output is conditioned, controlled and focussed to form a precise spot for the direct imprinting of optical waveguides.

3.2 Deposition Techniques

In order to form planar optical waveguides with micrometer dimensions, the first step is to form micrometer scale thin films of the sol-gel materials on a solid substrate. Typically, glass or silicon is used as the support for the thin films. Silicon is advantageous due to its excellent planarity and the ability to cleave it precisely over long distances along crystallographic planes. Glass, on the other hand, is transparent, which is necessary for some applications. The means of depositing ultra thin films of sol-gel on any of these substrates mainly exploits two methods; dip- and spin-coating.

3.2.1 Dip-Coating

Dip-coating is a means of producing high quality optical thin films and, though not limited to small samples, dip-coating lends itself well to samples which are limited in one dimension. The procedure first involves immersion of the substrate in the fluid (in this case the sol) and then withdrawal of the substrate at constant speed. The thickness of the film obtained (h) is proportional to the withdrawal speed (U) as shown by the equation [1],

$$h = 0.94 \frac{(\eta U)^{\frac{2}{3}}}{\gamma_{LV}^{\frac{1}{6}} (\rho g)^{\frac{1}{2}}} \tag{3.1}$$

where η is the viscosity, ρ is the density, γ_{LV} is the liquid-vapour surface tension, g the acceleration due to gravity and U is the dip-speed. From this equation it is clear that the slower the withdrawal speed of the substrate the thinner the sol-gel film obtained, which at first can seem counter-intuitive.

To understand this, the net forces acting on the film as it is being formed can be divided into two opposing sets of forces. On the one hand there are those forces which tend to keep the fluid on the substrate: the fluid viscosity which resists movement of the fluid from the substrate. On the other hand, there are forces that tend to drag the fluid away from the substrate: viscous drag of the fluid in the container, and the gravitational force.

At lower dip speeds, the fluid in the container exerts a stronger influence on the fluid of the coating by means of viscous drag, thereby more efficiently draining the fluid from the substrate at the coating-fluid interface. Though the behaviour of sols can be somewhat more complicated than that indicated in the above equation (mainly due to evaporative thinning of the sol during coating [2]), investigations carried out by Brinker et al. [1] have shown that for a variety of silicate sols, h varies approximately as $U^{2/3}$ in accordance with equation 3.2.1.

3.2.2 Spin-Coating

The spin-coating technique is commonly used in the semiconductor industry for the uniform deposition of photoresist materials across the surface of a wafer. It is ideally suited to coating of circular substrates such as wafers as it uses centrifugal forces to evenly spread an initial volume of material from the center to the wafer edges. In a review by Bornside, the process has been divided into four stages:

deposition, spin-up, spin-off and evaporation [3]. Deposition involves dispensing an initial volume of sol in the centre of the substrate. In the spin-up stage, liquid is driven radially from the centre covering the surface of the substrate. Spin-off refers to the stage where excess sol is driven off the surface by flowing to the wafer edge and forming droplets. The evaporation stage refers to the thinning of the film even after radial outflow of fluid has ceased, by evaporation of solvent from the surface of the film. The main parameters that govern the final film thickness (h_f) achieved by spin-coating are the flow and evaporation characteristics of the sol as illustrated by Meyerhofer's equation [4];

$$h_f = c_0 \left(\frac{3\nu\epsilon}{2(1-c_0)\omega^2} \right)^{\frac{1}{3}} \tag{3.2}$$

where c_0 is the initial concentration of solids in the liquid, ν is the viscosity, ϵ is the rate of evaporation, and ω is the angular velocity. The important point to note here is that film thickness decreases for increasing spin speed, as $h_f \propto \omega^{-2/3}$.

As in the case of dip-coating, evaporation also plays a slightly more complicated role in the spin-coating of sol-gel films because here the evaporation phase strongly overlaps with the spin-off stage [2].

3.3 UV Mask Photolithography

Photolithography is the process by which surface relief structures are formed in a photosensitive thin film of material by means of exposure to electromagnetic radiation. The selective irradiation of the thin film is achieved by use of a photomask. As illustrated in Figure 3.1, there are three main types of photolithography [5];

- contact photolithography - where the mask is in direct physical contact with the surface of the thin film
- proximity photolithography - where a small gap (z) in the order of micrometers is kept between the mask and the thin film
- projection photolithography - where an optical projection system is used to demagnify the image produced by the mask to achieve smaller feature sizes on the thin film

The photosensitive thin films are either positive-tone, or negative-tone depending upon their behaviour on irradiation [6]. The difference is elaborated in Figure

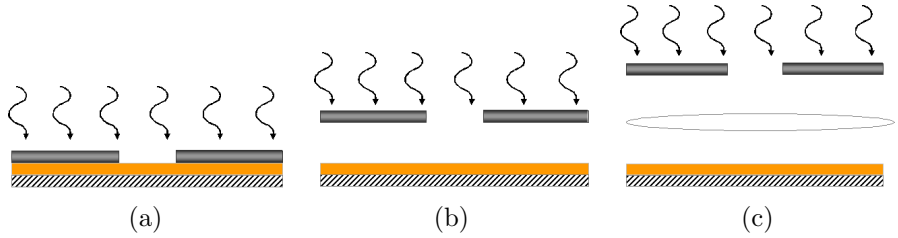

Figure 3.1: *Schematic diagrams of a) contact, b) proximity and c) projection photolithography*

3.2 where, after irradiation, positive-tone films can be etched away in the areas exposed while the unexposed areas remain. The opposite is the case for negative-tone materials, i.e., on irradation they typically polymerise so that the irradiated areas remain and the unexposed areas are removed when etched. Photolithography is an essential microfabrication tool for many technological industries, notably the semiconductor industry. In this case, the photosensitive films used to construct microprocessors are called photoresists, and commercial photoresists have been used in this work. However, photolithography has been employed mainly in conjunction with a class of photosensitive materials developed in our laboratory known as hybrid sol-gel materials, for the fabrication of planar lightwave circuits. In the following sections, some key features of photolithographically formed structures will be described, and related to material and optical system characteristics.

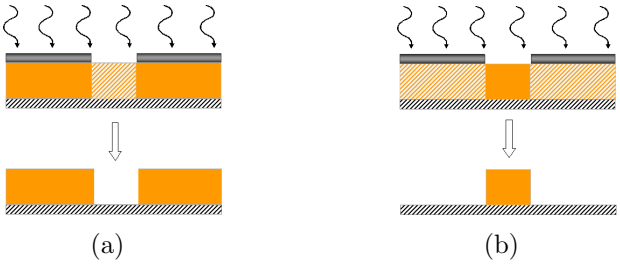

Figure 3.2: *Selective UV irradation of; a) positive-tone, and b) negative-tone photopatternable materials*

3.3.1 Sidewall Verticality

This work is concerned mainly with the use of photolithography for optical waveguide fabrication. Therefore, the slope of the sidewall of the photolithographically defined features is very important, as changes in the waveguide cross-sectional structure will change the

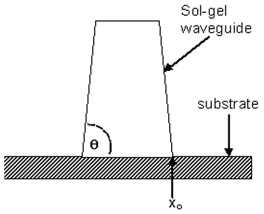

Figure 3.3: *Sidewall slope*

optical properties of the waveguide. Since all waveguides have been modelled assuming a square cross-sectional structure, the aim of the photolithography process is to match this as closely as possible. The sidewall slope of a feature is defined as [7],

$$tan(\theta) = \frac{dT}{dx} \tag{3.3}$$

where θ is the sidewall angle as illustrated in Figure 3.3 and T is the thickness of the thin film (i.e. the distance from the substrate to the top of the film). T can vary between zero and the initial thin film thickness, depending upon the level of crosslinking of the material, which is directly related to the UV exposure dose. Equation 3.3 can be expressed as,

$$\frac{dT}{dx} = \frac{dT}{dD}\frac{dD}{dx} \tag{3.4}$$

with D the exposure dose defined as,

$$D(x) = I(x)t \tag{3.5}$$

where I(x) is the intensity distribution and t is the exposure time. Equation 3.4 allows convenient separation of the terms dictating the resist profile, where dT/dD is a characteristic only of the sol-gel thin film (encompassing photoreactivity and processing conditions), and dD/dx is solely determined by the light intensity distribution in the thin film (which is a function of the photomask feature size and the optics of the exposure system). This equation clearly demonstrates how the material properties and the exposure optics interact in the formation of features that have sidewalls with a high degree of verticality.

Material contrast

The first part of equation 3.4 above is related to the contrast of the sol-gel thin film. In Figure 3.4, the relationship between the thickness of a thin film polymerised in response to different UV exposure doses is shown for a typical negative photoresist (analogous to sol-gel). Using Figure 3.4, the contrast of the film (γ) is defined as the slope of the graph [6] (dT/dD) such that,

$$\frac{dT}{dD} = \gamma = log\frac{D_g^i}{D_g^o} \tag{3.6}$$

where D_g^i is the critical exposure dose corresponding to onset of crosslinking and D_g^o is the exposure dose required to reach 100% of the initial film thickness.

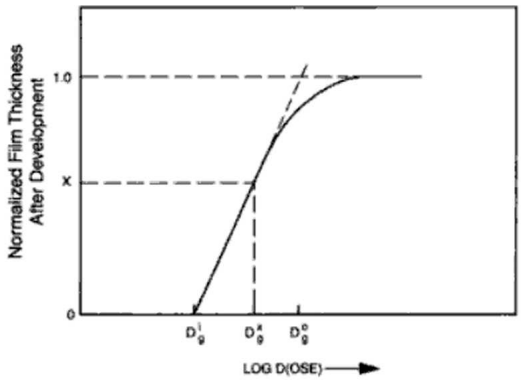

Figure 3.4: *Determination of the contrast of a negative-tone photoresist/sol (from [6])*

Films with a small difference between D_g^o and D_g^i have a high contrast, which, according to equation 3.4, contributes to the formation of a sidewall with high verticality. The material contrast is intimately linked to the photoreactivity of the film, and that depends not only on its chemical formulation but also on the process conditions (pre-exposure baking, exposure time and intensity) to which it is subjected. Therefore, depending upon the treatment of a particular material, the sidewall slope of the resulting features can vary widely.

Intensity distribution

The second part of equation 3.4 also has a role to play in the degree of verticality of the sidewall. It relates to the intensity profile of light (I(x)) produced by the optical system, which, for a mask photolithography system, is primarily dictated

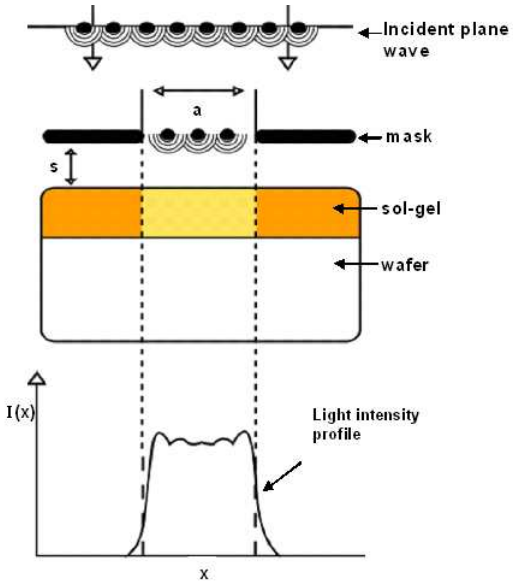

Figure 3.5: *Formation of the Fresnel diffraction pattern by UV exposure through a narrow linewidth mask feature*

by diffraction at the mask opening edge. Given the proximity of the thin film to the mask, the Fresnel diffraction pattern is responsible for deviations of the intensity profile from the ideal square wave distribution [8], as illustrated in Figure 3.5. The undesirable effects of this intensity pattern are especially evident when two features are in close proximity, where the sidelobes of the intensity profile can add together so that they exceed the critical polymerisation exposure dose causing unwanted polymerisation of material in masked areas. Strategies for improving process performance in these cases include a lowering of the exposure wavelength, hence a progression toward deep UV and x-ray sources in semiconductor processing [6]. Phase shift masking is another method that is effective in reducing the effects caused by summation of diffracted light from adjacent features [7], and works by causing destructive instead of constructive interference to occur between the overlapping diffracted rays, which is achieved by shifting the phase of light through one of the openings by 90°.

3.3.2 Resolution

The resolution of an exposure system refers to the minimum separation of features that is theoretically possible, and may be calculated from the equation,

$$\text{Resolution} = 2b_{min} \approx 3\sqrt{\lambda(s + \frac{d}{2})} \tag{3.7}$$

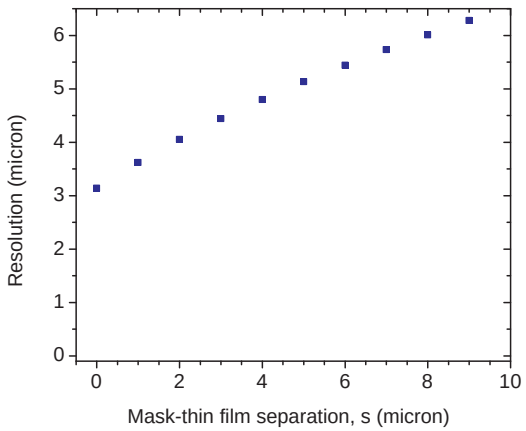

Figure 3.6: *Theoretical effect on resolution of photolithographic process with change in the mask to thin film separation ($\lambda = 365nm$)*

where λ is the exposure wavelength, s is the separation gap between the mask and the thin film (s=0 for contact), d is the film thickness [6, 9]. Using this equation, the mask aligner instrument used in this work (Karl Suss, MA56) is theoretically capable of achieving resolution of 3.2 μm for a 6μm thin film thickness in contact mode (s = 0) at $\lambda = 365nm$. Deviations from contact mode can occur due to contamination such as particles, uneven sol coating, or edge bead which is a thicker layer of material at the wafer edge where sol tends to gather during spin-off. Figure 3.6 illustrates the effects on resolution of the gap between mask and sol-gel surface, and shows the importance of obtaining a thin film that has high uniformity and low defects in order to avoid gaps and ensure high resolution. In summary, the resolution parameter of the system is important in defining the density of features that can be formed on a wafer surface, which is of great importance when features are placed in close proximity.

3.3.3 Properties of the UV Mask Aligner

Figure 3.7: *Karl Suss MA56 mask aligner*

Throughout this work, the UV Mask-Alignment system (Karl-Suss MA56) shown in Figure 3.7) was employed. This can operate in both contact and proximity mode. The UV light source is a mercury lamp the spectrum of which is shown in Figure 3.8. The effect of a i-line filter is evident, which is fitted so that exposure is confined to a band centering on 365 nm. The mask aligner has been used in contact mode in order to maximise the resolution and fidelity of the transferred pattern.

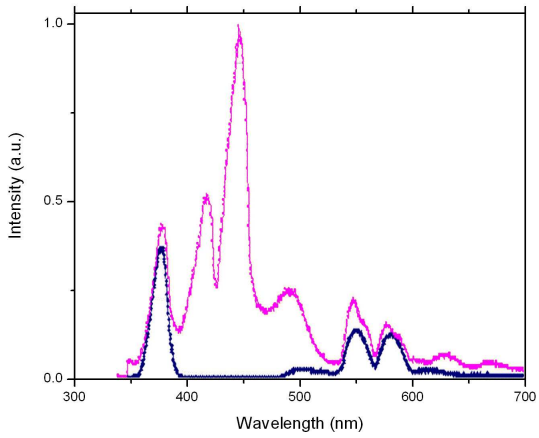

Figure 3.8: *Emission spectrum of the mercury lamp of the mask aligner with and without an i-line filter*

3.4 Direct Laser Writing

In this Section, the technical details of the direct laser writing system are outlined and related to formation of the UV light intensity profile at the image plane. In order to move the sol-gel sample beneath the stationary UV spot, a set of linear motors has been employed in this system. To allow convenient programming of the motors for fabrication of complex planar waveguide circuits, a LabView program was written.

3.4.1 Optics of the System

The components that form the direct laser writing (DLW) system are described in Figure 3.9. The UV source is a He-Cd laser (Kimmon Electric Co. Ltd., TEM_{00}) which emits two high intensity lines at $\lambda = 325$ and 440 nm. The 325 nm wavelength is used throughout this work as it overlaps well with the absorption spectra of the photoinitiators used in the hybrid sol-gel materials. The output power of the laser is controlled by passing the beam through an acousto-optical modulator (AOM) (Opto-Electronique AA.MQ.110/A3-uv), which splits the beam into a number of diffraction orders. The AOM works by creating a diffraction grating in a quartz crystal by application of a sinusoidally varying acoustic wave [10]. The intensity of the light in each diffraction order is adjustable by varying the applied acoustic wave power (either manually or programmatically via computer interface) while keeping a constant frequency, thus giving light intensity control. In this system, the first diffraction order was used as it has

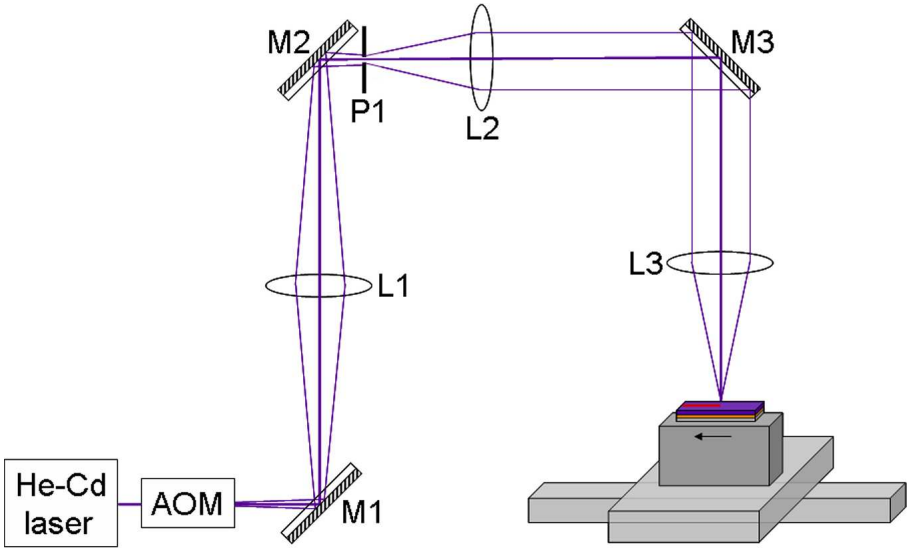

Figure 3.9: *Schematic of the direct laser writing system*

the highest intensity. The light from this order was deflected by mirror M1, and focussed using lens L1 onto the pinhole P1 (via the second mirror M2). The pinhole aperture had a 30 μm circular diameter and was used in order to ensure a perfectly uniform source for the eventual focussed spot. During tuning of the system alignment, the position of L1 was critical in the determination of intensity at the output plane, as the tightness of focus of L1 determined the amount of light incident on the pinhole.

Light leaving the pinhole had a typical Airy pattern as expected due to diffraction at the edges of the pinhole aperture [8]. The second lens (L2) had a focal length of 100 mm so that it could collect approximately three rings of the Airy diffraction pattern, which is necessary for faithful reproduction at the system focal point, of the top-hat light intensity distribution at the pinhole. L2 was positioned 100 mm from the pinhole (precisely at its focal point) so that the incident Airy pattern left L2 completely collimated. During tuning this condition was verified by collecting the collimated Airy pattern a distance of several meters from L2, where it had the same diameter as at L2. Finally, the collimated Airy pattern was reflected from M3 onto the third lens (L3), the function of which is to form the final focussed spot with the desired diameter and intensity distribution.

The diameter of the focussed spot is dictated by the interplay of the collimating and focussing lenses (L2 and L3) such that,

$$\text{Spot Diameter} = \text{Pinhole Diameter}\frac{f(L3)}{f(L2)} = (30\mu m)\frac{20}{100} = 6\mu m \qquad (3.8)$$

where f(L2) and f(L3) are the focal lengths of L2 and L3. Effectively, the top-hat intensity profile by pinhole (P1) is recreated by the optical system at the focal point. With capture of all of the diffraction orders of the Airy pattern, a complete recreation of the top-hat profile is theoretically possible. However, since the lenses of the system can capture only 3 rings of the Airy pattern a complete reconstruction of the top-hat intensity profile is not possible, and so slight degradation of the profile results at the system focal point.

3.4.2 Motion Control

A Labview software interface was designed to facilitate easy motion control of the set of linear motors, allowing the direct laser writing of any PLC. The software also controls motor speed and laser beam energy (via the acousto-optical modulator) which are two critical parameters that must be optimised in order to deliver the correct UV dose to the sol-gel guiding layer (GL). This is important for single-mode operation, because for a given RI contrast between guiding and buffer layer materials, a specific waveguide dimension must be achieved. The interaction of all components of the motion control system is depicted in Figure 3.10. Effectively the Labview program developed acts as a compiler for a text file loaded by the user, where input simple instructions are converted to machine code which is recognised by the motion controller hardware. The text file contains a set of instructions for the system to follow which comprises motor speed, acceleration, deceleration, AOM power for intensity control, line lengths, arc angles, etc.. For the writing of more complex geometries, such as MMICs (where the laser beam must overlap with adjacent lines in building up a wide multi-mode waveguide) specific subroutines have been developed which save the user from making exacting calculations. Once the appropriate machine code has been generated by the compiler, the instructions are queued in the motion controller hardware where each instruction is then fed to the motors in order at the appropriate time. The program user interface is shown in Figure 3.11.

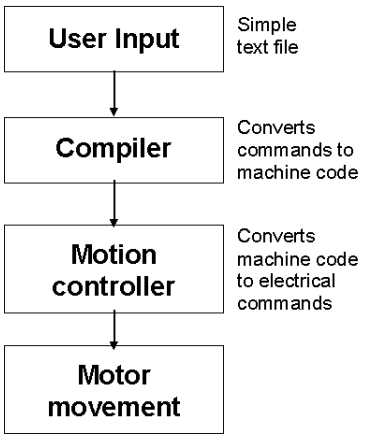

Figure 3.10: *Motion control system diagram*

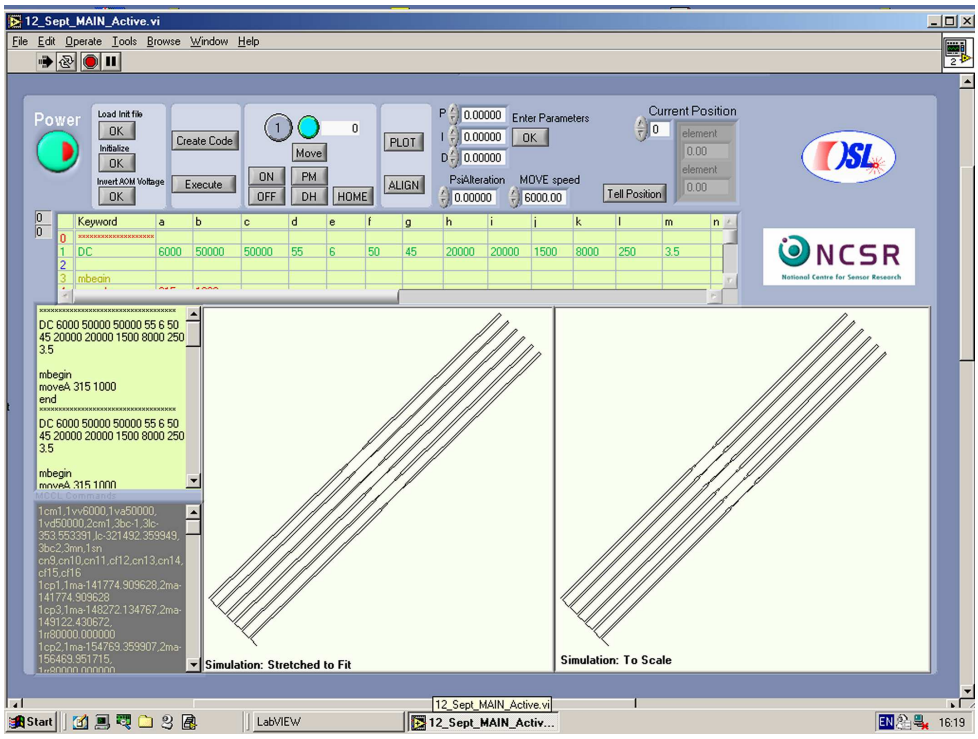

Figure 3.11: *Labview motion control program user interface*

3.4.3 Laser Beam Energy Density Determination

For experiments concerning the photoreactive properties of sol-gel materials, it was necessary to determine the energy density (mJ/cm^2) of the UV laser spot. A number of parameters interact to determine the UV energy density received by the photocurable thin film in such a system. For a laser writing system, energy density is dependent on two factor: scanning speed of the thin film sample beneath the stationary laser spot, and the intensity of the laser spot. For high throughput manufacturing, a high scanning speed is desirable in order to increase yield. This requires a high laser spot intensity in order to deliver the same energy density to the film as is the case at lower scanning speed and intensity. Assuming that the intensity distribution of the laser spot can be approximated by a top-hat profile, the energy density was calculated according to the formula,

$$(\text{Energy density}) = \frac{\text{Laser Power}}{\text{Area scanned per second}}. \tag{3.9}$$

First, the power of the laser beam was measured as a function of the AOM setting (8-bit number from 0 - 255) by placing a silicon photodiode (Thorlabs, DET210) directly under the laser spot near to the focal point of the system. The laser power was calculated from photocurrent by dividing by the spectral responsivity

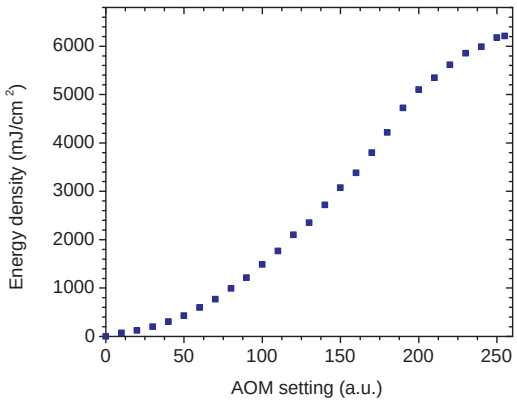

Figure 3.12: *Variation in the UV energy density as a function of the 8-bit AOM control setting*

of the detector, which at 325 nm was 0.05 W/A. To calculate the area scanned per second, the following approximation was used,

$$\text{Area scanned per second} = \text{Scan speed} \times \text{Beam diameter} \tag{3.10}$$

where the beam diameter at focus is 6 μm according to calculations above and the scan speed typically used was 0.6 mm/s. Energy density was calculated for each laser power and is shown in Figure 3.12.

3.5 Conclusion

This Chapter has outlined the main microfabrication techniques used throughout this work, focussing on thin film deposition techniques and photolithography. Models describing thin film deposition were presented for both dip- and spin-coating. The UV mask alignment technique was described in detail with emphasis on a theoretical treatment of the process, which illustrates that both material and optical exposure parameters are involved in the determination of feature sidewall verticality.

In addition, the theoretical resolution of a contact exposure system, such as the one exploited in this work, was discussed, with emphasis on the reduction in resolution caused by thin film defects and non-uniformity. Finally, the construction of the direct laser writing system was described in detail, with explanation of the formation of the output intensity profile distribution.

References

[1] C. J. Brinker and G. W. Scherer, *Sol-gel science : The physics and chemistry of sol-gel processing.* Academic Press, New York, 1990.

[2] D. E. Bornside, C. W. Macosko, and L. E. Scriven, "Spin coating - one-dimensional model," *Journal of Applied Physics*, vol. 66, pp. 5185–5193, 1989.

[3] D. E. Bornside, C. W. Macosko, and L. E. Scriven, "On the modeling of spin coating," *Journal of Imaging Technology*, vol. 13, pp. 122–130, 1987.

[4] D. Meyerhofer, "Characteristics of resist films produced by spinning," *Journal of Applied Physics*, vol. 49, no. 7, pp. 3993–3997, 1978.

[5] I. Brodie and J. J. Muray, *The physics of microfabrication.* New York: Plenum Press, 1982.

[6] M. J. Madou, *Fundamentals of microfabrication.* London: CRC Press, 1997.

[7] P. Rai-Choudhury, *Handbook of microlithography, micromachining, and microfabrication.* London: Institution of Electrical Engineers, 1997.

[8] R. Newman, *Fine line lithography.* Amsterdam: North-Holland, 1980.

[9] S. Franssila, *Introduction to microfabrication.* John Wiley and Sons, 2004.

[10] D. Beach, A. Shotwell, and P. Essue, *Applications of lasers and laser systems.* Englewood Cliffs, New Jersey: PTR Prentice Hall, 1993.

Chapter 4

Sol-gel Material: Development and Optimisation

Development and optimisation of the sol-gel materials used in this project was carried out in parallel with the application of these materials in sensing and telecommunications devices, as outlined in Chapter 1. Observation of the material properties and the performance of resulting waveguides have informed the optimisation work. Two main groups of materials were investigated in this work: the baseline material (so-called because it has been a point of reference for other material development), and tailored sol-gel materials. Examination, understanding and optimisation of the baseline material forms a large part of this chapter and has been given most attention because it is also the material that has found widest applicability throughout this project. In addition to this optimisation work on the baseline material, a number of other materials were developed for waveguide fabrication, with various enhanced properties. Characterisation of these materials is outlined, and one particular material has been studied in greater depth, revealing its improved transmission in the third telecommunications window (wavelength of 1.55 μm).

4.1 Sol-gel Material

4.1.1 Definitions

Before concentrating on the specifics of the work carried out here, it is useful to take a broader perspective on sol-gel processing, and in so doing, define the relevant terms that apply to a sol-gel material. Firstly, a sol is a mixture where one

substance (the dispersed or internal phase) is dispersed evenly throughout another (continuous phase) [1]. Sols are not only engineered materials, but also exist in the natural state as inert materials such as clays or inks [2], and living materials such as serum or milk [3]. They are generally defined as colloidal suspensions, in which sub-micrometer sized particles are homogeneously dispersed within a liquid, the viscosity of which is between that of water and light oils.

A gel is an intermediate state between a liquid and a solid. It results from the progressive densification of a liquid and can be modelled as a solid, the porosity of which is partially filled with liquid. The removal of the liquid, and the means by which this is carried out allows the definition of a wide variety of solid materials. When the liquid is water, the gels are called "aquagels" or "hydrogels". When the liquid is mainly composed of alcohol, the gels are called "alcogels". If the removal of alcohol is carried out by thermal evaporation (either at room temperature or assisted by a heating moderately) the resulting gels are called "xerogels" [1]. However, some gels are not sufficiently resistant to heat treatments and crack. To avoid this, a hypercritical drying is required to minimise the interfacial liquid-solid energy, and such gels are called "aerogels" [4].

With careful control of the synthesis conditions and precursors, followed by a higher temperature treatment of the resulting films, densified sol-gel coatings can be formed which are not porous. Such materials and processes are the focus of this work, as densified non-porous films are essential for the fabrication of optical waveguides with low scattering losses.

4.1.2 The Sol-gel Process

The sol-gel process in its most general sense, is characterised by reactions between liquid phase precursors which result in the formation of the dispersed phase within a liquid phase. Central to many sol-gel processes is the hydrolysis of a metal alkoxide precursor in the presence of water. The general hydrolysis reaction is described in equation 4.1, where M represents the metal atom (M=Si,Zr,Ti...). The reaction involves the replacement of alkoxide groups (OR) with hydroxyl groups (OH), by the nucleophilic attack of oxygen on the metal atoms (R repre-

sents an alkyl group) [1].

$$\equiv M - OR \;+\; H_2O \;\rightleftharpoons\; \equiv M - OH \;+\; ROH \tag{4.1}$$

$$\equiv M - OR \;+\; HO - M \equiv \;\rightleftharpoons\; \equiv M - O - M \equiv \;+\; ROH \tag{4.2}$$

$$\equiv M - OH \;+\; HO - M \equiv \;\rightleftharpoons\; \equiv M - O - M \equiv \;+\; H_2O \tag{4.3}$$

Hydrolysis of the metal alkoxide is influenced by both the pH and the R-value (molar ratio of water to total alkoxide groups). The hydrolysis is generally favoured by decreasing the pH, which acts as a catalyst for the removal of the OR groups [1]. Larger R-values also tend to increase the hydrolysis rate by the provision of a greater number of water molecules. However, for most metal alkoxides there is an upper limit to the R-value that can be employed as excessive water promotes the formation of particles within the sol, which is generally to be avoided.

The hydrolysed precursor is an intermediate step between the raw ingredients and the end-product. Once hydrolysed, the precursor can take part in sol-gel condensation reactions, which are shown in equations 4.2 and 4.3. Condensation reactions occur via a nucleophilic attack and produce metal-oxo bonds, $\equiv M - O - M \equiv$, together with by-products of alcohol or water. Usually, condensation starts before hydrolysis is complete. After a period of aging a suitable viscosity level is reached to permit coating of the sol to form a thin gel film.

4.1.3 Hybrid Sol-gel Materials

Hybrid sol-gel materials are a group of materials synthesised via the sol-gel route that generally contain both an organic and inorganic part [5]. The synthesis of hybrid sol-gel materials includes the hydrolysis and condensation reactions of the inorganic network that are central to sol-gel processing. However, hybrid materials are generally more diverse than the conventional inorganic sol-gel materials because the incorporation of the appropriate organic component can give the material a wide range of tailored properties [5] including 1) modification of the mechanical properties [6, 7] (elasticity, scratch resistance etc), 2) improved processing of films, 3) mouldability [8] , 4) porosity control, 5) hydrophilicity/hydrophobicity [9, 10]. The organic component often contributes to a peculiar material functionality such as; 1) optical [11, 12], 2) electrical [13], 3) electrochemical [14], 4) chemical or biochemical functionality [15–17]. The condensed inorganic backbone is generally considered to give enhanced mechanical

and thermal strength, while also allowing the tuning of refractive index [18, 19], or other interesting electrochemical, electrical or magnetic properties [5, 20].

Due to the wide variety of material structures that are possible, a classification scheme has been developed to more precisely specify the type of hybrid material. There are two general classes; Class I corresponds to hybrid systems in which organic molecules are simply embedded in inorganic matrices with weak bonding between phases (hydrogen, van der Waals bonds etc..). Previous work in this laboratory has focussed on the development of such material as porous sensor films whereby organic dye molecules which are sensitive to the presence of certain gases (notably oxygen and carbon dioxide) are entrapped in the inorganic porous matrix during synthesis.

Class II corresponds to hybrid organic-inorganic materials where both the organic and inorganic components are bonded through stronger covalent or iono-covalent chemical bonds. This is the class of hybrid materials of interest in this work. These materials have been developed for optical waveguide applications. ORMOSILs (ORganically MOdified SILicates) belong to the class II hybrids as they are composed of inorganic molecules to which a functional organic group has been covalently attached in order to give a particular material property.

In this work, hybrid class II sol-gel materials have been developed, based on the photocurable ORMOSIL precursor 3-methacryloxypropyltrimethoxysilane (MAPTMS, Assay 99% in methanol, Aldrich), the chemical structure of which is shown in Figure 4.1. The hydrolysis and condensation of MAPTMS results in a hybrid organosilicate material, in which the organic group of MAPTMS gives the property of photocurability to the material, which is essential for the fabrication of optical waveguides by selective UV-irradiation. The photochemical mechanisms by which the organic groups of MAPTMS are cross-linked upon UV irradiation, are described in the following section.

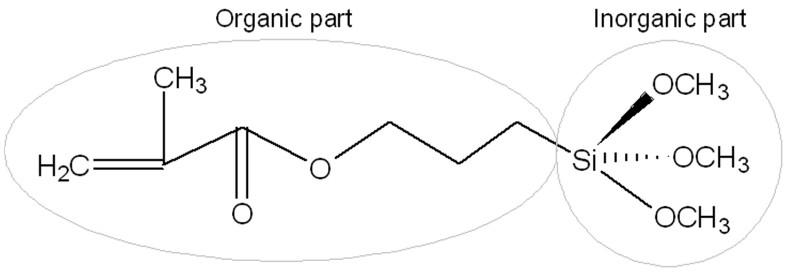

Figure 4.1: *Chemical structure of MAPTMS*

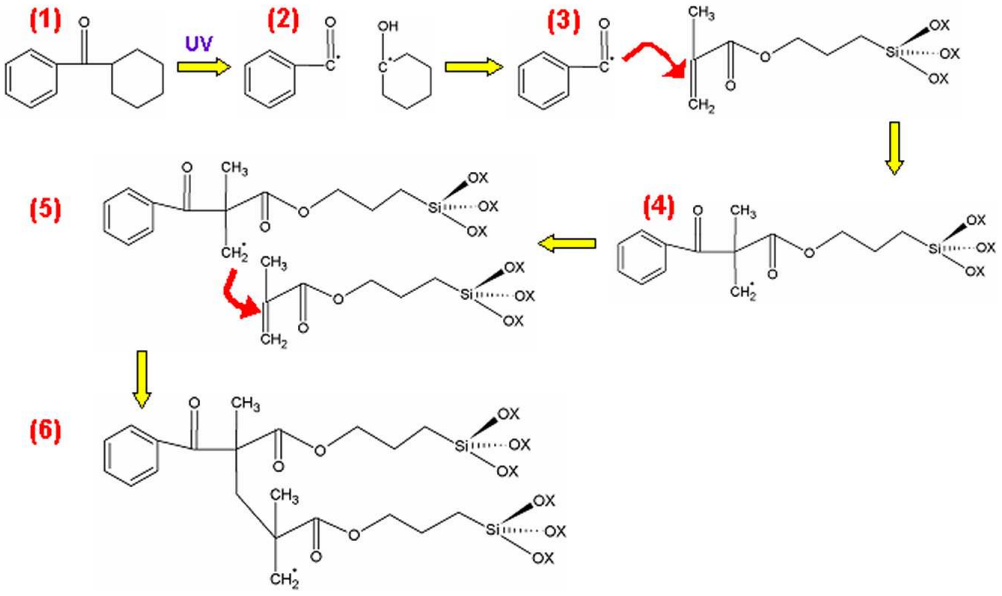

Figure 4.2: *Schematic diagram showing photoinitiator radical formation and reaction with MAPTMS under UV exposure*

4.1.4 Radical Photopolymerisation

As mentioned in previous Sections, the organosilane precursor MAPTMS is used for sol-gel synthesis in this work because, with the addition of a photoinitiator, the resulting sol becomes photopolymerisable/photocurable. Photoinitiators can be defined as macromolecular systems that contain chromophores which through a light absorption process can generate active species able to initiate the polymerisation and cross-linking of mono and multi-functional monomers and oligomers [21]. This photocurability allows the formation of channel optical waveguides by selective UV-irradiation of a thin film of the sol-gel material. The organic part of the MAPTMS molecule is involved in the photoreaction, specifically the methacrylic group (carbon double bond). A typical reaction mechanism is shown in Figure 4.2 (using the photoinitiator Irgacure-184® for illustration purposes), and involves three main steps: 1) initiation, 2) propagation, and 3) termination. Initiation starts in Step 1 with the UV irradiation of the photoinitiator, progressing to step 2 which shows the UV-induced splitting of the photoinitiator (photolysis) to create two radicals. Radicals are defined as atomic or molecular species with unpaired electrons on an otherwise open shell configuration, and have extremely high reactivity [21]. In step 3, one of the radicals produced is in close proximity with the MAPTMS molecule, with the arrow indicating the methacrylic bond which the radical is able to break. The start of propagation is shown in step 4, where the radical has broken the methacrylic bond of MAPTMS,

thus creating a larger radical molecule. In step 5, propagation continues as this larger radical is pictured in proximity to another MAPTMS molecule where it can once again break a methacrylic bond in order to form an even larger radical (shown in step 6). This process will continue until it is terminated by reaction with another radical (either one of the photoinitiator fragments from step 2, or another large radicals like itself). In this way, UV exposure of the sol-gel thin film causes crosslinking of the organic components of the network, notwithstanding the inorganic network which is already formed to an extent which depends upon the sol aging time. The cross-linked parts of the film are now quite durable even when immersed in alcohol, while the unexposed parts are readily rinsed away by alcohol. In this way, various structured patterns, such as ridge channel waveguides, can be formed.

4.1.5 General PLC Fabrication Process

Having established the microfabrication techniques for PLC fabrication, and now with knowledge of the basics of the hybrid sol-gel materials, it is possible to outline the basic steps of PLC fabrication. The fabrication process generally consists of 5 main steps as illustrated by Figure 4.3:

1. Buffer layer deposition (via dip- or spin-coating) followed by a temperature treatment to stabilise the layer

2. Guiding layer deposition (the layer in which the PLC will be patterned)

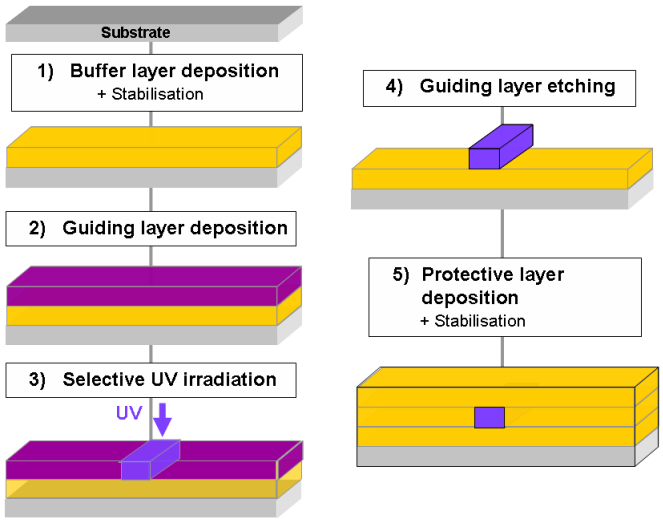

Figure 4.3: *Diagram showing the general PLC fabrication steps*

3. Selective UV irradiation (using laser writing or mask photolithography) of the guiding layer to define the PLCs

4. Etching of the unirradiated regions of the guiding layer using a solvent

5. Deposition of the protective layer (typically the same material as the buffer layer) followed by a temperature treatment to stabilise the entire structure

The processing parameters employed for device development depend upon the specific sol-gel formulation employed, and in each chapter PLC fabrication will be described in more detail.

4.2 Characterisation Techniques

The characterisation techniques described in this Section were employed throughout this work. Refractometry allows characterisation of the refractive index of the various different hybrid sol-gel materials developed. On the other hand, UV-Visible (UV-Vis) spectroscopy and nuclear magnetic resonance (NMR) were utilised to characterise the chemical properties of these materials, permitting rational optimisation to be carried out.

4.2.1 Refractometry

One of the fundamental characteristics of any material for application in integrated optics is its refractive index. In a waveguide, the refractive index contrast between the core of the waveguide (guiding layer material) and the surrounding cladding region (buffer layer material) is among the most important parameters affecting waveguide performance, as it determines the number of modes that the waveguide can support. Waveguide dimensions (width and height) are equally important in this regard. In order to accurately and conveniently measure the thickness and refractive index of thin films, the prism coupling technique was employed (using the Metricon 2010 Prism Coupler instrument). As its name suggests, the technique makes use of a prism to couple laser light into the thin film under investigation as shown in Figure 4.4. In this instrument the prism, sample, coupling head, and photodetector are all mounted on a motor-controlled turn-table. For measurement, the stationary laser beam (λ=635nm) is incident upon the slowly rotating prism face. Normally, the light is reflected from the base

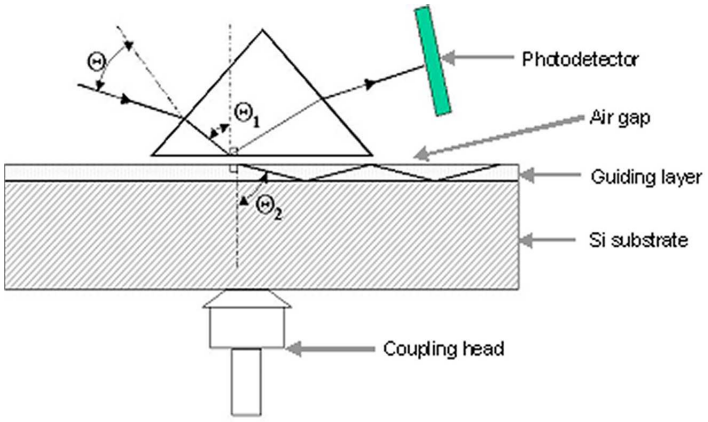

Figure 4.4: *Schematic diagram of the Metricon 2010 Prism Coupler instrument*

of the prism at the prism/thin film interface whereupon it is measured by a photodetector. However, at particular angles of incidence known as 'mode angles', the propagation constant of the evanescent field from the prism matches that of the mode in the thin film, and so coupling of energy from the evanescent field into the thin film mode is possible [22]. This is detected as a sharp drop in the intensity detected by the photodiode for this particular angle. The thicker the film the larger number of modes it supports and hence the more dips in the resulting spectrum (also known as M-line spectroscopy). By entering two or more of these angles into a set of complex transcendental equations which must be solved numerically, both the film thickness and refractive index are yielded with a high degree of accuracy.

4.2.2 UV-Visible Spectroscopy

The UV-Visible (UV-Vis) spectroscopy technique was used primarily in order to characterise the evolution of the sol depending upon alterations to the synthesis. Chemical changes in response to these alterations were highlighted by shifts in the absorption spectra in the UV wavelength range in which these sol-gel formulations have been designed to react. The UV-Vis absorption spectra (200-800 nm) were obtained using a Cary Varian 50 scan spectrophotometer with a resolution of 1 nm. The scan speed used was 600 nm per minute. In all cases, samples were prepared by sandwiching the liquid sol between two quartz films in order to obtain a film of 100 μm thickness.

4.2.3 ^{31}P-NMR

The ^{31}P-NMR technique allows observation of the local environment of phosphorus nuclei in a sample. It is based upon the detection of shifts in the resonance frequency of an applied magnetic field, away from the resonance frequency of a single unbound phosphorus nucleus. If the phosphorus nucleus in a molecule is well shielded by surrounding electrons, the energy needed to attain resonance with the nucleus will be lower. Therefore, changing peaks in the NMR spectra of a sol can be attributed to chemical changes involving the phosphorus nucleus over time. The chemical shifts were measured relative to tetramethylsilane (TMS), used as external reference. The FID (Free induction decay) processing used a 10 Hz line broadening, and a 4 s recycle delay time with a 6 μs pulse duration was found to be sufficient for quantitative measurements. Each recorded spectrum is an average of 500 scans which were accumulated for each sample.

4.3 The Baseline Material

The photocurable material from which the majority of the optical circuits in this work have been fabricated will be referred to as the "baseline material".The baseline material formulation was first developed in this laboratory by Dr. Mohamed Oubaha. It is a hybrid organic-inorganic sol-gel material comprised of a mixture of the ORMOSIL precursor MAPTMS (allowing photocuring), and a zirconate complex, which is employed to give control of the refractive index of the material, and also improves the mechanical properties of the optical coatings.

4.3.1 Synthesis and Properties of the Baseline Material

Synthesis of the baseline material follows the general hydrolysis and condensation reactions outlined in Section 4.1.2. In this Section, the details of material synthesis are described. This is accompanied by an in-depth explanation of the reactions occurring within the sol during each stage of synthesis. The synthesis procedure is depicted schematically in Figure 4.5 and can be divided into three main steps:

1. pre-hydrolysis of MAPTMS,
2. synthesis of the zirconate complex,

3. mixture of the products from step 1 and 2, and final hydrolysis of the mixture.

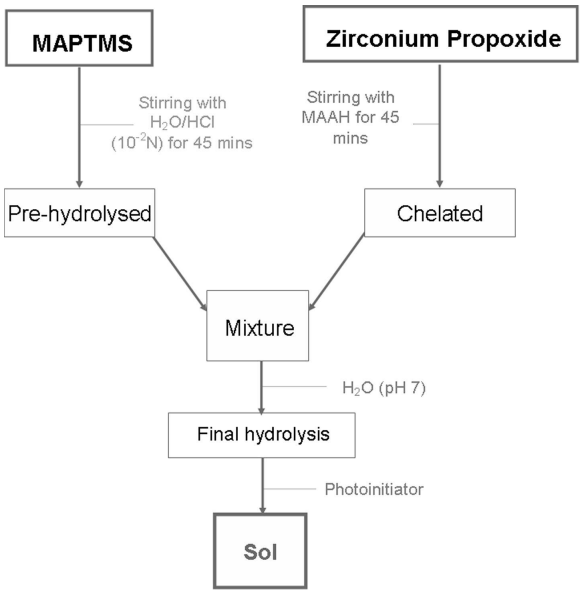

Figure 4.5: *Schematic diagram showing the sol-gel synthesis steps for the baseline material*

Pre-hydrolysis of MAPTMS:
MAPTMS is partially hydrolysed with an aqueous solution (HCl 0.01N), employing a water to alkoxide ratio of 1.00:0.75. HCl is added to the water as a catalyst to hydrolysis, as it aids in the formation of protons which are responsible for attack of the alkyl groups on MAPTMS, leaving a vacancy for hydroxyl ions to bond to the silicon.

Species	Notation
$RSi(OMe)_3$	T_0^0
$RSi(OMe)_2OH$	T_0^1
$RSi(OMe)OH_2$	T_0^2
$RSi(OH)_3$	T_0^3
$RSi(OMe)_2$-O-Si	T_1^0
RSi(OMe)OH-O-Si	T_1^1
$RSi(OH)_2$-O-Si	T_1^2
RSi(OMe)-$(O\text{-}Si)_2$	T_2^0
RSi(OH)-$(O\text{-}Si)_2$	T_2^1
$RSi(OSi)_3$	T_3

Table 4.1: *Monomeric and oligomeric species obtained during hydrolysis and condensation reactions in MAPTMS*

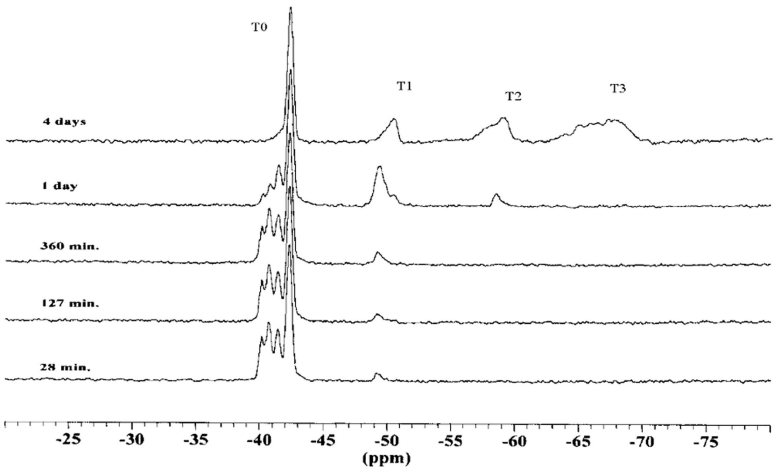

Figure 4.6: ^{29}*Si NMR spectra of MAPTMS pre-hydrolysis up to four days of aging [23]*

As MAPTMS and water are not miscible, the hydrolysis was performed in a heterogeneous manner. After 20 minutes of stirring, the production of methanol became sufficient to allow the miscibility of all species present in solution. MAPTMS has been studied extensively and a brief examination of the ^{29}Si-NMR spectra in Figure 4.6 [23] reveals how the reactions progress in the sol during hydrolysis and condensation. In order to interpret the spectra a system of notation identifying the various monomeric and oligomeric species in the sol is presented in Table 4.1. During the first minutes of hydrolysis of MAPTMS, the four T_0 peaks appear which correspond to the 4 stages of hydrolysis of MAPTMS (where either 0, 1, 2 or 3 of the methoxy groups have been been replaced by hydroxyl groups). As mentioned above, during this reaction methanol is released according to equation 4.4 (where R' denotes the organic group of MAPTMS) which allows homogeneous mixing of water and MAPTMS. After 28 minutes of reaction, a T_1 peak can be observed which indicates the beginning of condensation. It is important to note that the formation of condensed oligomers (T_2 and T_3 species) appears after 1 and 4 days aging respectively. This shows that the formation of a 3 dimensional network in pure MAPTMS is very slow. However, the inclusion of the zirconate species in the second hydrolysis has a strong influence on the system, changing the properties significantly compared to pure MAPTMS. Therefore, it is sufficient to pre-hydrolyse MAPTMS for just 45 minute given the strong reactions caused by addition of the zirconate complex.

$$\equiv R'Si(OCH_3)_3 \; + \; X(H_2O) \quad \longrightarrow \equiv R'Si(OCH_3)_{3-X}(OH)_X \; + \; X(CH_3OH) \tag{4.4}$$

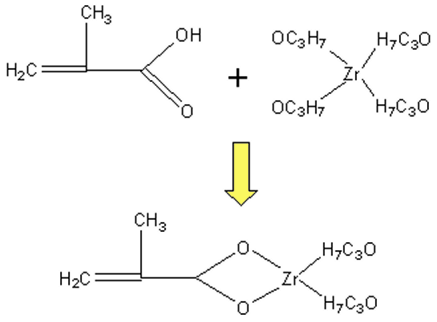

Figure 4.7: *Chelation of zirconium n-propoxide by MAAH*

Synthesis of the zirconate complex:
The zirconate complex is included so as to enable refractive index tuning, and to improve the mechanical properties of the material. It is synthesised using the precursor zirconium n-propoxide, $Zr(OC_3H_7)_4$. However, due to the strong electropositivity of this precursor compared to silicon alkoxides (electronegativity = 1.33 compared to 1.90), it reacts rapidly with water (readily attracting hydroxyl groups) and typically forms particles. In order to avoid particle formation, the hydrolysis reaction must be restrained and this is done by replacing some of the reactive propoxy groups of the precursor with ligands which are unreactive with water. In this case, methacrylic acid (MAAH) was used to covalently chelate the zirconium atom through two propoxy groups as shown in Figure 4.7. In general, chelation refers to the binding of a single ligand to another molecule at two or more binding sites. In order to chelate $Zr(OC_3H_7)_4$, MAAH was added dropwise with a 1:1 molar ratio. Due to the equimolar proportions of alkoxide and MAAH in this preparation, the most probable resulting complex is $Zr(OnC_3H_7)_2$MAAH as indicated in Figure 4.7.

Final hydrolysis of mixture:
At this stage of synthesis, the refractive index of the final material must be specified. To achieve this, an appropriate concentration of the zirconate complex was placed in a vial. The partially hydrolyzed MAPTMS was slowly added to the zirconate complex, with the mixture characterized by an exothermic reaction, indicating the formation of irreversible bonds. The molar ratio of the zirconate complex is varied as shown in Table 4.2, to synthesise the typical guiding layer formulation from which waveguides were formed.

Precursor	Guiding layer	Buffer layer
MAPTMS	1	1
$Zr(OC_3H_7)_4$	0.4	X
MAAH	0.4	X
H_2O	2.12	2.12
Irgacure 819	0.011	0.011
Irgacure 1800	0.039	0.039

Table 4.2: *Molar concentrations (for guiding and buffer layers) of the baseline hybrid sol-gel materials*

For the buffer layer, a lower ratio of zirconate complex is present (where X $<$ 0.4), the value of which depends on the refractive index required (which is determined by the wavelength of light that the waveguides carry, their dimensions or whether they are single- or multi-mode waveguides). Once the pre-hydrolysed MAPTMS and zirconate complex had mixed for approximately 2-3 minutes, water (pH 7) was added to this mixture so as to complete the hydrolysis of just over 50% of the alkoxide groups in the sol. This second hydrolysis lead to a stable and homogeneous sol only when the first hydrolysis of the MAPTMS was carried out in proportions of 1.00:0.75 (MAPTMS:H_2O). Below this molar ratio, precipitation of the zirconate species occurred during the second hydrolysis [23]. Examination of Figure 4.8 reveals the reactions that occur in the sol during addition of the zirconate complex and final hydrolysis.

Firstly, when the zirconate complex reacts with the pre-hydrolysed MAPTMS a spontaneous increase in the condensation of the siloxane network is observed, as seen by the sudden appearance of T_1 and T_2 species (spectrum M). The zirconate complex has the ability to catalyse the self-condensation of the siloxane network. After final hydrolysis is complete, the disappearance of all T_0 species (hydroxy-

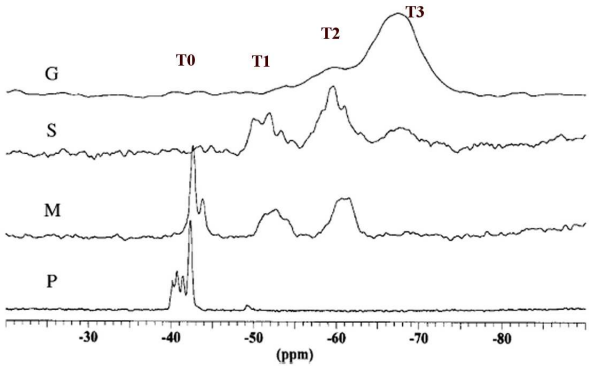

Figure 4.8: ^{29}*Si NMR spectra of sol during different stages of synthesis [23]*

lated MAPTMS) is observed with the appearance of T_3 species corresponding to a highly linked inorganic network (spectrum S). After depositing and drying the final sol, analysis of the solid reveals that T_3 species (with some T_2) are in the majority (spectrum G).

Final hydrolysis and condensation reactions were allowed to proceed during constant stirring for an aging time of 24 hours. After this aging time, the viscosity increased via the polycondensation reactions discussed above to a degree such that sol-gel films of approximately 6 microns could easily be formed by spin- or dip-coating. Once aging of the sol had been completed, photoinitiator was added to the sol and stirred for 1 hour before filtering and use. The function of the photoinitiator is to provide a ready source of radicals, which can cause rapid crosslinking of the organic components of the sol. Different photoinitiators were tested throughout this work, all of which absorbed light strongly around the UV exposure wavelengths (325 nm for direct laser writing, and 365 nm for the mask aligner)

As indicated in Table 4.2, two photoinitiators were blended in the baseline sol, Irgacure 819 and Irgacure 1800, the chemical structures of which are shown in Figure 4.9. It was found that using Irgacure 819 alone led to waveguides with a more square cross-sectional shape with less rounding at the top. However, problems with waveguide adhesion and photostability of the sol were also noted. Irgacure 1800 on the other hand gave greater photostability to the sol but produced waveguides with slightly more rounding at the top corners. The best compromise was found by blending Irgacure-819 with -1800 in a 1:3.5 molar ratio, giving a total photoinitiator to methacrylic bond ratio of 1:20.

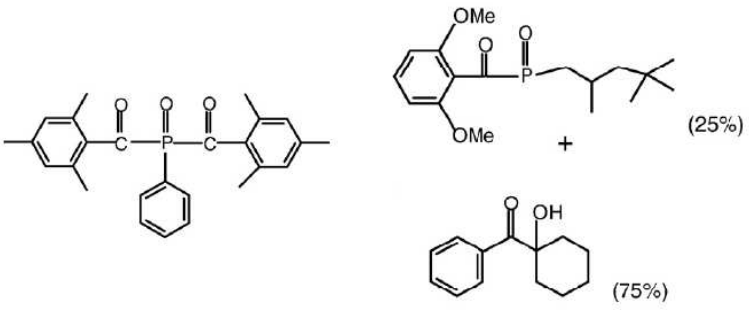

(a) (b)

Figure 4.9: *Chemical structure of a) Irgacure 819 and b) Irgacure 1800*

4.3.1.1 Refractive index modification

As mentioned above, by varying the concentration of the zirconate complex in the sol, the refractive index can be tuned over quite a wide range. In order to observe the dependence of the refractive index of the sol-gel thin films on zirconate concentration, a number of sols were prepared as outlined previously. Each sol had a slightly different zirconate concentration, covering a molar concentration range between 0 and 0.4 relative to MAPTMS. The sols were spin-coated onto silicon substrates and stabilised by UV exposure followed by baking at 100 °C for 2 hours. The refractive indices of the resulting films were measured using the prism coupling technique (as outlined in Section 4.2.1) and the results are shown in Figure 4.10. Within the resolution of the instrument (0.001 RIU), the refractive index of the stabilised sol-gel films increases linearly with increasing zirconium content, allowing precise control of refractive index over a wide range.

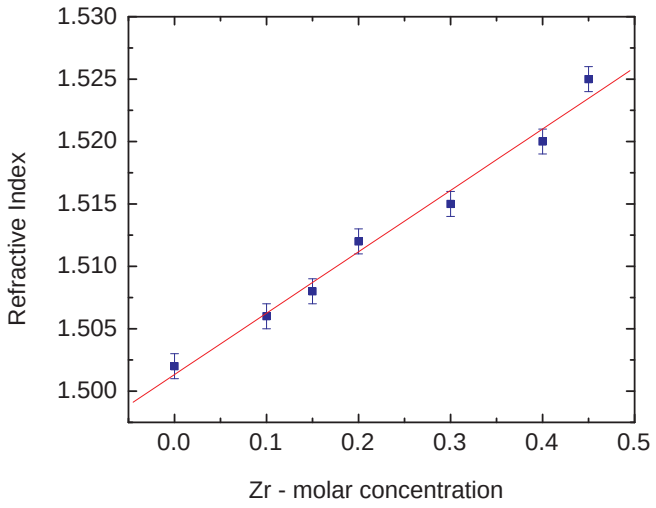

Figure 4.10: *Change in refractive index of stabilised sol-gel films as a function of the molar concentration of the zirconate complex*

4.3.1.2 Photostability

Observation of the behaviour of the baseline material in response to standard UV exposure techniques (outlined in the previous chapter) revealed that it was possible to fabricate waveguides with a square cross-section and the desired dimensions. However, it was also noted that there was a difference in the width of waveguides depending upon the length of time between addition of photoinitiator and use of the sol (for waveguides fabricated using the same UV exposure

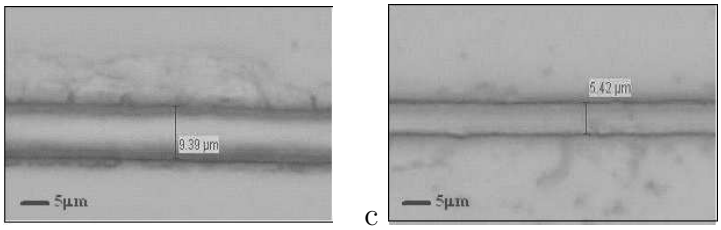

(a) (b)

Figure 4.11: *Optical microscope images of waveguides obtained from the baseline guiding layer sol after aging for a) 1 h, and b) 4 days. Laser beam energy=1217 mJ/cm*^{2}

parameters). This is evident in Figure 4.11, where the waveguide fabricated from a sol used 1 hour after photoinitiator addition, was approximately 4 μm wider than the waveguide fabricated from the same sol, which had been aged 4 days before use. This instability in the material photoreactivity is an undesirable material characteristic as it demands strict synchronisation of any fabrication steps with the addition of photoinitiator in order to fabricate waveguides of repeatable dimensions, which is critical for all integrated optical applications.

The material instability has been characterised fully as shown in Figure 4.12, which shows the width of waveguides fabricated from a sol aged for 1 hour after photoinitiator addition, compared those fabricated from the same sol after a further 4 days of aging. Over the entire range of UV energy densities used in waveguide fabrication, it is clearly evident that waveguides fabricated from the 1 hour aged sol are wider than those fabricated from the 4 day aged sol. This con-

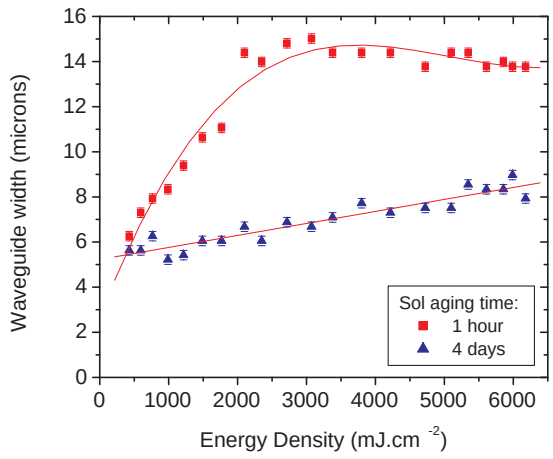

Figure 4.12: *Waveguide width as a function of energy density for two sols aged by 1 hour and 4 days*

firms the early qualitative observations and suggests a link between the width of the waveguides and the photoreactive properties of the sol, which are intimately linked to the state of the photoinitiator within the sol.

4.3.2 Optimisation of the Photostability

The data of the previous Section points to an evolution of the photoinitiator within the sol, such that its photoreactivity is degraded gradually over time. In this Section, the chemical reactions occurring in the sol which are responsible for degradation of the photoinitiator are reported on. This led to an understanding of the mechanism by which this degradation occurs, and ultimately to optimisation of the material by eliminating this attribute.

4.3.2.1 UV-Visible analysis

Analysis of the baseline sol

UV-Vis measurements were first conducted on the photoinitiators Irgacure-819 and -1800 (dissolved at 0.001 wt% in acetonitrile) using the experimental conditions outlined in Section 4.2.2 throughtout. As shown in Figure 4.13, the high characteristic absorption of each compound around the UV wavelengths of interest are evident (325 nm for laser writing and 365 nm for mask alignment instrument). The figure also shows the linkage between the characteristic features of the spectra and the chemical bonds within the compounds. These links were made using density functional theory (DFT) simulations, which were carried

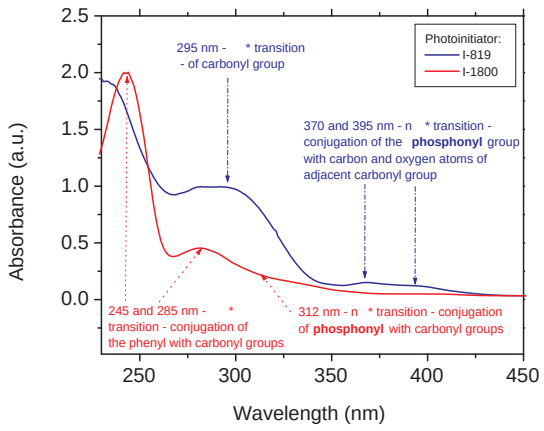

Figure 4.13: *UV-Vis spectra for Irgacure-819 and -1800 photoinitiators separately dissolved in acetonitrile*

out by our collaborators in the Université de Haute Alsace [24].

Turning attention to the behaviour of the sols, the baseline sol guiding layer formulation detailed in Table 4.2 was subjected to UV-Vis spectroscopy, to indicate whether chemical reactions were occurring in the sol with the progression of time. For these measurements, the sol was synthesised both with and without the photoinitiators, the sol without photoinitiator (Sol A) serving as a reference from which to evaluate the sol containing photoinitiator (Sol B). Examination of the UV-Vis spectrum in Figure 4.14a shows that, for Sol A, there is no change in absorbance between the 1 hour and 120 hour aged sol. This strongly suggests that no significant chemical reactions are occurring in the sol that can be detected in the spectral range of interest.

The UV-Vis spectrum in Figure 4.14b shows that the addition of photoinitiator substantially changes the absorbance of Sol B compared to Sol A, so that the spectrum now shows some of the characteristic features of the photoinitiator spectra including a strong trough around 350 nm and peaks around 370 and 395 nm associated with the phosphonyl groups. Of critical interest is the evolution of the spectrum as aging proceeds, where it can be seen that after 120 hours of aging with the photoinitiator, the sol evolves toward a stable spectrum that more closely resembles the spectrum of Sol A with the disappearance of the above-mentioned photoinitiator characteristics. Comparison of this evolving absorption spectrum with the unchanging spectrum of Sol A, leads to the clear conclusion

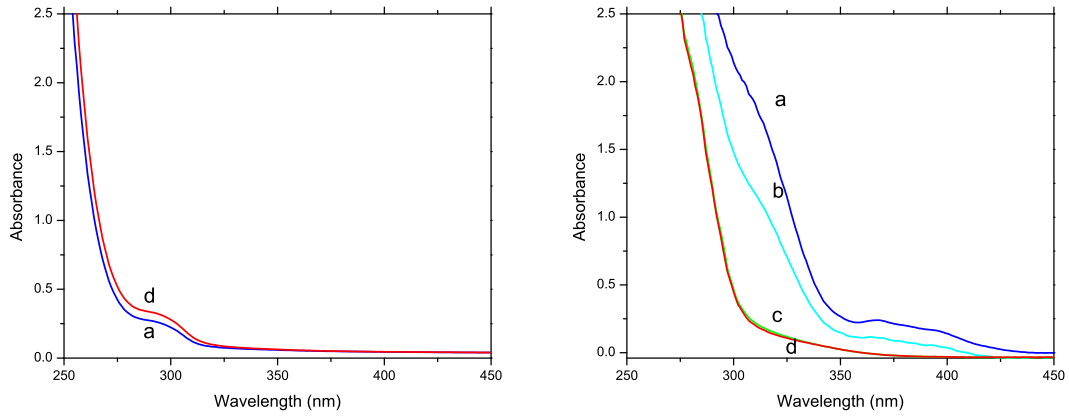

(A) (B)

Figure 4.14: *UV-Vis spectra for A) "sol A", and B) "sol B", which were aged for: a) 1 hr, b) 24 hrs, c) 96 hrs and d) 120 hrs after addition of photoinitiator*

that once photoinitiator is added to the sol, the absorbance value evolves over time indicating the occurrence of chemical change in the sol. It is very likely that the previously observed decrease of photostability of the sol is linked to the chemical changes in the sol, with a degradation of the photoinitiator(s) being the most likely cause of these observations.

Analysis of precursors

In order to understand the mechanism of degradation of the the photoinitiator, it was first necessary to determine the component of the sol that both Irgacure-819 and -1800 were reacting with. To achieve this, each compound was separately dissolved in each of the main precursors of the sol; 1) MAPTMS, 2) MAAH and 3) $Zr(OC_3H_7)_4$. UV-Vis spectra were recorded for each solution after aging for a) 1 hr, b) 18 hrs, c) 24 hrs and d) 69 hrs and the results are shown in Figure 4.15a for Irgacure-819 and Figure 4.15b for Irgacure-1800. It is evident from these figures that when each photoinitiator is separately dissolved in both MAPTMS and MAAH, there is negligible change in the UV-Vis spectra over time. Conversely, the spectra of both compounds in $Zr(OC_3H_7)_4$ evolves significantly during the aging period. This clearly indicates that the mechanism by which the photointiators are degraded involves reaction with the $Zr(OC_3H_7)_4$ precursor and not with MAPTMS nor MAAH.

Having isolated the component of the sol which is active in the degradation of the photoinitiator, a deeper insight into the mechanism of degradation can be found by closer examination of the spectrum of I-1800 in $Zr(OC_3H_7)_4$. A characteristic knee at $\sim$285 nm appears in the spectrum at 18 hours and remains largely unchanged in measurements at 24 and 69 hours. Reference to the spectrum of pure I-1800 in Figure 4.13, shows that this feature has been attributed to the conjugation of phenyl with carbonyl groups in I-1800. As shown in Figure 4.9b, these groups are only present in 75% of I-1800, with the other 25% being composed of a different compound. Therefore the stability of this characteristic knee at 285 nm indicates that this component of the photoinitiator is not degraded (75% of I-1800). However, observation of the spectrum reveals that while the characteristic knee remains stable, other parts of the spectrum continue to evolve. It is reasonable to conclude that the evolution of these parts of the spectrum is solely due to the degradation of the second component. The second component is composed of a phosphonyl-based molecule, similar to that of I-819 (compare Figure

4.9a and b).

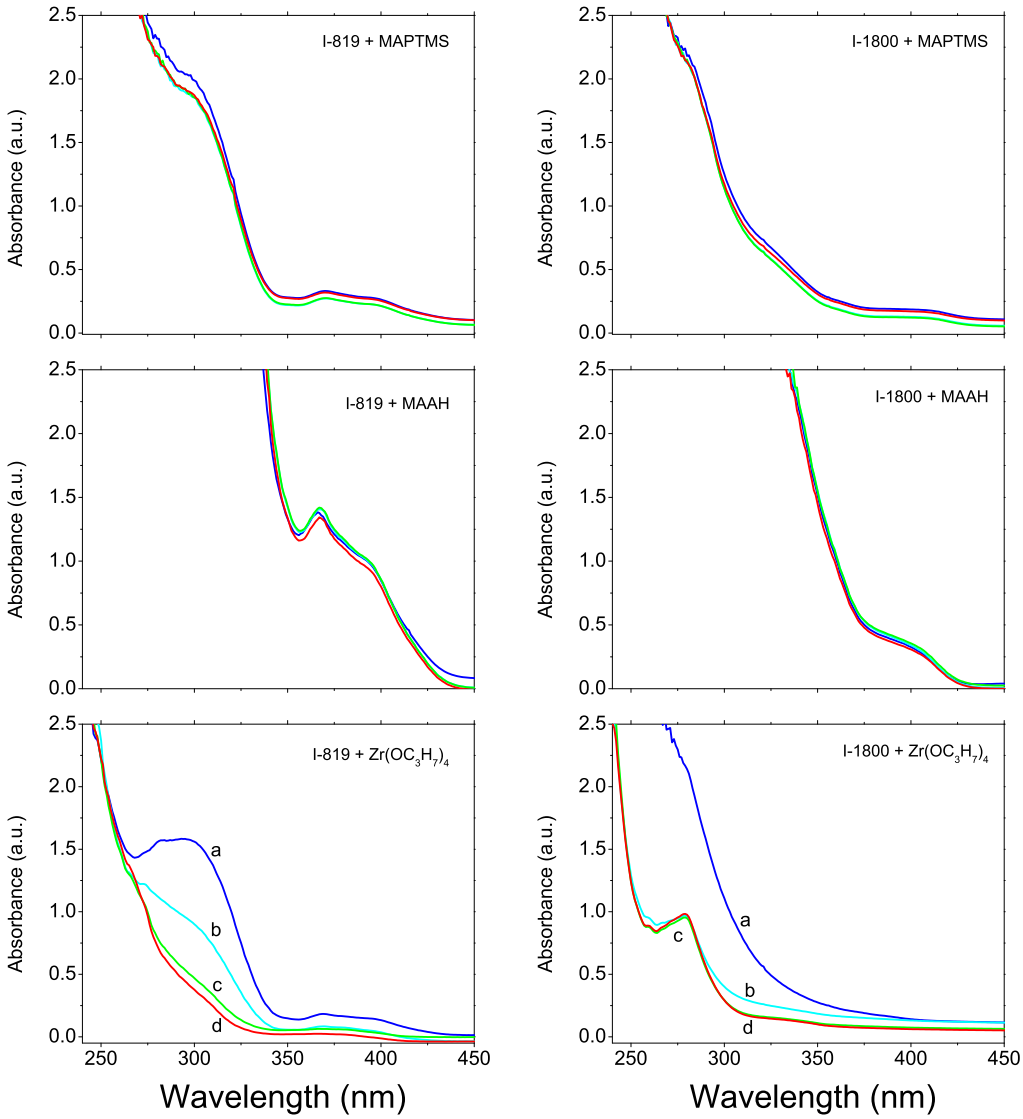

Figure 4.15: *UV-Vis analysis of A) I-819 and B) I-1800 dispersed in each of the sol-gel precursors and aged in each precursor for; a) 1 hour, b) 18 hours, c) 45 hours, and d) 69 hours*

4.3.2.2 ^{31}P-NMR study

In order to study the exact mechanisms of photoinitiator degradation, and given the likelihood of phosphorus involvement revealed in the preceding Section, a ^{31}P-NMR study was carried out to monitor the environment of the phosphorus atoms in the sol at an atomic/molecular level. As both photoinitiators contain a phosphonyl group, it was decided to focus the NMR study on sol containing only Igracure 819, as it is the photoinitiator with the highest concentration of phosphonyl groups. For this study the standard sol formulation was used (that of Sol A) except that Irgacure 819 alone was mixed with a 1:20 molar concentration relative to MAPTMS. The ^{31}P liquid NMR spectrum of pure Irgacure 819 (not shown) displays a single peak at -1.54 ppm demonstrating the high purity of the compound. The spectra exhibited in Figure 4.16 show the response of the sols containing Irgacure 819, aged for three different times. Spectrum M was recorded after stirring the sol with Irgacure 819 for only 10 minutes, and shows the disappearance of the main peak initially located in the precursor at -1.54 ppm and the appearance of two new peaks at -6.57 and -6.72 ppm, respectively. Spectrum M1 was obtained after stirring the same sol for 24 hours, and highlights the presence of three peaks located at -6.45 (84.3%), -17.34 (5.6%) and -18.88 ppm (10.1%), with the disappearance of the two peaks observed for sample M also observed. After 48 hours of aging, the spectrum obtained (M2) shows the exact same peaks observed for spectrum M1, but with different contributions (75.7%, 8.3% and 16%, respectively). Such behaviour can only be explained by a strong chemical reaction of the photoinitiator with the reactive groups present in the sol. In a previous study [23], it has been determined that Zr-OH species are formed in the sol during the catalysis of the

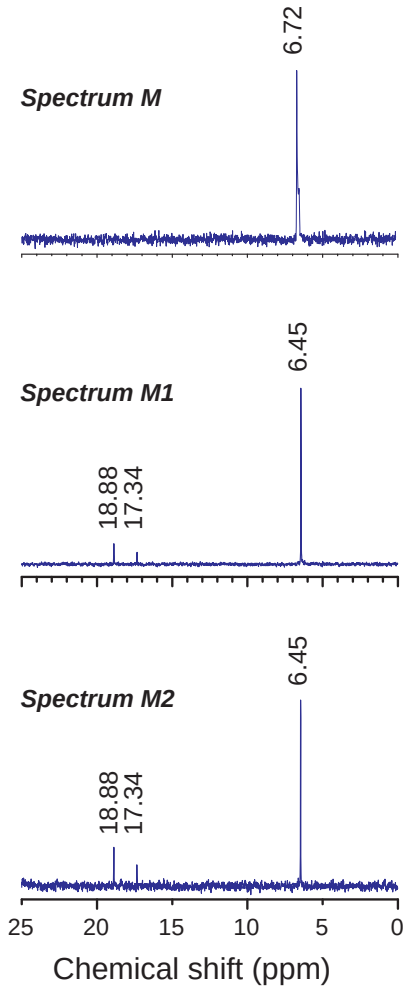

Figure 4.16: *^{31}P-NMR spectra of the sols after 10 mins (spectrum M), 24 hours (spectrum M1), and 48 hours (spectrum M2)*

Chemical shift (ppm)	Assignment
6.4-6.7	P-O-Zr
17.3	$P(O\text{-}Zr)_2$ linear oligomers
18.8	$P(O\text{-}Zr)_3$ cyclic or polycyclic oligomers

Table 4.3: *Assignment of the ^{31}P-NMR signals*

siloxane network by the zirconate complex (explained in Section 4.3.1). After hydrolysis of the silanol groups and subsequent polycondensation, these Zr-OH groups are the main reactive species remaining in the sol apart from the propoxy groups of the zirconate complex which have already been shown to react with photoinitiator. As such, we can expect that the degradation of the photoinitiator is caused by oxidation reactions of the phosphonyl groups of the photoinitiator with $ZrOC_3H_7$ and/or Zr-OH groups. Moreover, the electropositive character of the phosphorus atom in the photoinitiator is reinforced by the presence of two adjacent carbonyl groups that favour the nucleophilic attack by the zirconate complex, as previously described [25, 26] in closely related materials. The numerous peaks observed were identified to originate from both the normal and the tridentate character of the phosphorus atom that can induce several kinds of oligomer structures [27]: linear, cyclic and polycyclic. On this basis, we can assign all the observed peaks as shown in Table 4.3. This result demonstrates that the degradation of Irgacure 819 is essentially caused by the presence of ZrOH and $ZrOC_3H_7$ groups in the solgel material. The aforementioned degradation provokes the formation of phospho-zirconate molecules exhibiting NMR peaks at lower chemical shifts, which can be explained by a progressive decrease of the sterical hindrance in the environment of the phosphorus nuclei. The increase of the cyclic or polycyclic concentration, from 10.1% in sample M1 to 16% in sample M2, also indicates an evolution toward an immobilised structure where the phosphorus atom is at the centre. The main conclusion of this study was that with the progression of time, phosphonyl containing photoinitiator molecules are subjected to nucleophilic attack by the Zr-OH reactive species in the sol, thus gradually rendering the photoinitiator insensitive to UV irradiation and therefore less able to initiate polymerisation.

4.3.2.3 Optimisation of the sol formula

Having first observed and quantified the problem of photostability relating to the width of optical waveguides, and then identified the cause of the changes in

the photoreactivity and the mechanism by which it occurred, optimisation of the formulation was undertaken. Given that the problem has been isolated to the nucleophilic attack of phosphonyl containing compounds within the photoinitiator, it was first decided to characterise the behaviour of Irgacure-1800 in the sol without the presence of Irgacure-819, as Irgacure-1800 contains only 25% of the a phosphonyl compound, with the other 75% expected to be non-reactive with the sol-gel matrix. An array of waveguides fabricated using different UV exposures were fabricated and measured, for a sol aged 1 hour and 4 days after addition of I-1800. The result shown in Figure 4.17 shows negligible difference in waveguide width between the 1 hour and 4 day aged sols. This verifies the fact that changes in photostability that were observed as a variation in waveguide width were due to the phosphonyl containing compounds, and are minimised by the use of I-1800 alone.

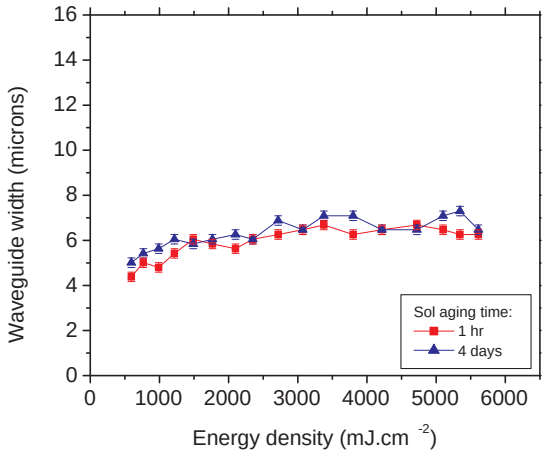

Figure 4.17: *Waveguide width as a function of UV-energy density for the optimised sol formulation aged for; a) 1 hour, and b) 4 days*

4.3.3 Influence of the Photoinitiator on Waveguide Structure

Having isolated the source of the photostability issues, it was now possible to study the influence of different photoinitiators on the waveguide structure and shape, secure in the knowledge that any differences observed in the waveguides were as a result of the different photoinitiator properties, and not the result of an evolution in photostability.

Waveguide width and UV-Vis analysis

The baseline sol formulation for the guiding layer was used to explore the effects of different photoinitiators on the resulting waveguide cross-sectional structure (using the formulation detailed in Table 4.2 but without the photoinitiator content there indicated). In light of the previous analysis, three different photoinitiators (Irgacure-184, -1800 and -907) which had little or no phosphonyl content, were separately dissolved in a sol with a 1:20 molar ratio of the photoinitiator relative to MAPTMS for each sol. Using each sol, thin films were formed by spin-coating, and waveguides were laser written over the available UV-energy density range, using the direct laser writing system described in Section 3.4 (has a 6 μm diameter laser spot). The width of each waveguide was measured by optical microscopy, and the results are displayed in Figure 4.18a.

Additionally, UV-Vis spectra measurements were conducted on each sol as shown in Figure 4.18b, allowing a relationship between the waveguide width and absorbance of the different sols to be established. Examination of Figure 4.18a shows that the width of waveguides fabricated using I-1800 and I-184 are very similar over the UV energy density range. This is expected as the absorbance of these two sols are very similar owing to the fact the I-1800 is in fact composed of 75% of I-184. However, the width of waveguides fabricated using I-907 is wider than either I-1800 or I-184, over the same range of UV energy density. It can be seen from the UV-Vis spectrum that the absorbance of I-907 at the UV-exposure

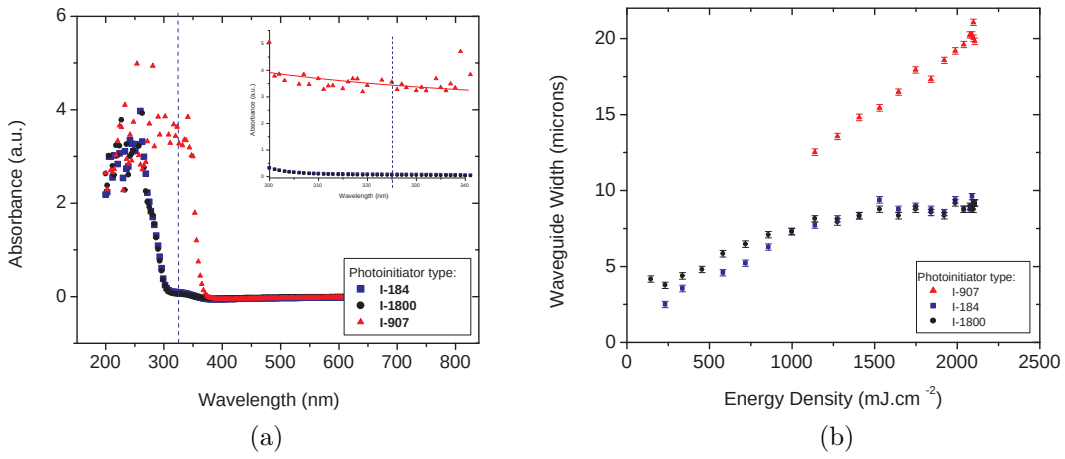

Figure 4.18: *a) UV-Vis spectrum of three different photoinitiators separately dissolved in the baseline sol, and b) waveguide width as a function of UV energy density for sols containing each photoinitiators (separately)*

wavelength of 325 nm (laser writing) is ∼35 times greater than that of I-1800/I-184. Therefore, there is a clear connection between a photoinitiator with higher absorbance (at the UV exposure wavelength) and the width of resulting waveguides. For a given concentration of photoinitiator, the higher the absorbance the greater the conversion rate of the photoinitiator molecules into radicals and therefore the higher the photoreactivity. This higher photoreactivity is responsible for the wider waveguides produced by I-907 when compared to the other two photoinitiators studied, as the greater conversion rate of photoinitiator to radicals is responsible for the propagation of the organic network farther into the area outside the laser beam spot by the formation of longer macromolecular chains [28]. At this stage it should be noted that the waveguides formed using I-907 were highly trapezoidal in shape, and the width value reported in Figure 4.18a is the width of the waveguide at the top, where it was widest. The consequences on waveguide cross-sectional shape of using a highly absorbing photoinitiator in the sol are explored in the following Section.

Internal filter and waveguide cross-section shape

As shown in Figure 4.19a, the waveguides fabricated using I-907 were highly trapezoidal in shape, and this can be linked to the high absorption of the photoinitiator at the UV laser writing wavelength of 325 nm. The high absorption of the sol at 325 nm, provides an internal filter effect to the coating. This means that a large portion of the incident UV radiation is absorbed near to the top surface of the coating [29]. Consequently the top of the coating is highly cross-linked with excessive lateral growth of the polymeric chains, which is evident in the large width of the waveguide at the top surface. Conversely, due to the fact that much of the light is absorbed near the surface, the progressively lower light intensity experienced by the material deeper in the film translates to a lower conversion rate of photoinitiator to radicals. At some point, the intensity threshold for photolysis is not reached at the substrate and so below this energy density the

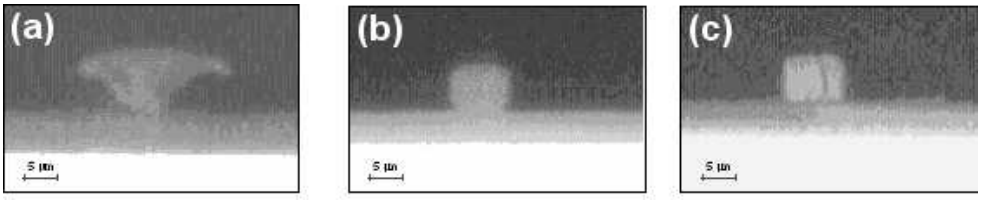

Figure 4.19: *Cross-section of waveguides resulting from sols containing a) I-907, b) I-184 and c) I-1800*

waveguides do not adhere to the substrate. Examination of Figure 4.18a shows that this occurs at an energy density of 1100 $mJ.cm^{-2}$ for waveguides formed using the I-907 sol. The narrowing of the waveguide near the substrate can be explained in the same way as the excessive width at the top of the waveguide. Here, the radical production is so low that they are consumed readily in the footprint of the laser spot and it is thought that the macromolecular network has a lower degree of cross-linking here with short macromolecular chains that do not grow beyond the laser spot footprint.

As a contrast to the I-907 sol, the waveguides produced using I-1800 and I-184 have a quasi-square cross-section as shown in Figure 4.18b and c. At this molar concentration these formulations give a good compromise between adhesion on the one hand and waveguide shape on the other. It is important that the formulation absorbs sufficient UV light in the footprint of the laser spot to ensure equivalent radical production and polymerisation at the top and bottom of the coating. Another factor must be considered when choosing the photoinitiator type and molar concentration, is oxygen inhibition. Oxygen inhibition refers to the inhibition of radical propagation (and therefore polymerisation) in a coating due to the absorption of atmospheric oxygen near to the surface [30, 31]. Oxygen has a very high affinity to bind with the radicals, creating peroxy radicals which are ineffective for initiating polymerisation [32]. The slight rounding of the top edges of the waveguides shown in Figures 4.18b and c is due to this phenomenon.

4.3.4 Influence of the Zirconate Complex and Chelating Agent on Photoreactivity

In this Section, data from experiments that were carried out to observe the effect on photoreactivity of changes in the degree of chelation of the zirconate complex are reported [33]. As mentioned in Section 4.3.1, zirconium is normally chelated by MAAH in a 1:1 stoichiometric ratio. It was suspected that photoreactivity could be changed by chelating the $Zr(OC_3H_7)_4$ to different degrees, as this could influence the sterical hindrance to the macromolecular chains affecting their ability to propagate. In order to test this theory, a number of formulations with different molar ratios of $Zr(OC_3H_7)_4$ to chelating agent were developed as shown in Table 4.4. In addition to changing the molar ratio of chelating agent to $Zr(OC_3H_7)_4$, another chelating agent - isobutyric acid (IBA, $C_4H_8O_2$, Assay 99%, Aldrich) was included in the study (in addition to the standard MAAH). As

Formulation	Chelating Agent	Molar ratio - MAPTMS : $Zr(OC_3H_7)_4$: Chelating Agent
A	MAAH	1.00 : 0.40 : 0.40
B	MAAH	1.00 : 0.56 : 0.40
C	MAAH	1.00 : 0.40 : 0.56
D	IBA	1.00 : 0.40 : 0.40
E	IBA	1.00 : 0.56 : 0.40
F	IBA	1.00 : 0.40 : 0.56

Table 4.4: *Molar ratios of the sol-gel formulations A-F*

summarised in Table 4.4, the molar ratios of the MAAH chelated sols (named A, B and C) were mirrored in the IBA chelated sols (named D, E and F) so as to allow direct comparison of the effects of the different chelating agents. Waveguides were fabricated over a range of UV energy densities for each sol, and by observing the dimensions of the resulting waveguides, it was possible to again comment on the photoreactivity of each formulation.

Comparing formulation A to C in Table 4.4, it is clear that both contain the same molar concentration of MAPTMS and $Zr(OC_3H_7)_4$, but formulation A is less chelated by MAAH than C. Examination of Figure 4.20a shows that waveguides fabricated from formulation A are wider than those from C, over the UV energy range. This means that formulation A is more reactive than C. The reason for this is clearly connected to the degree of chelation of $Zr(OC_3H_7)_4$. Two possible explanations for the observed effects present themselves. Firstly, it may be pos-

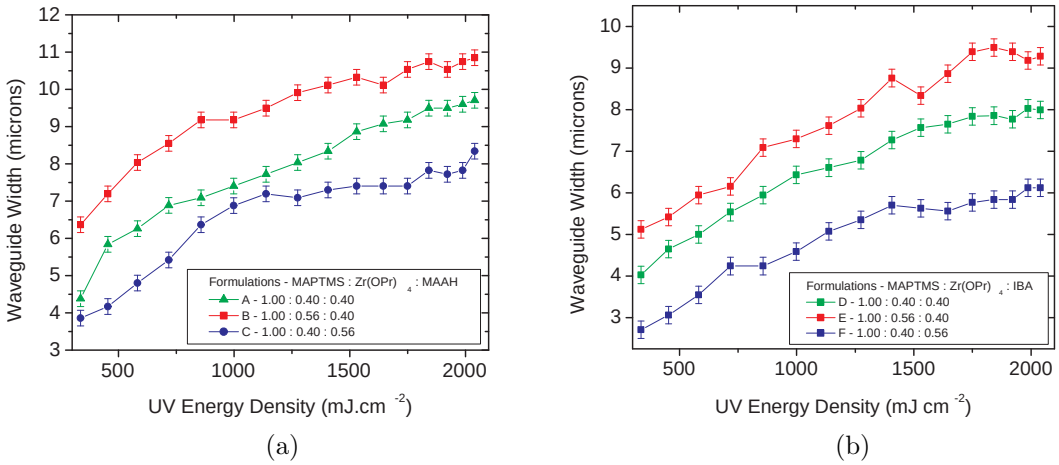

Figure 4.20: *Waveguide width as a function of UV-energy density for; a) formulations A, B, C, and; b) formulations D, E, F*

sible that $Zr(OC_3H_7)_4$ is directly involved in photopolymerisation, and that the more chelated the $Zr(OC_3H_7)_4$ molecule, the less possibility it has for crosslinking. However, this phenomenon has never been previously reported. Another possibility still concerning the contribution of $Zr(OC_3H_7)_4$ to the photopolymerisation, is that $Zr(OC_3H_7)_4$ in some way interacts with the photoinitiator to more efficiently produce radicals. For a less chelated $Zr(OC_3H_7)_4$ molecule we can speculate that again, the unchelated parts are free to contribute to radical production.

Comparing formulation A and B, we see that in this case the molar concentration of the chelating agent MAAH in the sols is kept constant. However, the concentration of $Zr(OC_3H_7)_4$ is increased in sol B compared to A. An important point can be clearly made in this situation. In sol B, the volume percentage of the photopolymerisable MAPTMS component in the sol is 6.6% lower than in sol A. Assuming that MAPTMS in conjunction with photoinitiator is the only component responsible for photopolymerisation, it is expected that the waveguides formed from sol B should be narrower in width owing to the reduced amount of MAPTMS per unit volume.

However, examination of Figure 4.20a shows that the opposite is the case, and sol B yields wider waveguides than sol A. Therefore, sol B is more reactive than sol A in spite of containing less MAPTMS per unit volume. The clear conclusion here is that $Zr(OC_3H_7)_4$ is not an inert component of the sol, but plays an active role in photopolymerisation. Preliminary studies into this phenomenon have begun within our research group [34], and indicate that the photoinitiator may form a chemical bond with $Zr(OC_3H_7)_4$. The proximity of the zirconium atom to the photoinitiator appears to provoke increased mobility of the electrons in the aromatic rings, thereby increasing absorption of incident light, which may be responsible for the increased photoreactivity.

Examination of the IBA chelated sols and comparison with the MAAH chelated sols also yielded useful results. For the IBA chelated formulations (D, E and F in Table 4.4), the same experiments were carried out as for A, B and C as analysed above, and the results are shown in 4.20b Exactly the same trends described above can be seen in formulation D, E and F. However, additional information is provided by these formulations relating to the photoreactivity of the sol as a function of the chelating agent in the sol. Comparing the coatings chelated by MAAH to IBA, it is clear that all of the IBA coatings give waveguides that are narrower in width (on average 1.8 μm). Also the range of waveguide widths is

smaller by an average of 2.1 μm for IBA chelated sols over the same range of UV energy.

These further experiments show that the chelating agent also has a role to play in the photoreactivity. However, it is difficult to distinguish the role played, in the context of the strong interaction of photoinitiator and zirconium. Two hypotheses to explain the observed differences between MAAH and IBA chelated sols are proposed. The first hypothesis relates to steric hindrance considerations. Examination of the structure of MAAH reveals that it contains a vinyl group, and so has a planar spatial configuration. IBA on the other hand has a non-planar spatial configuration, and therefore a higher steric hindrance by virtue of its fully saturated alkyl groups. This means MAAH sols are susceptible to provide greater freedom of movement of the organic polymerisable species, with the effect that the waveguides fabricated from it are wider at the same energy density than those fabricated using IBA.

The second hypothesis to explain the difference between MAAH and IBA chelated sols is related to the behaviour of each molecule in the zirconate complex. Following on from the hypothesis to explain the active role of zirconium in the coatings, it is possible that MAAH contributes further to this enhancement due to the presence of a methacryloxy group in the organic chain. This has the capability to induce a strong electro-attractive mesomeric effect in the complex, further increasing electronic mobility and therefore, absorption. Though IBA is chemically similar to MAAH, it does not contain an organic group capable of provoking the same phenomenon, thereby accounting for the lower photoreactivity of IBA-chelated coatings.

Experiments are on-going to establish the prevalent mechanism by which the chelating agent affects the photoreactivity of the material.

4.3.4.1 Material for thermo-optical switch fabrication

Prior to development of the baseline material, a hybrid sol-gel material similar to the baseline material was developed (by a colleague, Dr. Jean-Marc Sabattie) for the fabrication of the thermo-optical switches presented in Chapter 7. The synthesis is identical to that outlined for the baseline material, except that the molar concentration of the constituents is changed as outlined in Table 4.5. These different molar ratios result in a refractive index of 1.50 and 1.49 for the guiding and buffer layer materials respectively. Also, processing conditions are slightly

Precursor	Guiding layer	Buffer layer
MAPTMS	10	10
Zr(OPr)4	0.58	0.15
MAAH	8.62	2.24

Table 4.5: *Constituents of the hybrid sol-gel material used for thermo-optical switch fabrication*

changed due to different physical properties of the materials (i.e. greater tackiness), and the fabrication process is presented in Section 7.6.2 for thermo-optical switch fabrication.

4.4 Characterisation of Tailored Hybrid Materials

Referring back to Section 4.1.3, it was emphasized that careful selection of an ORMOSIL precursor with specific organic group(s) could confer many useful properties on the resulting hybrid material. In this Section, the characterisation of a number of different hybrid sol-gel materials is presented where different organosilane precursors have been combined to produce a range of homogeneous, multifunctional hybrid materials with a number of attractive and enhanced properties.

4.4.1 Refractive Index Characterisation of Co-Organosilane Hybrid Materials

A range of different co-organosilane hybrid materials were prepared via the sol-gel process by the combination of two or more different organosilane precursors. The sols were prepared from combinations of the following precursors: MAPTMS, diphenyldiethoxysilane (DPHDES, Sigma-Aldrich, 98%), phenyltriethoxysilane (PHTES, Sigma- Aldrich, 98%) and vinyltriethoxysilane (VTES, Fluka, 98%), which were used without further purification. MAPTMS was included as the basis for each sol, as it is the only precursor here that is photocurable, allowing direct UV photopatterng of PLCs.

However, previous studies have shown that MAPTMS contains aliphatic CH groups, which have been shown to contribute to absorption at 1.55 μm [35]. Aliphatic groups are defined by the presence of carbon atoms joined together

by straight chains, branched chains or rings. On the other hand, vinylic groups (present in VTES) and aromatic groups (present in DPHDES and PHTES) do not absorb at this wavelength [35]. Aromatic groups such as the phenyl group seen in these precursors, are characterised by a conjugated ring of unsaturated bonds which displays cyclic delocalisation of electrons leading to a stabilisation that is stronger than would be expected by conjugation alone.

In order to incorporate these low absorbing components into photocurable hybrid materials, the following process was carried out. MAPTMS was first pre-hydrolysed as described in Section 4.3.1. According to the diagram in Figure 4.21a, VTES and DPHDES were individually added to the pre-hydrolysed MAPTMS to form sol Q and R respectively. Referring to Figure 4.21b, DPHDES was blended with VTES, and the mixture was added to the pre-hydrolysed MAPTMS to form sol S. Similarly, DPHDES was blended with PHTES and then the mixture was added to the pre-hydrolysed MAPTMS to form sol T.

To characterise the refractive index behaviour of each sol type (Q, R, S and T), different variations of each formulation were synthesised with a varying molar ratio of the precursors in each. For all sols, the final hydrolysis was performed on the mixtures with a 1:1 water to alkoxide ratio. After aging for 45 minutes, a photoinitiator (Irgacure 1800) was added to each sol in a 1:20 molar ratio with MAPTMS. After mixing for a further hour, each different sol was filtered through a 0.2 μm teflon filter and spin-coated onto a silicon substrate to obtain a film of

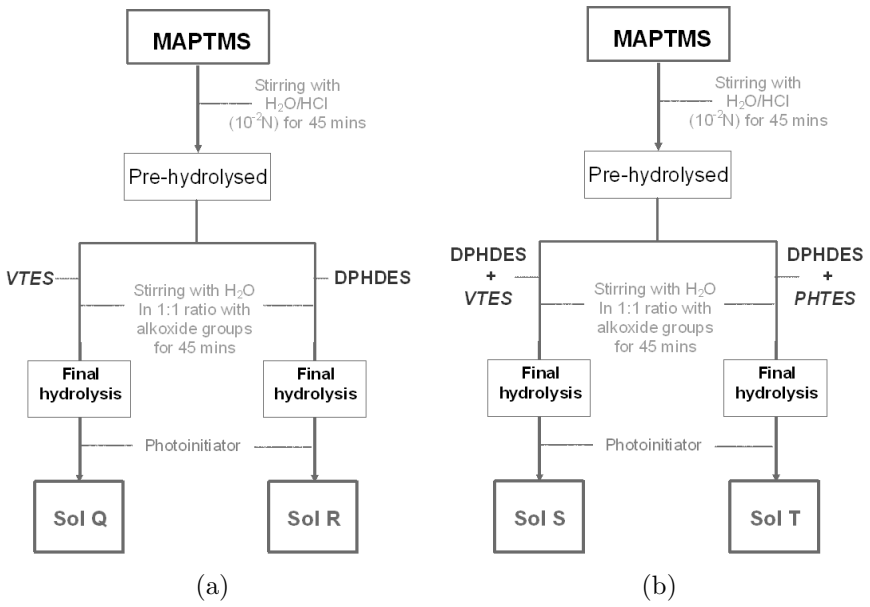

Figure 4.21: *Process diagram explaining the formation the co-organosilane hybrid sol-gel materials; a) sol Q and R, and b) sol S and T*

approximately 6 μm. To obtain fully densified coatings, each sample was baked at 120 °C for 24 hours.

The refractive index of each coating was measured using the prism coupling technique. The refractive index variation of two material types is plotted in Figure 4.22a: Sol Q, containing varying concentrations of VTES, and, Sol R containing varying concentrations of DPHDES. With increasing VTES content Sol Q exhibits a decrease in refractive index of -0.0002 per mole percent of VTES. On the other hand, Sol R shows in increase in refractive index of +0.0008 per mole percent of DPHDES.

The differences between Sol Q and R is attributable to the difference in molar refraction of VTES and DPHDES respectively, in comparison to that of MAPTMS. Molar refraction is a physical parameter that refers to the refractive index of a compound modified by the compounds molecular weight and density, also known as the Lorentz-Lorenz molar refraction [36]. It is a useful parameter in describing optical characteristics of multi-component materials. Sol R shows an increase in refractive index because of the high molar refraction of DPHDES, which is derived from the presence of two aromatic phenyl groups which have a high polarisability. The linear refractive index behaviour for both sol Q and R indicates that the refractive index follows the law of composition of mixtures, where the total molar refraction is equal to the sum of the individual contributions [37]. The suggests a group of materials that are well mixed at a molecular

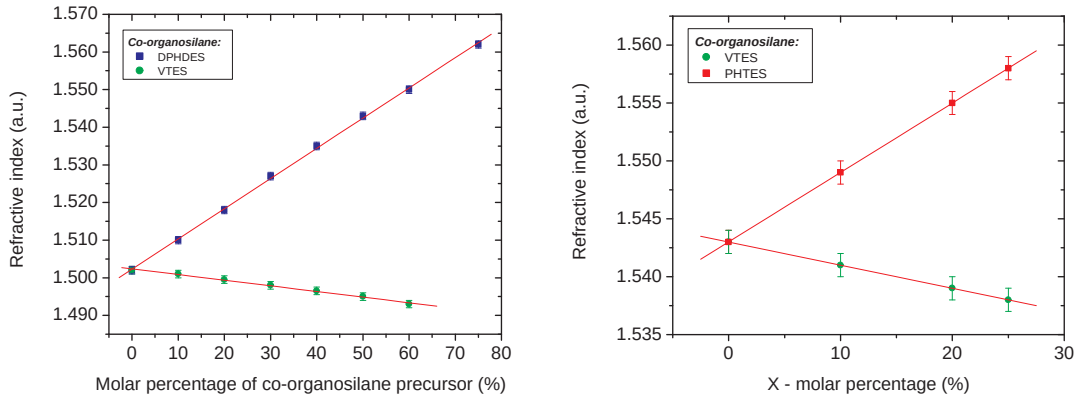

(a) (b)

Figure 4.22: *Variation of refractive index for sol-gel coatings composed of different molar percentages of; a) VTES or DPHDES combined with MAPTMS, and b) VTES or PHTES (with a molar concentration of X) combined with DPHDES and MAPTMS such that MAPTMS : DPHDES : VTES/PHTES = 50-X : 50 : X*

scale, and this has been confirmed by a subsequent structural characterisation of the materials which shows the good insertion of the aromatic species within the aliphatic moieties during the sol-gel synthesis [38].

In Figure 4.22b, the refractive index characterisation of sols S and T are presented. Sol S exhibits an increase in refractive index with a slope of +0.0006 per mole percent of PHTES. These materials verify that tri-organosilane hybrids can be synthesised and the linear behaviour of refractive index again suggests a good insertion of the aromatic species within the aliphatic MAPTMS giving homogeneous materials with controllable refractive index. Figure 4.22b shows again that as VTES is increased in this tri-organosilane sol, the refractive index decreases linearly.

The refractive index characterisation of this novel family of materials shows in each case a linear refractive index variation as a function of composition, with an achievable refractive index range of 1.49 - 1.562 reported here (corresponding to materials with 0% DPHDES and 0% VTES respectively). This work also shows that the aliphatic component of the sol (MAPTMS) can be minimised and replaced by low loss aromatic precursors. In the next Section, one of these novel materials is characterised in greater detail to yield the propagation losses of optical waveguides.

4.4.2 Characterisation of a Low-Loss Material at 1.55 μm

4.4.2.1 The material

To determine the improvement in waveguide propagation losses that is attainable by use of these tailored co-organosilane materials, waveguides were fabricated using Sol R (the synthesis and refractive index characterisation of which was outlined in the previous Section). In order to reveal the improvement in transparency of this material at 1.55 μm, a near infrared spectrum was recorded through a monolith formed by the gelation of the guiding layer sol (50% DPHDES) [19]. The result shown in Figure 4.23, reveals that the absorption is extremely low around 1.55 μm and is in fact reduced by 30% with respect to our baseline material [19]. The guiding layer and buffer layer were formed from a sol containing 50% and 40% of DPHDES respectively.

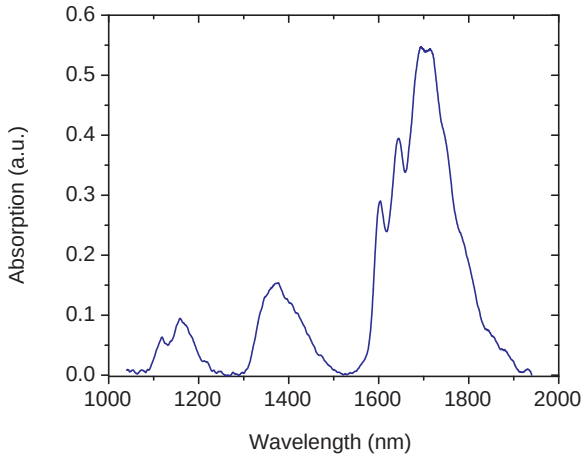

Figure 4.23: *Near infrared absorption spectrum of a monolith of sol R containing 50% DPHDES*

4.4.2.2 Waveguide array fabrication

To characterise the waveguide propagation losses, an array of 10 waveguides was first fabricated, each waveguide having identical cross-sectional dimensions of 7 x 7 μm thus giving single mode operation with the coatings employed (Δn = 0.008). The general steps for PLC fabrication described in Section 4.1.5 were employed, with selective UV exposure being carried out by the direct laser writing process (Energy density = $\sim$ 1500 mJ/cm^2).

4.4.2.3 The cut-back technique

Utilising the setup shown in Figure 4.24, the optical propagation losses were measured via the cut-back technique [19]. The cut-back technique first involves cleaving the input edge of the waveguide chip across a crystallographic plane using a diamond tipped scribe, so as to obtain a straight cleave across all of the waveguides [39–41]. Then the output end of the chip is cleaved in the same way, exposing the output facet of the waveguides. Light from a pig-tailed laser diode is coupled into the waveguides by end-fire coupling from a fiber. Light exiting the waveguides is collected with a microscope objective and focussed onto a photodiode (Thorlabs, DET210) which is connected to a multimeter for detection. The position of each component in the system (input fiber, chip, objective lens and detector) is adjusted using piezoelectric micropositioners until the maximum light intensity is recorded. The attenuation loss was calculated according to the following equation [39],

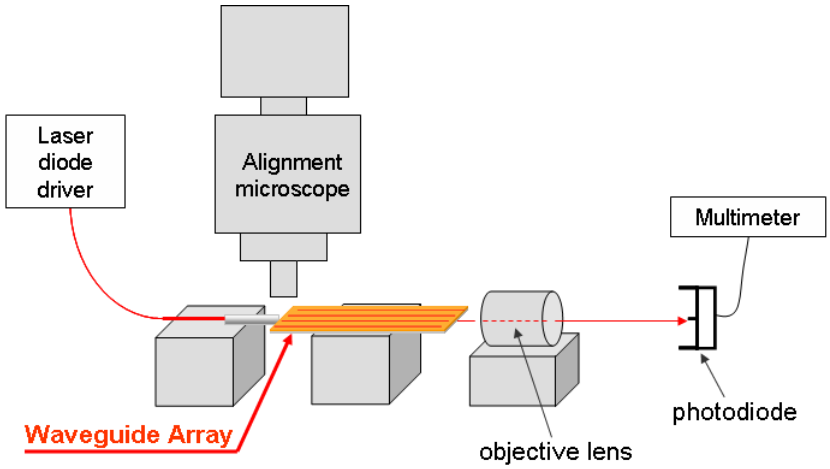

Figure 4.24: *Experimental setup for the characterisation of waveguide propagation loss via the cut-back technique*

$$\text{Attenuation Loss} = 10\log\frac{P_i}{P_j} \tag{4.5}$$

where P_i and P_j are the input and output light intensities from the chip, respectively. This was repeated for each identical waveguide in the array, allowing the estimation of uncertainty in Figures 4.25a and b using the standard deviation of the measurements. When this procedure has been carried out for all waveguides, and at the wavelengths 1.31 and 1.55 μm (2^{nd} and 3^{rd} telecommunications windows), then the output facet of the chip was once again cleaved, or 'cut-back' and the process was repeated for this length of waveguide. In this way it is possible to measure the change in output as a function of waveguide length, giving a measurement of the propagation loss or the loss per unit length of light travelling in the waveguide.

4.4.2.4 Propagation Losses

The results are shown in Figures 4.25a and b for both 1.31 and 1.55 μm, and extraction of the slope of this graph allow quantification of the propagation loss per unit length of waveguide, which is 0.500 $\pm$ 0.051 dB/cm for 1.31 μm and 1.560 $\pm$ 0.096 dB/cm for 1.55 μm. These are among the lowest propagation loss values reported for hybrid sol-gel waveguides operating at these wavelengths [42, 43]. In comparison to the baseline material [44], these optimised materials offer a decrease of 20% and 65% in propagation loss at 1.31 and 1.55 μm, respectively [19].

The propagation loss of a waveguide is caused by two phenomena: firstly, the intrinsic absorption and scattering losses of the waveguide material, and sec-

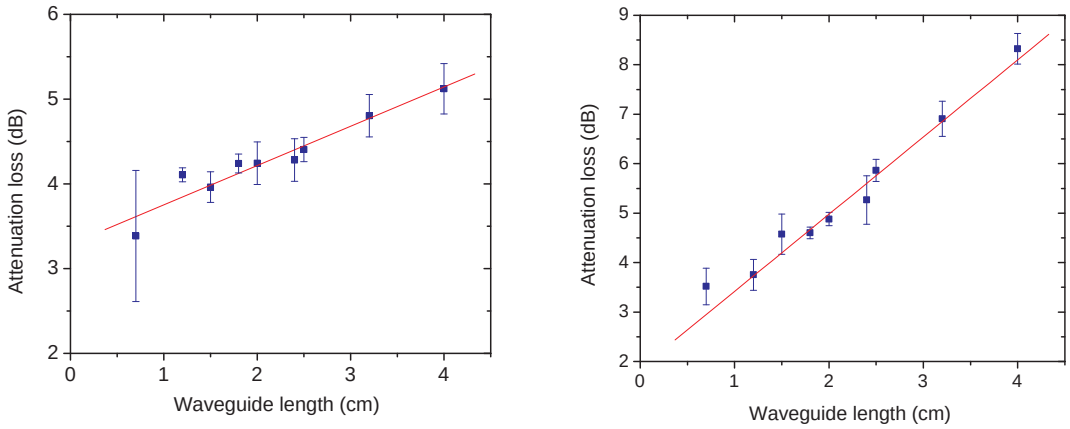

(a) (b)

Figure 4.25: *Graphs of insertion loss versus waveguide length for at a wavelength of a) 1.31 μm, and b) 1.55 μm*

ondly, the scattering losses due to roughness at the waveguide boundaries. These two phenomena combine to give an overall waveguide propagation loss, which is quoted above for the co-organosilane material. However, it is possible to further improve the propagation loss of waveguides fabricated from these materials, by further reducing the waveguide surface roughness. In the next Section, a methodology for substantially improving the uniformity and reducing the roughness of spin-coating sol-gel layers is presented, which provides a means by which waveguide propagation losses can be further reduced.

4.5 Optimised Spin-Coating Procedure

Having developed and optimised a number of hybrid sol-gel materials, a spin-coating procedure was developed, the basic physical principles of which are outlined in Section 3.2. At the initial stages, it was found that films coated in atmospheric conditions were often of poor quality with striations radiating from the center of the wafer as described above. In order to improve the quality of these films, vials containing isopropanol were placed around the bowl of the spin-coater in order to saturate the atmosphere with alcohol and thereby reduce the evaporation of alcohol from the film during spin-coating [45, 46]. This approach produced visible improvements to the coatings, with less dimpling and striations visible to the eye.

Following this improvement, the spin-coater was adapted to receive alcohol

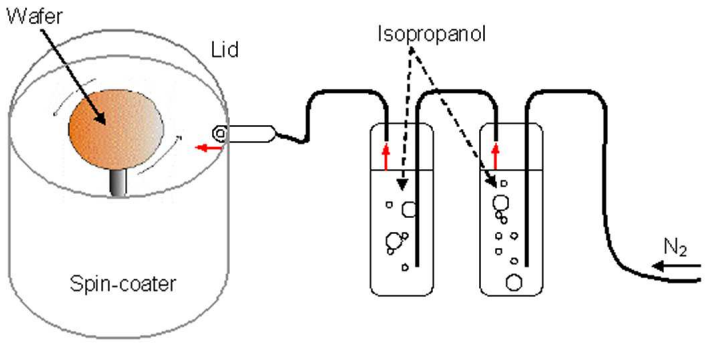

Figure 4.26: *Generation of an IPA-saturated in the environment for improvement of the surface quality of spin-coated sol-gel films*

saturated nitrogen which was produced by flowing nitrogen through sealed flasks containing isopropanol, as illustrated in Figure 4.26. This greatly improved film quality as it not only increased the alcohol vapour concentration in the spin-coater bowl but it also removed almost all humid air from the bowl during coating (as measured by a humidity probe), which can also induce rapid hydrolysis and condensation reactions to form a surface gel layer during spinning, which is responsible for coating defects [46].

Optical profilometry measurements of buffer layer films, allowed comparison of the spin-coating process in atmospheric and alcohol saturated conditions. In Figure 4.27(a), the surface map of a film coated in atmospheric conditions is presented, from which an average roughness value of ∼717nm was derived. The vast improvement given by coating in the optimised setup shown above is evident in the surface map in Figure 4.27(b), from which an average surface roughness of

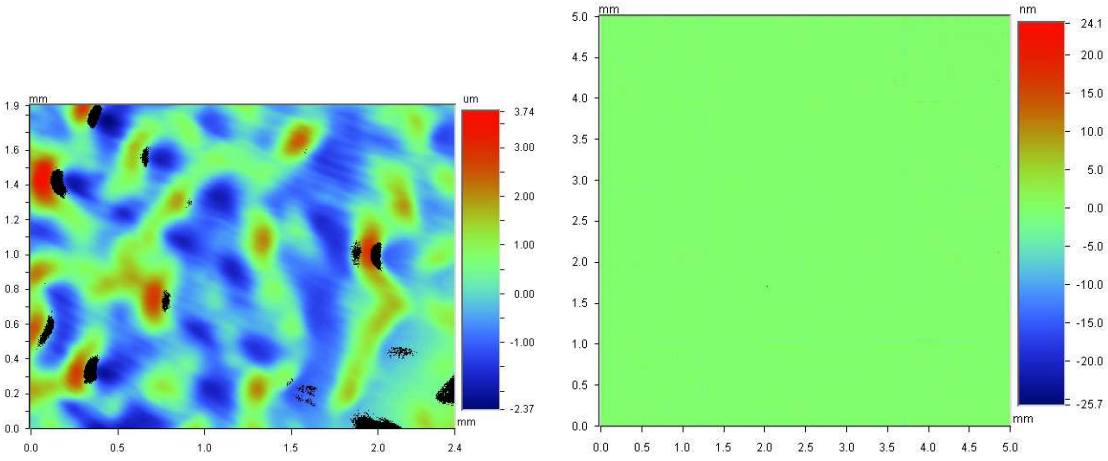

(a) (b)

Figure 4.27: *Optical profilometry of baseline buffer layer sol-gel coatings deposited under a) atmospheric conditions and b) using the alcohol-saturated atmosphere*

just 0.67nm was measured using the same measurement parameters as for the map in Figure 4.27(a). This clearly demonstrates the exceptional surface uniformity and low roughness given by the optimised spin-coating process developed here.

4.6 Conclusion

In conclusion, this Section has outlined the synthesis and chemical constitution of the baseline material. Deficiencies in photostability were identified and the source of this instability was found to lie in the nucleophilic attack of phosphonyl-containing photoinitiators by active species in the zirconate complex within the sol. In light of this discovery, optimisation of the baseline sol formulation has focussed on the use of non-phosphonyl-containing photoinitiators which have produced waveguides of equivalent dimensions even with a 4 day difference in aging time.

Having stabilised the formulation, a study was carried out, showing the effect that different types of photoinitiator have on the waveguide cross-sectional shape. It was shown that the correct concentration of photoinitiator is critical in order to obtain square waveguides with good adhesion to the substrate. The influence of chelating agent on photoreactivity of the sol was also studied revealing an important and surprising result in the active role of the zirconate complex in photopolymerisation. It appears that the complex is responsible for catalysing the production of radicals from the photoinitiator, thus increasing the photoreactivity of the sol.

Finally, the tunability of the sol-gel process was demonstrated with the characterisation of several new co-organosilane hybrid materials, where refractive index control of the sol relied not on the inclusion of a zirconate complex, but on the control of the relative proportions of organosilanes which have a different molar refraction. New materials containing aromatic precursors were formed and waveguides were fabricated from one sol in particular, the characterisation of which revealed low propagation losses of 0.500 and 1.560 dB/cm at 1.31 and 1.55 μm, respectively.

References

[1] C. J. Brinker and G. W. Scherer, *Sol-gel science : The physics and chemistry of sol-gel processing.*

[2] L. J. Michot, I. Bihannic, S. Maddi, C. Baravian, P. Levitz, and P. Davidson, "Sol/gel and isotropic/nematic transitions in aqueous suspensions of natural nontronite clay. influence of particle anisotropy. 1. features of the I," *Langmuir*, vol. 24, pp. 3127–3139, 2008.

[3] B. Trinh, D. Haisman, and K. T. Trinh, "Rheological characterisation of age thickening with special reference to milk concentrates," *Journal of Dairy Research*, vol. 74, pp. 106–115, 2007.

[4] F. Ferri, B. J. Frisken, and D. S. Cannell, "Structure of silica-gels," *Physical Review Letters*, vol. 67, pp. 3626–3629, 1991.

[5] C. Sanchez and F. Ribot, "Design of hybrid organic-inorganic materials synthesized via sol-gel chemistry," *New Journal of Chemistry*, vol. 18, pp. 1007–1047, 1994.

[6] G. S. Sur and J. E. Mark, "Elastomeric networks cross-linked by silica or titania fillers," *European Polymer Journal*, vol. 21, no. 12, pp. 1051–1052, 1985.

[7] A. Morikawa, Y. Iyoku, M. Kakimoto, and Y. Imai, "Preparation of new polyimide silica hybrid materials via the sol-gel process," *Journal of Materials Chemistry*, vol. 2, pp. 679–690, 1992.

[8] H. Schmidt and M. Popall, "Inorganic-organic composites (ORMOCERs) for optical application," *Sol-Gel Optics*, vol. 1328, pp. 249–257, 1990.

[9] K. Izumi, H. Tanaka, M. Murakami, T. Deguchi, A. Morita, N. Tohge, and T. Minami, "Coating of fluorine-doped ZrO_2 films on steel sheets by sol-gel method," *Journal of Non-Crystalline Solids*, vol. 121, pp. 344–347, 1990.

[10] Y. Chujo and T. Saegusa, "Organic polymer hybrids with silica-gel formed by means of the sol-gel method," *Advances in Polymer Science*, vol. 100, pp. 11–29, 1992.

[11] D. Avnir, D. Levy, and R. Reisfeld, "The nature of the silica cage as reflected by spectral changes and enhanced photostability of trapped rhodamine-6g," *Journal of Physical Chemistry*, vol. 88, no. 24, pp. 5956–5959, 1984.

[12] B. Dunn and J. I. Zink, "Optical-properties of sol-gel glasses doped with organic-molecules," *Journal of Materials Chemistry*, vol. 1, pp. 903–913, 1991.

[13] G. Schottner, "Hybrid sol-gel-derived polymers: Applications of multifunctional materials," *Chemistry of Materials*, vol. 13, pp. 3422–3435, 2001.

[14] P. Audebert, P. Griesmar, and C. Sanchez, "Electrochemical probing of the sol-gel xerogel evolution," *Journal of Materials Chemistry*, vol. 1, pp. 699–700, 1991.

[15] L. M. Ellerby, C. R. Nishida, F. Nishida, S. A. Yamanaka, B. Dunn, J. S. Valentine, and J. I. Zink, "Encapsulation of proteins in transparent porous silicate-glasses prepared by the sol-gel method," *Science*, vol. 255, pp. 1113–1115, 1992.

[16] S. A. Yamanaka, F. Nishida, L. M. Ellerby, C. R. Nishida, B. Dunn, J. S. Valentine, and J. I. Zink, "Enzymatic-activity of glucose-oxidase encapsulated in transparent glass by the sol-gel method," *Chemistry of Materials*, vol. 4, pp. 495–497, 1992.

[17] P. Audebert, C. Demaille, and C. Sanchez, "Electrochemical probing of the activity of glucose-oxidase embedded sol-gel matrices," *Chemistry of Materials*, vol. 5, pp. 911–913, 1993.

[18] B. Wang, G. L. Wilkes, C. D. Smith, and J. E. Mcgrath, "High refractive-index hybrid ceramer materials prepared from titanium tetraisopropoxide and poly(arylene ether phosphine oxide) through sol-gel processing," *Polymer Communications*, vol. 32, no. 13, pp. 400–402, 1991.

[19] M. Oubaha, R. Kribich, R. Copperwhite, P. Etienne, K. O'Dwyer, B. MacCraith, and Y. Moreau, "New organic inorganic solgel material with high transparency at 1.55 μm," *Optics Communications*, vol. 253, pp. 346–351, 2005.

[20] Y. Sorek, M. Zevin, R. Reisfeld, T. Hurvits, and S. Ruschin, "Zirconia and zirconia-ormosil planar waveguides prepared at room temperature," *Chemistry of Materials*, vol. 9, pp. 670–676, 1997.

[21] C. Decker, "The use of UV irradiation in polymerization," *Polymer International*, vol. 45, pp. 133–141, 1998.

[22] P. K. Tien and R. Ulrich, "Theory of prism-film coupler and thin-film light guides," *Journal of the Optical Society of America*, vol. 60, no. 10, pp. 1325–, 1970.

[23] M. Oubaha, M. Smahi, P. Etienne, P. Coudray, and Y. Moreau, "Spectroscopic characterization of intrinsic losses in an organicinorganic hybrid waveguide synthesized by the solgel process," *Journal of Non-Crystalline Solids,*, vol. 318, pp. 305–313, 4/15 2003.

[24] D. L. Versace, M. Oubaha, R. Copperwhite, C. Croutxe-Barghorn, and B. D. MacCraith, "Waveguide fabrication in UV-photocurable solgel materials: Influence of the photoinitiating system," *Thin Solid Films,*, vol. In Press, Corrected Proof.

[25] G. Guerrero, P. H. Mutin, and A. Vioux, "Organically modified aluminas by grafting and sol-gel processes involving phosphonate derivatives," *Journal of Materials Chemistry*, vol. 11, no. 12, pp. 3161–3165, 2001.

[26] G. Guerrero, P. H. Mutin, and A. Vioux, "Mixed nonhydrolytic/hydrolytic sol-gel routes to novel metal oxide," *Chemistry of Materials*, vol. 12, pp. 1268–1272, 2000.

[27] G. Guerrero, "PhD Thesis, Montpellier, France," 2000.

[28] K. S. Anseth, C. M. Wang, and C. N. Bowman, "Kinetic evidence of reaction-diffusion during the polymerization of multi(meth)acrylate monomers," *Macromolecules*, vol. 27, pp. 650–655, 1994.

[29] C. Decker, "Photoinitiated crosslinking polymerisation," *Progress in Polymer Science,*, vol. 21, no. 4, pp. 593–650, 1996.

[30] C. Decker and A. D. Jenkins, "Kinetic approach of oxygen inhibition in ultraviolet- and laser-induced polymerizations," *Macromolecules*, vol. 18, no. 6, pp. 1241–1244, 1985.

[31] A. K. O'Brien and C. N. Bowman, "Modeling the effect of oxygen on photopolymerization kinetics," *Macromolecular Theory and Simulations*, vol. 15, pp. 176–182, 2006.

[32] F. R. Wight, "Oxygen inhibition of acrylic photo-polymerization," *Journal of Polymer Science Part C-Polymer Letters*, vol. 16, no. 3, pp. 121–127, 1978.

[33] R. Copperwhite, M. Oubaha, D. L. Versace, C. Croutxe-Barghorn, and B. D. MacCraith, "The role of photoinitiator and chelating agent in the fabrication of optical waveguides from UV-photocurable organo-mineral solgel materials," *Journal of Non-Crystalline Solids*, vol. 354, pp. 3617–3622, 7/15 2008.

[34] A. Ovsianikov, et al, "Ultra-low shrinkage hybrid photosensitive material for two-photon polymerization microfabrication," *Submitted to Advanced Materials.*

[35] M. Oubaha, P. Etienne, S. Calas, R. Sempere, J. M. Nedelec, and Y. Moreau, "Spectroscopic characterization of solgel organo-siloxane materials synthesized from aliphatic and aromatic alcoxysilanes," *Journal of Non-Crystalline Solids,*, vol. 351, pp. 2122–2128, 8/1 2005.

[36] B. Giner, I. Gascon, H. Artigas, A. Villares, and C. Lafuente, "Volumetric and refractive properties of binary mixtures containing 1,3-dioxolane and isomeric chlorobutanes," *Journal of Thermal Analysis and Calorimetry*, vol. 83, pp. 735–745, 2006.

[37] J. Schuyer, L. Blom, and D. W. Vankrevelen, "The molar refraction of condensed aromatic compounds," *Transactions of the Faraday Society*, vol. 49, no. 12, pp. 1391–1401, 1953.

[38] M. Oubaha, M. Dubois, B. Murphy, and P. Etienne, "Structural characterisation of a sol-gel copolymer synthesised from aliphatic and aromatic alkoxysilanes using Si-29-NMR spectroscopy," *Journal of Sol-Gel Science and Technology*, vol. 38, pp. 111–119, 2006.

[39] J. M. Senior, *Optical fiber communications : Principles and practice 2nd ed.*, 1992.

[40] T. Tamir, *Guided-wave optoelectronics: 2nd ed.* Berlin; New York: Springer-Verlag, 1990.

[41] S. O. Kasap, *Optoelectronics and photonics : Principles and practices*. London: Prentice Hall, 2001.

[42] X. Zhang, M. Qian, X. Zeng, Z. Zhao, J. Lasante, and P. Plante, "Design and fabrication of single mode rib waveguides using sol-gel derived organic-inorganic hybrid materials," *Journal of Sol-Gel Science and Technology*, vol. 45, pp. 103–107, 2008.

[43] S. Jeong and J. Moon, "Fabrication of inorganic-organic hybrid films for optical waveguide," *Journal of Non-Crystalline Solids*, vol. 351, pp. 3530–3535, 2004.

[44] M. Oubaha, M. Smaihi, P. Etienne, P. Coudray, and Y. Moreau, "Spectroscopic characterization of intrinsic losses in an organic-inorganic hybrid waveguide synthesized by the sol-gel process," *Journal of Non-Crystalline Solids*, vol. 318, pp. 305–313, 2003.

[45] D. E. Bornside, C. W. Macosko, and L. E. Scriven, "Spin coating - one-dimensional model," *Journal of Applied Physics*, vol. 66, pp. 5185–5193, 1989.

[46] D. P. Birnie, "Surface skin development and rupture during sol-gel spin-coating," *Journal of Sol-Gel Science and Technology*, vol. 31, pp. 225–228, 2004.

Chapter 5

Refractometric Sensors

5.1 Introduction

This chapter describes the development of two novel refractometric sensing platform. The sensing principle of both platforms is based on differential optical path lengths caused by refractive index changes. This in turn leads to phase changes which result in an interference pattern change. The state of the art for refractometric sensing is first described. This is followed by an explanation of the principles of operation of the novel platforms developed in this work. A brief simulation study is presented showing the behavior of these platforms in response to changing refractive index. The planar lightwave circuits (PLCs) at the core of these platforms have been fabricated using the reference sol-gel materials processed by the direct laser writing technique. For platform characterisation, a humidity sensing layer was developed and applied to the platforms as a proof-of-principle. In this layer, changes in relative humidity result in a refractive index change and the response of both platforms to this is reported.

5.2 State of the art

This section serves to give a brief overview of the current techniques employed in the area of refractometric sensing. As mentioned in the Chapter 1, refractometric sensing platforms are useful in situations where a change in analyte refractive index signals a chemical/bio-chemical change in the analyte. A large variety of techniques for this purpose have been developed over the past decades, and this section will summarise only the most important recent developments in the field. Sensors based on surface plasmon resonance (SPR) are perhaps the most

widely known examples of refractometric optical sensor platforms. The SPR technique relies upon excitation of a special mode of electromagnetic field, a surface plasmon-polariton (SPP), which travels along a thin metal film on the platform surface [1]. The SPP is typically excited by light incident at a particular angle on the metal film, coupled either through a prism or a grating. Changes in the refractive index of the material on top of the metal layer cause a measurable shift in a number of characteristics of the reflected excitation light including resonance angle, wavelength spectrum of polychromatic beams, intensity, or phase [2]. Using this technique, refractive index changes of 10^{-5} can be detected [3]. However, on-going research in the field has steadily increased the resolution, with a value of 3×10^{-8} RIU recently reported by the Homola group in a configuration based on the spectroscopy of long-range surface plasmons [4]. A number of systems are commercially available, notably from the pioneers in the field, Biacore.

Many other prominent refractometric techniques are based on planar waveguide-based platforms, where interferometric configurations and resonators have dominated recent research [5]. The interferometric techniques are based generally on a number of different interferometer configurations, with the Mach-Zehnder interferometer (MZI) configuration the most widely employed. It typically consists of a y-junction splitter which divides a single input into two arms: a reference arm, and a sensing arm which is exposed to the analyte. Changes in analyte refractive index introduce a phase shift in the light propagating in the sensing arm. This causes a change in the interference pattern to occur when the light from the two arms is recombined, resulting in a detectable change in output intensity. Using serrodyne modulation techniques, which involves inserting electro-optic modulators into each branch of the platform, a refractive index resolution of 2×10^{-8} RIU has been reported [5].

Other interferometric techniques used for refractive index sensing are mainly derivatives of the MZI configuration. The Young interferometer is identical to the MZI except that the reference and sensing arms are not recombined on chip, but instead the light from the two arms leaves the chip separately where it is recombined to form an interference pattern that is measured by a CCD sensor array. A noteworthy example of this configuration has been commercialised by Farfield Scientific, the so-called Dual Polarisation Interferometer [3]. Refractive index resolutions down to 10^{-8} RIU have been reported [6].

Ring resonators are another type of integrated optical platform that are capable of detecting extremely low refractive index changes. They are based on a ring

waveguide structure, where resonance is obtained when the length of the ring is equal to an integer times the wavelength of light in the propagating mode. Ring diameters can be as low as 15 μm which is promising for the fabrication of ultra compact platforms. Theoretical calculations have been performed indicating a resolution of 10^{-9} RIU could be possible [7]. However, this performance has not yet been verified, though such platforms have been demonstrated to be effective for biosensing with 6.8 ng/ml detection limits recently demonstrated for avidin [8]. A limitation of these platforms is that for detection, they require the use of expensive tunable lasers or high resolution spectrophotometers [5]. Additionally, the manufacturing tolerances are extremely exacting which impacts upon the real-world applicability of these platforms.

In contrast to this, the novel sensor platforms proposed in this work require simple laser-diode excitation and inexpensive photodetectors. Additionally, they have been fabricated using a low cost material and mass-producible fabrication process, making them cost-competitive with the other platforms outlined here.

5.3 Principle of Operation

In this section, two novel refractometric sensing platforms are presented: the multi-mode interference coupler (MMIC), and the mult-channel directional coupler (MCDC) platforms. Having established the general structure of both platforms, the principles of operation are explained in detail.

5.3.1 Multi-Mode Interference Coupler (MMIC) Platform

The MMIC sensor platform consists of a multi-mode interference coupler which is accessed centrally from each side by input and output single-mode waveguides, as shown in Figure 5.1. The sensing principle relies upon the creation of an interference pattern within the MMIC which can be seen in Figure 5.2. This interference pattern is created as follows. Firstly, light coupled into the input waveguide is incident upon the multi-mode section. The incident single-mode light distribution $\Psi(y, z)$ is coupled into the various modes of the MMIC as [9]

$$\Psi = \sum_{\nu} c_{\nu}\psi_{\nu} \tag{5.1}$$

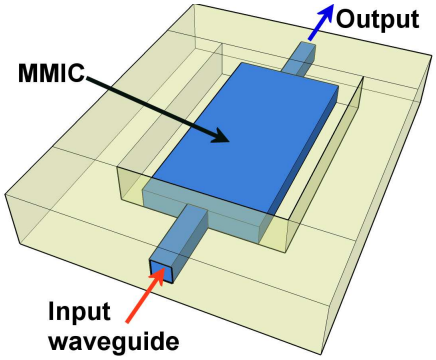

Figure 5.1: *Structure of the MMIC sensor platform*

where ψ_ν is the profile of mode ν in the MMIC and c_ν are the field excitation coefficients calculated according to equation 2.38. Light in each mode has a different propagation constant β_ν, due to the different optical path of each mode. Consequently, as light propagates away from the input, a different phase shift evolves for each mode, which results in the creation of the interference pattern.

Examination of the interference pattern in Figure 5.2a, shows that the input light distribution from the single-mode waveguide is recreated within the MMIC a certain distance away from the input. This phenomenon occurs at the point where light in the various modes of the MMIC reaches a phase-matched state, and is known as self-imaging. The platform length is defined to enable complete capture of the self-image by the output waveguide at a specific refractive index

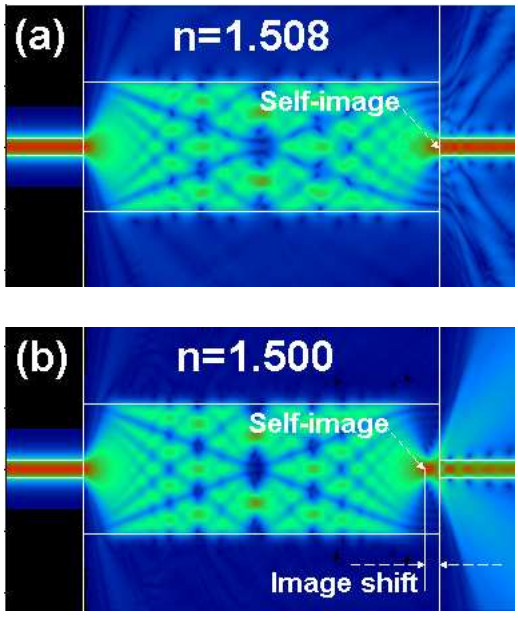

Figure 5.2: *BPM electric field distributions showing a) the complete capture of the first self-image at the output waveguide for the "working point" refractive index of 1.508, and, b) the shift in the self-image position when refractive index changes to 1.500*

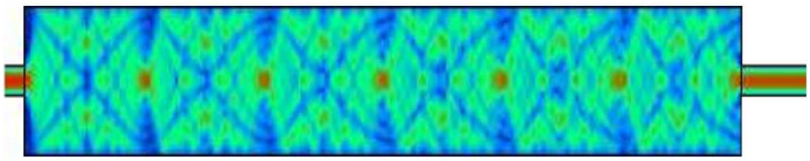

Figure 5.3: *BPM simulation image showing the capture of the 6^{th} self image*

known as the "working point" (see Figure 5.2a).

The sensing mechanism of the platform exploits the sensitivity of this interference pattern, and more specifically the position of the self-images to the refractive index surrounding the MMIC section. As refractive index increases the interference pattern elongates. Conversely, when refractive index decreases, the interference pattern contracts as illustrated in Figure 5.2b. The result is that the high intensity self-image captured fully by the output waveguide at the "working point" refractive index moves away from the output waveguide, and so the intensity of light collected by a photodetector positioned at the output waveguide is decreased, as shown in Figure 5.2b.

The analysis so far has only considered the first self-image. However, if the length of the MMIC is increased, other self images can be captured as shown in Figure 5.3, where the 6^{th} self-image is captured by the output waveguide. Repetitive self-imaging occurs because as the platform length is increased there are a number of positions where a phase-matched state is reached. Self-image rank (M) is the term used to distinguish between these self-images, with the first self image denoted by M = 1, the second M = 2 and so on. Design of the platform to capture self-images of higher rank can be advantageous for sensing because for a given refractive index change, these self-images are shifted in position by a greater distance and therefore there is a larger change in output intensity from the platform (i.e. greater sensitivity).

The length of the centre-fed MMIC platform used in this work is [9, 10]

$$L = \frac{3ML_\pi}{4N} \tag{5.2}$$

where L_π is the beat length of the structure, as defined in Chapter 2 (equation 2.35) In practice, this formula is used as a guide when specifying the MMIC length necessary to capture a particular self-image. Usually the MMIC length to completely capture the self-image is shifted from the calculated value by a small offset. BPM simulation has been shown to be a reliable method of precisely

specifying the length of these platforms [11].

5.3.2 Multi-Channel Directional Coupler (MCDC) Platform

The multi-channel directional coupler (MCDC) platform is similar to the MMIC in a number of respects. The structure of the platform is shown in Figure 5.4 and comprises a central waveguide which runs from the platform input to the output. In the sensing region of the platform, this central waveguide is flanked on each side by another waveguide which has an identical cross-section. The key to this design is the proximity of the waveguides in the sensing region. A multi-channel directional coupler (MCDC) is formed if the waveguides are close enough for optical power to be able to transfer between them ($\sim$ 1-4 μm separation for these waveguides). Power transfer occurs in the same way as for a standard directional coupler (employed elsewhere in this work). That is, light in the central waveguide couples into the adjacent waveguides via the evanescent tail of light extending away from the waveguide surface, which overlaps with the modal profiles of the adjacent waveguides. As a result of these interactions, a self-imaging phenomenon occurs similar to that in the MMIC, where the input field is recreated periodically along the length of the central waveguide in the MCDC. This can best be explained by considering the three waveguides as one system, which have a number of system modes (also known as supermodes). Similar to the MMIC, self-imaging occurs at the particular position where light in each of the supermodes again matches the initial phase conditions met when coupling into the MCDC section. Using this theory it has been shown that the output

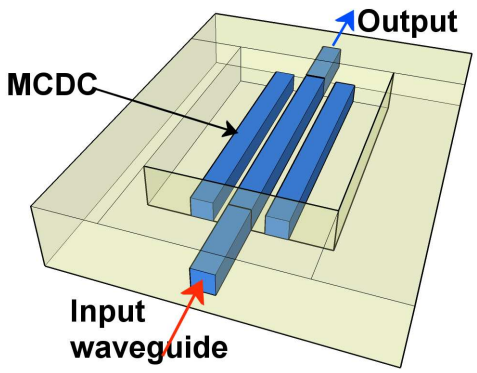

Figure 5.4: *Structure of the MCDC sensor platform*

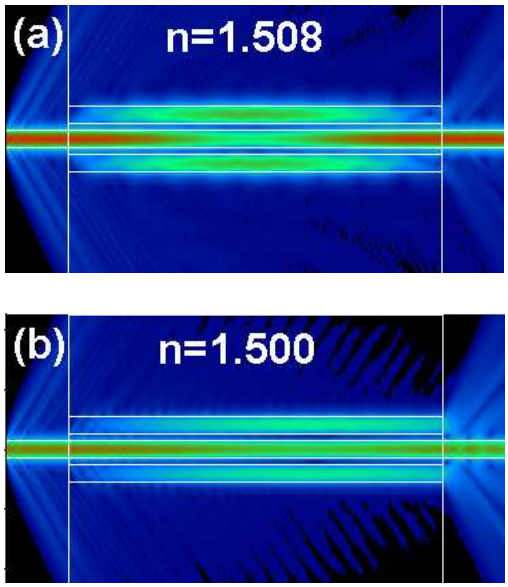

Figure 5.5: *BPM electric field distributions for a MCDC platform (M=1) showing a) the capture of the self-image at the output waveguide for the "working point" refractive index of 1.508, and, b) the change in the captured intensity when refractive index changes to 1.500*

power from waveguide n is given by [12],

$$J_n^2(2\kappa z)e^{-\alpha z} \tag{5.3}$$

where J_n represents the Bessel function of n^{th} order, α is the attenuation coefficient of a single waveguide, z is the distance along the propagation direction of the MCDC, n denotes the output waveguide where the central waveguide is numbered 0, and κ is the coupling coefficient between two adjacent waveguides as defined in equation 2.57. The sensing mechanism of this platform exploits the sensitivity of this power transfer to changes in the refractive index of the material that occupies the space between the waveguides (i.e. the analyte, in this case the humidity sensing layer). This is illustrated in Figure 5.5, where the BPM simulation image shows the electric field distribution in the platform for two different analyte refractive indices. As for the MMIC platform, this platform is designed to fully capture a self-image at a "working point" refractive index (as shown in Figure 5.5a at n=1.508). Figure 5.5b clearly shows that the reduction in analyte refractive index elongates the interference pattern formed by the interaction of the 3 waveguides, and so pushes the self-image away from the output waveguide resulting in a reduction in output intensity.

In another parallel with the MMIC platform, an increase in the MCDC length results in the capture of self-images of higher rank (M), as shown in Figure 5.6.

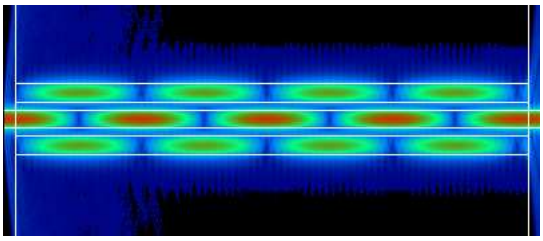

Figure 5.6: *BPM simulation image of a MCDC structure capturing the 4^{th} self-image (M=4)*

The self-images of higher rank can be exploited for higher sensitivity detection, as outlined for the MMIC.

5.4 Simulation

The aim of this section is to demonstrate the use of 3D BPM, to simulate the behavior of the MMIC and MCDC platforms. The simulation wavelength was 1.31 μm, and the finite-difference discretisations used were 0.25, 0.45 and 0.25 μm in the x, y and z directions respectively.

5.4.1 MMIC Platform Simulation

Simulation of the MMIC platform was carried out to observe the platform response to changing analyte refractive index, and in particular to characterise the enhancement in sensitivity that could be derived from the use of higher self-image ranks. A 23 μm wide MMIC was chosen for simulation because it minimised the platform length while still supporting a large enough number of modes to produce well resolved self-images. It also served to allow comparison with the MCDC platform in the following section. A working point refractive index of 1.508 was chosen for simulation, at which point each platform was designed to capture the maximum intensity of the self-image.

As shown in Figure 5.7a, a range of different length MMIC platforms capturing different self-images were simulated. As expected, the capture of higher rank self-images results in a larger change in output intensity over a given analyte refractive index range (i.e. greater sensitivity to refractive index). Sensitivity has been extracted for each M in Figure 5.7a by fitting a line to the linear portions of each response curve near to the working point refractive index of 1.508.

Sensitivity is plotted against self image rank in Figure 5.7b (normalised against

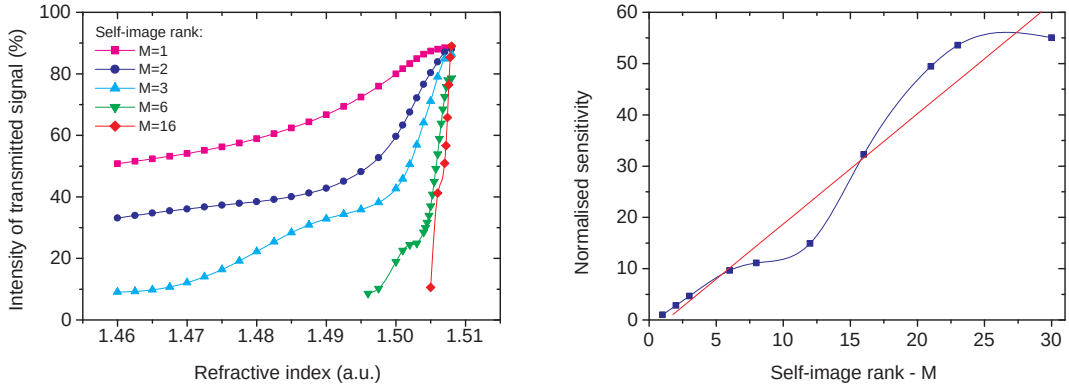

(a) (b)

Figure 5.7: *Simulation results of a) the intensity transmitted by the platform as a function of refractive index, and b) the sensitivity enhancement factor as a function of the self-image rank captured at the output waveguide*

the sensitivity of the M=1 platform). It was expected that sensitivity would increase in direct proportion with M, as the logic dictates that the M=2 self-image is shifted twice as much as the M=1 self-image and thereby sensitivity is doubled. However, this direct proportionality has not been observed. Instead, two points were noted. Firstly, the sensitivity enhancement is greater than that expected, in some instances twice that expected - for example the M=21 self-image has a sensitivity $\sim$ 50 times greater than M=1. Secondly, the enhancement does not follow a strict linear relationship. Instead, the relationship varies about the line fitted through it.

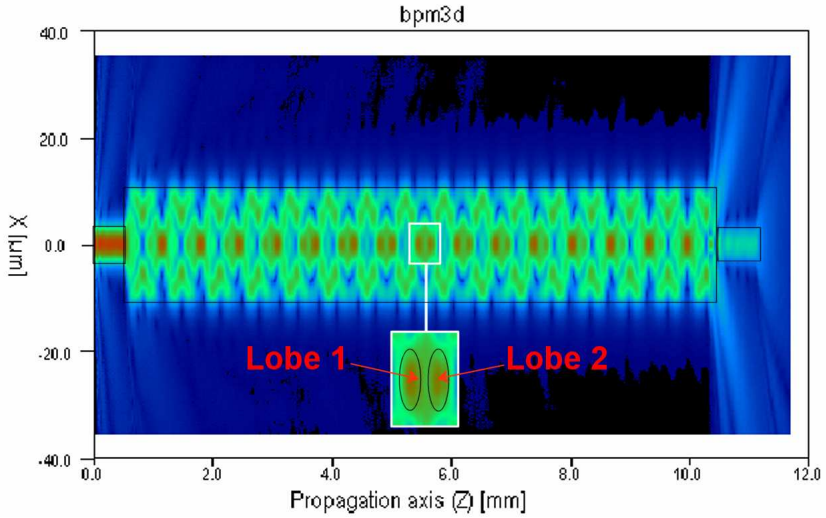

Figure 5.8: *Illustration of the splitting of self-images into 2 part (inset is a blow up of the 8^{th} self-image)*

This is attributed to an unexpected behavior of some of the high rank self-images. Analysis of these self-images showed that there are two distinct regions/lobes within the self-image (as shown by Figure 5.8), which tend to transfer power between one another as refractive index is varied. For some self-images, this localised power transfer tends to increase the intensity change for a given refractive index change (and thereby sensitivity). In other instances, the opposite case was observed resulting in a decrease in sensitivity.

Though the sensitivity varies in a non-linear fashion according to self-image rank, the length of the MMIC platform shows a linear increase according to the self-image captured as shown by Figure 5.10a.

5.4.2 MCDC Platform Simulation

Simulation of the MCDC platform focused on an MCDC that has a separation of 2.5 μm between adjacent waveguides, giving an overall MCDC width of 23 μm (i.e. equal to the MMIC). Though the sensing principles of the MCDC and MMIC sensor platforms are similar, the simulated output response shows some major differences. Firstly, in Figure 5.9a, it can be seen that the MCDC response is an oscillatory intensity pattern over a large refractive index range. Though the MMIC interference pattern is also repetitive, only the parts near to the self-image are really useful as the other portions of the interference pattern vary non-linearly in intensity as refractive index changes, rendering them unsuitable for sensing.

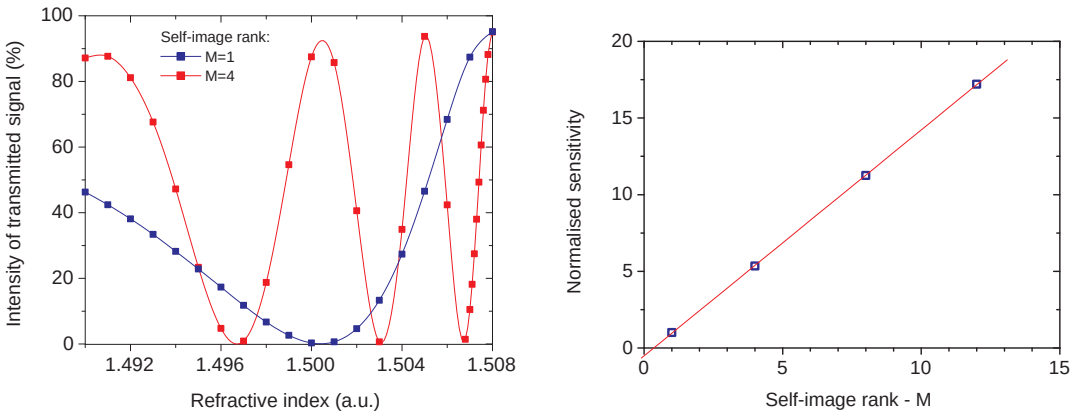

(a) (b)

Figure 5.9: *Simulation results of a) the intensity transmitted by the platform as a function of refractive index, and b) the sensitivity enhancement factor as a function of the self-image rank captured at the output waveguide*

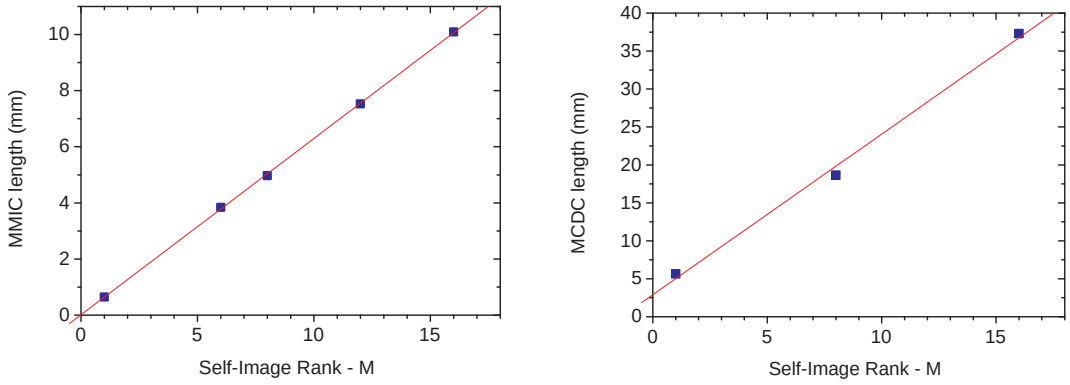

(a) (b)

Figure 5.10: *Simulation results showing the increase in sensitivity of the, a) MMIC, and b) MCDC platforms of different length*

In Figure 5.9a, the response of platforms operating at M=1, and M=4 is shown. It is clear that the M=4 platform shows a larger intensity change than the M=1 platform and therefore is more sensitive as expected. However, as sensitivity increases the sensing range decreases, which is a factor that must be considered when employing both the MCDC and MMIC platforms. The sensitivity enhancement derived from capturing higher rank self-images is shown in Figure 5.9b. Unlike in the case of the MMIC, the sensitivity of the MCDC follows a linear relationship with respect to self-image rank. However, similar to the MMIC, the sensitivity increase given by capture of higher rank self-images is greater than expected, with the M=10 self-image being $\sim$ 14 times more sensitive than M=1.

The relationship between MCDC length and self-image rank is shown in Figure 5.10b. A linear relationship is noted in this graph, as is also the case for the MMIC platform (in Figure 5.10a).

5.4.2.1 Comparison of MMIC and MCDC sensitivities

Analysis of the simulated data from both platforms resulted in a comparison of the sensitivity of both platforms with respect to the platform length, as shown in Figure 5.11. It is clearly evident from these data that this configuration of MCDC platform (with waveguide separation of 2.5 μm) is theoretically more sensitive than an MMIC platform of equivalent length. Taking the slopes of the lines fitted through both sets of data, this MCDC sensor configuration is on average $\sim$1.35 times more sensitive than an MMIC platform of equal length.

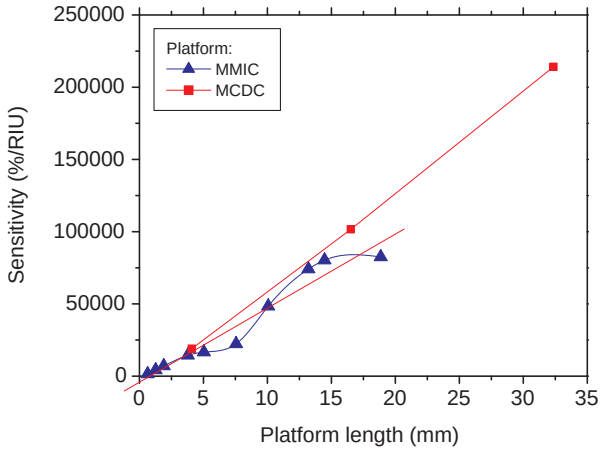

Figure 5.11: *Comparison of the sensitivity of different MMIC and MCDC sensor platforms as a function of their length*

However, this is not to suggest that the MCDC is superior in all respects than the MMIC. There are some applications (such as biosensing) for which employment of the MCDC would not be suitable, as the refractive index of all the material in between the waveguides must be subject to change for reliable detection. On the other hand, the MMIC platform is ideally suited to bio-(chemical) interactions as it probes only the refractive index changes in the vicinity of the MMIC surface, making it an interesting candidate for label-free biosensing.

5.5 Experimental

This section presents the experimental work carried out during sensor platform fabrication and characterisation. Firstly, the synthesis and characterisation of a humidity sensing layer is detailed. This layer was then applied to the platforms to enable characterisation of the sensor response to changes in refractive index.

5.5.1 Humidity Sensing Layer

The main requirements of the humidity sensing layer are: porosity to allow permeation of humidity, appropriate refractive index, hydrophilicity to allow coating on the platforms, and a reversible refractive index change when permeated by humidity. To satisfy these requirements a sol-gel layer was developed by a colleague, Dr. Mohamed Oubaha.

5.5.1.1 Sol-gel synthesis

The humidity sensing layer was synthesised via the sol-gel process. A mixture of MAPTMS, phenyltriethoxysilane and tetraethyl orthosilicate (TEOS) was employed, in a molar ratio of 1.6:3.4:5.0. These precursors were mixed together and hydrolysed with an aqueous solution (HCl 0.01N), employing 1:1 water to alkoxide ratio. The sol was left stirring for 24 hours to age before use.

MAPTMS was included to control viscosity and thereby improve the coatability of the material. Phenyltriethoxysilane was employed as a means of controlling the refractive index of the coating [14, 15] (as shown in Section 4.4.1), permitting the material working point refractive index to be obtained. TEOS is the main component of this sol and is known to produce porous coatings [16], the refractive indices of which are sensitive to relative humidity [17]. The humidity-dependent refractive index change of such materials has also been shown to be reversible [18]. The combination of these precursors in the proportions indicated resulted in the development of a humidity sensing layer that had a satisfactory performance to enable characterisation of the sensing platforms.

5.5.1.2 Characterisation

Firstly, a sample of the humidity sensing layer was deposited on a piece of silicon and subjected to a 2 hour heat treatment at 100 °C, which, for this particular material, resulted in the removal of alcohol and water from the layer without collapsing the pore structure. Characterisation of the humidity sensing layer was carried out by another colleague Dr. Jan Hradil, using a spectroscopic ellipsometer (Horiba Jobin Yvon UVISEL). The refractive index of the layer was measured at a number of discrete relative humidity (RH) values.

In order to control and change the RH, the sample was sealed into a specially designed flow cell which was accessible to the probe beam of the ellipsometer by an input and output window. A system to deliver different levels of RH to the sample was designed, utilising N_2 as a carrier gas. This was achieved by bubbling N_2 through two flasks which contained de-ionised water as illustrated in Figure 5.12. The various levels of RH were produced by mixing the N_2 which was humidity saturated with dry N_2, using two computer-controlled mass-flow controllers (MFCs) (Celerity, Ireland) to control the relative proportions of wet and dry N_2 in the mix. The MFCs were interfaced with the computer via an

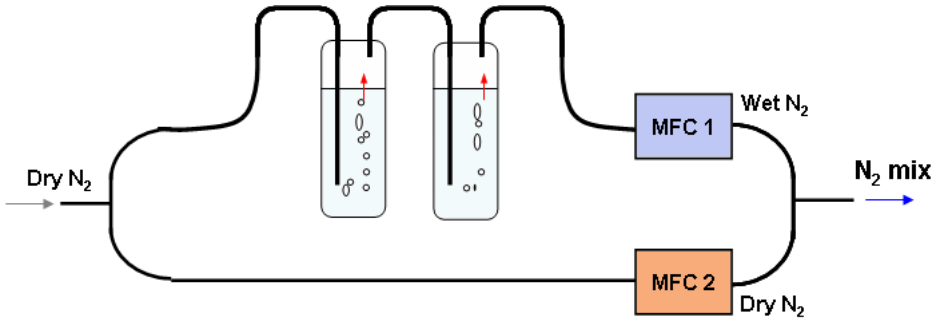

Figure 5.12: *System for generating humidified nitrogen used in sensor platform characterisation*

in-house manufactured circuit board, which also acquired the signal from a commercial humidity sensor (Honeywell) which had been sealed into the flow chamber so that RH values could be directly determined.

Because ellipsometry is a model based technique, the resulting ellipsometric data had to be fitted to a model in order to extract the refractive index value of the layer at each RH value. A Cauchy dispersion model was fitted to the experimental data using an iterative Levenberg-Marquardt algorithm [19], until a good fit of model and experimental results was obtained as indicated by a χ^2 fitting parameter < 1. As shown in Figure 5.13, a sigmoidal curve was fitted ($R^2 = 0.96$) to resulting refractive index values, as this curve best approximated the behaviour of the data. Using the equation of this curve and the fit parameters a calibration equation for conversion of RH to refractive index was established as shown in the following equation,

$$\text{Refractive index} = \frac{a}{1 + e^{(-k(RH - x_c))}} \tag{5.4}$$

where a = 1.50821, k = 0.05262, and x_c = -129.78333.

5.5.2 Microfabrication

The microfabrication of sensor platforms used here first involved cleaving a silicon wafer into pieces. The buffer layer sol (standard recipe from Table 4.2) was dip-coated onto the silicon piece at a dip-speed of 2.5 mm/s which gave a 6 μm layer. This was stabilised with a 4 minute UV exposure and then baked for 2 hours at 100 °C. The guiding layer (also from Table 4.2) was dip-coated in the same way and then directly laser written to form the MMIC or MCDC structure, the dimensions of which had been specified by simulations, as shown in the previous section. In this case, an MMIC of 10094 μm length was written which was

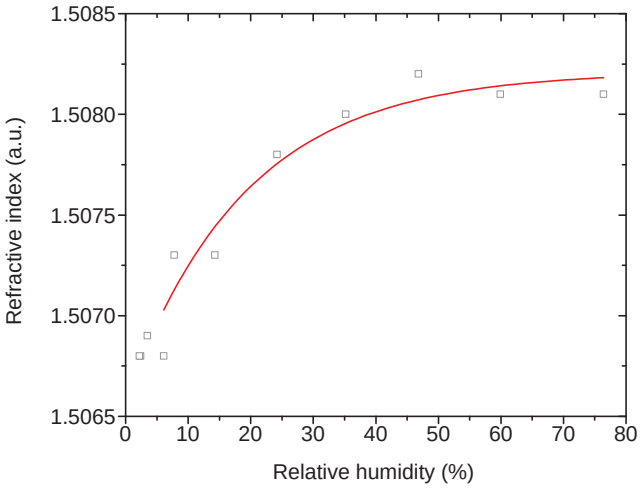

Figure 5.13: *Refractive index as a function of RH (measured by Dr. Jan Hradil)*

designed to capture the 16^{th} self-image. The MCDC structure was designed to operate at the 1^{st} self-image, and therefore had a length of 5650 μm. The laser writing of the MCDC structure was relatively straightforward, simply comprising 3 waveguides written side-by-side, separated by 2.5 μm in accordance with the simulations. However, in order to form the MMIC structure, a detailed laser writing input file had to be constructed which would allow the laser to overlap sufficiently in order to build-up the MMIC section to a predefined width. The movement of the linear motors is described by Figure 5.14 which shows the way in which the linear motors were rastered beneath the stationary laser spot, building up the MMIC structure from the outside in.

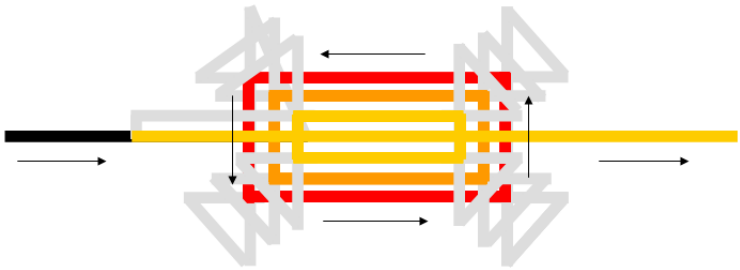

Figure 5.14: *Rastering pattern for linear motors of laser writing system used to form the MMIC sensor platform*

Having completed laser writing, the platforms were etched in a bath of 1-butanol with gentle agitation for ~40 s in order to remove the unexposed regions. At this stage, the platform was again subjected to a 2 hour bake at 100 °C, in order to stabilise the ridge waveguide structures. Then the input and output

waveguides were dip-coated in the buffer layer sol to form a protective layer over these waveguides, making them single-mode. Stabilisation of these layers was carried out in the same way as for the initial buffer layer.

The final step was to deposit the humidity sensing layer on the chip, covering the MMIC section and also the protective layer. This was done by spin-coating at 1000 rpm, and the layer was stabilised as described in the previous section.

5.5.3 Characterisation System

The system used to characterise the response of the platform to changes in RH is outlined in Figure 5.15. It comprises of two main parts, firstly the means by which relative humidity could be controlled (employing the same system described in Section 5.5.1.2 for the characterisation of the humidity sensing layer), and secondly a system to inject light into the platform and collect the output at the detector.

The humid N_2 mix was introduced to the chip via a polymer flow cell, which had been clamped over the sensing platform on the optical bench. A commercial humidity sensor (Honeywell) was embedded within the flow cell in order determine the exact RH in the flow cell at a particular time, for correlation with the output signal from the chip. Acquisition of the RH values was carried out using the control board for the MFCs.

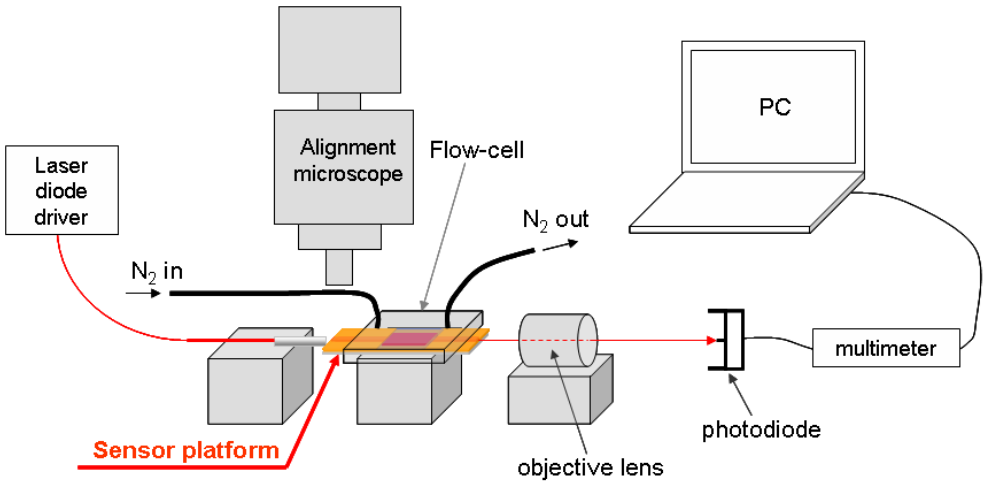

Figure 5.15: *System for characterising the platforms*

5.5.3.1 Alignment

In order to inject excitation light into the chip and collect light from the output, both end faces of the chip were cleaved using a diamond-tipped scribe revealing the input/output waveguides. The chip was secured in place on top of the pedestal. The fiber from the pig-tailed laser diode (Thorlabs, $\lambda = 1.31$ μm, maximum output power = 3.1 mW) was aligned to the input waveguide of the platform (end-fire coupling), first by course manual alignment (using the microscope as a guide). Similar course alignment of the output waveguide, objective lens and photodiode was carried out until a strong signal was measured by the photodiode. Then fine alignment of all system components was done, by iteratively adjusting the position of each component using piezo-controllers until an optimum photodiode signal was obtained. Alignment of the fiber position to the input was a critical parameter in determination of the output response of the chip, and, as such, the output signal from the platform was extremely sensitive to environmental perturbations such as air currents and vibration.

5.5.3.2 Data processing

The photodiode output was measured by a multimeter (Keithley), and recorded continuously by a computer via a National Instruments digital acquisition card. Using this setup, it was possible to simultaneously vary the applied RH, and quantify the resulting changes in signal from the platform.

5.5.4 Results and Discussion

Before presenting and discussing the results, a number of terms used to quantify the performance of the platforms fabricated here are defined. Firstly, the sensitivity of the platforms to changes in analyte is defined as,

$$\text{Sensitivity} = \frac{\Delta(\text{Signal})}{\Delta(\text{Concentration})}. \tag{5.5}$$

In this instance, relative humidity measurement was employed as a useful means of achieving small refractive index changes in the sensing region of the platforms without disturbing the in-coupling of light to the platforms. In order to evaluate the refractive index response of the platforms, ellipsometric data was used establish a response curve for the humidity sensing layer as outlined in Section 5.5.1.2.

Therefore, the sensitivity of the platform to changes in refractive index is defined as,

$$\text{Refractive index sensitivity} = \left(\frac{\Delta\text{Signal}}{\Delta(\text{RH})}\right)\left(\frac{\Delta(\text{RH})}{\Delta(\text{RI})}\right). \tag{5.6}$$

One of the most important characteristics of a sensor platform/system is the resolution. Resolution is defined as the lowest detectable change in analyte that can be resolved by the system and is typically limited by sources of noise in the system, such that,

$$\text{Resolution} = \frac{3\sigma}{\text{Sensitivity}} \tag{5.7}$$

where 3σ is the noise level of the system, and is usually taken as 3 times the peak to peak noise value of the sensor output signal, at a steady-state analyte level.

5.5.4.1 MMIC platform characterisation

The response curve from the MMIC sensor platform is shown in Figure 5.16. The data recorded were an average of the output signal taken once the relative humidity value had stabilised at a particular value. Using equation 5.5, the RH sensitivity of this response was -1.92 $\times$ 10^{-8} Amps/%. For determination of the RH resolution, the 3σ noise value was determined from Figure 5.17 which was a representative portion of the output signal around a stable RH value. This analysis resulted in a 3σ noise value of 5.4 $\times$ 10^{-8} Amps, which using equation 5.7 resulted in a RH resolution of $\sim$2.81%. The RH resolution value is mainly a function of the very small refractive index change exhibited by the

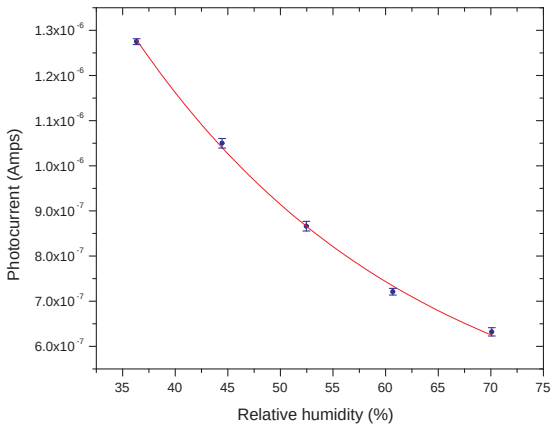

Figure 5.16: *Response curve relating output intensity to relative humidity for the MMIC platform tested*

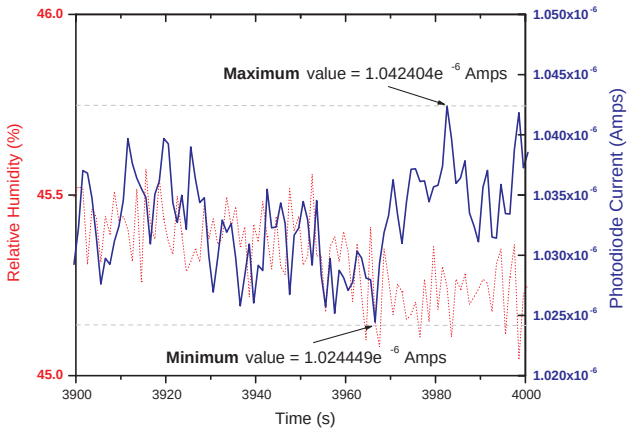

Figure 5.17: *Noise in the data at a steady RH level*

humidity sensing layer. No effort was expended on optimisation of this layer, as the main focus of this work to characterise the refractive index sensitivity and resolution by means of the RH response. To this end, using the calibration equation 5.4, each RH value was converted to refractive index. Using equation 5.7 a refractive index resolution of 1.67×10^{-5} was calculated. Given that minimal efforts were made to minimise the noise levels of the system, this is an extremely promising result from a novel platform. In the context of other techniques, this result demonstrates equivalent resolution to that of the basic SPR systems. As with SPR, many avenues are open to improve resolution, chief among which will be a more robust in- and out-coupling arrangement, which will reduce or possibly eliminate noise originating from physical perturbation of coupling at either end of the chip. Further investigations will also focus on an experimental determination of the sensitivity/resolution enhancement derived from the use of longer MMIC sections. Another possibility to increase resolution is to design a platform exploiting the ability of the MMIC to discriminate between wavelengths. The employment of this format has the potential to improve resolution as well as eliminate temperature sensitivity which has not been addressed in this work, but is an issue for all refractometric sensing platforms. In summary, this work has demonstrated the great promise of this platform with a number of avenues open for further exploration.

5.5.4.2 MCDC platform characterisation

The response curve for the MCDC platform is shown in Figure 5.18, which was obtained by characterising the platform employing the same methods and systems as described for the MMIC platform. Here, the data were fitted by a sigmoidal curve, which shows an especially close correlation to the data in the 0-30% RH range ($R^2 = 0.9914$). Using this section of the graph to calculate the sensitivity and resolution, the refractive index resolution of this MCDC platform was 4.16×10^{-4}. The high sensitivity and resolution of the sensor response at low RH values is a notable feature of this response curve, and demonstrates the tunability of these platforms for high sensitivity detection at low analyte concentrations.

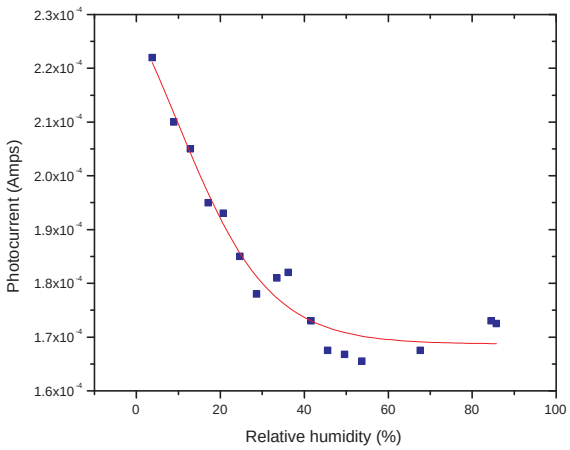

Figure 5.18: *Response curve relating output intensity to relative humidity for the MCDC platform tested*

5.6 Conclusion

Two novel refractometric sensing platforms have been designed, in each case exploiting the sensitivity of an interference pattern generated within the multi-mode structures. Simulation of the two platforms revealed that sensitivity can be increased by capturing higher ranking self-images, which are found by extending the length of the platforms. The MCDC platforms simulated are on average ~1.35 times more sensitive than an MMIC of equivalent length, although the factor varies due to the non-linear sensitivity enhancement of the MMICs.

Fabrication of the platforms exploited the direct laser writing system to form the waveguiding structures, upon which a sol-gel humidity sensitive layer was

deposited. The refractive index of this layer changes in response to changing RH, as characterised by ellipsometry. This layer provided a means to characterise the platforms without disturbing the in-coupling of light. The refractive index resolution of the MCDC platform was calculated as 4.16×10^{-4}, and the MMIC as 1.67×10^{-5}, which is comparable with basic SPR configurations previously reported. This work has successfully verified the operation of these novel refractometric sensing platforms, indicating the strong potential for application in diverse areas such as label-free biosensing and environmental monitoring.

References

[1] J. Homola, S. S. Yee, and G. Gauglitz, "Surface plasmon resonance sensors: review," *Sensors and Actuators B-Chemical*, vol. 54, no. 1-2, pp. 3–15, 1999.

[2] J. Homola, "Surface plasmon resonance sensors for detection of chemical and biological species," *Chemical reviews*, vol. 108, pp. 462–493, 2008.

[3] C. McDonagh, C. S. Burke, and B. D. MacCraith, "Optical chemical sensors," *Chemical reviews*, vol. 108, pp. 400–422, 2008.

[4] R. Slavk and J. Homola, "Ultrahigh resolution long range surface plasmon-based sensor," *Sensors and Actuators B: Chemical*, vol. 123, pp. 10–12, 4/10 2007.

[5] P. V. Lambeck, "Integrated optical sensors for the chemical domain," *Measurement Science Technology*, vol. 17, pp. R93–R116, 2006.

[6] A. Ymeti, J. S. Kanger, J. Greve, P. V. Lambeck, R. Wijn, and R. G. Heideman, "Realization of a multichannel integrated young interferometer chemical sensor," *Applied Optics*, vol. 42, pp. 5649–5660, 2003.

[7] E. Krioukov, J. Greve, and C. Otto, "Performance of integrated optical microcavities for refractive index and fluorescence sensing," *Sensors and Actuators B-Chemical*, vol. 90, pp. 58–67, 2003.

[8] A. Ksendzov and Y. Lin, "Integrated optics ring-resonator sensors for protein detection," *Optics Letters*, vol. 30, pp. 3344–3346, 2005.

[9] L. B. Soldano, F. B. Veerman, M. K. Smit, B. H. Verbeek, A. H. Dubost, and E. C. M. Pennings, "Planar monomode optical couplers based on multimode interference effects," *Journal of Lightwave Technology*, vol. 10, pp. 1843–1850, 1992.

[10] M. Bachmann, P. A. Besse, and H. Melchior, "Overlapping-image multimode interference couplers with a reduced number of self-images for uniform and nonuniform power splitting," *Applied Optics*, vol. 34, pp. 6898–6910, 1995.

[11] L. Caruso and I. Montrosset, "Analysis of a racetrack microring resonator with mmi coupler," *Journal of Lightwave Technology*, vol. 21, pp. 206–210, 2003.

[12] S. Somekh, E. Garmire, A. Yariv, H. L. Garvin, and Hunsperg.Rg, "Channel optical waveguide directional couplers," *Applied Physics Letters*, vol. 22, no. 1, pp. 46–47, 1973.

[13] K. J. Ebeling, *Integrated optoelectronics : Waveguide optics, photonics, semiconductors*. New York: Springer-Verlag, 1993.

[14] M. Oubaha, R. Copperwhite, B. Murphy, B. Kolodziejczyk, H. Barry, K. O'Dwyer, and B. D. MacCraith, "Development of photo-patternable organo-mineral hybrid films from the sol-gel condensation of alkoxysilanes," *Thin Solid Films*, vol. 510, pp. 334–338, 2006.

[15] G. R. Atkins, R. M. Krolikowska, and A. Samoc, "Optical properties of an ormosil system comprising methyl- and phenyl-substituted silica," *Journal of Non-Crystalline Solids*, vol. 265, pp. 210–220, 2000.

[16] B. D. MacCraith, C. McDonagh, A. K. Mcevoy, T. Butler, G. OKeeffe, and V. Murphy, "Optical chemical sensors based on sol-gel materials: Recent advances and critical issues," *Journal of Sol-Gel Science and Technology*, vol. 8, no. 1-3, pp. 1053–1061, 1997.

[17] D. X. Li, L. Shang, L. Y. Liu, L. Xu, and W. C. Wang, "Investigation of thermo-optical characteristic of the organic-inorganic hybrid material," *Rare Metal Materials and Engineering*, vol. 33, pp. 93–96, 2004.

[18] M. S. W. Vong and P. A. Sermon, "Observing the breathing of silica sol-gel-derived anti-reflection optical coatings," *Thin Solid Films*, vol. 293, pp. 185–195, 1997.

[19] S. Gupta, B. R. Weiner, and G. Morell, "Spectroscopic ellipsometry studies of nanocrystalline carbon thin films deposited by HFCVD," *Diamond and Related Materials*, vol. 10, pp. 1968–1972, 11 2001.

Chapter 6

Multianalyte Biosensor Platform

6.1 Introduction

This chapter describes the design and fabrication of a multianalyte biosensor platform, exploiting the sol-gel materials and microfabrication processes developed in this work. The platform concept is based upon the detection of fluorescently labelled probe molecules, in order to determine the concentration of specific analytes in a test solution. The surface of the platform consists of an optical waveguiding circuit, used to deliver excitation light to multiple sensor windows on the platform. Fluorescence is excited by means of the evanescent wave in each sensor window. This chapter details a number of optical circuit designs, as well as the development of a novel simulation method for evaluation of the evanescent wave intensity. Using this methodology, an evanescent wave enhancement strategy was developed, which has impacted upon the eventual fabrication process. The microfabrication techniques and sol-gel materials established in Chapters 3 and 4 were exploited in order to fabricate a chosen design. An appropriate surface functionalisation technique was employed in order to attach the recognition antibodies to the waveguide surface in each sensor spot. Finally, the results of a proof-of-principle immunoassay carried out on the chip are presented.

6.2 State of the art

Currently, a great deal of research is being conducted in the area of biosensors for a variety of different applications. The need for development and commercialisation of multianalyte biosensors for point-of-care diagnostic testing has been highlighted as an area of particular interest, which has the potential to

have a number of positive social and economic effects. In this regard, recent developments in the area have focussed on a small number of techniques capable of delivering the performance necessary (sensitivity, selectivity and rapidity) in a economically viable format. These techniques include surface plasmon resonance (SPR) [1–3], electrochemiluminescence [4–6], optical fiber platforms for fluorescence-based sensing [7–9] and evanescent wave excitation techniques based on planar waveguide-based platforms. The work conducted here belongs to the last category, and therefore this section will concentrate on discussion of the platforms in this area.

A group at the Naval Research Laboratory (NRL) in Washington have developed a robust chip employing evanescent wave excitation, which employs a glass slide patterned with biomolecules [10]. This platform has been successfully employed for the sensitive detection of a number toxins [11] including biowarfare agents (ricin, anthrax) [12–14], food borne pathogens [15], and disease markers [16]. Commercially available platforms based on this work include the RAPTOR system which was the highest rated biosensor system in NATO tests conducted in 2004 [17], showing the strength of this detection principle. However, improvements can be made to a number of aspects of the platform, including more efficient delivery of the excitation light to the sensor spots which can be achieved using waveguides. In addition, the microfluidics of this platform have not been optimised to reduce the amount of reagents needed for analysis. This is a consideration that can be addressed by the technology proposed here, by incorporating microfluidic channels in the design for the patterned sol-gel protective layer.

Another successful platform technology based on evanescent wave excitation of fluorescence is that developed by Zeptosens, which utilises diffraction gratings to couple light into a nano-scale Ta_2O_5 layer for fluorescence excitation of biomolecules. However, the manufacturing costs of this platform are relatively high, and therefore it is typically targeted toward drug discovery applications, rather than POC diagnostics.

A multianalyte biosensor platform, also based on evanescent wave fluorescence excitation, has been developed by a consortium of European researchers within the AWACCS (Automated water analyser computer-supported system) project. Low detection limits (< 0.02 μg/l) have been reported [18], for a range of environmental pollutants including estrone and atrazine. This platform employs a y-junction splitter design similar to one of the designs described in this work.

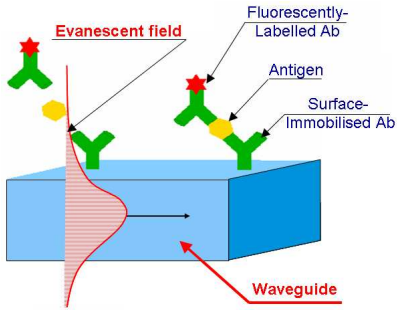

Figure 6.1: *Illustration of a sandwich assay with evanescent wave fluorescence excitation on a waveguide surface*

Fabrication of the platform involves imprinting of a PLC in a glass slide by means of potassium ion-exchange. This technology requires a number of steps including photolithography, metal mask deposition and high temperature (400 °C+) immersion in a molten KNO_3 salt solution in order to form the PLC [18]. The need for metal deposition equipment and high temperature furnaces renders this process more costly and time consuming than the hybrid sol-gel route.

Due to the relative success of the evanescent wave fluorescence excitation technique, this approach was chosen for development in this work in conjunction with the low-cost hybrid sol-gel materials and mass-producible microfabrication techniques, the combination of which will enable the fabrication of low-cost disposable biosensing platforms for use in POC diagnostic testing.

6.3 Optical Circuits

6.3.1 Platform Concept

As mentioned in the introduction, the basic principle of this multianalyte platform is to excite fluorescently-labelled antibodies using the evanescent wave of guided radiation in a waveguide as illustrated in Figure 6.1. Multianalyte capability is achieved by the formation of an optical circuit that delivers light from a single excitation source to multiple sensor windows on the platform. A number of optical circuit formats were developed during the course of this work, and these involved patterning of both the optical circuit layer, and the protective layer of the platform.

The design illustrated in Figure 6.2a, for example, comprises an initial single-mode waveguide, which facilitates optimal power coupling from a fiber pig-tailed laser diode. The single-mode waveguide tapers into a wider waveguide on top of

which eight sensor windows have been defined. The taper has been introduced in order to gradually enlarge the waveguide width, so as to obtain a larger sensor spot.

A more complex design is illustrated in Figure 6.2b, utilising cascaded y-junction splitters in order to distribute the input light signal equally among four waveguide arms, thus providing a four-fold increase in the number of sensor spots. The y-junction splitters of this design are implemented using single-mode waveguides, as means of minimising variations in the splitting ratio [19].

Another design yielding a similar increase in sensor spots is provided by the platform illustrated in Figure 6.2c, which utilises a multi-mode interference coupler (MMIC) in order to split the input light signal into four outputs of equal intensity. The design in Figure 6.2a has been fully developed here as this design most easily facilitated the acquisition of a number of techniques necessary for successful implementation of the platform, including microfabrication of the patterned protective layer, biochip surface functionalisation and image processing. The other two designs have been explored in simulation studies with the next stage of development being the fabrication and testing of these designs (outside the scope of the work reported here).

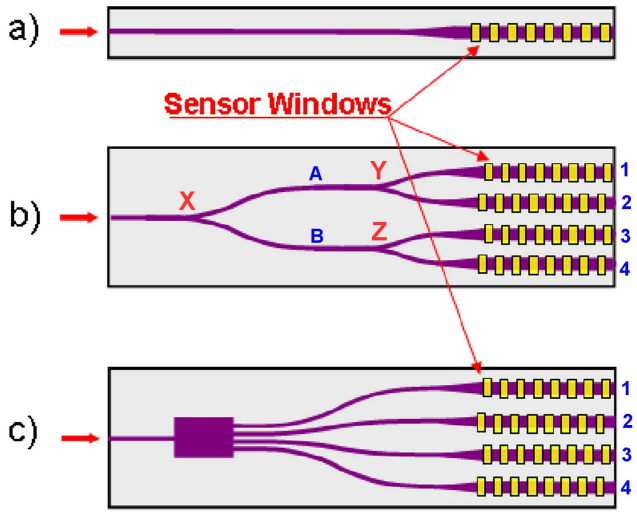

Figure 6.2: *Schematic diagrams of the biosensor platforms under development employing; a) a single tapered waveguide, b) y-junction splitters and c) MMIC splitters*

6.4 Simulation

6.4.1 Determination of Waveguide Dimensions and Refractive Indices

In this instance, the platform was designed for the excitation of fluorescence from Cy5 labelled antibodies, and so it was necessary to design optical waveguides which are single-mode at 635 nm (wavelength of the laser diode employed). To this end, the OlympIOs cross-sectional mode solver was again employed in order to determine the refractive index contrast and dimensions necessary to produce single-mode waveguides for this wavelength.

Given that the laser writing system was optimised to produce a laser spot of 6 μm, it was decided to maintain a 6 x 6 μm waveguide cross-section. Moreover, given our experience working with the reference guiding layer formulation which has a refractive index of 1.52, there was no compelling reason to alter this material. Therefore, for single-mode operation, the refractive index of the buffer layer was the only parameter varied. According to the simulations carried out, this waveguide is single-mode at 635 nm provided there is a refractive index contrast of $\Delta n = \sim 0.002$ between the guiding and buffer layers, which determines a refractive index of 1.518 for the buffer layer.

6.4.2 Simulation of Optical Splitter Circuits

6.4.2.1 Y-junction splitter circuit

Simulation of the y-junction splitters that are inherent to the design presented in Figure 6.2b was carried out using the 3D BPM software. Referring to the schematic diagram of the biosensor chip depicted in Figure 6.2b, the outputs from the first y-junction are denoted A and B, and the four outputs of the second phase of y-junctions are denoted 1-4 (from top to bottom). Of greatest interest here, is the behavior of a y-junction splitter with imperfections, rather than that of an ideal y-junction. The main source of imperfections is likely to originate from the finite resolution of the photolithographic process in defining the y-junction. Therefore, simulations were not carried out on a sharply defined y-junction, which is extremely difficult to fabricate repeatably. Instead, the structure illustrated in

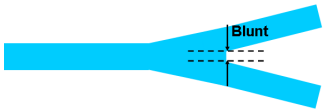

Figure 6.3: *Y-junction with blunt element*

Figure 6.3 was simulated, where a "blunt" section was incorporated between the output waveguides, in order to represent a more realistic situation.

In order to give an indication of the resolution that will be needed to repeatably fabricate these circuits, the size of the "blunt" was varied during simulation and the optical power at each of the four output waveguides was monitored. This was carried out first for the ideal circuit, where the blunt element of the three y-junctions (X, Y and Z) was set to zero. The bar chart in Figure 6.4a, illustrates the percentage of the input optical power that is found first in regions A and B, and subsequently in the four output waveguides labelled 1 - 4. In this case, there is perfect splitting of the input signal at y-junction X, with negligible loss of light. With reference to the output waveguides, it is notable that the two central output waveguides (labelled 2 and 3) have an equal, and slightly higher intensity than the outermost waveguides (labelled 1 and 4). This slight imbalance appears to originate from perturbations that are introduced into the light field, as it traverses the s-bend that joins the first y-junction X to the other y-junctions (Y and Z). Apart from this slight imperfection, the result is as expected with an almost equal division of light in the four output waveguides (∼25% each).

Having established the behavior of the ideal circuit as a reference, it was then possible to simulate the effect of design perturbations. Firstly, a single y-junction was analysed in isolation to evaluate the effect of blunt size on the splitting ratio. The result of this study is shown in Figure 6.4b, where it is evident that

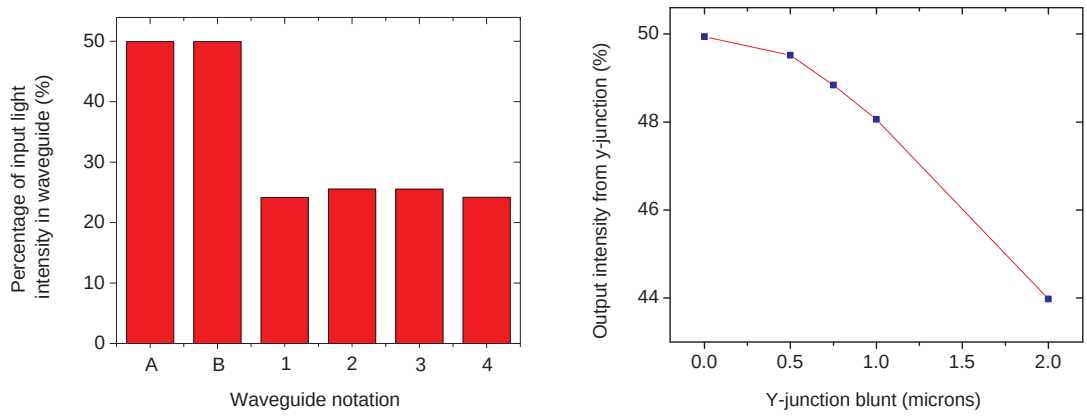

(a) (b)

Figure 6.4: *a) Output power from each of the labelled waveguides for the ideal y-junction optical circuit (blunt = 0 μm), and b) simulation of the output power from a single y-junction as a function of blunt size (both output waveguides show the same power)*

as the blunt size is increased, the intensity captured from an output waveguide decreases first slowly, and then more rapidly at a rate of ∼4% per μm. However, the difference between the optical power found in the output waveguides was negligible (on the order of 0.01%), which is a promising result as it points to the possibility to deliberately incorporate blunts in a design which is easily resolvable by the fabrication process, at the cost of a small amount of excitation intensity.

Simulations were then carried out on the whole optical circuit, to evaluate the output optical power when the blunt size of y-junction X is set to 1 μm and that of Y and Z was varied. The result is plotted in Figure 6.5 and reveals a number of trends. Firstly, similar to the ideal circuit, the intensity of the two central output waveguide (2 and 3) shows identical behavior for each blunt size, with the two outer waveguides (1 and 4) also mirroring one another. As blunt size is increased from 0, the output power found in the central pair decreases while there is an increase in the power found in the outer pair. This behavior stems from the light perturbation incurred in traversing the s-bends, which continues into the tapered section (just before the y-junction Y or Z) causing an unequal light intensity to be incident on the two output waveguides of the junction. In Figure 6.5, the desired situation where all outputs have equivalent optical power would be found for a blunt size of ∼0.45 μm (i.e., where the two curves intersect). The curves converge toward another intersection at a blunt size of ∼2.1 μm, but the disadvantage here is that some of the power is lost (∼2% from each output waveguide). These results

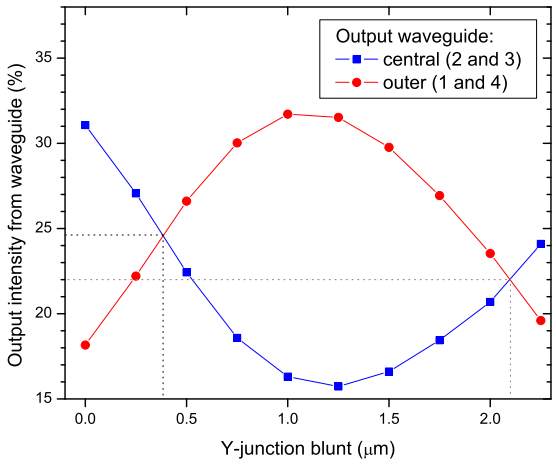

Figure 6.5: *Output optical power for an optical circuit where the first y-junction (X) has a blunt size of 1 μm, and the blunt size of the second phase of y-junctions (Y and Z) is varied*

highlight to the need to carefully design an optical circuit containing y-junction splitters, accounting for the capabilities of the fabrication process in question. However, the ability to design an effective circuit even with the incorporation of blunt elements is a promising outcome of these simulations.

6.4.2.2 MMIC splitter circuit

Simulation of the MMIC-based optical splitter circuit illustrated in Figure 6.2c was also carried out using the 3D BPM method. Having established the general theory behind the operation of the MMIC in Section 2.3, this section concentrates on the simulation steps that were involved in the specification of a 1x4 MMIC power splitter circuit. Firstly, the width of the MMIC was fixed at 60 μm, permitting a good separation of the input (and output) waveguides. This relaxes the requirement to define waveguides in close proximity, which tests the resolution of the optical system and contrast of the material as discussed in Section 3.3. The length of the centre-fed MMIC for 1x4 power splitting was defined using the characteristic equation of the MMIC such that,

$$L_{\mathrm{MMIC}} = \frac{M}{N}\frac{3L_{\pi}}{4} \tag{6.1}$$

where M is the self-image rank (M=1 for the recreation of the input field in the shortest MMIC length possible), N denotes the number of equal intensity self-images created at the MMIC output (M=4 in this case), and L_{π} is the beat length of the MMIC structure defined in equation 2.35.

To determine the MMIC length, the cross-sectional mode solver was used firstly to calculate the effective refractive indices of the fundamental and first order mode of the MMIC cross-section, as required for the determination of L_{π} in equation 2.35, which at 635 nm was found to be ~12.6 mm ($(n_{\mathrm{eff}_0}\text{-}n_{\mathrm{eff}_1})$ was ~2.5x10^{-5}). Inserting this quantity into equation 6.1 the theoretical MMIC length was calculated to be ~2.36mm. This value is usually quite close to the actual value, but simulation often reveals a small offset that needs to be introduced to this value of MMIC length, to obtain exact splitting of the input into N outputs of equal intensity.

Therefore, using the 3D BPM software, the structure was simulated a number of times, in each instance introducing a slightly different offset to the length of the MMIC and observing the optical power at the output. Referring briefly to the optical circuit schematic in Figure 6.2c, it was found for all length offsets

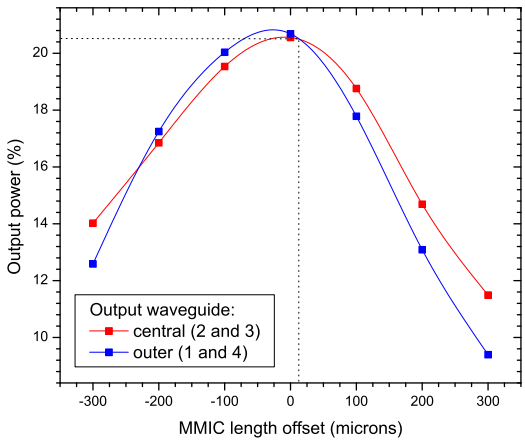

Figure 6.6: *Output power from output waveguides (central and outer) as a function of the offset on the MMIC length*

simulated that the two central waveguides (2 and 3) had equivalent intensity, with the same trend noted for the outer waveguides (1 and 4). In order to find the offset point where all output waveguides carry the same optical power level, the output power from the central and the outer waveguide groups are plotted as a function of the length offset in Figure 6.6.

In this particular instance, the first estimate of the MMIC length given by the analytical formulae was extremely accurate with almost equal splitting among the outputs found for zero offset. According to the simulation, equal splitting among all output waveguides occurs at an offset of +14.5 μm at which point each of the four output waveguides has a 20.5% share of the input signal. This also indicates a loss of $\sim$18% in traversing the MMIC structure and the subsequent s-bends and tapers that form the path to the output. This loss is greater than in the case of the ideal y-junction circuit described above. However, due to the fact that the photolithography process or material resolution limits are not challenged by this design (no closely spaced features), along with the greater process latitude inherent to the design (as seen by the relatively large tolerance on the MMIC length shown in Figure 6.6), this design is an extremely attractive proposition for future development.

6.4.3 Evanescent Wave Simulation

Evanescent wave excitation is the core principle underpinning this platform. In this context, the objective of this section is to present a methodology that was

developed to enable the simple determination of the intensity carried by the evanescent wave of any arbitrary waveguide structure. Although it is possible to calculate the evanescent wave penetration depth (the distance from the waveguide boundary to where the intensity drops by a factor of $1/e^2$) using the analytical equations outlined in Section 2.2.2, it is not easily possible to analytically determine the optical power that resides in the evanescent wave of a given waveguide structure, especially if it is more complex than a simple 3-layer waveguide structure (buffer/guiding/protective layer). To effectively address this challenge, a numerical approach to evanescent wave intensity simulation was developed, utilising the 2D BPM software. This allowed the construction of a given waveguide structure from a side-on perspective, which permits the definition of all layers in the vertical plane, whilst simultaneously allowing observation of how light behaves in all layers of the structure as it propagates along the direction of the waveguide. With the use of Pade approximant operators and a high discretization of the finite difference grid (discretization used in the x- and z-directions were 1 nm and 0.2 μm respectively), it has been shown that the BPM method can accurately handle high refractive index contrasts [20].

In order to conveniently extract the evanescent wave optical power from the BPM data files, a Labview program was developed. Firstly, once the BPM simulation had been completed, the output electric field distribution was exported to a simple text file. The Labview program was designed to read in this text file and store it in a large array. For data processing the electric field values were squared because Intensity $\propto E^2$. One of the main objectives of the data processing algorithm was to locate the intensity value at the waveguide boundary. However, since the BPM algorithm is based on finite-difference methods, its output consists of a grid of discrete E-field values. A discrete value does not usually appear exactly at the spatial position desired without careful calculation. Therefore, one of the primary objectives of the Labview program was to fit an exponential curve to the evanescent field values, which would allow exact calculation of the intensity at the waveguide boundary. Having determined the value of the intensity at the waveguide boundary, calculation of the penetration depth simply involved multiplication by the $1/e^2$ factor. Penetration depths were evaluated for a number of symmetric and asymmetric waveguide structures. Comparison of these values to analytically derived values, showed an exact match in all cases as expected, thus giving a high degree of confidence in the developed methodology.

The second important piece of information that could be extracted from the BPM data was the total optical intensity carried in the evanescent wave, from the waveguide boundary out to one penetration depth from the boundary. This was calculated by means of integrating the intensity values described above, using a trapezoidal integration algorithm which involves splitting the intensity profile into discrete trapezoidal areas as shown in Figure 6.7, and then summing the individual trapezoids according to,

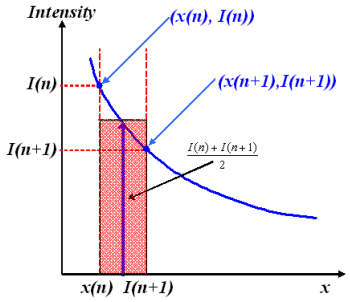

Figure 6.7: *Illustration of trapezoidal integration method*

$$\text{Intensity integral} = \sum_{n=1}^{n} \left[(x_n - x_{n-1}) \frac{(I_n + I_{n-1})}{2} \right] \tag{6.2}$$

to arrive at the total integrated intensity, where n is the number of discrete trapezoidal elements that approximates the curve. This was done for each discrete slice along the z-direction of the waveguide (propagation direction) and the resulting values were averaged, with differences in intensity along the length of the waveguide represented by the standard deviation of the calculated integrals.

The first problem to which this method was applied was the determination of the evanescent field power of a bare sol-gel waveguide. The function shown in Figure 6.8 was the result of this investigation, and analysis of the BPM data revealed that only ∼0.0066% of the light intensity was carried by the evanescent wave. This value is extremely small, and prompted investigation into various

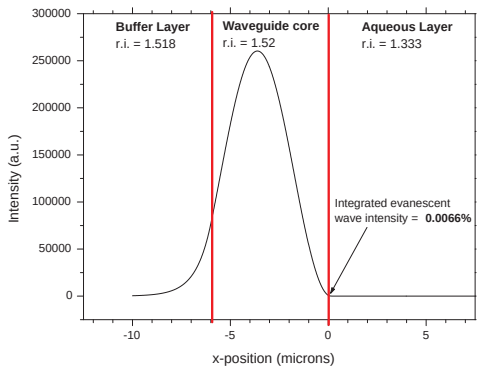

Figure 6.8: *Mode profile of the single-mode sol-gel waveguide*

ways of increasing the evanescent wave intensity. Two means of achieving this aim were examined: a) alteration of the platform design to form reverse symmetry waveguides, and b) the deposition of a thin, high refractive index layer on top of the waveguide. A reverse symmetry waveguide is one where the refractive index of the superstrate layer is greater than that of the substrate layer. An example of this is the use of a glass slide as a waveguide with an air substrate and a aqueous superstrate layer. However, this configuration does not lend itself to microscale manipulation of light for multianalyte sensing, which is the objective of this work. The second solution involves the deposition of a high refractive index layer on top of the waveguide. In this work, it was decided to investigate the use of tantalum pentoxide (Ta_2O_5) as the high refractive index layer, as it has a refractive index of 2.11 (at 635 nm) and is optically transparent at the fluorescence excitation and emission wavelength [21].

6.4.4 Enhancement of Evanescent Wave Intensity

Utilising the simulation methodology outlined above, it was possible to simulate the effects on evanescent wave intensity resulting from the introduction of a nano-scale Ta_2O_5 layer on top of the sol-gel planar waveguide, as depicted in Figure 6.9. Though the standard waveguide thickness of 6 μm was used in this work due to the ease of coupling to the pig-tailed laser diode offered by the 6 x 6 μm dimensions, it was instructive to consider waveguides with both a lesser and a greater thickness for comparison. Therefore, three separate waveguide geometries were simulated, with waveguide thicknesses of 3, 6 and 9 μm. Firstly, the effects of deposited Ta_2O_5 over a thickness range of 0-60 nm was considered for each waveguide separately. A simple evanescent wave enhancement factor was calculated according to the following relation;

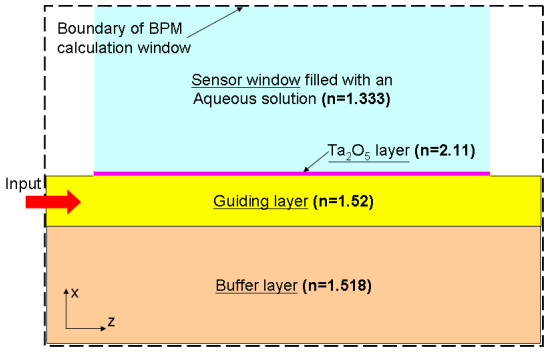

Figure 6.9: *Sideview waveguide structure used for 2D BPM simulation of the evanescent wave*

$$\text{Enhancement factor} = \frac{\text{Intensity integral[waveguide with X nm } Ta_2O_5\text{]}}{\text{Intensity integral[waveguide with 0 nm } Ta_2O_5\text{]}} \quad (6.3)$$

The enhancement factors for each waveguide geometry can be seen in Figures 6.10a and b, and 6.11a, allowing a number of observations to be made. Firstly, the form of each curve is approximately the same, that is, the enhancement factor shows an almost imperceptible increase until a thickness of ∼20-25 nm, at which point it increases rapidly to a peak value around 35 nm. At this peak value, the Ta_2O_5 layer in itself is essentially a single-mode waveguide, and so strictly speaking, the improvement in evanescent field intensity at Ta_2O_5 thicknesses of 35 nm and above is not considered enhancement. This is because the light that has coupled from the sol-gel waveguide is now confined within the Ta_2O_5 layer, and is therefore not easily coupled back into the sol-gel waveguide. In this context, enhancement of the evanescent wave of the sol-gel waveguide reaches its maximum value when a Ta_2O_5 layer just below 35nm is deposited on top (just below cut-off thickness for a Ta_2O_5 single-mode waveguide). Given that 35 nm is the cutoff thickness, the peak enhancement factors in these simulations are quoted at this thickness, in order to allow comparison of the different configurations investigated.

The peak enhancement factor for the 9 μm waveguide is ∼920 at 35 nm of Ta_2O_5, which is a substantial enhancement of the initially very small intensity. For the 6 μm waveguide this factor drops to ∼440, while for the 3 μm waveguide it decreases further to ∼135. Therefore, according to these simulations the greatest increase in evanescent wave intensity is for the 9 μm waveguide at a Ta_2O_5

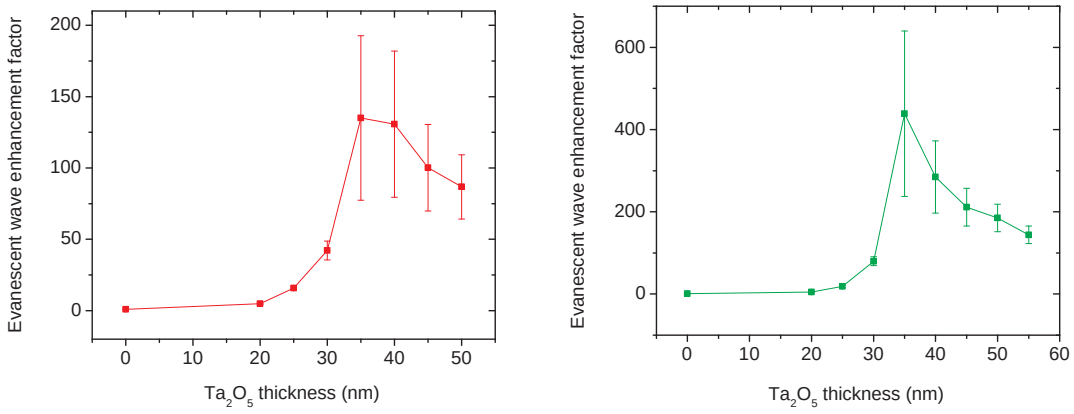

(a) (b)

Figure 6.10: *Evanescent wave enhancement factor as a function of Ta_2O_5 thickness for a waveguide thickness of; a) 3 μm, and b) 6 μm*

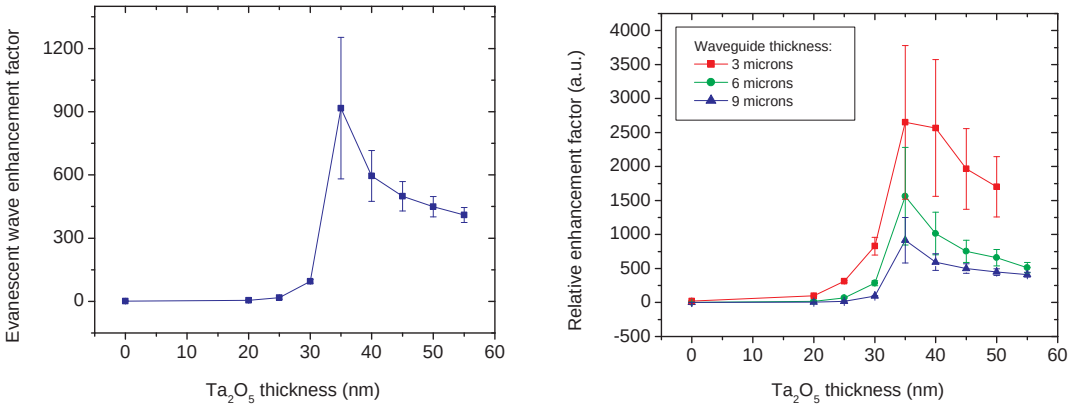

(a) (b)

Figure 6.11: *a) Evanescent wave enhancement factor as a function of Ta_2O_5 thickness for a waveguide thickness of 9 μm, and b) relative evanescent wave enhancement factor for the three waveguide geometries*

thickness of 35 nm.

The error bars of each data point express the spatially periodic variations in evanescent wave intensity shown by the simulation images in Figure 6.12 (equal to ± 1 standard deviation).

To permit comparison between the different waveguide geometries investigated here, a reference enhancement factor needed to be defined. Therefore, the smallest evanescent wave intensity value was used for this purpose, that of the uncoated 9 μm waveguide. With the reference established, a relative enhancement factor was calculated according to,

$$\text{Relative enhancement factor} = \frac{\text{Intensity integral[Y } \mu\text{m waveguide \& X nm } Ta_2O_5]}{\text{Intensity integral[9 } \mu\text{m waveguide \& 0 nm } Ta_2O_5]}. \quad (6.4)$$

Using this definition, the relative performance of each of the configurations could be plotted as shown in Figure 6.11b. According to these data, the configuration that has the highest evanescent field intensity is that of the 3 μm waveguide coated with a 35 nm layer of Ta_2O_5. The integrated intensity of the evanescent wave of this configuration is approximately 2650 times greater than that of a bare uncoated 9 μm waveguide, which is a substantial improvement over this configuration. Since, a 6 μm thick waveguide was the chosen configuration for the first experiments the enhancement factor of 440 was the most pertinent result here. However, the results from the other configurations will certainly guide future work

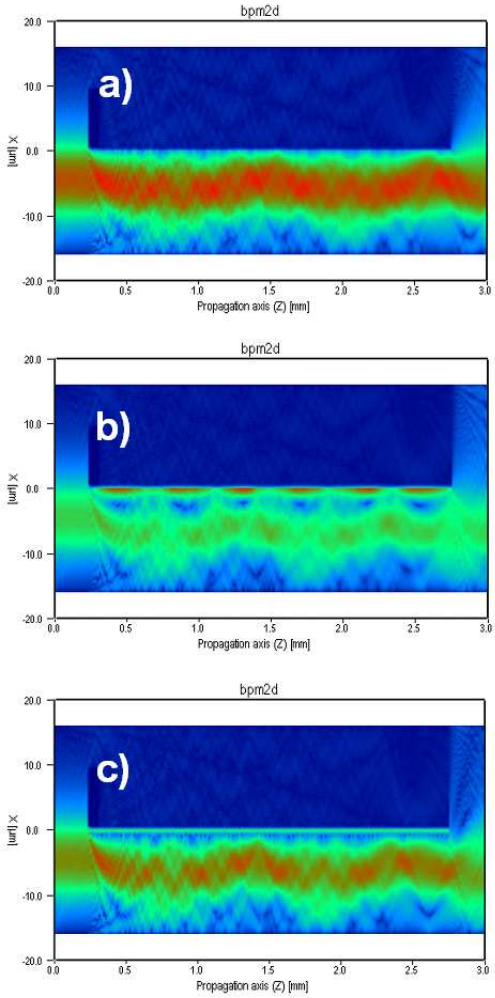

Figure 6.12: *BPM electric field distributions of light in a the waveguide system which has; a) 25 nm, b) 35 nm and c) 45 nm of Ta_2O_5 deposited on top of a 9 μm thick sol-gel waveguide*

when more advanced waveguide coupling strategies will be investigated, such as grating or prism couplers which will reduce the necessity to adhere to a 6 x 6 μm input waveguide cross-sectional geometry.

6.5 Experimental

6.5.1 Fluorescence Detection System

In this Section, the fluorescence detection system is outlined, along with a brief study carried out to determine the choice of the objective lens for optimal SNR performance. The setup illustrated in Figure 6.13, uses a adjustable rail-mounted microscope (Olympus) on an optical bench, to which the CCD camera (Starlight Xpress M7) was coupled along with an emission filter (Semrock). This allows

collection of fluorescence from the chip, by first focusing optically on the waveguide surface using the eyepiece of the microscope, and then switching the output to the CCD camera for fluorescence detection. The aim in characterising the detection system was to determine experimentally, which microscope objective lens would result in the highest collected intensity per pixel on the CCD detector. A theoretical formula has been given by Glasenapp [24], which predicts the intensity per pixel of light collected by the CCD as a function of lens magnification (M) such that,

$$\text{I-collected} = \frac{M^2}{16N f_{\#}^2 (1+M)^2} \tag{6.5}$$

where N is the number of pixels and $f_{\#}$ is the f-number of the lens which is described by,

$$f_{\#} = \frac{\text{focal length}}{\text{lens diameter}} = \frac{f}{D} = \frac{1}{2NA} \tag{6.6}$$

with NA denoting the numerical aperture of the lens (NA = n.sin(θ), θ is half the acceptance cone of the lens). In order to simulate a sensor spot, a tiny pinhole was made in a foil target and illuminated from beneath by a fiber optic illuminator from a white light source. The microscope was focused onto the illuminated pinhole for each objective lens under test, and images were captured with the CCD camera using a 100 ms integration time. Using image analysis software (Image-J), the image of the pinhole was extracted from the dark background and the average intensity of a pixel in the pinhole image was calculated for each lens.

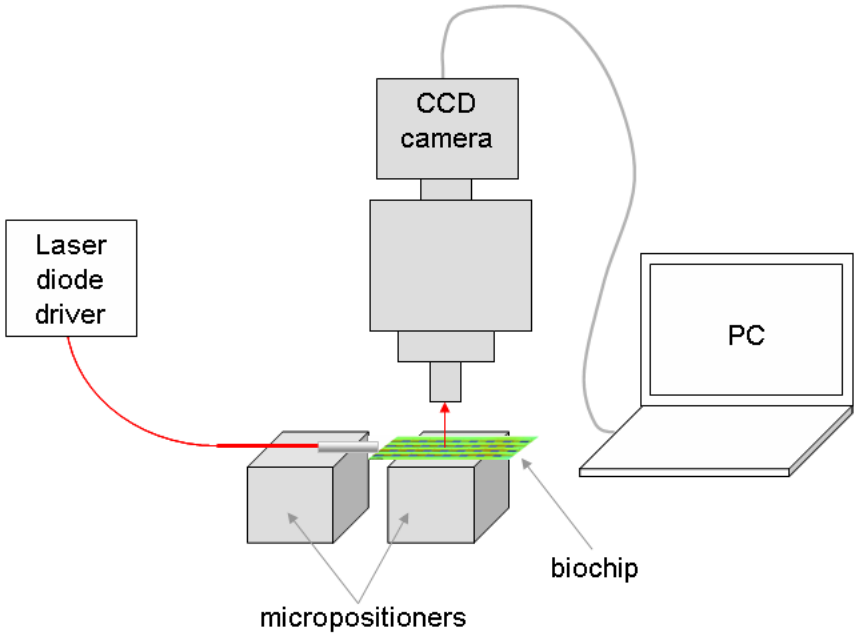

Figure 6.13: *Fluorescence detection setup*

To compare with the experimental technique, the theoretical treatment modeled the optical system using equation 6.5, and the normalised intensity per pixel as a function of lens magnification is displayed in Figure 6.14 for both experimental and theoretical values. Here, it is clear from both theory and measurement that the highest captured pixel intensity occurs for the lower magnification lens.

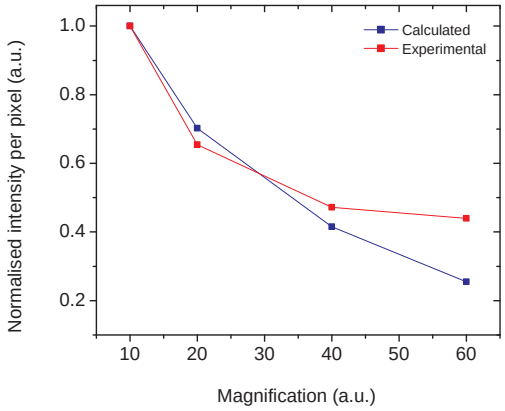

Figure 6.14: *Comparison of the calculated and measured pixel intensity as a function of objective lens magnification*

6.5.1.1 Discrimination of excitation and emission using filters

In many sensor configurations, discrimination of scattered excitation light from the emitted fluorescence necessitates the use of an excitation and emission filter. The function of the excitation filter is to filter out of the excitation light any faint wavelengths that might overlap with the emission spectrum of the fluorophore (such as from the tail of a laser diode which can extend over many tens of nanometers from the peak wavelength).

In this work an excitation filter (Semrock FF01-628/40) was selected the transmission spectrum of which can be seen in Figure 6.15, along with the absorption spectrum of Cy5 and the laser emission line. This filter satisfies the main criteria; it passes the laser diode emission line easily within its pass-band, and it provides excellent attenuation (ND5) of wavelengths in the region of Cy5 emission. However, the emission filter is perhaps of greater importance as it blocks wavelengths coming from the spectral region of the laser diode emission peak, which is typically at a high intensity in order to excite fluorescence. Therefore, without the use of an emission filter, any scattering of these wavelengths will be easily detected by the CCD and mistaken for fluorescence. The emission filter

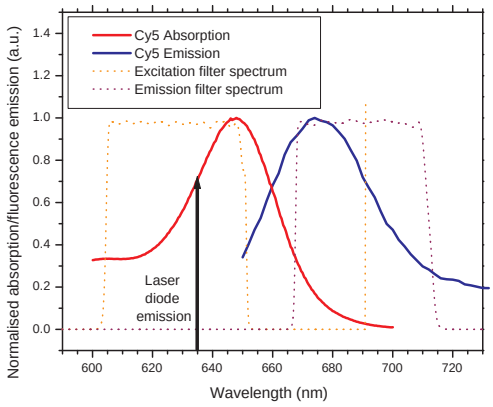

Figure 6.15: *Transmission spectra of the filter set chosen for use with the Cy5 fluorophore, and for comparison the absorption/emission spectra of Cy5*

used here (Semrock FF01-692-40-25) passes light above ∼665 nm and so is certain to block the vast majority of excitation light while capturing the peak of the Cy5 emission.

6.5.2 Microfabrication

The microfabrication process of this multianalyte platform bears similarities to other processes employed for device fabrication throughout this thesis, and the global steps for optical circuit fabrication and photopatterning the protective layer are depicted in Figure 6.16a and b respectively. However, many of the specific details pertain only to work carried out on this particular platform, and these will be described in the following section.

6.5.2.1 Optical circuit fabrication

The first step of the development process was to establish the composition of the buffer layer material that would satisfy the refractive index requirement as specified by simulation in Section 6.4.1. As outlined in Section 4.3.1.1, the refractive index of the reference material is easily altered by varying the molar concentration of the zirconate complex in the sol. In this case, the sol composition indicated in Table 6.1 was found to yield the required buffer layer refractive index of 1.518. Deposition of the buffer layer sol onto a glass slide was carried out using the optimised spin-coating setup (described in Section 4.5), employing a spin-speed of 750 rpm. Stabilisation of the coating involved a 4 minute UV exposure, followed

Precursor	Guiding layer
MAPTMS	1
$Zr(OC_3H_7)_4$	0.385
MAAH	0.385
H_2O	2.12
Irgacure 184	0.050

Table 6.1: *Constituents of the sol-gel material for the buffer/protective layer*

by baking at 120 °C for 2 hours, which gave a final buffer layer thickness of 6 μm.

The optical circuits were fabricated using an optimised reference sol-gel composition, exploiting the insights gained in Chapter 4. In this instance, the guiding

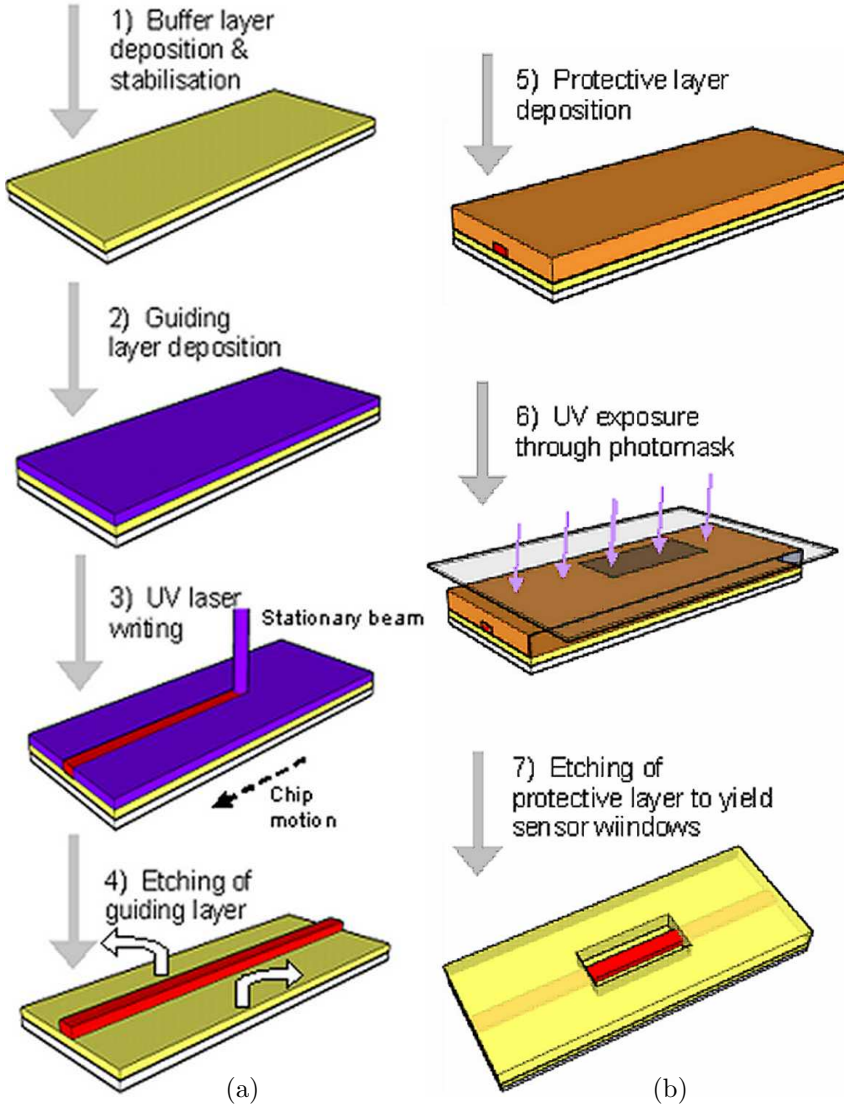

Figure 6.16: *Fabrication process for biosensor chip; a) optical waveguide processing, and b) patterning of protective layer*

Figure 6.17: *Laser writing of the tapered single- to multi-mode waveguide by overlapping of lines*

layer recipe described in Table 4.2 was used, with the photoinitiators I-1800 and I-819 being replaced by I-184 which was added to the guiding layer in the standard 1:20 molar concentration ratio with respect to MAPTMS. Spin-coating was carried out as above with an identical spin speed giving the desired 6 μm guiding layer thickness. The direct laser writing system described in Section 3.4 was used for optical waveguide fabrication, using a scan speed of 0.6 mm/s throughout, at an energy density of 1100 mJ/cm^2. In order to form the tapered waveguide shown in Figure 6.2a, a specific laser writing system input file was developed which would overlap the 6 μm laser spot a number of times in order to build up the 30 μm multi-mode waveguide, as shown in Figure 6.17.

Optical profilometry of the single-mode and multi-mode structures is shown in Figure 6.18a and b respectively. A slight undulation of the top surface of the multi-mode waveguide can be observed which is due to the slight rounding of the top surface of the single-mode waveguide, due to oxygen inhibition of polymerisation.

6.5.2.2 Protective layer patterning development

The general steps for protective layer patterning are shown in Figure 6.16b, with the first step being to deposit the protective layer sol. The protective layer sol has

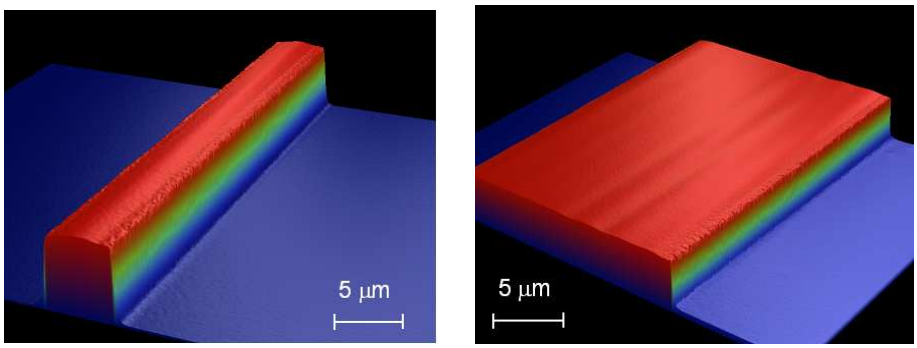

(a) (b)

Figure 6.18: *Optical profilometry images of; a) single-mode ridge waveguide, and b) multi-mode ridge waveguide, both before protective layer deposition and patterning*

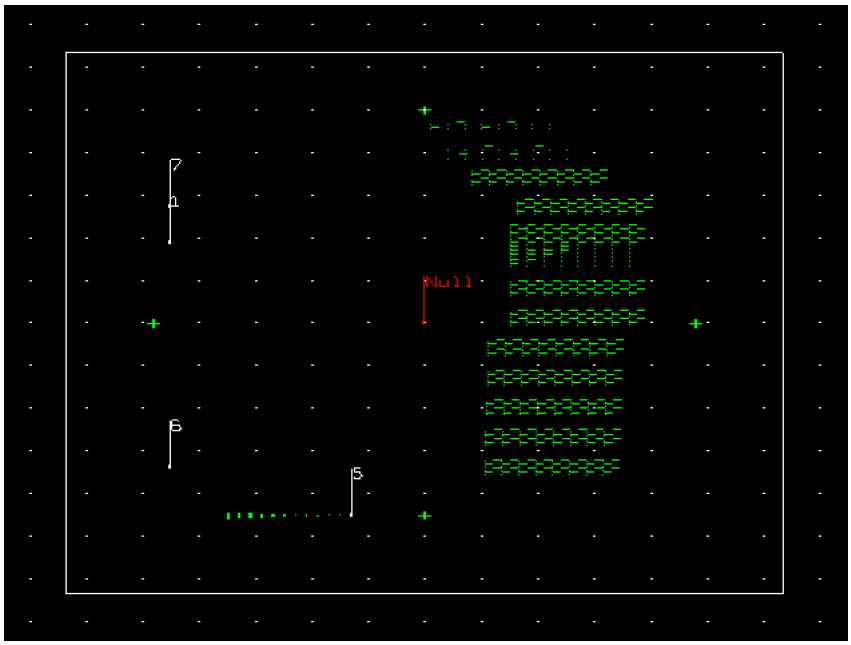

Figure 6.19: *Bright field mask for photopatterning the protective layer*

exactly the same formulation as that used for the buffer layer, the difference in name denoting the different function of the layers in the optical chip. Spin-coating of the protective layer was carried out as indicated above for the buffer and guiding layer sols. The chip was transferred directly to the mask aligner (Karl Suss MA56), where alignment markers that had been laser written in the guiding layer were aligned with complementary markers on the protective layer mask (shown in Figure 6.19). An exposure of 3 minutes was sufficient to photopattern the protective layer, whilst maintaining the dimensions of the multiple wells/sensor spots that had been defined over the waveguides.

The most critical process step was the post-exposure baking (PEB) step as this impacted upon a number of chip characteristics including window dimensions, the etching process and surface roughness of the wells. Initial investigations without any PEB, showed that the patterned protective layer was attacked during etching of the sensor windows in a bath of isopropanol, resulting in excessive dissolution of the layer and damage to the features. Therefore, the PEB step was included in the process, after which is was necessary to etch in a sonicated isopropanol bath for 40 s, in order to properly etch the corners of the sensor spot wells, which were not well etched by simple immersion in isopropanol. The optimum PEB time was found to be in the region of 10-15 minutes at 100°C.

Optical profilometry measurements of the roughness of the sensor window well after etching (as shown in Figure 6.20), revealed an average roughness of ∼8 nm

for the 10 minute PEB, and ∼5.1 nm for the 15 minute PEB. Based on this study, a PEB time of 15 minutes has been selected for the eventual fabrication of the platforms. Following on from the simulations detailed in Section 6.4.4, a Ta_2O_5 layer of 35 nm was deposited on top of the protective layer of the patterned chip in order to enhance the intensity of the evanescent wave.

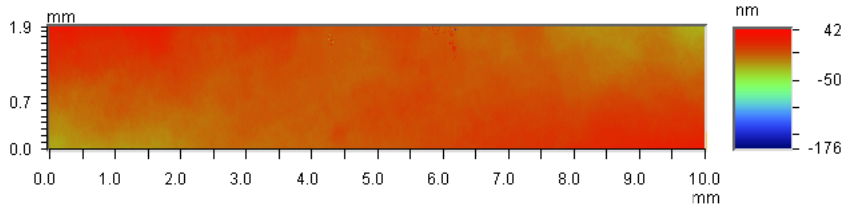

Figure 6.20: *Optical profilometry of the sensor window well bottom after processing showing the low surface roughness*

6.5.3 Surface Functionalisation

In order to immobilise a capture antibody on the surface of the waveguide in each of the sensor windows on the platform, a means of functionalising the surface of the platform is typically used. This often involves grafting functional groups onto the surface (such as amines), which form an ultra-thin intermediate layer which binds to both the platform surface and the antibodies.

Preliminary studies were first carried out on a planar sol-gel guiding layer surface, which was modified by a number of methods including; attachment of an epoxy-linker layer, attachment of an amine-linker layer, or oxygen plasma treatment of the sol-gel surface. To evaluate the performance of each immobilisation strategy Cy5 labelled antibodies were printed directly on the variously modified sol-gel surfaces using a pin-printer (Omnigrid Micro; Genomic Solutions, U.K.), and images were captured using a fluorescence scanner (Genomics Microsystems). For each image shown in Figure 6.21, rows of 0.5, 1.0, 1.5 and 2.0 μg/ml concentrations of mouse IgG labelled with Cy5 (from top to bottom), were deposited in discrete spots. Comparison of the signal from the 2.0 mg/ml row (marked by a white box) in each of the images shows clearly that of all of the surfaces evaluated, the untreated sol-gel surface gave the highest fluorescence signals, which are visually brighter than the epoxy-, amine- or O_2 plasma-modified surfaces. The quality of the spotting on the sol-gel surface is also superior with the spots being more uniform with less blurring into surrounding areas. This is a very promising result for the development of future platforms based on the sol-gel materials.

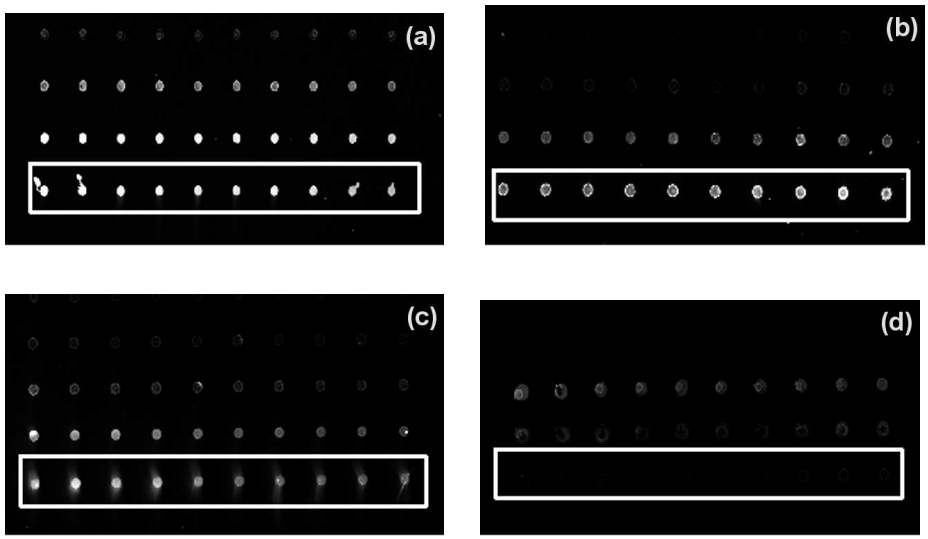

Figure 6.21: *Captured fluorescence from arrays of Cy5 labelled antibodies on a sol-gel surface which was a) not modified, b) modified by an epoxy linker layer, c) modified by an amine linker layer, and d) O_2 plasma modified*

However, due to the later deposition of the Ta_2O_5 on the platform for evanescent wave enhancement, the conditions of surface functionalisation were changed during the project. The best strategy developed for the sol-gel surface - using direct adsorption - was tried on the Ta_2O_5-coated surface. However, when scanned, no fluorescence was detected from the chip surface indicating that immobilisation through direct adsorption on Ta_2O_5 was not possible. Concurrent work in the laboratory developed by a colleague Mr. Scott Spillman, provided an alternative route to the above-mentioned immobilisation strategies. This new strategy involved the use of polyelectrolyte multilayers as an immobilisation scaffold, and has been effective for antibody immobilisation on a wide range of substrate materials.

The use of polyelectrolyte multilayers (PEMs), pioneered by Decher et al. in the early 1990's, has rapidly expanded over the last decade as a simple and effective method to modify surfaces for a variety of applications [25]. In this work, PEMs were used to form an intermediate layer which would bind strongly to both the Ta_2O_5-coated sol-gel waveguide and to the capture biomolecule. PEMs are typically formed by electrostatic attraction between alternate oppositely charged layers, in this case layers of poly(allylamine hydrochloride) (PAH) and poly(styrene sulfonate) (PSS). Briefly, the chip was immersed in 2 mg/ml PAH in water (pH 7.4) for 10 minutes, followed by a vigorous rinse in de-ionised water. Next, the chip was immersed in 2 mg/ml PSS in PBS (pH 7.4) for 10 minutes, followed by another rinse in de-ionized water. This process was then repeated until a multilayer composed of (PAH/PSS)5.5 was assembled, with PAH being the out-

ermost layer. Initial tests of the PEM-modified Ta_2O_5 surface showed that immobilisation of the biomolecules was possible via this strategy, as shown by the fluorescence captured from the waveguide surface in Figure 6.22.

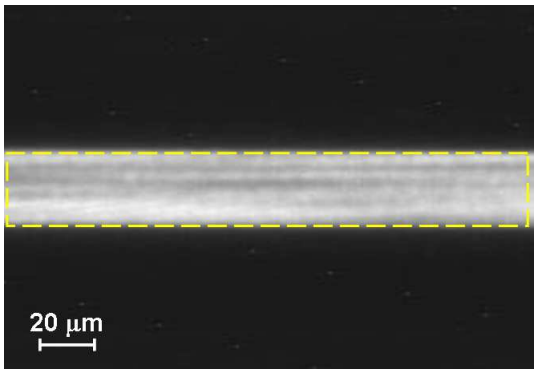

Figure 6.22: *Fluorescence image from PEM-functionalised Ta_2O_5-coated waveguide*

6.5.4 Characterisation of the Platform Response

6.5.4.1 Immunoassay protocol

The platform was characterised using a proof-of-principle assay in a direct immunoassay format. This generally involves the immobilisation of a capture antibody to a substrate surface. Antigens are then introduced, and binding occurs. For direct detection the antigens are typically fluorescently labelled. Direct assays can also be performed by immobilising the antigen onto the surface and detecting using a labelled antibody. This method was chosen for platform characterisation in this work, as it was the simplest to implement.

Mouse IgG antigen was immobilised on the platform surface and detected using Cy5-labelled anti-mouse IgG antibody. A 1:2 serial dilution of mouse IgG antigen in PBS were prepared with the highest concentration starting at 1000 μg/ml. 1 μl of each concentration was manually deposited in a separate sensor window by micropipette. After allowing 30 minutes for binding to take place at room temperature, the chip was washed three times in PBST (phosphate-buffered washing solution) with 2 mg/ml poly(acrylic acid) (PAC), and then a further three times in PBS (phosphate-buffered solution).

Blocking refers to the process where a molecule not relevant to the immunoassay (sometimes another protein/antibody) is used to block all other areas of the platform to which an antigen or antibody could potentially bind (non-specific binding) as this gives rise to a higher background signal, which degrades the

SNR. The chip was blocked by immersion in a solution of PBS and PAC for 15 minutes, followed by a de-ionised water rinse. With the immobilisation step complete the chip was immersed in a solution of Cy5-labelled mouse IgG antibody, which had been diluted to 2 mg/ml in a mixture of PBS and 2% BSA (bovine serum albumin). This was stored at room temperature to allow binding of the Cy5-labelled IgG to the immobilised antigen. After 1 hour, the chip was removed and washed three times in PBST followed by three times in PBS and finally dried under a nitrogen flow.

6.5.4.2 Fluorescence detection and image analysis

The characterisation setup described in Figure 6.13 was used in order to excite and detect fluorescence from the platform. Cleaving of the input waveguide and alignment of the chip in the system follows the procedure outlined in Section 5.5.3 for the refractometric sensor platform. In this case, the excitation source was a fiber pig-tailed laser diode (Thorlabs, λ = 635 nm, maximum output power = 8.64 mW) which was aligned to the input waveguide using the microscope as a visual guide.

In order to measure fluorescence from the platform, the microscope was moved to the sensor window of interest and focused precisely onto the surface of the waveguide. With the lab in complete darkness, the laser diode was switched on to maximum power, and at the same time the CCD camera was activated for fluorescence collection over a 10 s integration time. After the integration time, the laser diode was immediately switched off to minimise photobleaching of the labelled antibodies. This was repeated for each sensor window along the waveguide, in which different concentrations of antigen had been immobilised. The resulting images of fluorescence from each sensor window were saved in a high resolution file format (FITS) for analysis. The image J analysis package was used for this purpose, and image analysis comprised of defining a region of interest (ROI) box around the waveguide boundaries, and using the package to calculate the average pixel intensity in this ROI.

The signal from a window on the platform where no biomolecules had been immobilised was measured in the same way, and this signal was taken as the background. The background was subtracted from each signal in order to determine the signal originating only from the labelled antibodies. This was repeated over 4 separate waveguides, and the fluorescence intensity for each concentration

was evaluated in the same way. Due to differences between the input waveguide facet and coupling conditions for each waveguide tested, the fluorescence intensities on each waveguide were normalised by the background intensity value which was a good measure of the intensity of the excitation light in the waveguide. Uncertainty in fluorescence intensity for each antigen concentration was calculated taking the standard deviation of the repetitions of each concentration.

6.5.4.3 Results and Discussion

The results of the immunoassay are plotted in Figure 6.23. A 3 parameter sigmoidal logistic curve has been fitted to the data as is standard procedure for immunoassays [26], with the experimental data showing good correlation to the curve ($R^2 = 0.9997$). The curve displays the typical sigmoidal characteristic at the upper concentrations, where the change in fluorescence intensity decreases over a given concentration range, due to saturation of the receptors on the surface. The results demonstrate that μg/ml concentrations of biomolecules are easily detectable by this platform, even without significant optimisation of antibody immobilisation, and fluorescence detection systems, both of which are critical factors in the attainment of low limits of detection. This proof-of-principle assay demonstrated the capability of the platform to be employed as a biosensor, which was the main objective of this work.

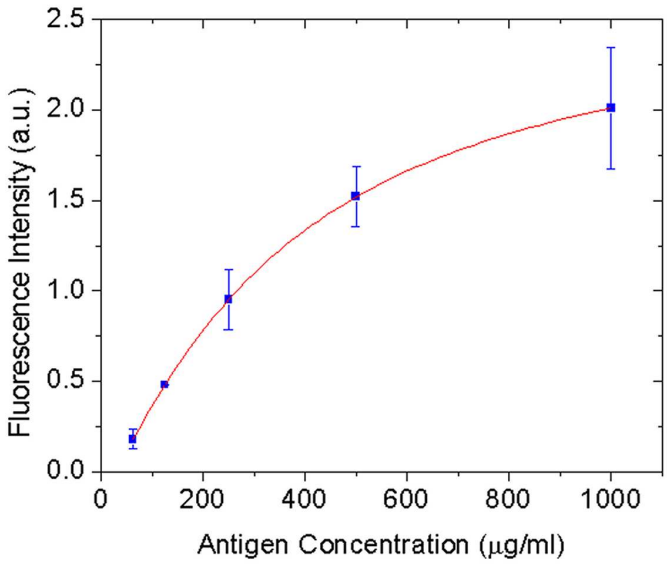

Figure 6.23: *Dose response curve for mouse IgG immunoassay*

6.6 Conclusion

This chapter describes the conception and design of biosensor platforms for the evanescent wave excitation of fluorescence from surface bound antibodies. In order to fabricate these platforms, the hybrid sol-gel materials and microfabrication techniques developed throughout this work have been employed. A characterisation system has been developed using piezo-controlled optical mounts for in-coupling of excitation light, with fluorescence detection carried out by a CCD camera coupled to an optical microscope. Surface functionalisation strategies were investigated, both for sol-gel surfaces, and for Ta_2O_5 coated surfaces, with the eventual choice of polyelectrolyte multilayers as the most appropriate option. For verification of the platform a mouse IgG immunoassay was carried out, achieving μg/ml detection levels which illustrates the enormous potential of this platform to address the needs for a low-cost, mass-producible, point-of-care testing platform.

Future work will include improvements to the platform itself, and the associated characterisation system. Platform improvements will focus on the development of an in-coupling strategy which does not require precise alignments of the excitation source to the platform. This is a critical requirement for employment of the platform in the target area of POC testing. Capture biomolecule immobilisation is another process step that will be examined and optimised further. This is a crucial step in any biosensor system, as the intensity of the fluorescence signal from the platform is dependent on the density of coverage of the capture biomolecules. Additionally, a dedicated fluorescence detection system must also be developed which will allow imaging of the entire platform in a one shot measurement. Further optimisation of the platform and detection system will allow extraction of a portion of fluorescence confined to the substrate in planar configurations. This is due to the anisotropic emission of fluorescence from surface bound fluorophores. The extraction of this portion of fluorescence will significantly improve the SNR of the platform.

References

[1] J. Homola, H. Vaisocherova, J. Dostalek, and M. Piliarik, "Multi-analyte surface plasmon resonance biosensing," *Methods*, vol. 37, pp. 26–36, 2005.

[2] M. J. O'Brien, V. H. Perez-Luna, S. R. J. Brueck, and G. P. Lopez, "A surface plasmon resonance array biosensor based on spectroscopic imaging," *Biosensors & Bioelectronics*, vol. 16, pp. 97–108, 2001.

[3] D. R. Shankaran, K. V. A. Gobi, and N. Miura, "Recent advancements in surface plasmon resonance immunosensors for detection of small molecules of biomedical, food and environmental interest," *Sensors and Actuators B-Chemical*, vol. 121, pp. 158–177, 2007.

[4] M. S. Wilson and W. Y. Nie, "Multiplex measurement of seven tumor markers using an electrochemical protein chip," *Analytical Chemistry*, vol. 78, pp. 6476–6483, 2006.

[5] M. S. Wilson and W. Y. Nie, "Electrochemical multianalyte immunoassays using an array-based sensor," *Analytical Chemistry*, vol. 78, pp. 2507–2513, 2006.

[6] J. M. Zen, Y. Y. Lai, H. H. Yang, and A. S. Kumar, "Multianalyte sensor for the simultaneous determination of hypoxanthine, xanthine and uric acid based on a preanodized nontronite-coated screen-printed electrode," *Sensors and Actuators B-Chemical*, vol. 84, pp. 237–244, 2002.

[7] B. G. Healey, L. Li, and D. R. Walt, "Multianalyte biosensors on optical imaging bundles," *Biosensors & Bioelectronics*, vol. 12, no. 6, pp. 521–529, 1997.

[8] F. J. Steemers and D. R. Walt, "Multi-analyte sensing: From site-selective deposition to randomly-ordered addressable optical fiber sensors," *Mikrochimica acta*, vol. 131, no. 1-2, pp. 99–105, 1999.

[9] D. R. Walt, "Molecular biology - bead-based fiber-optic arrays," *Science*, vol. 287, pp. 451–452, 2000.

[10] J. P. Golden, C. R. Taitt, L. C. Shriver-Lake, Y. S. Shubin, and F. S. Ligler, "A portable automated multianalyte biosensor," *Talanta*, vol. 65, pp. 1078–1085, 2005.

[11] C. A. Rowe, L. M. Tender, M. J. Feldstein, J. P. Golden, S. B. Scruggs, B. D. MacCraith, J. J. Cras, and F. S. Ligler, "Array biosensor for simultaneous identification of bacterial, viral, and protein analytes," *Analytical Chemistry*, vol. 71, pp. 3846–3852, 1999.

[12] F. S. Ligler, C. R. Taitt, L. C. Shriver-Lake, K. E. Sapsford, Y. Shubin, and J. P. Golden, "Array biosensor for detection of toxins," *Analytical and Bioanalytical Chemistry*, vol. 377, pp. 469–477, 2003.

[13] C. A. Rowe-Taitt, J. P. Golden, M. J. Feldstein, J. J. Cras, K. E. Hoffman, and F. S. Ligler, "Array biosensor for detection of biohazards," *Biosensors & Bioelectronics*, vol. 14, pp. 785–794, 2000.

[14] C. A. Rowe-Taitt, J. W. Hazzard, K. E. Hoffman, J. J. Cras, J. P. Golden, and F. S. Ligler, "Simultaneous detection of six biohazardous agents using a planar waveguide array biosensor," *Biosensors & Bioelectronics*, vol. 15, pp. 579–589, 2000.

[15] K. E. Sapsford, M. M. Ngundi, M. H. Moore, M. E. Lassman, L. C. Shriver-Lake, C. R. Taitt, and F. S. Ligler, "Rapid detection of foodborne contaminants using an array biosensor," *Sensors and Actuators B-Chemical*, vol. 113, pp. 599–607, 2006.

[16] M. Sanchez-Carbayo, L. C. Shriver-Lake, C. Cordon-Cardo, and F. S. Ligler, "Multianalyte biosensor for bladder cancer diagnostics," *Journal of Urology*, vol. 175, pp. 316–317, 2006.

[17] "NRL press release.", http://www.nrl.navy.mil/pressRelease.php?Y=2004R=26-04r, 2008

[18] J. Tschmelak, G. Proll, J. Riedt, J. Kaiser, P. Kraemmer, L. Barzaga, J. S. Wilkinson, P. Hua, J. P. Hole, R. Nudd, M. Jackson, R. Abuknesha, D. Barcelo, S. Rodriguez-Mozaz, M. J. L. de Alda, F. Sacher, J. Stien, J. Slobodnik, P. Oswald, H. Kozmenko, E. Korenkova, L. Tothova, Z. Krascsenits, and G. Gauglitz, "Automated water analyser computer supported system (AWACSS) part I: Project objectives, basic technology, immunoassay development, software design and networking," *Biosensors & Bioelectronics*, vol. 20, pp. 1499–1508, 2005.

[19] J. M. Ruano, A. Glidle, A. Cleary, A. Walmsley, J. S. Aitchison, and J. M. Cooper, "Design and fabrication of a silica on silicon integrated optical biochip as a fluorescence microarray platform," *Biosensors & Bioelectronics*, vol. 18, pp. 175–184, 3 2003.

[20] G. R. Hadley, "Wide-angle beam propagation using pade approximant operators," *Optics Letters*, vol. 17, pp. 1426–1428, 1992.

[21] S. Pissadakis, A. Ikiades, C. Y. Tai, N. P. Sessions, and J. S. Wilkinson, "Submicron period grating structures in Ta_2O_5 thin oxide films patterned using UV laser post-exposure chemically assisted selective etching," *Thin Solid Films,*, vol. 453-454, pp. 458–461, 4/1 2004.

[22] K. Schmitt, K. Oehse, G. Sulz, and C. Hoffmann, "Evanescent field sensors based on tantalum pentoxide waveguides - a review," *Sensors*, vol. 8, pp. 711–738, 2008.

[23] G. L. Duveneck, M. Pawlak, D. Neuschafer, E. Bar, W. Budach, and U. Pieles, "Novel bioaffinity sensors for trace analysis based on luminescence excitation by planar waveguides," *Sensors and Actuators B-Chemical*, vol. 38, pp. 88–95, 1997.

[24] C. Glasenapp, W. Monch, H. Krause, and H. Zappe, "Biochip reader with dynamic holographic excitation and hyperspectral fluorescence detection," *Journal of Biomedical Optics*, vol. 12, no. 1, 2007.

[25] G. Decher, "Fuzzy nanoassemblies: Toward layered polymeric multicomposites," *Science*, vol. 277, pp. 1232–1237, 29 1997.

[26] J. W. A. Findlay and R. F. Dillard, "Appropriate calibration curve fitting in ligand binding assays," *AAPS Journal*, vol. 9, no. 2, pp. E260–E267, 2007.

Chapter 7

Thermo-Optical Switches

7.1 Introduction

Optical switch components are essential for the widespread deployment of all-optical networks, and are necessary to solve the bandwidth restrictions of current telecommunications networks. This chapter presents the development of optical switching solutions, exploiting the high thermo-optic coefficient of hybrid sol-gel materials. The state of the art for optical switching is first described, followed by the principles of operation of the switches developed here. Simulation studies have been carried out in order to specify the PLC design of the switches. Also, a temporal analysis of heat flow through the waveguide cross section is presented, from which switching time predictions were made. The microfabrication process utilises a sol-gel formulation and the mask alignment technique in order to form both the optical circuits and the thin film metal heaters/electrodes. The development of a methodology for attachment of the metal films to the surface of the protective layer is described. Finally, switch characterisation is reported showing measurements of crosstalk, switching time and power consumption.

7.2 State of the Art

A large variety of techniques have been developed in recent years in order to satisfy the requirements for all-optical switching technology. This is particularly relevant in present-day telecommunications networks, where increasing demand for bandwidth is driving fiber optical communications closer toward the end-user. Many of the multinational companies have been involved in development of various technological solutions since the mid- to late-1990's.

MEMS (Microelectromechanical Systems) based switches have been investigated by a large number of companies including Alcatel-Lucent, Analog Devices and Nortel Networks. They consist of micro-scale hinged mirrors the movement of which is controlled by electric or magnetic fields, in order to divert light into a number of different output ports [1]. Though they have proven performance, they are more expensive to manufacture than other less complicated structures, and their high-speed performance is not necessary in every application, such as protection and restoration switching.

Bubble switches are a novel mixture of integrated optics and microfluidics, in which a bubble of high refractive index liquid moves back and forth in a liquid-filled microfluidic channel that crosses two intersecting waveguides. When the bubble is present total internal reflection causes diversion of light into one output, when the bubble is moved away the liquid present in the channel allow light to pass straight through, into the other output. This technology has been pioneered mainly by Agilent [2], but like MEMS based systems, physically moving parts are sometimes viewed with suspicion in industry, where solid-state solutions are generally preferred [1].

Some of the preferred solid-state solutions employ switchable holograms [3] and Bragg gratings [4], using electro- and acousto-optic materials respectively. High loss is a challenge typically associated with holographic switches, while acousto-optic switches are typically bulkier than competing technologies with intensity crosstalk being a particular problem [5]. Other solid-state solutions focus on the use of PLC-based devices exploiting the thermo- or electro-optic properties of materials. The main electro-optic materials are lithium niobate ($LiNbO_3$) and polymers [5]. Polymers have a high electro-optic coefficient but this is not stable. $LiBbO_3$ has a lower but stable electro-optic coefficient, and is widely employed when its high switching speed is needed [6]. Thermo-optic solutions are often based on lower cost technologies and materials including polymer, sol-gel and silica. Though the switching speed is typically in the millisecond regime, due to lower costs, thermo-optic modulation is preferable in applications where ultra-high switching speed is not a requirement.

The main switching technologies have been outlined above. At present, however, none of these are yet firmly established for widespread use in networks. The key question is which of these technologies will deliver critical requirements such as scalability, switching speed, reliability, low light losses, cost, and power consumption. It is likely that there will not be a single winning technology, because

all-optical switches are likely to be used in a very wide range of applications. As a result, some switching fabrics will win acceptance in equipment like large-scale optical cross-connects, while other technologies will turn out to be more appropriate for optical add-drop multiplexers or gear used in metro rather than long-haul networks.

The high thermo-optic coefficient of the hybrid sol-gel materials developed in this project enables the development of a mass-producible and low-cost switching platform addressing the need for protection and restoration switches as the current optical-electrical-optical components reach their limitations.

7.3 Thermo-optic Coefficient

The strong thermo-optic response of the hybrid sol-gel material is the key characteristic that makes this class of materials suitable for use in optical switch fabrication. The thermo-optic coefficient (TOC) quantifies the change in refractive index of the material per unit temperature change. The material characteristics that dictate the size and sign of the TOC are predominantly the density and the electronic polarisability change with temperature [7] such that

$$\frac{dn}{dT} = f(n)(\Phi - \beta) \tag{7.1}$$

where Φ is the temperature coefficient of the electronic polarisability, β is the volume expansion coefficient, and f(n) is defined as

$$f(n) = \frac{(n^2 - 1)(n^2 + 2)}{6n} \tag{7.2}$$

From equation 7.1 it can be seen that if the electronic polarisability term is dominant, the refractive index increases with temperature. On the other hand, the TOC is negative if the thermal expansion term is dominant. For organic polymers, the electronic polarisability term is negligible and therefore their high negative TOCs depend almost exclusively on their volume expansion term. Similar TOC values have been recorded for hybrid sol-gel materials [7–9], facilitating the use of these materials for thermo-optic devices.

7.4 Optical Circuits

7.4.1 Mach-Zehnder Switch

7.4.1.1 Switch design

The primary switch design is based on the well-known Mach-Zehnder interferometer configuration and is illustrated in Figure 7.1. This design may be divided into five sections:

Section 1: The incident light signal to be switched is coupled into an input waveguide (in this case consider light injected into input waveguide A).

Section 2: The light is incident on a splitter. The splitter chosen here is a directional coupler splitter, which consists of two equivalent waveguides in close proximity to one another. Here light carried by one waveguide can couple into the adjacent waveguide by means of its evanescent field, which overlaps with the mode profile of the adjacent waveguide. After a certain length of propagation, half of the light has coupled into the adjacent arm, thus splitting the input light into two parts of equal intensity (see Section 2.4 for electromagnetic theory of directional couplers).

Section 3: One part of the light travels in the reference arm of the interferometer and is not subject to any perturbations. The second part travels in the heater arm of the interferometer where the phase can be altered (via the thermo-optic effect) by heating of the thin film electrode.

Section 4: The light from the reference and heater arms coincides again in this section which consists of another directional coupler (identical to that in section 2). Here, the light is recombined and depending upon the phase change introduced in section 3, it is distributed in different ratios between the two output waveguides. For a particular applied phase change, all of the light can be switched from the output waveguide B to waveguide A.

Section 5: The final section consists of the two output waveguides (A and B),

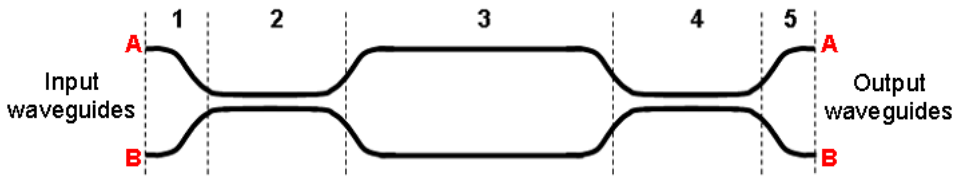

Figure 7.1: *Schematic diagram of Mach-Zehnder configuration switch*

which lead to separate network paths.

7.4.1.2 Directional coupler design

One of the most critical aspects of the MZ-switch design is the length of the directional couplers. This is an extremely sensitive parameter with regard to the amount of light lost in switching. Indeed 100% amplitude modulation is achieved only if the coupling length is specified exactly. For equal splitting of the input signal, the length (L) of the directional coupler is defined by,

$$L = \frac{L_c}{2} \tag{7.3}$$

where L_c is the coupling length defined by equation 2.56. Since the L_c is a difficult parameter to accurately calculate using analytical expressions, numerical methods have been employed here for the coupling length determination and will be shown in section 7.5. In design of the directional couplers, the objective is to minimise the extinction ratio. The extinction ratio is defined as,

$$\text{Extinction ratio} = 10\log_{10}\frac{P1}{P0} \tag{7.4}$$

where P1 is the power transmitted by the desired output port, and P0 is the parasitic power that is lost through the other output port. Ideally P0 = 0 giving an extremely low extinction ratio and a high performance switch.

7.4.1.3 Phase evolution

Application of heat in the heater arm of the switch results in a change in the refractive index of the single-mode waveguide in this arm (via the thermo-optic effect). This refractive index shift changes the optical mode of the waveguide, thus slowing the light travelling in the waveguide of the heater arm. The slowing of light in the heater arm introduces a phase difference between this and the reference arm.

The phase of light incident on the directional coupler in section 4 is a critical parameter in the determination of the interference pattern formed between the two arms of the directional coupler, and therefore it determines how light is divided between the output waveguides in section 5. The exact analysis of devices based on directional couplers usually requires solution of the coupled-mode equations numerically, which will be presented in Section 7.5. However, in order to

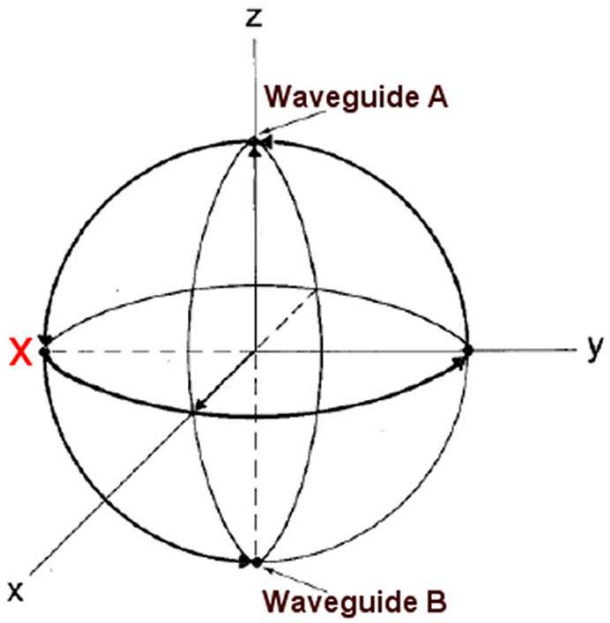

Figure 7.2: *Three-space representation of light behaviour in the MZ optical circuit [10]*

formulate a more intuitive understanding of the evolution of both magnitudes and phases of light in both waveguide arms of the system, the approach of Korotky will be employed [10]. This approach makes use of a three-dimensional graphical representation in order to illustrate clearly the transfer characteristics of coupled systems, and is particularly suited to the Mach-Zehnder interferometer configuration. Using Figure 7.2 as an aid, consider the path of light through the switch under conditions of equal phase and then phase mismatch.

Sections prior to phase mismatch: Initially, if the light power is injected into waveguide A, this is represented in Figure 7.2 as a point at the north pole. After having traversed the first directional coupler in section 2 (see Figure 7.1) the light is split with equal power in both arms. However, the relative phase of the fields is 90°apart. Therefore, the state entering the heater arm in section 3 is described by the point on the equator (point X) in the -y direction. This point represents an equal intensity in the waveguide A and B, but a 90°phase shift of light in waveguide B relative to A.

No phase mismatch: If no phase change is applied by the heater, the directional coupler in section 4 will behave as the one in section 2, continuing to rotate the state vector in the counter-clockwise direction. At the output of the directional coupler the light is all in waveguide B, as represented in Figure 7.2 where the state vector is now pointing at the south pole. This represents a total phase change of 180°in traversing the two directional couplers.

Phase mismatch: If a phase change of π is applied by the heater in section 3, the

state vector is rotated about the z-axis (from -y to +y in the equatorial plane), by the action of the induced $\Delta\beta$. Now, when incident on the directional coupler in section 4, the state vector is once again rotated about the x-axis in an counter-clockwise direction as previously described. This brings the state vector back to its starting position at the north pole. Therefore, a phase change of π results in the input signal appearing at output waveguide A.

7.4.2 MMIC Switch

7.4.2.1 Design

Though the main focus of switch design and development was devoted to the Mach-Zehnder design, an extension of this work involved brief investigation into the replacement of directional coupler optical splitter in the MZ-design with multi-mode interference couplers. The theory presented in section 2.3 shows how an MMICs can be used to split light from a single input waveguide into multiple self-images which have equal intensity. From a functional perspective the design as shown in Figure 7.3 works in the same way as the MZ-switch; a single input arrives at one of the input waveguides to the MMIC power splitter. After it traverses the MMIC it is split into equal intensity images, which are then subject to phase shifting in the interferometer arms via the thermo-optic effect. Finally, the phase shifted light is recombined in the final MMIC where the interference properties of the coupler cause the reappearance of the input signal at one of the output ports (which port depends upon the phase shift applied). The state of the light at the end of the MMIC power splitter is analogous to that at the end of the directional coupler splitter; images of same intensity but different phase.

In order to achieve switching between the four outputs of the design shown, the application of appropriate phase shifts in the heater array is subject to strict criteria [9]. These criteria were used in order to direct the design of the novel heater circuit of this design, where a single electrical signal (i.e. the heaters are

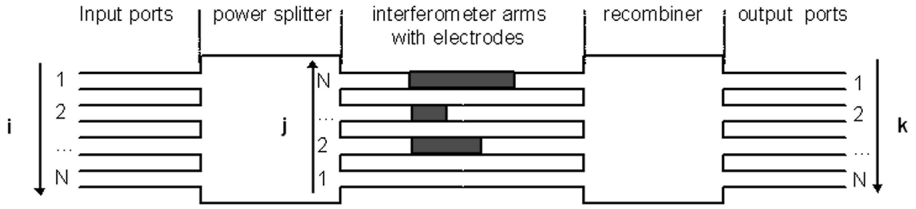

Figure 7.3: *4x4 MMIC switch schematic*

connected in series) can cause different phase shifts in each arm because each heater arm has a different length. Switching between output states is achieved by applying different a drive voltage to the heater circuit.

7.5 Simulation

7.5.1 Single-mode Waveguides

In order to carry out simulations of the switch behaviour, the first step was to determine the material and structural parameters of the single-mode waveguides upon which the devices would be based. Using the sol-gel material described in section 4.3.4.1, a guiding layer refractive index of 1.50 was measured. In order to fabricate single-mode waveguides with this material as the core, simulations (see Figure 7.4) showed that a core geometry of 6 x 6 μm was necessary, with the refractive index of the surrounding layers (buffer layer underneath and protective layer on the sides and top of the waveguide core) equal to 1.49, giving a Δn value of 0.01.

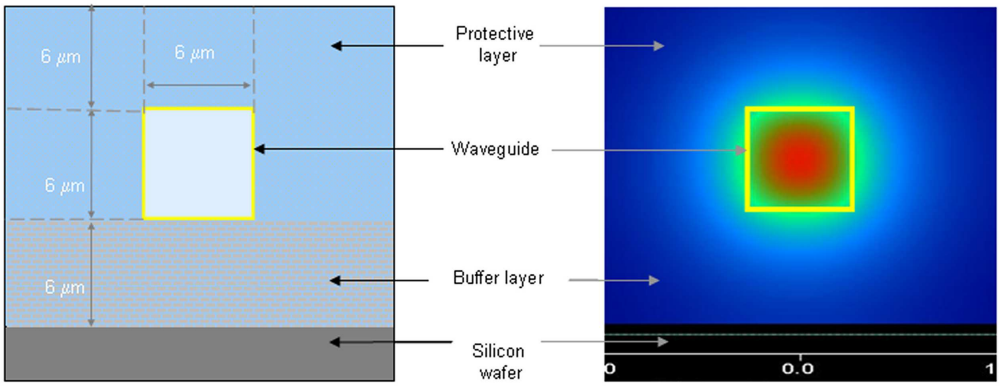

Figure 7.4: *a) Transverse structure of single-mode waveguides used for PLCs, b) simulated electric field profile of the single-mode waveguide*

7.5.2 Directional Coupler Splitting Ratio

The 3D BPM method was employed in order to determine the length of the directional couplers needed for equal power splitting. A discretisation of 0.25, 0.28 and 1 μm was used in the x, y and z directions respectively. A typical BPM simulation image is shown in Figure 7.5 showing equal splitting between the two output waveguides as desired. Investigations focussed on the determination of

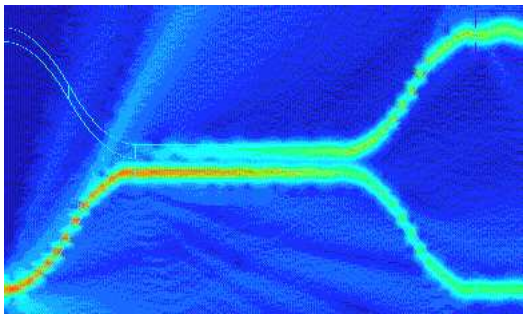

Figure 7.5: *BPM simulation image showing equal division of light at the outputs of a directional coupler*

the directional coupler length when the waveguides were separated by 4 μm (as this was the separation on the photomask). The splitting ratio was recorded for a number of simulations where the length was varied and the result is shown in Figure 7.6. The optimal directional coupler length from these data is 3726 μm.

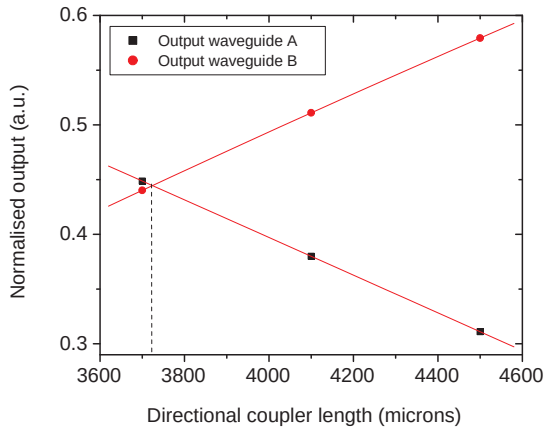

Figure 7.6: *Simulation data showing the effect of directional coupler length on intensity in the two output waveguides (A and B) for a 4 μm waveguide separation*

7.5.3 Effect of Heating the Single-mode Waveguide

The OlympIOs cross-sectional mode solver also contains a temperature module, which permits calculation of refractive index change (Δn_T) of a waveguide structure upon application of specific steady-state temperatures (see Appendix A for more details). This (Δn_T) value can be exported from the software and utilised to carry out BPM simulations of the switch behaviour at different applied temperatures, as will be shown in the next section. In the initial thermal simulations of the cross-section it was found that, regardless of the thermal parameters used for the

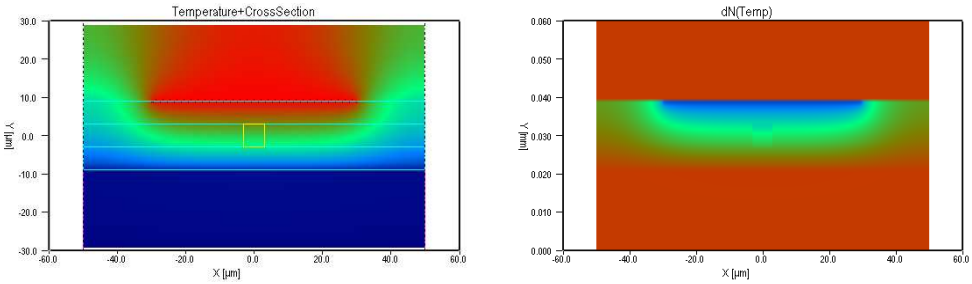

Figure 7.7: *Steady state temperature profile of the cross-sectional structure*

various sol-gel layers (thermal conductivity and heat capacity), the steady-state (Δn_T) was approximately the same even when extreme values were employed. Thus, it was concluded that the materials thermal properties do not have significant influence in the steady-state response of the waveguide to the applications of a specific temperature. However, the temperature module also facilitates calculation of heat flow in the defined cross-sectional structure as a function of time - the transient response of the system. Observations of the transient behaviour of heat flow indicate that the thermal parameters impact upon the power consumption of the switch and the switching time between output states (dictated by the time taken to reach the target temperature).

7.5.4 Steady-state Switch Output Behaviour

The steady-state switch output was simulated by first defining the Mach-Zehnder switch structure represented in Figure 7.1, in the 3D BPM software interface. Then steady-state thermal simulations were carried out on the waveguide cross-section (as depicted by Figure 7.7) for different applied temperatures. These refractive index changes were exported from the cross-sectional mode solver, and then imported into the 3D BPM software where they were superimposed on the heater waveguide arm, enabling simulation of the switch response at different applied temperatures. The response from each switch output as a function of applied temperature is shown in Figure 7.8. From this data, an applied temperature difference of 20K is necessary in order to switch the light from output B to output A.

Estimation of the expected switch power consumption was made using an expression derived by Hida et al [11] for a Mach-Zehnder switch configuration such

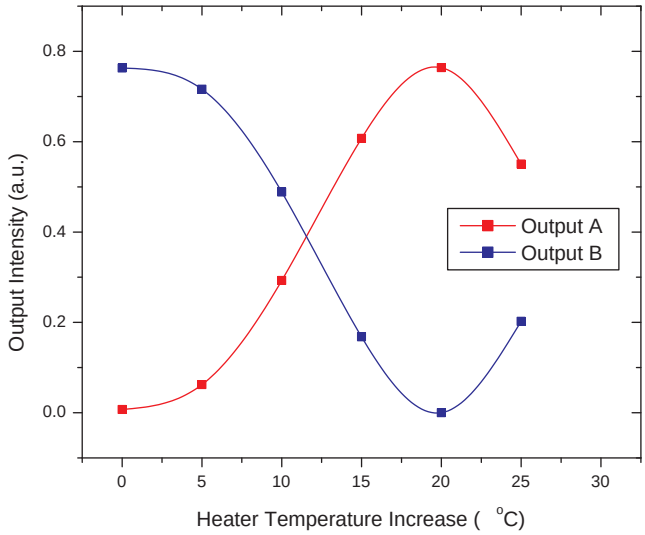

Figure 7.8: *Output as a function of temperature*

as the one described, in which the switching power P is expressed as

$$P = \frac{\lambda \kappa_W \left(\frac{W_H}{t_W} + 0.88 \right)}{\left| \frac{\partial n}{\partial T} \right|} \tag{7.5}$$

where λ is the wavelength of 1.31μm, κ_W is the thermal conductivity value of the sols estimated to be approximately 0.16 W/(m.K), W_H is the heater strip width of 100 μm, t_W is the height of sol-gel material between the silicon substrate and the heater which is 18μm in this design, and finally $\partial n/\partial T$ is the TOC of the guiding layer films which is -1.5x10^{-4} K^{-1}. Using these parameters in Equation 7.5, an extremely low power consumption of 8.4mW was calculated which compares very favorably with other reported power consumption values, particularly those of silica based thermo-optic switches where a classical thermo-optic switch needs from 400 to 700 mW heater power for switching, and even complicated designs which have been optimised for lower power consumption [12] do not compete with the power consumption calculated here.

7.5.5 Transient Switch Response

7.5.5.1 Variation of material thermal parameters

The primary aim of this section is to investigate how the transient response of the switch varies as a function of the material and structural properties of the waveguide cross-section. The response time of the switch is directly related to the time taken for the material to reach the desired equilibrium temperature state. It has been established for the reference structure shown in Figure 7.4, that for total switching of light from one output to the other, an equilibrium temperature in the waveguide core of 9.85K must be reached. For this particular structure, this temperature was reached for an applied temperature of 20K at the heater which is on top of the protective layer. The metric that is widely used to quantify the response time of a transient system to a step input, is the time taken to reach 90% of the steady-state response (referred to as t_{90}) [13–15]. For all structures under consideration here, t_{90} was calculated and conclusions regarding the optimum parameters were drawn.

The data displayed in Figure 7.9(a) show the variation of temperature in the waveguide core over time for a variety of material thermal conductivity values. A value for the thermal conductivity of the hybrid sol-gel material could not be found in the literature. Therefore, a thermal conductivity estimate of 0.16 W/(m.K) has been selected as it is representative of a range of polymer materials, which have similar TOC values to that of they hybrid sol-gel. The general trend

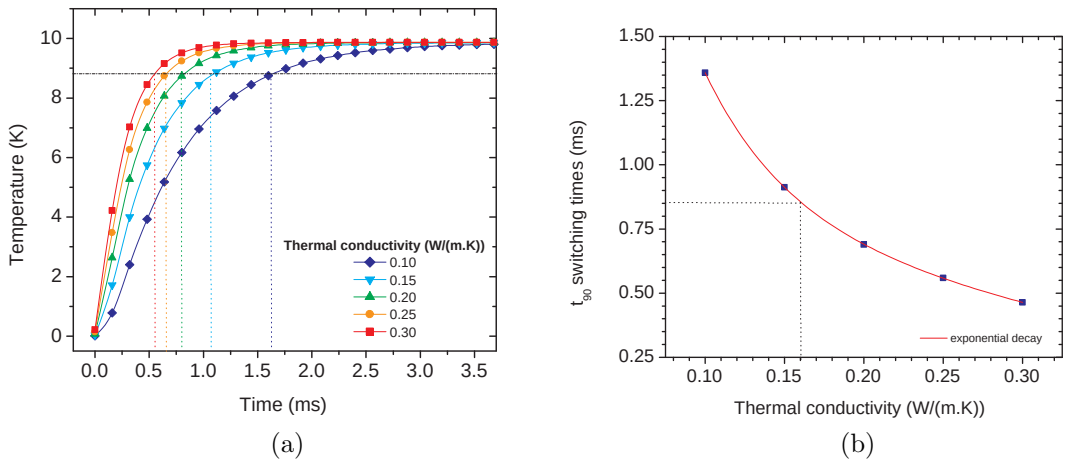

Figure 7.9: *(a) Waveguide core temperature versus time (applied temperature = 20K) for different material thermal conductivity values, and (b) t_{90} time of structure as a function of thermal conductivity.*

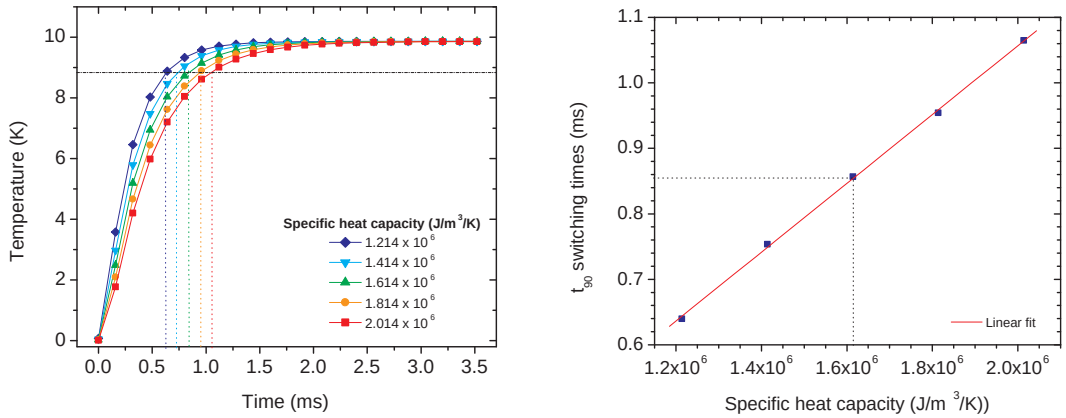

(a) (b)

Figure 7.10: *(a) Waveguide core temperature versus time (applied temperature = 20K) for different material specific heat capacity values, and (b) t_{90} time of structure as a function of specific heat capacity.*

that can be observed is that the lower the thermal conductivity value the slower the waveguide core temperature is to reach a steady-state condition. The t_{90} time for each thermal conductivity value has been extracted and displayed in Figure 7.9(b) where an exponential decay in t_{90} is evident with increasing thermal conductivity. Therefore we can conclude that materials with a higher thermal conductivity reach the equilibrium temperature needed for total switching at a quicker rate.

The variation of temperature in the waveguide core over time for a range of material heat capacity values is shown in Figure 7.10(a). t_{90} times have been extracted for each heat capacity value and plotted in Figure 7.10(b). It is clear that the variation in t_{90} is linear with respect to specific heat capacity. From these studies, the ideal switch material would combine a high thermal conductivity with a low specific heat capacity yielding low switching times. For the switch fabricated in this work, the estimated switching time is ~0.85 ms (assuming thermal conductivity of 0.16 W/(m.K) and heat capacity of 1.614 x 10^6) J/m^3/K.

7.5.5.2 Optimisation of the cross-sectional geometry

In this section, the cross-sectional geometry of the heater arm of the switch was varied in order to ascertain the optimal configuration for a fast response time. Having fixed the waveguide dimensions to obtain single-mode operation, the geometric parameters varied here were the buffer layer and the protective layer thicknesses. These parameters have an effect on how quickly heat flows through

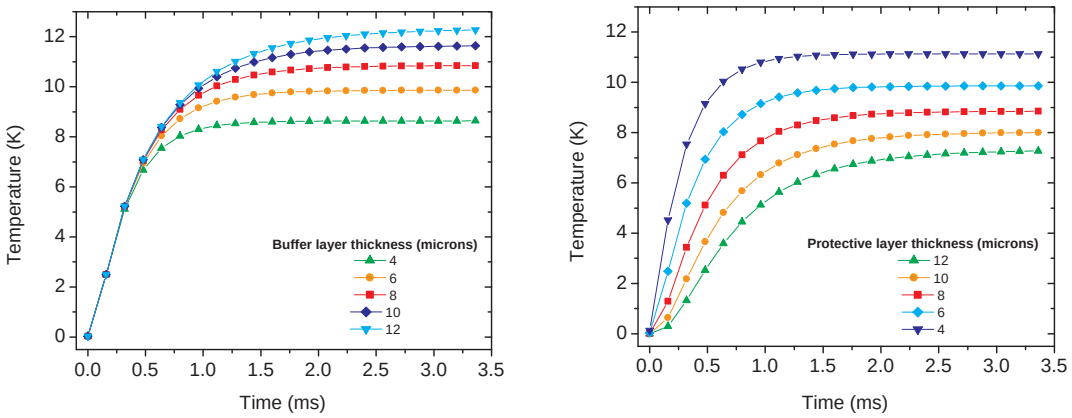

Figure 7.11: *Waveguide core temperature versus time (applied temperature = 20K) for various (a) buffer layer thicknesses, and (b) protective layer thicknesses.*

the structure, and therefore how quickly a steady-state condition is reached.

For application of a temperature of 20 K, as in the above simulations, Figure 7.11(a) shows how the temperature of the waveguide core varies as a function of time elapsed, for a range of BL thicknesses. The clear trend here is that as BL thickness increases, so does the maximum core temperature. It is notable, though, that the higher core temperatures reached for the thicker BLs take a longer time to stabilise.

In Figure 7.11(b), a range of PL thicknesses were simulated keeping the BL constant at 6 μm. Here, for the higher PL thicknesses simulated, both the maximum temperature reached, and the time taken to reach this temperature, are less than for thinner PLs. However, these results are not directly applicable to the switch structure as represented by the simulation in Figure 7.8 because the core temperature reached for each one of these different geometries deviates from the value of 9.85K, which has been shown to be necessary for total switching. Therefore, in order to accurately compare the effect of different geometries on switch performance, an adjustment of the applied temperature to each individual geometry must be carried out to achieve a stable waveguide core temperature of 9.85K in the steady-state. The method used to establish the applied temperature necessary for each geometry is illustrated for the case of BL=12 μm in Figure 7.12(a). From this graph, the asymptotic steady-state temperature at the waveguide core was determined for each of the applied temperatures. In Figure 7.12(b), the perfect linear relationship between core and applied temperatures is shown, and this relationship holds for all geometries simulated. This relationship

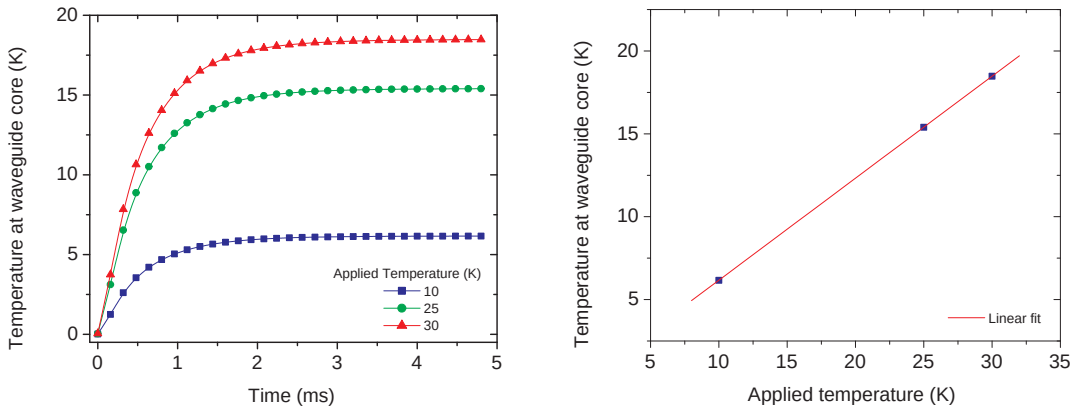

Figure 7.12: *For a cross-sectional geometry with BL=12µm; (a) Waveguide core temperature versus time elapsed for different applied temperatures, and (b) the relationship between waveguide core temperature and applied temperature.*

enabled the precise calculation of the applied temperature that would produce a core temperature of 9.85 K as desired for every geometry.

Utilising the method described, optimised temperatures for each geometry were calculated and transient simulations were carried out for a range of BL and PL thicknesses, as shown in Figures 7.13(a) and 7.13(b). It is clear that each of these plots reaches a steady-state value of 9.85K as specified, and with this data a direct comparison of the response time of each geometry is possible. t_{90} times were extracted from these data and graphed in Figure 7.14(a). It is immediately apparent that there are positive linear relationships between t_{90} response times and

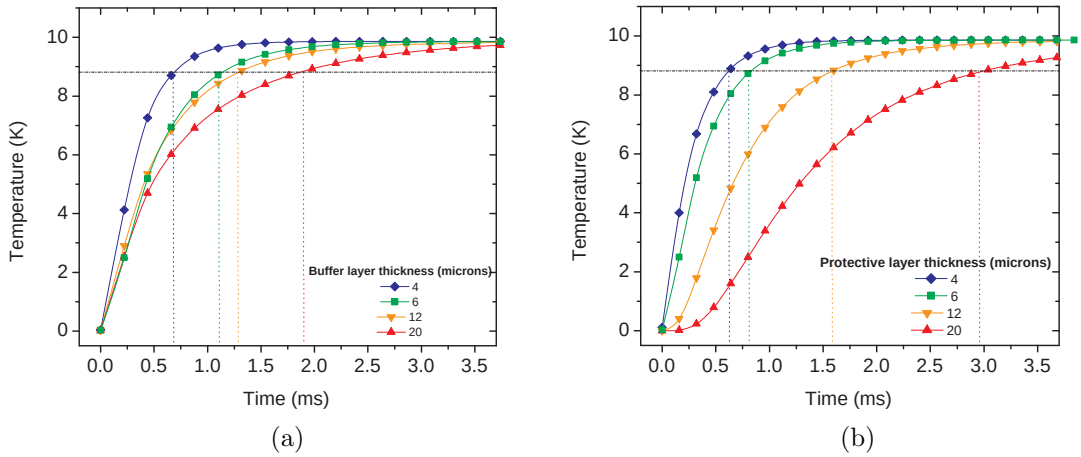

Figure 7.13: *Waveguide core temperature versus time elapsed for, (a) a range of BL thicknesses, and (b) a range of PL thicknesses (all matched to optimised applied temperatures).*

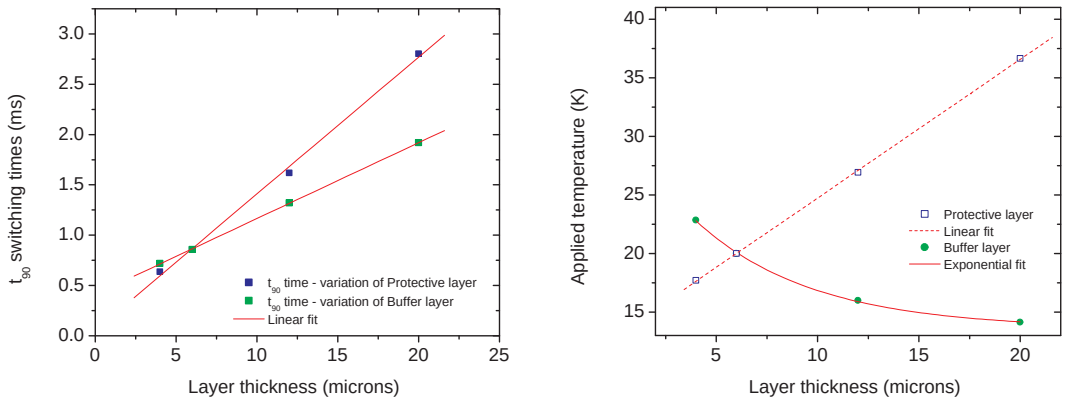

Figure 7.14: *(a) t_{90} time, and (b) applied temperature, both as a function of BL and PL layer thicknesses*

layer thickness for both BL and PLs. Therefore the fastest responding switches are to be found with the lowest possible BL and PL thicknesses. However, there are limitations to the thickness of these layers from an optical point of view, as they provide protection from the absorption of both the substrate and the heater materials. Despite this, the general trend shows that thinner BL and PLs result in low t_{90} response times.

Examination of Figure 7.14(b) shows that the applied temperature necessary for switching has a more complicated relationship with each of the layer thicknesses. For increasing PL thicknesses, there is a positive linear relationship with applied temperature. Therefore, a low PL thickness not only reduces the t_{90} response time of the switch, but it also impacts positively upon the power consumption, reducing the applied temperature needed for total switching. However, for a low BL thickness Figure 7.14(b) shows that a higher applied temperature is necessary for switching. Hence there is a trade-off to make here between low temperature/power consumption and low response time, which is dependent upon the required switch specifications. In most cases a response time of a few ms is sufficient for protection and restoration switching applications and so it would be preferable to reduce power consumption by maximising the BL thickness.

7.5.6 MMIC Switch

Simulation of the MMIC switch design was carried out by a colleague, Dr. Raphael Kribich, in order to specify device dimensions prior to fabrication. Figure 7.15 shows that, with careful design of heaters, it is possible to control the phases of

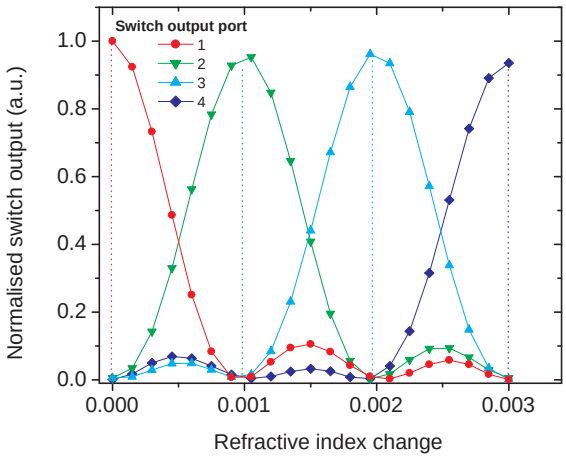

Figure 7.15: *Simulation data for the 4x4 MMIC switch design*

light in the waveguide array arms such that light will appear at only one output waveguide for a particular refractive index shift (via temperature change).

7.6 Experimental

In this section, experimental determination of the thermo-optic coefficient of the sol-gel materials is first presented. The experimental processes undertaken for the fabrication of the optical circuits and the thin film heaters are explained in detail. Characterisation of the fabricated switches is presented, giving rise to directions for future work.

7.6.1 Thermo-optic Coefficient Measurement

To characterise the thermo-optic response of the materials, the prism coupler instrument (described in Section 4.2.1) was fitted with an auto-controlled hot stage. This allows both the prism and the coupling head to be heated to a specified temperature, thus allowing heating of the thin film. The thermo-optic coefficient is obtained by recording the refractive index at a number of discrete temperatures over a wide range, and calculating the slope of the refractive index versus temperature plot.

Synthesis of the hybrid sol-gel materials used for thermo-optical switch development is reported in Section 4.3.4.1. Characterisation of the thermal response

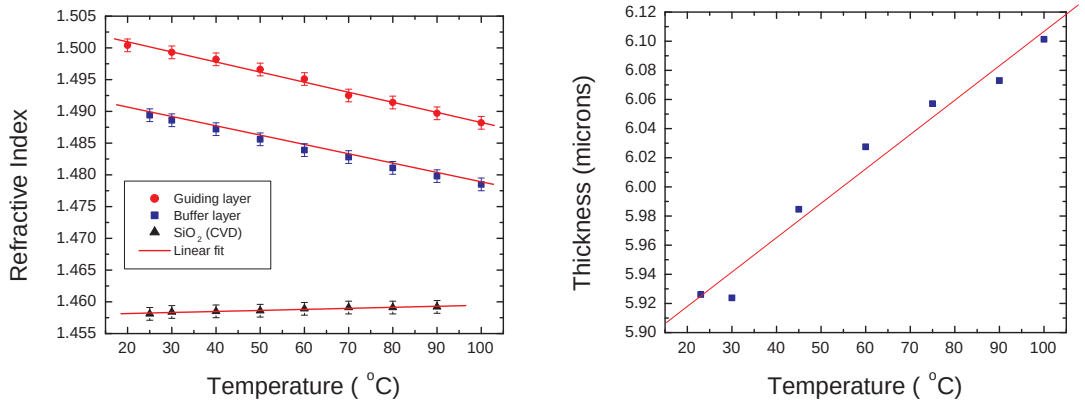

Figure 7.16: *(a) Refractive index response, and (b) thickness, both as a function of the hybrid sol-gel material temperature*

of both the buffer and guiding layer films is presented in Figure 7.6.1a. Thermo-optic coefficient (TOC) values of -1.46 x 10^{-4} K^{-1} and -1.57 x 10^{-4} K^{-1} were extracted from these data for the buffer and guiding layer materials respectively. Both of these TOCs are an order of magnitude higher than the TOC of silica ($+1.1$ x 10^{-5} K^{-1}), which has commonly been employed for thermo-optical switch fabrication. It is also notable that the TOC of the hybrid sol-gels is negative compared to the positive TOC of the silica. The reason for these negative quantities is attributable to the polymer-like behaviour of these materials, where the TOC is mainly due to thermal expansion of the material [7]. This is supported by the slight increase in film thickness noted in Figure 7.6.1b in response to increasing applied temperature.

7.6.2 Optical Circuit Fabrication

The hybrid sol-gel material used for thermo-optic switch fabrication was described in Section 4.3.4.1. This material was developed prior to the baseline material, and though they are similar in composition, they exhibit different physical properties which demanded slightly different processing conditions.

The fabrication process followed the generic process steps as outlined in section 4.1.5, that is; buffer layer coating and stabilisation, coating and UV-exposure of the guiding layer to form the optical circuits, and, protective layer deposition to encapsulate the optical circuit. The fabrication process first involved deposition of 3 ml of the buffer layer formulation at a spin-coating speed of 3000 rpm, in order to form a buffer layer of 6 μm thickness. Small bottles of IPA were placed

around the bowl of the spin-coater in order to reduce the evaporation of solvent from the layer during spin-coating which reduces coating defects as outlined in Section 4.5 (this method was employed until the optimised method described in Section 4.5 had been developed). After coating, the wafer was baked directly for 2 hours at 120°C. Compared to the baseline materials, the higher baking temperature reflects the lower amount of zirconium complex in this buffer layer sol. As a consequence, the coatings were wetter and more sticky, and therefore required a slightly higher temperature treatment for stabilisation.

After allowing time to cool, the guiding layer formulation was spin-coated also at 3000 rpm, and was then pre-exposure baked for 15 minutes at 120°C on a hotplate. This heat treatment is not necessary with the baseline material, again due to the lower wettness of the material. Damage to the photomask results if the film is not sufficiently dried.

The wafer was then UV-exposed through the photomask shown in Figure 7.17, for 5 minutes using the mask-alignment instrument at a power of 7.5 W. After exposure, the wafer was directly etched in an IPA bath for approximately 3 minutes, to remove the unexposed portions of the thin-film leaving behind the optical circuits. Finally, the protective layer was coated in two steps separated by a 5 minute baking step (120 °C), which was necessary to give sufficient physical toughness to the first layer, avoiding dissolution by the solvents in the second layer. Coating parameters were equivalent to those described for buffer layer coating. The application of two coatings ensured a 6 μm layer coverage on top of the waveguides. A final baking step of 120 °C for 2 hours ensured stabilisation

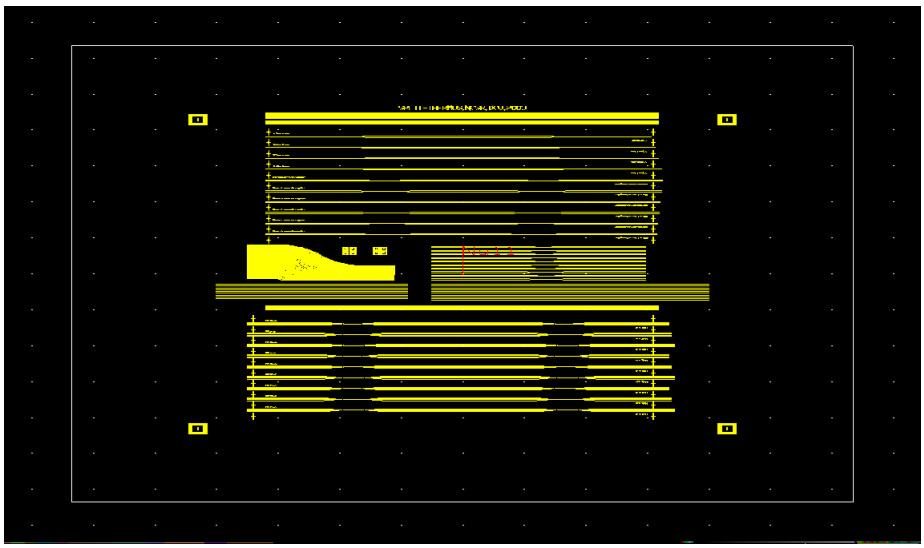

Figure 7.17: *Mask for patterning the optical circuits*

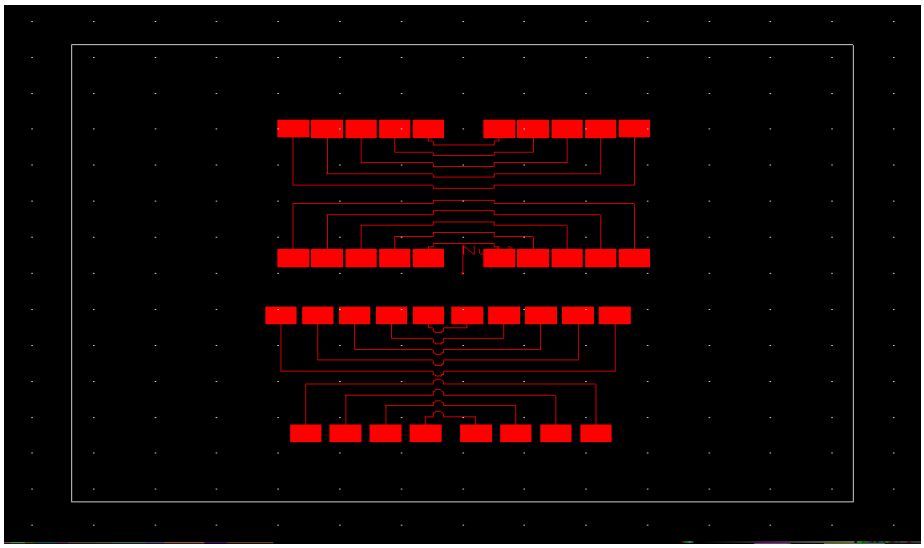

Figure 7.18: *Mask for patterning the heater circuits*

of the protective layer coatings.

7.6.3 Thin Film Heater Fabrication

The major development work pertaining solely to the thermo-optical switch was the development of a patterning and deposition process for the thin-film heaters, which are an integral part of the design. In this section, the full range of techniques and processes developed for thin film heater fabrication will be presented.

The development of thin film heaters was comprised of two interrelated steps. Firstly, methods to enhance the adhesion of the heater material to the top layer of the chip (protective layer) were developed. Secondly, in order to form the heater circuit patterns, processes for the use of photopatternable materials such as commercial photoresists and also sol-gel were developed. Through development, a number of improvements have been made to the process resulting in a substantial improvement in repeatability and yield.

The general techniques used throughout to carry out heater material deposition and evaluation of the strength of binding to the sol-gel protective layer surface are presented in the following section.

7.6.3.1 Techniques employed

This section comprises a brief description of the coating techniques for the heater material as well as the method in which bond strength between the sol-gel layer

and the heater material was determined.

Physical vapour deposition

Silver was chosen as the material for heater/electrode fabrication due to its resistance to oxidation [16], its stability in pure air and water [16, 17], its previously successful employment in this role [18] and given that it has the lowest cost of all precious metal contact materials [19]. On account of these factors, it provided an ideal choice for this initial proof-of-concept work. Physical vapour deposition was employed for deposition of the silver heaters and electrodes throughout this work. The term physical vapour deposition pertains to a variety of methods commonly used to deposit thin metal films by the condensation of a vaporized form of the material. In the initial stages of development electron-beam deposition was employed, using an Edwards Auto 306 instrument. This technique heats the material to be deposited to a high vapor pressure by electron bombardment in a high vacuum. At later stages, the more simple thermal evaporation technique was used, by which the deposition target was heated to a high vapor pressure by electrically resistive heating in a slightly lower vacuum than utilised for e-beam deposition. Both techniques produced similar results but the advantage of using the e-beam chamber was that two layers of different material could be deposited sequentially without the necessity to break the vacuum in order to change the deposition target.

Metal film adhesion testing

The silver coatings were tested extensively for adhesion to the protective layer surface via the scotch tape test. This involves first scoring the surface of the silver coated sample to divide the surface into a grid. This process forms a large number of edges, and so is an effective test of the ability of the silver to adhere to the surface at these edges. After scoring the surface, a piece of adhesive scotch tape is applied firmly to the surface avoiding bubbling of the tape. This is followed by the prompt removal of the tape in a swift movement with steady application of pulling force. Though this is not a quantitative technique, it provides a convenient and satisfactory means of assessing the adhesion characteristics of a thin metal film to the switch surface.

7.6.3.2 Photoresist-based patterning process

Photoresist patterning

The first process developed utilised a commercially available positive-tone photoresist (Shipley SPR220-7). This allowed the complete coverage of the chip except for areas that would be UV-exposed, where trenches for silver deposition were formed. This process is illustrated in Figure 7.19 steps 1-4. The photoresist was spin-coated at 3000 rpm for 30s, and then soft-baked at 115 °C for 2 minutes. Using the mask aligner, it was possible to align the second layer mask shown in Figure 7.18, with the alignment markers that had been defined during optical circuit patterning in the sol-gel guiding layer. Once alignment had been optimised the photoresist layer was UV-exposed for 70s. After 1 hour of exposure to air

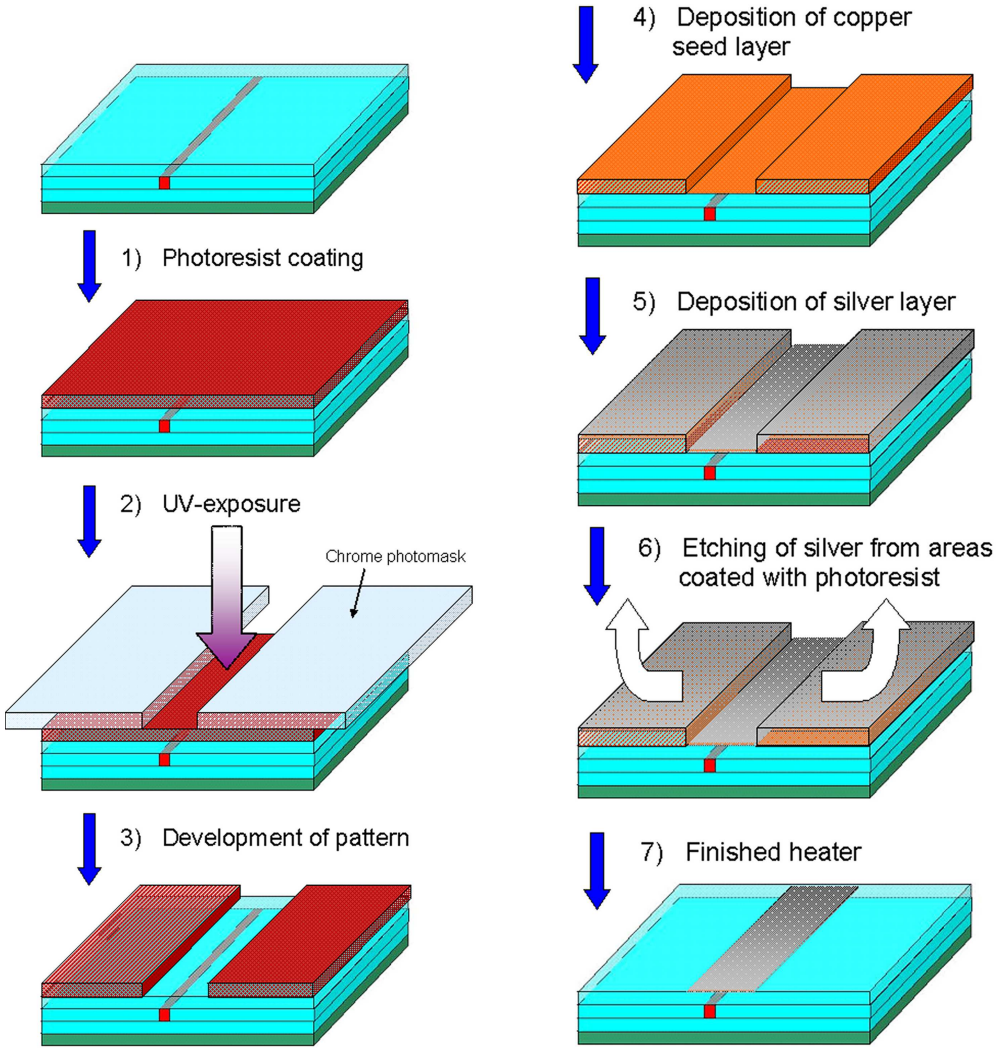

Figure 7.19: *Process schematic for the deposition of thin film heaters using the SPR220-7 positive-tone photoresist as a patterning medium*

(to aid the development process by allowing the diffusion of water back into the layer), the photoresist was developed (using the developer MF-26A) in order to etch away the exposed parts leaving the patterned trenches for silver deposition.

Heater deposition

Initial trials of silver deposition were carried out on unpatterned protective layer samples. Immediately, it was clearly apparent that silver adhesion to the sol-gel surface was extremely poor, the silver could be wiped off simply by using a finger. To address this, an intermediate seed layer was required to anchor silver to the substrate. Titanium was tried at first, and deposition was carried out by means of electron-beam evaporation. However, the results with titanium were erratic, so a ∼20nm copper seed layer was tested instead. This provided more consistent results than titanium, as titanium is more difficult to coat repeatably. The difficulty was due to its high vapor temperature which tended to cause problems with degassing of the holder (carbon), causing an increase in pressure within the chamber. With use of the copper seed layer, it was no longer possible to simply rub away the silver that had been deposited on top of the copper. However, the results of the scotch tape test were not excellent, with patchy adhesion of the metal layers (∼20-40% was the average coverage remaining after test). However, the result was significantly better than the use of silver alone, and so this method was employed for switch fabrication.

Having patterned the chip with photoresist as described in section 7.6.3.2, the remaining process steps as depicted in Figure 7.19 steps 5-8 were carried out beginning with copper seed layer/silver deposition by e-beam deposition. After blanket metal deposition on the chip, the metal-coated photoresist areas needed to be etched away as shown in Figure 7.19 step 6, revealing the pattern of heaters/electrodes. The positive-tone photoresist stripping solution SVC-175 was used. In order to effectively remove the photoresist the solution was placed in a petri dish and heated to a temperature of ∼65 °C on a hotplate. A major problem was observed here as it was found that although the copper seed layer improved adhesion, the removal of the photoresist which was covered with a continuous layer of metal resulted in tearing away parts of the heater circuit as well. This was due to the insufficient bond strength of the metals to the sol-gel surface. Despite this problem of repeatability, it was possible to fabricate a number of chips in this way - though the yield from the process was extremely low.

7.6.3.3 Development of an intermediate silver binding layer

A number of iterative improvements to the thin film heater fabrication process are presented in this section. Building upon the conclusions from the previous sections, a new strategy to anchor silver to the surface of the protective layer was developed. This strategy involves the deposition of an intermediate binding layer (hereafter referred to as the "binding layer") directly onto the protective layer surface before coating with silver.

Synthesis and coating of the binding layer

The binding layer was synthesised via a sol-gel process first involving the hydrolysis of the precursor 3-Mercaptopropyltrimethoxysilane. This precursor was chosen because it contains thiol groups which are able to form a strong covalent bond with silver, and at the same time it was found to bind strongly with the protective layer surface. Absolute ethanol was added to the solution after 1 hour of aging to ensure that viscosity was kept low so that sub-micron layer thicknesses could be achieved. After 45 minutes of stirring, the nanoparticulate zirconium complex (synthesis found in section 4.3.1) was added to the pre-hydrolysed solution. This was added because it was found to enhance the coating properties of the sol, giving thin layers of high-uniformity and adhesion to the surface of the protective layer. The intermediate binding layer was deposited by dip-coating at a speed of 3 mm/s. Then the samples were baked in an oven at 100 °C for 30 minutes in order to dry them.

Evaluation of the coatings

Silver films were deposited onto the "binding layer" coated samples as described above. The silver coatings were tested extensively via the scotch tape test described in section 7.6.3.1. All of the silver-coated samples under test withstood de-adhesion over the entire surface. Tests were carried out both by depositing the binding layer directly onto silicon pieces, and by depositing onto protective layer coated pieces. The scotch tape test on the directly coated silicon pieces showed absolutely no de-adhesion. On the protective layer coated samples, the only de-adhesion that occurred was of the protective layer from the silicon wafer, thereby illustrating that the bonds anchoring the binding layer to the protective layer on one side, and to silver on the other side, were both stronger than the bond between protective layer and silicon wafer.

Integration of binding layer with previous process

In order to integrate the use of the new binding layer with the process as described in Figure 7.19, it was necessary to insert a new process step prior to the deposition of the photoresist (step 2), for the deposition and stabilisation of the binding layer. This was carried out as described above, and silver was successfully coated onto the patterned surface using thermal evaporation. However, scotch tape testing of the silver deposited onto this surface showed that the adhesion to the binding layer was very poor, with all of the deposited silver easily removed. Tests revealed that the adhesion of silver to the binding layer was degraded after the binding layer had first been covered with the SPR220-7 photoresist. After similar tests, none of the other chemical compounds involved in the process (MF-26A photoresist developer, SVC-175 positive photoresist stripper, or IPA) were found to cause a degradation in the performance of the coating. It is difficult to specify the exact mechanism by which the binding layer reacts with SPR220-7 because the composition of SPR220-7 is a trade secret. However, it appears evident that the reactive thiol groups are involved in the reaction and so are unavailable for subsequent reaction with silver. Therefore, it was clear that this binding layer could not be used directly in conjunction with the SPR220-7 photoresist.

7.6.3.4 Development of optimised process

In order to exploit the excellent adhesion of silver to the sol-gel surface via the binding layer developed in the last section, an alternative to the SPR220-7 process for creating the heater/electrode patterns was developed. This involved use of a commonly available photoresist, SU-8. Since SU-8 is a negative-tone photoresist, as opposed the positive tone photoresist used before, the process needed to be modified. The new process is depicted in Figure 7.20, where initially a blanket layer of silver is deposited on top of the binding layer. Then the areas to be patterned for heaters/electrodes are masked off so that the rest of the silver layer can be removed. The standard photolithographic procedure was employed for patterning the SU-8 layer, and the process protocol is fully outlined in Table 7.1.

Development of the exposed pattern was achieved by immersion of the chip in Microposit EC solvent solution (SU-8 developer), whilst sonicating for approximately 3 minutes. Again however, adhesion to silver was problematic and the process yield was worse than that described in section 7.6.3.2.

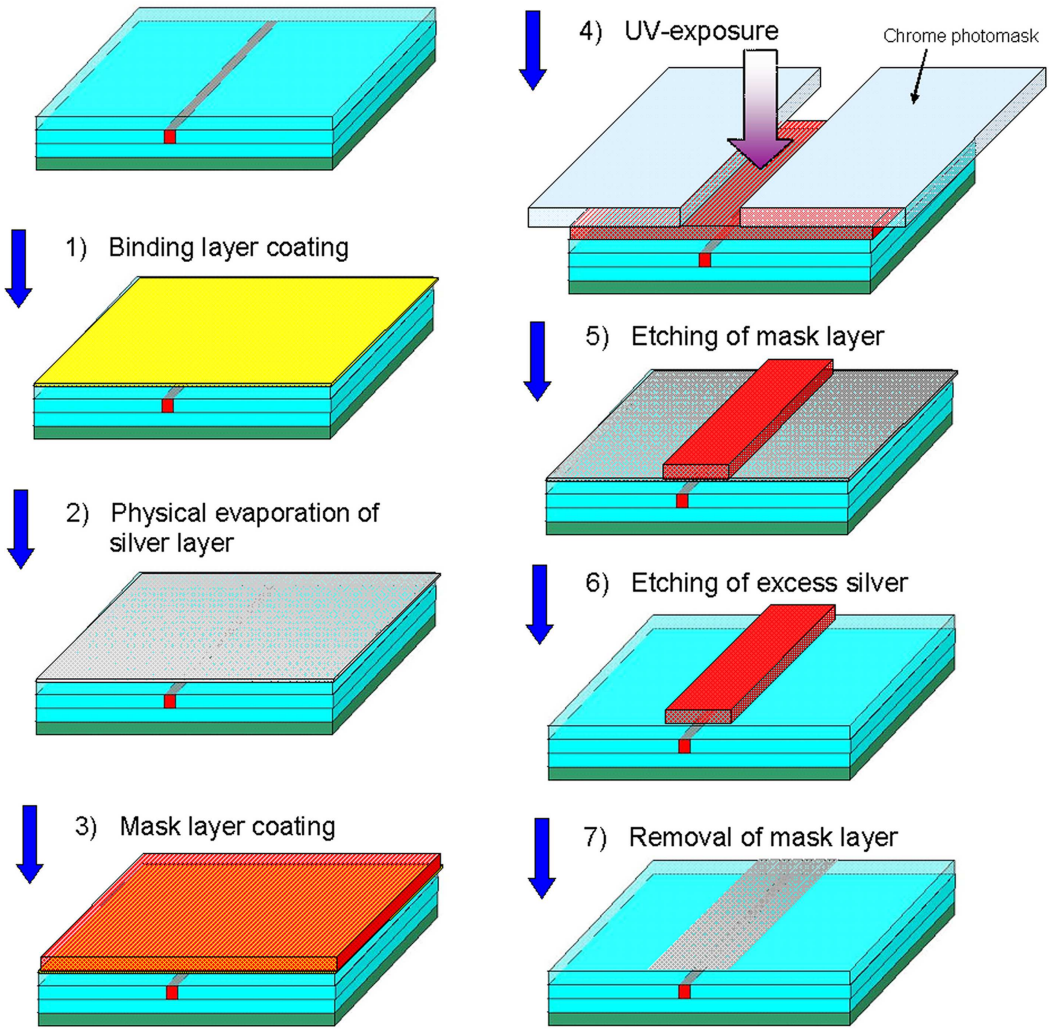

Figure 7.20: *Process schematic for the deposition of thin film heaters using the binding layer for adhesion and a sol-gel layer as a photopatternable mask layer*

As an alternative, one of the sol-gel materials (baseline sol) was employed as the masking layer instead of SU-8. Since deposition of the guiding layer sol was taking place on top of silver, and also since the process requirements and tolerances were a little more relaxed than in the case of optical waveguides, a different set of process parameters were employed here. In this case, the sol was directly spin-coated at a speed of 1300 rpm followed by a 5 min pre-exposure bake on a hotplate at 100 °C. This step was found to aid with adhesion. Then the heater circuit photomask was aligned with the optical circuits (which were still visible through the 100nm silver layer), and the sol-gel layer was exposed for 500s. Then the chip was immersed in a clean bath of 1-butanol for 30s with gentle agitation. This was repeated in a clean bath of 1-butanol two more times followed by a final rinse for 10s with clean 1-butanol and blow drying with N_2. The continu-

SU-8 coating and photolithography process parameters	
Spin-coating	
Dispense volume	4 ml
Maximum speed	4000 rpm
Acceleration	330 rpm/s
Time	40 s
Pre-exposure bake	
2 mins	65 °C
4 mins	95 °C
UV-exposure	
90 s	10W
Post-exposure bake	
1 min	65 °C
2.5 mins	95 °C

Table 7.1: *Coating and photolithography parameters for SU-8 photoresist patterning*

ous cycling of the chip among three clean baths of 1-butanol was necessary to completely remove all sol-gel mask residues because these were found to interfere with the silver etching process to follow. The distinguishing feature of this process from the previous one, is the necessity to etch away the blanket deposition of silver on top of which a guiding layer sol-gel mask has been patterned in order to protect those areas that are covered. Two silver etching processes were developed to this end.

$Fe(NO_3)_3$ etching

The advantage of using an $Fe(NO_3)_3$ solution to etch silver were its low toxicity and cost compared to other options such as ferricyanide etchant solutions. $Fe(NO_3)_3$ crystals (ferric nitrate) were dissolved in water to form an aqueous solution (0.05 M). This solution reacts with and removes silver from the surface via the following reaction [20]:

$$Ag(s) \quad + \quad Fe(NO_3)_3(aq) \quad \rightleftharpoons \quad AgNO_3(aq) \quad + \quad Fe(NO_3)_2(aq) \qquad (7.6)$$

The etching rate (nm/s) increases linearly with increasing concentration of $Fe(NO_3)_3$, and has been quoted as being equal to $46.7[Fe(NO_3)_3](M)$ [20]. Although this method did prove successful in etching silver on the test samples, the main problem associated with this method was found to be that the solution was able to attack any cracks or defects on the edges of the sol-gel masking layer and etch

across the narrow heater element (100 μm) causing electrical discontinuities. Despite its advantages, $Fe(NO_3)_3$ etching was found to be unsuitable for use with the sol-gel masking layer and alternatives were pursued.

O2 Plasma Etching

As an alternative, oxygen plasma etching was investigated for the etching of the excess silver. The process was carried out using an Oxford Instruments Plasmalab 80-Plus. The parameters of the plasma etching process are shown in Table 7.2. It was found that after 1 hour of etching under these conditions, all of the silver in the unmasked areas was removed, whilst that covered by the sol-gel protective layer was undamaged. This was confirmed by electrical continuity testing of 5 chips (each containing 6 electrical circuits). The sol-gel protective mask was removed by sonicating the chips in acetone for 15 minutes and blow drying the chips in N_2. The optimised thin film heater process results in a high yield of repeatable and fully functional heater circuits, as shown in Figure 7.21.

Plasma etch process parameters	
Time	60 mins
O2 flow	100 sccm
Ar flow	20 sccm
Pressure	40 mTorr
Power	300 W

Table 7.2: *Oxygen plasma etching parameters*

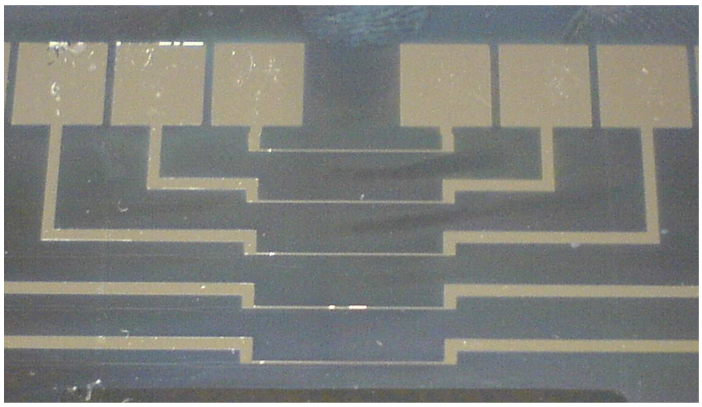

Figure 7.21: *Example of a chip with heaters/electrodes processed using the optimised patterning and deposition process*

7.7 Switch Characterisation

The characterisation of the switch which was fabricated as described in the previous section is presented here. The main parameters of interest are the division of power between the output waveguides of the switch, the power consumption and the switch response time. The characterisation setup shown in figure 7.22 was used for switch characterisation. Cleaving of the input waveguide and alignment of the chip in the system follows the procedure outlined in section 5.5.3 for the refractometric sensor platform. In this case, the excitation source was a fiber pig-tailed laser diode (Thorlabs, $\lambda = 1.31$ μm, maximum output power = 3.1 mW).

7.7.1 Characterisation of Optical Power Division

In order to characterise the response of the chip to changes in input electrical power, the voltage applied to the heater was increased in discrete steps of ~0.05 V. For each voltage, the photocurrent was recorded for one output waveguide. Then the voltage was returned to zero, and the photodiode was aligned with the other output waveguide and the procedure was repeated. Applied electrical power was calculated using the formula $P = V^2/R$, where R was measured as 70 Ω. Images of the output states of the switch were captured using a Hamamatsu IR camera (Vidicon camera C2741-03) (7.27), whilst the full switch power division response curves are shown in Figure 7.24.

Ideally, for no application of heat, all of the input light would be found at one of the outputs. In the case of heating, the light would then switch entirely to the other output. As may be seen in Figure 7.27 and 7.24, this is not the case for this particular switch. The cross-talk value for this switch is approximately -8

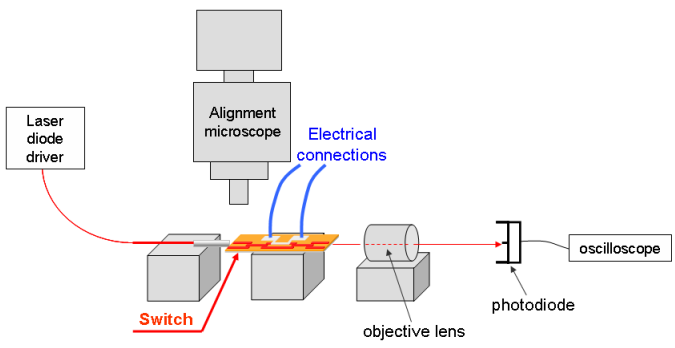

Figure 7.22: *Setup employed for characterisation of the thermo-optical switch*

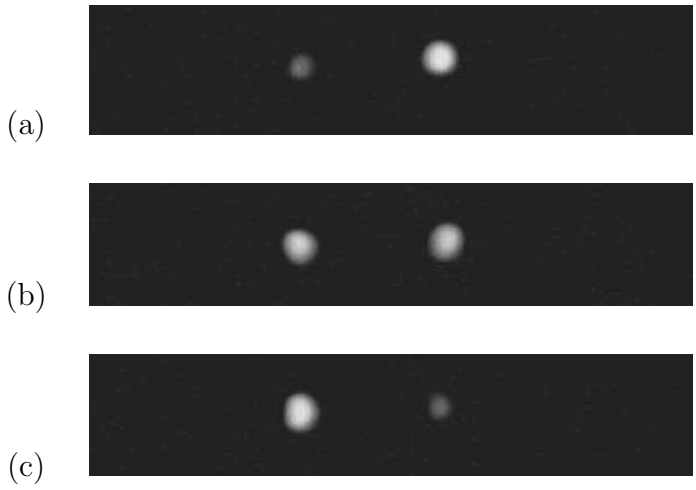

Figure 7.23: *Output switching states for; (a) right output on, (b) 3dB splitter, and (c) left output on*

dB, meaning that at the optimum point in the response, about 90% of the input light is found in the intended output waveguide, with the remaining 10% found in the other.

The cause of incomplete switching is most likely due to a combination of two factors. Firstly, it is possible that the directional coupler length was not well specified, in which case light is not equally split at the output from either splitter. This is a requirement for complete switching between the outputs.

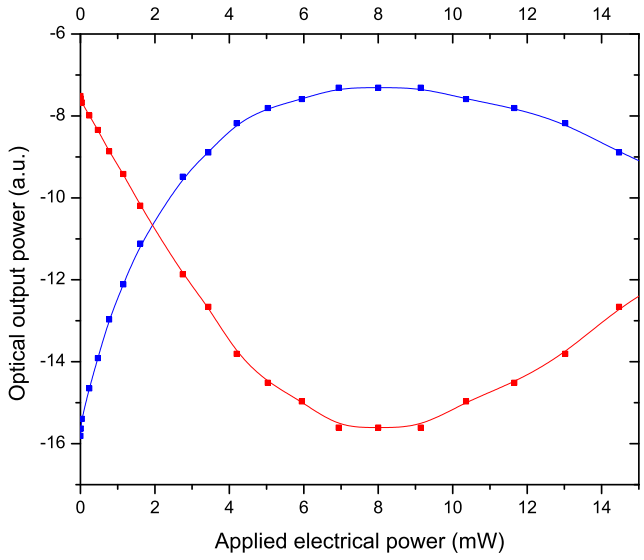

Figure 7.24: *Experimental response of the switch output intensity as a function of the applied electrical power*

The second possible explanation for incomplete switching is due to poor etching between the arms of the directional coupler. Figure 7.25 shows a cross-sectional image of the waveguides in a directional coupler fabricated using the process described here. It is clear that the etching between the waveguides in the coupling region is not performed to the bottom of the guiding layer.

The reasons for incomplete etching are thought to originate from diffracted light at the mask openings. When exposing through a mask, a part of the UV light is diffracted at the side of the apertures. This parasitic energy, which is usually negligible is more significant when two or more waveguides are in close proximity, because of the summation of the diffracted energies from each aperture. In this case it seems that the polymerisation threshold of the material is at a level where the summation of the diffracted energies can cause polymerisation, where normal diffracted energies are unable to do so.

Another possible contribution to this problem is deviations in the uniformity of the guiding layer thin film. As outlined in Section 3.3.2, the larger the distance between mask and film, the lower the resolution making it is more difficult to resolve adjacent lines in a pattern. Local non-uniformity of the film, as well as separation caused by the slightly thicker ring of sol at the wafer perimeter (edge-bead), may contribute to a reduced resolution, resulting in difficulty in resolving the adjacent waveguides.

One solution to reduce this effect is to expose thinner layers, which results in increased resolution according to equation 3.7, but this results in smaller waveguides with higher coupling losses to optical fibers. A more attractive approach would be to review the fabrication process and material composition so as to increase the material contrast to a level where even the summation of diffracted energies cannot cause polymerisation. In this vein, it would be interesting to

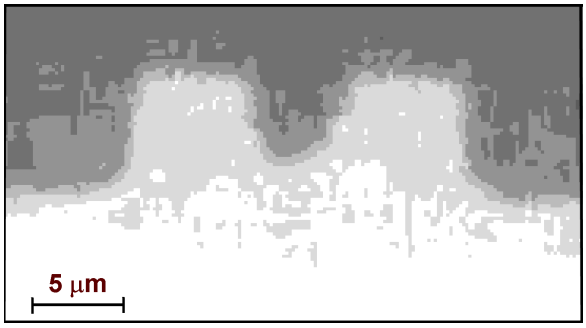

Figure 7.25: *Cross-sectional image of waveguides in a directional coupler showing poor etching of material between the waveguides*

continue the work outlined in Section 4.3.4, where the influence of the zirconium complex on the photoreactivity of the sol was characterised. This indicates a promising route to optimisation of the material contrast in order to eliminate photopolymerisation between the arms of a directional coupler. Another useful measure would be to implement an edge-bead removal system to make the entire surface of the wafer more planar, so as to permit a more repeatable photolithography step.

7.7.1.1 Electrical Power Consumption

The power consumption of the chip is extremely low with only 8 mW necessary for switching as seen from Figure 7.24. This corresponds very closely with the value of 8.4 mW that was predicted by theory in section 7.5.4. In comparison with other switches in the literature, this power consumption is extremely competitive. This is especially so in comparison to silica-based thermo-optic switches, where a classical thermo-optic switch needs from 400 to 700 mW heater power for switching, and designs which have been optimised for lower power consumption still do not compete with the power consumption calculated here [12]. The low power consumption is one of the key strengths that arises from the use of hybrid sol-gels, due to their high thermo-optic coefficient.

7.7.2 Characterisation of the Transient Switching Response

Having optimised the alignment as described previously, an alternating current electrical signal was applied to the chip using a signal generator. The heater was driven with a square-wave voltage input of approximately 0.75 V in order to drive the response instantaneously between switching states. The result of this is displayed in Figure 7.26. From these data, it is possible to calculate a t_{90} switching time of 1.2 ms for switching on (rise-time) and 1.8 ms for switching off (fall-time). The rise-time value is again very closely matched with the value estimated by the simulations shown in section 7.5.5.1. The variation of $\sim$0.35 ms between these values is attributable to the difference between the estimated and actual thermal properties of the sol-gel materials. As a response time for a restoration/protection switch, which is the intended market for this switch, this is a very competitive response time and certainly satisfies the requirements of the application.

The difference between rise-time and fall-time is attributable to a slower prop-

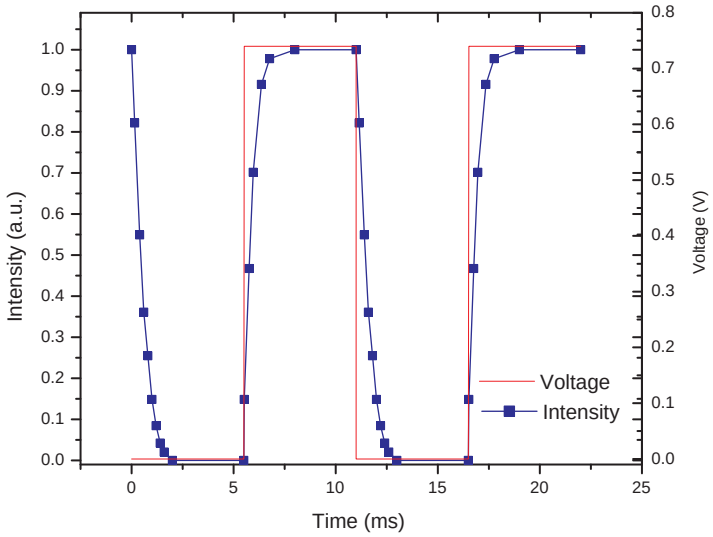

Figure 7.26: *Experimental temporal response of the thermo-optic switch*

agation of thermal energy when cooling down. When heating up, the silicon substrate (which is considered as a heat sink), is at ambient temperature while the electrode is at temperature T1. When cooling, no electrical power is applied anymore and so both electrode and substrate are at room temperature while the middle of the transverse structure is at an intermediate temperature T2=T1/2. The temperature gradient is thus smaller and the heat exchange is slower. A cooling step could be added to accelerate cooling down but the switching command would then be more complex.

7.7.3 MMIC Switch

Characterisation of the MMIC switch consisted in capture of light from the four output waveguides by the IR camera. The heater electrodes were connected to a power supply, and the voltage was varied until each switching state was captured by the camera, as shown in Figure 7.27. According to the design, light should emerge from only one of the four waveguides for each switching state. Examination of the images shows that for switching state (a) and (c), the parasitic light emerging from output ports is significant (ports 2 and 4 for state (a), and, 3 and 4 for state (c)). On the other hand, for switching state (d), a good performance in achieved in terms of the brightness of the output port 1 compared

to any parasitic light that has emerged from the other three outputs. A similar result has been obtained for switching state (b).

This initial characterisation of the platform has proved the principle that a multi-port thermo-optical switch can be fabricated from low-cost hybrid sol-gel materials, incorporating a novel single electrode circuit, greatly simplifying the electrical command to the switch. Given the capability of MMICs to split an input signal between a large number of outputs, in principle, this concept is extendable to switching between many more outputs ports.

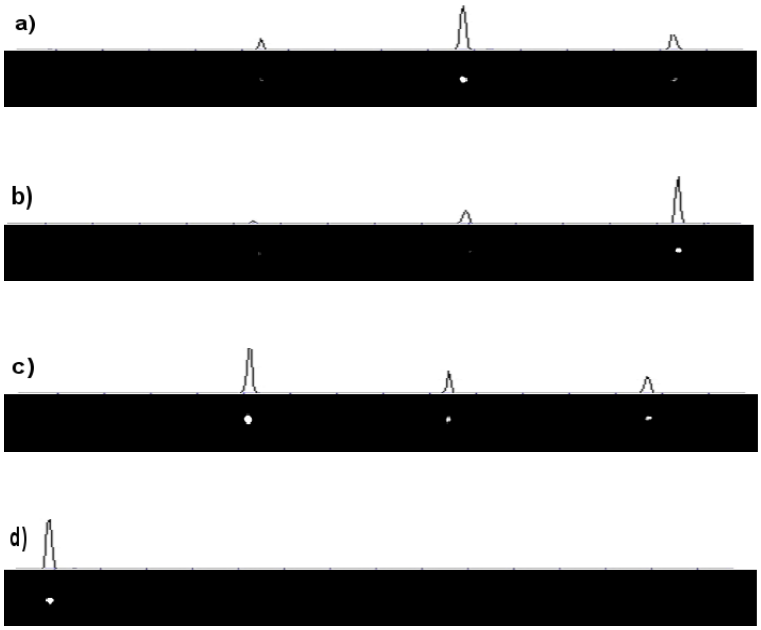

Figure 7.27: *Different output switching states for the MMIC switch*

7.8 Conclusion

Two thermo-optic switch platforms have been described, one based on a Mach-Zehnder interferometer configuration and the other using MMICs as light splitting components. Extensive simulation of the Mach-Zehnder design allowed estimation of the switch behaviour in response to application of heat to a thin film heater on one of the interferometer arms. Transient thermal simulations were also carried out predicting switching times in the region of ~ 0.85 ms. A brief simulation study of the MMIC switch was presented which allowed determination of the device length needed for switching.

Fabrication of the switches was carried out by UV mask photolithography. Patterning and deposition of a thin film heater and electrodes involved deposition

of an intermediate binding layer on the chip, upon which a layer of silver was deposited. Patterning of this layer involved deposition of the guiding layer sol, which was UV exposed in order to mask off the heater/electrode circuits. The unmasked regions were removed by an oxygen plasma etching step.

A high thermo-optic coefficient of approximately -1.5 x 10^{-4} K^{-1} was measured for the hybrid sol-gel materials. Switch characterisation revealed cross-talk of 8 dB between the outputs, a low power consumption of 8 mW and average switching times in the region of 1.5 ms.

This is an extremely promising platform for future work, which will focus on improvement in the cross-talk value. An increase in the material contrast is the main step needed to improve cross-talk, as this is predicted to reduce/eliminate photopolymerisation between the arms of the directional coupler which is the main source of the problem.

References

[1] J. Hecht, "Many approaches taken for all-optical switching," *Laser Focus World*, vol. 37, pp. 125, 2001.

[2] J. J. Uebbing, S. Hengstler, D. Schroeder, S. Venkatesh, and R. Haven, "Heat and fluid flow in an optical switch bubble," *Journal of Microelectromechanical Systems*, vol. 15, pp. 1528–1539, 2006.

[3] P. Arora, V. M. Petrov, J. Petter, and T. Tschudi, "Fast electrically switchable holographic optical elements in $LiNbO_3$," *Optics Communications*, vol. 281, pp. 1455–1460, 2008.

[4] J. Aboujeib, V. Quintard, A. Perennou, and J. L. Bihan, "Experimental study of losses and cross talk in a multitransducer acousto-optic switch," *Optical Engineering*, vol. 47, p. 035007, 2008.

[5] L. Eldada, "Optical communication components," *Review of Scientific Instruments*, vol. 75, pp. 575–593, 2004.

[6] E. L. Wooten, K. M. Kissa, A. Yi-Yan, E. J. Murphy, D. A. Lafaw, P. F. Hallemeier, D. Maack, D. V. Attanasio, D. J. Fritz, G. J. McBrien, and D. E. Bossi, "A review of lithium niobate modulators for fiber-optic communications systems," *IEEE Journal of Selected Topics in Quantum Electronics*, vol. 6, pp. 69–82, 2000.

[7] E.-S. Kang, J. Y. Bae, and B.-S. Bae, "Measurement of thermo-optic coefficients in sol-gel hybrid glass films," *Journal of Sol-Gel Science and Technology*, vol. 26, no. 1-3, pp. 981–984, 2003.

[8] E.-S. Kang, W.-S. Kim, K.-S. Kim, and B.-S. Bae, "Modification of thermo-optic characteristics of sol-gel inorganic-organic hybrid materials," *Journal of Sol-Gel Science and Technology*, vol. 32, no. 1-3, pp. 277–280, 2004.

[9] K. R. Kribich, H. Barry, R. Copperwhite, B. Kolodziejczyk, K. O'Dwyer, J. M. Sabattie, and B. D. MacCraith, "Thermo-optic switches using sol-gel processed hybrid materials," *Proceedings of SPIE*, vol. 5451, p. 518, 2004.

[10] S. K. Korotky, "3-space representation of phase-mismatch switching in coupled 2-state optical-systems," *IEEE Journal of Quantum Electronics*, vol. 22, pp. 952–958, 1986.

[11] Y. Hida, H. Onose, and S. Imamura, "Polymer wave-guide thermooptic switch with low electric-power consumption at 1.3 μm," *IEEE Photonics Technology Letters*, vol. 5, pp. 782–784, 1993.

[12] M. P. Earnshaw, "Ultra-low power thermo-optic silica-on-silicon waveguide membrane switch," *Electronics Letters*, vol. 43, no. 7, pp. 393–394, 2007.

[13] M. Kuratli and E. Pretsch, "Sulfur dioxide-selective optodes," *Analytical Chemistry*, vol. 66, pp. 85–91, 1994.

[14] S. Krause, W. Moritz, and I. Grohmann, "Improved long-term stability for an LaF(3) based oxygen sensor," *Sensors and Actuators B-Chemical*, vol. 18, pp. 148–154, 1994.

[15] G. Gerlach and K. Sager, "A piezoresistive humidity sensor," *Sensors and Actuators A-Physical*, vol. 43, pp. 181–184, 1994.

[16] J. Lv, F. C. Lai, L. M. Lin, Y. Z. Lin, Z. G. Huang, and R. Chen, "Thermal stability of Ag films in air prepared by thermal evaporation," *Applied Surface Science*, vol. 253, pp. 7036–7040, 2007.

[17] J. Lv, F. C. Lai, L. M. Lin, Y. Z. Lin, Z. G. Huang, and R. Chen, "Thermal stability of Ag films in air prepared by thermal evaporation," *Applied Surface Science*, vol. 253, pp. 7036–7040, 2007.

[18] S. Sogaard and J. Henningsen, "Thermal tuning and modulation of a DFB fibre laser with a thin-film heater," *Applied Physics B-Lasers and Optics*, vol. 75, pp. 497–501, 2002.

[19] "Contact performance in relays.", http://www.leachintl2.com, 2008

[20] Y. Xia, E. Kim, and G. M. Whitesides, "Microcontact printing of alkanethiols on silver and its application in microfabrication," *Journal of the Electrochemical Society*, vol. 143, pp. 1070–1079, 1996.

Chapter 8

Conclusion

In this work, a variety of concepts for PLC platforms have been successfully developed for application in sensing and telecommunications. The adaptability of the photocurable hybrid sol-gel materials and the associated microfabrication processes developed was demonstrated in the design and fabrication of these platforms.

The objectives of this work, as described in Chapter 1, were realised.

1. A suite of photolithographic microfabrication processes for the formation of PLCs was developed, encompassing mask alignment and the development of a direct laser writing system

2. A range of novel waveguide-based devices were design and simulated, exploiting the intrinsic advantages of PLC platforms for:

   (a) Refractometric sensing

   (b) Fluorescence-based multianalyte biosensing

   (c) Optical telecommunications switching

3. Photocurable hybrid sol-gel materials were characterised both in terms of their optical performance (exhibiting low propagation losses of 0.5 dB/cm in the best case), and in terms of photostability and chemical constitution, leading to optimised formulations.

4. The developed materials and processes, were applied to the fabrication of the PLC platforms outlined in point 2, leading to:

   (a) An MMIC-based refractometric platform with high refractive index resolution of $\sim 1.5 \times 10^{-5}$

(b) The successful realisation of a multianalyte biosensor platform, allowing the development of a range of fabrication and surface functionalisation techniques for the achievement of μg/ml concentrations in a proof-of-principle immunoassay

(c) Measurement of a high thermo-optic coefficient of -1.5 x 10^{-4} K^{-1} for the sol-gel material, and subsequent development of a thermo-optical switch with 8 dB cross-talk, low power consumption (8 mW) and average switching times in the region of 1.5 ms.

Future work will involve parallel developments in both the material/process aspects of the project and on refinement and further development of the PLC platform concepts.

Some of the more recent low-loss photocurable materials developed have not yet been fully optimised for planar waveguide fabrication. Optimisation of the fabrication step for these materials should result in waveguides that exceed the low propagation losses already exhibited here.

Having developed a suite of novel photocurable materials, future work will aim to incorporate increased functionality in the resulting photonic devices. In particular, plans to exploit the material for recording volume and/or surface relief diffractive optical elements (DOEs) are at an advanced stage. Such components will add value to all of the platforms already developed in this work, in particular to the sensor platforms, where DOEs can be formed to facilitate in- and out-coupling of light. Coupling is routinely achieved using fiber pig-tailing technology, but this solution is in some instances financially impractical for sensor platforms, as many applications demand that the platform is disposable and therefore low in cost (especially in POC testing).

The above-mentioned development of DOE couplers has direct impact on the future applicability of the multianalyte biosensor platform, which is one example of where a low cost coupling methodology will be essential. In this regard, investigations will center on the use DOEs but also surface-relief slanted gratings which in theory allow high coupling efficiencies at normal incidence. These are extremely attractive characteristics for any PLC-based device, not only in sensing but also in telecommunications.

The evanescent wave enhancement strategies investigated will be pursued in greater detail aiming to verify the enhancement factors calculated by simulation. In addition, a sol-gel method for the production of the high refractive index

layers needed for enhancement will be investigated, eliminating the need to utilise expensive CVD or physical deposition methods.

Developments of the refractometric sensing platforms will focus mainly on the evaluation of the temperature dependence of the platforms. Preliminary studies indicate that design of the platforms to accept multiple wavelength excitation could potentially be used in order to reference out any temperature dependent effects, which are the chief difficulty of refractometric sensing platforms. Finally, future work on the thermo-optical switch platform will focus mainly on the improvement of the etching of the directional couplers, which should allow the attainment of low cross-talk values.

All of the technologies developed in this thesis have the potential to impact considerably on future industrial developments. The use of hybrid sol-gel materials is inherently one of the most rapid and cost effective means of mass-producing PLC components. The employment of sol-gel PLCs in diverse applications demonstrated here is timely and has the potential to have significant impact in each area.

List of Publications and Conference Presentations

Oral presentations:

1. "Characterisation of novel multimode interference sensing systems", SPIE Opto-Ireland, Dublin, 4-6th April, 2005.

2. "Characterisation of novel refractometric sensing systems", International Conference SPIE: Optics East, Boston, September 2005.

Poster Presentations:

1. R. Copperwhite, M. Oubaha, and B.D. MacCraith, "Multianalyte bio-diagnostic chip based on Ta_2O_5-coated sol-gel planar waveguides", Europt(r)ode IX, 30 March-2 April 2008, Dublin, Ireland.

2. R. Copperwhite, M. Oubaha, and B.D. MacCraith, "Novel bio-diagnostic chip based on sol-gel planar waveguides", Photonics Ireland, 24-26 September 2007, Galway, Ireland.

3. R. Copperwhite, J. Hradil, M. Oubaha, G. Town, K.R. Kribich and B.D. MacCraith, "Sensitivity enhancement in generic planar lightwave circuit refractometric sensing platforms", Europt(r)ode VIII, Tubingen, Germany, 2-5 April 2006.

4. R.Copperwhite, K.Kribich, B.Kolodziejczyk, H.Barry, J.M.Sabattie, K. O'Dwyer and B.D.MacCraith, "Thermo Optic Switches using Sol-Gel processed Hybrid Materials", Institute of Physics in Ireland, Spring Weekend, Newbridge, Co. Kildare, March 2005.

5. C. Charlton, R. Copperwhite, R.K. Kribich, K. O'Dwyer, A. Katzir, B. D. MacCraith, B. Mizaikoff, "Integrated mid-infrared sensing platforms with quantum cascade lasers coupled to tailored planar silver halide fibres", International Conference SPIE: Opto Ireland, Dublin (Ireland), April 2005.

6. M. Oubaha, R. Copperwhite, K. O'Dwyer and Brian D. MacCraith "Contribution of the aromatic groups to the improvement of the transmission at 1550 nm in organo-siloxane sol-gel materials", SOL-GEL 2005, 13th International Workshop on Sol-Gel Science and Technology, UCLA, Los Angeles. 22-26 August 2005.

7. M. Oubaha, R. Copperwhite, K. O'Dwyer and Brian D. MacCraith "Contribution of the aromatic groups to the improvement of the transmission at 1550 nm in organo-siloxane sol-gel materials", UK-Ireland Sol-Gel, Institute of Physics, United Kingdom, 22 March, 2005.

8. R.K. Kribich, R. Copperwhite, B. Kolodziejczyk, H. Barry, J.M. Sabattie and B.D. MacCraith, "Novel chemical/biosensor platform based on multimode interference couplers", Europt(r)ode VII, Madrid, 6 April, 2005.

9. C. Croutxe-Barghorn, D.L. Versace, M. Oubaha, R. Copperwhite, and B.D. MacCraith, "UV-curable organic-inorganic sol-gel waveguides: Comprehension and optimisation of the photochemical pathway", XIVth International Sol-Gel Conference, 2-7 September 2007, Montpellier, France.

Peer-Reviewed Publications:

1. R. Copperwhite, M. Oubaha, D.L. Versace, C. Croutx-Barghorn and B.D. MacCraith, "The role of photoinitiator and chelating agent in the fabrication of optical waveguides from UV-photocurable organo-mineral solgel materials", J. Non-Crystalline Solids, Volume 354, Issue 30, 15 July 2008, Pages 3617-3622.

2. R.K. Kribich, R. Copperwhite, B. Kolodziejczyk, H. Barry and B.D. MacCraith, , "Novel Chemical/Bio-Sensor platform based on multimode interference couplers", Sensors and Actuators B, vol. 107(1), pp.188-192, May 2005.

3. M. Oubaha, R. Copperwhite, B. Murphy, B. Kolodziejczyk, H. Barry, K. O'Dwyer, and B.D. MacCraith, "Development of photo-patternable organo-mineral hybrid films from the sol-gel condensation of alkoxysilanes", Thin Solid Films, v 510, n 1-2, Jul 3, 2006, p 334-338.

4. D.L. Versace, M. Oubaha, R. Copperwhite, C. Croutxe-Barghorn, B.D. MacCraith, "Waveguide fabrication in UV-photocurable solgel materials: Influence of the photoinitiating system", Thin Solid Films, Volume 516, Issue 18, 31 July 2008, Pages 6448-6457.

5. M. Oubaha, R.K. Kribich, R. Copperwhite, P. Etienne, K. O'Dwyer, B.D. MacCraith and Y. Moreau, "New organic inorganic sol-gel material with high transparency at 1.55 μm", Optics Communications, v 253, n 4-6, Sep 15, 2005, p 346-351.

Conference Proceedings

1. R. F. Copperwhite, M. Oubaha, G. E. Town, R. Kribich, K. O'Dwyer, B. D. MacCraith, "Characterization of novel refractometric sensing systems", pp. 78-88, Proceedings of SPIE volume 5993, Advanced Environmental, Chemical, and Biological Sensing Technologies III, OpticsEast, Boston, 23-26th October, 2005.

2. G. E Town, R. F. Copperwhite, R. Kribich, K. O'Dwyer, B.D. MacCraith, "Comparison of multimode and multichannel couplers for evanescent sensing of refractive index", Proceedings, 30th Australian Conference on Optical Fibre Technology (ACOFT2005), Sydney, 4th-9th July, 2005.

3. R.K. Kribich, H. Barry, R. Copperwhite, B. Kolodziejczyk, K. O'Dwyer, J.-M. Sabbattie and B.D. MacCraith, "Thermo-optic switches using sol-gel processed hybrid materials", Proceedings of SPIE - Photonics Europe (Strasbourg, France), v 5451, Integrated Optics and Photonic Integrated Circuits, 2004, p 518-528.

Appendix A

This appendix is devoted to the derivation of the partial differential equation of heat conduction in its general form, and then reducing it to its more particular cases. Heat transfer can takes place by by three different mechanisms; conduction, convection and radiation. For the case of heat transfer through a solid material convection and radiation can normally be considered negligible, so conduction is the phenomenon that is of interest here. Conduction is defined as heat transfer in which energy exchange takes place from a region of high temperature to one of lower temperature, either by means of the kinetic motion or direct impact of molecules, or by the drift of electrons. Generally, it is true that good electrical conductors are also good thermal conductors. The basic constitutive relation that defines heat conduction is one based on experimental observations made by Biot, but is generally named after the French mathematician Joseph Fourier. For heat flow in the x direction for example, the Fourier law is given as

$$Q_x = -k_x A \frac{\partial T}{\partial x} \tag{8.1}$$

$$q_x = \frac{Q_x}{A} = -k_x \frac{\partial T}{\partial x} \tag{8.2}$$

where Q_x is the rate of heat flow through area A in the positive x direction, and q_x is called the heat flux in the positive x direction. The proportionality constant k_x is the thermal conductivity (in the x direction) of the material through which heat is travelling. The thermal conductivity value of a material can sometimes have a different value depending upon the direction, for example in some composite materials containing fibers, heat preferrentially travels in the direction of orientation of the fibers. However, for this derivation we assume an isotropic medium, that is, one in which the thermal conductivity is constant regardless of direction. Therefore, we generalise equation 8.2 so that,

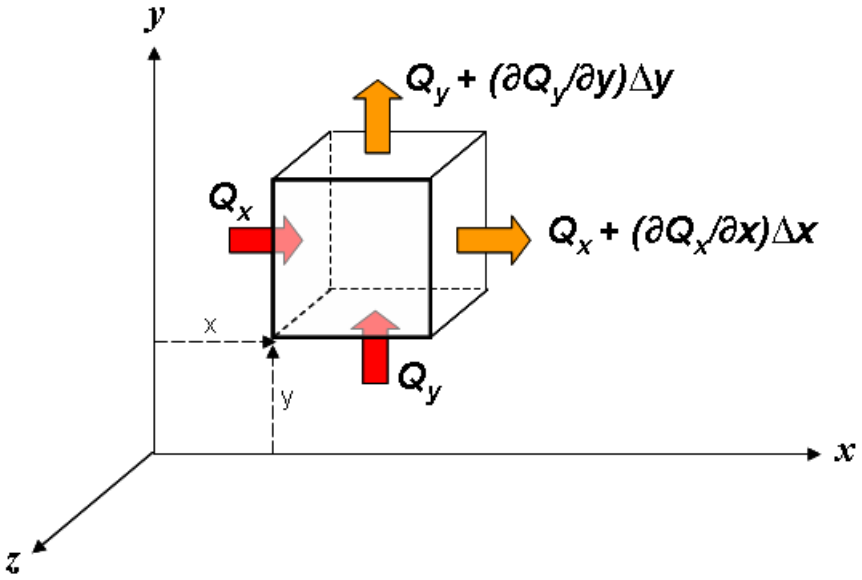

Figure 8.1: *Heat conduction through a volume element*

$$\begin{aligned} q_x &= \frac{Q_x}{A} = -k\frac{\partial T}{\partial x} \\ q_y &= \frac{Q_x}{A} = -k\frac{\partial T}{\partial y} \\ q_z &= \frac{Q_x}{A} = -k\frac{\partial T}{\partial z}. \end{aligned} \tag{8.3}$$

These equations imply that the heat flow in the x, y and z directions can be computed if the temperature gradients in those directions are known. In order to compute the temperature gradients at each point in a volume, the general temperature distribution must be known. The temperture distribution can be computed by solution of the differential equation of heat conduction, which is derived as follow;

The fundamental relation that underlies this derivation is that the net rate of energy tranfer into volume added to the rate of energy generation in the volume must equal the rate of increase of internal energy in that volume. This is more easily understood in the form of the following equation,

$$\begin{pmatrix} \text{Net rate of heat} \\ \text{entering into} \\ \text{element } \Delta x\Delta y\Delta z \end{pmatrix} + \begin{pmatrix} \text{Rate of energy} \\ \text{generated in} \\ \text{element } \Delta x\Delta y\Delta z \end{pmatrix} = \begin{pmatrix} \text{Rate of increase of} \\ \text{internal energy of} \\ \text{element } \Delta x\Delta y\Delta z \end{pmatrix}. \tag{8.4}$$

To solve for the first component of equation 8.4 consider the volume element depicted in Figure 8.1. Here, the net rate of heat entering the volume by conduction

is determined by summing up the discrete heat flow components in the x, y and z directions. Using equations 8.3, the rate of heat flow **entering** the volume in the x, y and z directions may be written as

$$\begin{aligned} Q_x &= q_x \Delta y \Delta z \\ Q_y &= q_y \Delta x \Delta z \\ Q_z &= q_z \Delta x \Delta y. \end{aligned} \tag{8.5}$$

Now, the rate of heat flow **leaving** the volume element through the surface at x+Δx is

$$\left(\begin{array}{c} \text{Rate of heat flow} \\ \text{leaving the volume} \end{array} \right)_x = Q_x + \frac{\partial Q_x}{\partial x} \Delta x \tag{8.6}$$

For each direction, the ***net*** rate of heat entering the volume element by conduction is simply the difference between the heat entering (equation 8.5) and leaving the volume (equation 8.6), which in the particular case of the x direction is expressed as

$$\begin{aligned} \left(\begin{array}{c} \text{Net rate of heat} \\ \text{entering the volume} \end{array} \right)_x &= Q_x + \frac{\partial Q_x}{\partial x} \Delta x - Q_x \\ &= \frac{\partial Q_x}{\partial x} \Delta x \\ &= \frac{\partial q_x}{\partial x} \Delta x \Delta y \Delta z \end{aligned} \tag{8.7}$$

Similarly, the net rates of heat entering the volume in the y and z directions respectively are,

$$\begin{aligned} &= \frac{\partial q_y}{\partial y} \Delta x \Delta y \Delta z \\ &= \frac{\partial q_z}{\partial z} \Delta x \Delta y \Delta z \end{aligned}$$

Summing all components, the total net rate of heat entering the volume element as a whole is

$$= \left(\frac{\partial q_x}{\partial x} + \frac{\partial q_y}{\partial y} + \frac{\partial q_z}{\partial z} \right) \Delta x \Delta y \Delta z \tag{8.8}$$

Rate of energy generation

A distributed heat source within the volume generating heat at a rate of g(x, y,

z, t) contributes to the second term in 8.4 as

$$= g(x, y, z, t)\Delta x\Delta y\Delta z \tag{8.9}$$

Rate of increase of internal energy

The rate of increase of internal energy in the volume as defined by the third term of 8.4 is reflected by the rate of energy storage in the volume given by

$$= \rho c_p \frac{\partial T}{\partial t}\Delta x\Delta y\Delta z \tag{8.10}$$

Partial differential equation of heat conduction

The substitution of each of the derived terms into equation 8.4 results in

$$-\left(\frac{\partial q_x}{\partial x} + \frac{\partial q_y}{\partial y} + \frac{\partial q_z}{\partial z}\right) + g(x, y, z, t) = \rho c_p \frac{\partial T}{\partial t}$$

Using equations 8.3, this can be expressed as

$$\frac{\partial}{\partial x}\left(k\frac{\partial T}{\partial x}\right) + \frac{\partial}{\partial y}\left(k\frac{\partial T}{\partial y}\right) + \frac{\partial}{\partial z}\left(k\frac{\partial T}{\partial z}\right) + g(x, y, z, t) = \rho c_p \frac{\partial T}{\partial t} \tag{8.11}$$

which is the partial differential equation of heat conduction, where T = T(x,y,z,t) and g = g(x,y,z,t).

Appendix B

This appendix is devoted to the development of basic concepts underlying the finite difference method of numerically solving differential equations. Approximate numerical solutions such as the finite difference method are sought in situations where the complicated nature of the geometry and boundary conditions precludes the use of analytical methods. The representation given here is not as complicated as some implementations and as such, serves to give an accessible introduction to the technique. There are three general steps to the method;

- Represent the region of interest by a series of discrete points, so that a mesh/grid is superimposed on the structure subdividing it into small equal sized portions. In a transient system it is also necessary to split the time into discrete intervals
- Replace the differential equation in question with an approximated finite difference equation. The differential equation of relevance here is the partial differential equation of heat conduction. This procedure results in a set of equations (one for each point in the grid) in terms of the temperature at these discrete locations.
- Solve the resultant set of equations to yield the temperature distribution within the medium. For transient problems the equations are solved at each time interval to yield the temperature throughout the time period of interest.

Taylor series expansion

At the heart of the finite difference method lies the Taylor series expansion. It enables the approximation of the next point on a curve given the point immediately before or after. The Taylor expansion is defined such that,

$$f(x) = f(x_0) + (x - x_0)\frac{\partial f(x_0)}{\partial x} + \frac{(x - x_0)^2}{2!}\frac{\partial^2 f(x_0)}{\partial x^2} + ... + \frac{(x - x_0)^n}{n!}\frac{\partial^n f(x_0)}{\partial x^n} + ... \tag{8.12}$$

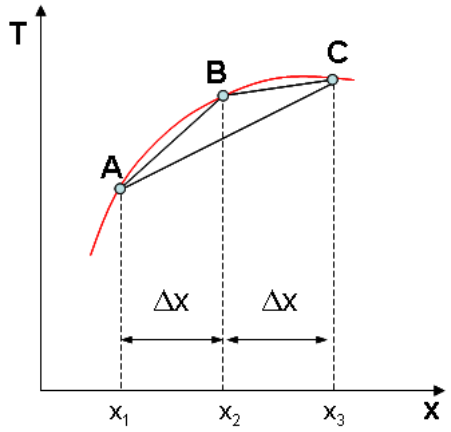

Figure 8.2: *Finite difference approximation of a 1-dimensional temperature gradient*

Application of the Taylor expansion

First taking a 1D problem, consider the temperature gradient represented by the curve in Figure 8.2. In order to approximate this curve using numerical methods it is first necessary to divide the spatial dimension into discrete intervals of equal length (Δx). The lines defined by x1, x2 and x3 intersect the curve at points A, B and C. The finite difference method makes use of Taylor expansions defined in equation 8.12, by first defining (x - x_0) as Δx. We can rewrite equation 8.12 in terms of the temperature T(x+Δx) of a discrete point (point C in this example) in the grid at a distance Δx beyond the point T(x) (point B), thus

$$T(x+\Delta x) = T(x) + \Delta x \left(\frac{\partial T}{\partial x}\right)_x + \frac{(\Delta x)^2}{2\times 1}\left(\frac{\partial^2 T}{\partial x^2}\right)_x + \frac{(\Delta x)^3}{3\times 2\times 1}\left(\frac{\partial^3 T}{\partial x^3}\right)_x + \ldots \tag{8.13}$$

and similarly, point A can be described as,

$$T(x-\Delta x) = T(x) - \Delta x \left(\frac{\partial T}{\partial x}\right)_x + \frac{(\Delta x)^2}{2\times 1}\left(\frac{\partial^2 T}{\partial x^2}\right)_x - \frac{(\Delta x)^3}{3\times 2\times 1}\left(\frac{\partial^3 T}{\partial x^3}\right)_x + \ldots \tag{8.14}$$

With equations 8.13 and 8.14 we can see that knowing point B in Figure 8.2, it is possible to calculate the temperature at points A and C. In order to do this, it is clear from the above equations that the gradient at point B must also be estimated, which is usually calculated via the forward, backward or central difference approximations.